UNIVERSITY OF LONDON

IMPERIAL COLLEGE OF SCIENCE AND TECHNOLOGY

Mechanical Engineering Department

London, SW7 2BX

TWO-PHASE FLOW PREDICTIONS BY A TIME-MARCHING METHOD

by

Layth Ali Radhi Mubarak, B.Sc(Hon.)

November, 1983

A thesis submitted for the degree of Doctor of Philosophy of the University of London and for the Diploma of Membership of Imperial College.

ABSTRACT

A review of calculation methods for two-phase and transonic one-phase steady flow has shown that time-dependent techniques are convenient for internal flows. While they are gaining popularity for one-phase flows, few applications to two-phase flows have been reported, and then usually with limited inter-phase coupling. The review has also revealed a lack of comprehensive numerical and experimental transonic flow results for two-phase flow systems. The present work is an attempt to extend the time-marching technique to two-phase flows and to provide some experimental data for comparison.

Numerical solutions of one- and two-dimensional two-phase transonic duct flows have been obtained by a time-marching method. The two-phase, unsteady flow equations, with mass, momentum and energy coupling between phases, have been formulated for finite-area "cells", then solved over a succession of small time intervals until steady-state solutions were achieved. The equations used are relevant to a number of multi-phase flow problems, including gas-solid and gas-droplet suspensions, as well as liquid-bubble systems. The spatial accuracy of the method is second-order while in time it is first-order.

In numerical tests for one-dimensional inviscid two-phase flows without inter-phase mass transfer, very satisfactory convergence rates were obtained. The influence of particle loading, density, size and specific heat on the flow process have been examined. The effects of inlet velocity and temperature lags between the particulate phase and the gas-phase have also been investigated. The method has been shown to be capable of handling wall friction, wall heat transfer and gravity effects. These tests provided a starting step for development of the two-dimensional model. Numerical tests for the two-dimensional model

similar to those for the one-dimensional case have also been carried out. Results obtained by the one-dimensional model showed good consistency with other model's predictions. The possibility of dealing with the process of condensation on existing droplets in vapour-droplet flows, as well as extension to polydisperse particle spectra, are discussed in detail.

A convergent-divergent duct test section was designed and set up vertically to provide data on air-glass bead flows for partial validation of the one-dimensional gas-solid model. The experimental work made use of an existing flow loop, which restricted the comparisons to subsonic flow fields. The solid particle velocities were estimated by double-flash photography. The measurements and calculations of pressure and velocities of both phases agreed within the error of the measurements. Limitations of the rig and means for extending the ranges of flow parameters are discussed.

ACKNOWLEDGEMENTS

The author would like to thank the following for their assistance :-

Dr. R.I. Crane for his guidance and comments. His suggestions on the work and comments on the thesis were invaluable.

Dr. J. Damia-Torres for his help and advice on the numerical method and for allowing the inspection of his one-phase flow numerical model.

Dr. J.D. Denton for his comments and suggestions on some aspects of the numerical method.

Professor W. Murgatroyd for his permission to use the gas-solids rig for the experimental part of the work.

Mr. P. Saunders for his help on the experimental test section design and for providing a technical drawing for the test section.

Mr. S. Farwagi for his help and advice on the double flash photography technique.

Mr. W. Lamburn for his help and advice on the technical matters.

Mr. S. Joseph for his help and assistance in operating the experimental rig and for building the test section.

The staff of the Mechanical Engineering Library, headed by Miss E. Archer for their assistance in finding many references.

Mrs. E.M. Pinn for patiently and skilfully typing the manuscript, and the Iraqi Ministry of Petroleum and Minerals for providing the grant during my study.

To

My Parents

CONTENTS

	Page
TITLE	i
ABSTRACT	ii
ACKNOWLEDGEMENTS	iv
CONTENTS	vi
NOMENCLATURE	
CHAPTER 1 : INTRODUCTION	1
1.1 The problem	1
1.2 Two-phase flows	2
1.2.1 Types of two-phase flow systems	2
1.2.2 Types of two-phase flow under consideration	4
1.2.3 Practical relevance of the flows under consideration	6
1.3 Physical consideration of turbomachinery flows	6
1.4 Types of partial differential equations	8
1.4.1 Numerical techniques for the treatment of partial differential equations	10
1.5 Transonic one-phase flow calculation methods	11
1.5.1 Hodograph methods	11
1.5.2 Method of characteristic	12
1.5.3 Streamline curvature method	13
1.5.4 Relaxation methods	13
1.5.5 Finite element method	14
1.5.6 Time-dependent techniques	15
1.6 Merits of the time-marching method	16
1.7 Objectives of the study	18
1.8 Outline of the thesis	19

		Page
CHAPTER 2 :	LITERATURE REVIEW	20
	2.1 Introduction	20
	2.2 Gas-particle flows in general	20
	2.2.1 Stokes number	22
	2.2.2 Knudsen number	24
	2.2.3 Dilute and dense gas-particle flows	24
	2.3 Gas-particle interaction (coupling phenomena)	27
	2.3.1 Inter-phase mass transfer	27
	2.3.2 Inter-phase momentum transfer	32
	2.3.3 Inter-phase heat transfer	36
	2.4 Two-phase flow calculation methods	39
	2.4.1 Equilibrium flow	39
	2.4.2 One-dimensional steady flows	41
	2.4.3 Two-dimensional steady flows	44
	2.4.4 Two-phase flow through normal shock waves	47
	2.5 One-phase flow time-dependent methods	49
	2.5.1 Some standard finite difference schemes	50
	2.5.2 Time-dependent methods in nozzle flows	52
	2.5.3 Cascade and turbomachinery flows	55
	2.5.4 Initial and boundary conditions	58
	2.6 Two-phase flow time-dependent methods	64
	2.7 Closure to chapter 2	68
CHAPTER 3 :	MATHEMATICAL FORMULATION OF TWO-PHASE TIME-DEPENDENT EQUATIONS	70
	3.1 Introduction	70
	3.2 One-phase flow time-dependent equations	70

Page

CHAPTER 3 : continued

3.2.1 One-phase viscous, heat conducting flow equations 70

3.3 Multiphase flow 73

3.3.1 Eulerian two-phase flow time-dependent equations 75

3.4 Two-phase time-dependent equations proposed for the model 77

3.4.1 Supplementary equations 86

3.5 Normalized form of the flow equations 88

3.5.1 One-dimensional two-phase flow equations 88

3.5.2 Two-dimensional two-phase flow equations 93

3.6 Closure to chapter 3 95

CHAPTER 4 : ONE-DIMENSIONAL MODEL 97

4.1 Introduction 97

4.2 Physical features and assumptions 98

4.3 Finite difference approximations 100

4.3.1 Mesh configuration 100

4.3.2 Finite-difference equations 100

4.3.3 Variables approximations 103

4.3.4 Inter-phase interaction 105

4.3.5 Wall friction and heat transfer 106

4.3.6 Numerical procedure 107

4.4 Boundary conditions 108

4.4.1 Inlet cell 108

4.4.2 Outlet cell 111

Page

CHAPTER 4 : continued

4.5 Initial conditions 112

4.5.1 Scheme one 113

4.5.2 Scheme two 114

4.5.3 Other schemes 117

4.6 Smoothing 117

4.6.1 Pressure field smoothing 118

4.6.2 Flow variables smoothing 118

4.7 Other computational aspects 120

4.7.1 Pressure updating 121

4.7.2 Convergence criterion 122

4.7.3 Time step updating 123

4.7.4 Organization of the model 126

CHAPTER 5 : ONE-DIMENSIONAL MODEL'S PREDICTIONS 128

5.1 Introduction 128

5.2 Mixture flow in convergent-divergent nozzle 128

5.2.1 Subsonic flow 129

5.2.2 Shocked flow 131

5.2.3 Flows with supersonic outlets 133

5.3 Parametric study 134

5.3.1 Particle size effects 135

5.3.2 Particle density effects 137

5.3.3 Effects of the particle mass flow rate fraction 139

5.3.4 Particle specific heat effects 142

5.3.5 Inlet velocity and temperature lags effects 142

		Page
CHAPTER 5 : continued		
5.4	Numerical assessment of the model	145
5.4.1	Effects of initial conditions	145
5.4.2	Effects of relaxation factor	146
5.4.3	Effects of time step updating	147
5.4.4	Effects of grid size	148
5.4.5	Effects of pressure updating and smoothing	149
5.5	Comparison with other work	150
CHAPTER 6 :	TWO-DIMENSIONAL TWO-PHASE TIME-MARCHING MODEL	157
6.1	Introduction	157
6.2	Finite-difference discretization	157
6.2.1	Mesh configuration	157
6.2.2	Finite difference form of the flow equations	158
6.2.3	Inter-phase interaction	163
6.3	Boundary conditions	164
6.3.1	Inlet plane	164
6.3.2	Exit plane	165
6.3.3	Solid wall boundary	166
6.3.4	Symmetry conditions	167
6.4	Initial conditions	168
6.5	Other computational features	169
6.5.1	Smoothing	169
6.5.2	Convergence criterion	171
6.5.3	Time step updating	172
6.6	Predictions of the two-dimensional model	173
6.7	**Deposition and collisions**	178

	Page
CHAPTER 7 : GAS-SOLID PARTICLES EXPERIMENT	184
7.1 Introduction	184
7.2 Previous work	184
7.3 Description of experimental apparatus	186
7.3.1 The existing rig	186
7.3.2 Rig's performance	187
7.3.3 The experimental nozzle	188
7.4 Instrumentation and measurements	191
7.4.1 Air velocity measurements	191
7.4.2 Solids velocity measurements	194
7.5 Experimental results	199
CHAPTER 8 : FURTHER DISCUSSIONS AND CONCLUSIONS	208
8.1 Introduction	208
8.2 The computational work	208
8.3 The experimental work	211
8.4 Suggestions for future work	212
APPENDIX A : Derivation of Inlet Boundary Relations	214
APPENDIX B : Wall Pressure Evaluation	217
REFERENCES	221
TABLES	245
FIGURES	248

LIST OF TABLES

TABLE 3.1 Reference Values

TABLE 5.1 Effects of B_1 and B_2 on the convergence rate

TABLE 7.1 Profile of the experimental nozzle

LIST OF FIGURES

Fig. 1.1 Flow patterns in a horizontal pipe

Fig. 2.1 Drag coefficient/Reynolds number relationship for spherical particle moving at uniform relative velocity

Fig. 2.2 Grid used in Denton's time-marching method

Fig. 3.1 Flow cell for one-dimensional flow

Fig. 3.2 Flow cell showing flow area vectors

Fig. 4.1 Mesh for the one-dimensional model

Fig. 4.2 Flow chart for the one-dimensional, two-phase flow, time-marching model

Fig. 5.1 Area distribution for nozzle N1

Fig. 5.2 Pressure distribution for fully subsonic mixture flow with Y_{fi} = 10%

Fig. 5.3 Gas-phase and particle velocities for subsonic mixture flow with Y_{fi} = 10%

Fig. 5.4 Gas-phase and particle temperatures for fully subsonic flow with Y_{fi} = 10%

Fig. 5.5 Pressure distribution for shocked mixture flow with Y_{fi} = 10%

Fig. 5.6 Gas and particle velocities for shocked mixture flow with Y_{fi} = 10%

Fig. 5.7 Gas and particle temperatures for shocked mixture flow with Y_{fi} = 10%

Fig. 5.8 Particle mass fraction distribution for subsonic and shocked mixture flow with Y_{fi} = 10%

Fig. 5.9 Supersonic gas-particle flow in nozzle N1 (Y_{fi} = 10%)

Fig. 5.10 Gas and particle temperatures for supersonic mixture flow with Y_{fi} = 10%

Fig. 5.11 Gas-phase Mach number distribution for supersonic mixture flow with Y_{fi} = 10%

Fig. 5.12 Pressure distribution for various particle sizes for subsonic mixture flow in nozzle N1

Fig. 5.13 Pressure distribution for various particle sizes for shocked mixture flow in nozzle N1

Fig. 5.14 Pressure distribution for various particle sizes for supersonic mixture flow in nozzle N1

Fig. 5.15 Effects of particle size on its velocity in a fully subsonic flow in nozzle N1

Fig. 5.16 Effects of particle size on its velocity in shocked mixture flow in nozzle N1

Fig. 5.17 Dispersed phase velocity for various particle sizes for supersonic mixture flow in nozzle N1

Fig. 5.18 Particle size effects on the gas velocity in a fully subsonic mixture flow in nozzle N1

Fig. 5.19 Particle size effects on the gas velocity in shocked mixture flow in nozzle N1

Fig. 5.20 Gas-phase velocity for various particle sizes for supersonic mixture flow in nozzle N1

Fig. 5.21 Particle temperatures for different particle sizes for a fully subsonic mixture flow in nozzle N1

Fig. 5.22 Particle size effects on the particle temperature in shocked mixture flow in nozzle N1

Fig. 5.23 Gas-phase and particle temperatures for a supersonic mixture flow in nozzle N1

Fig. 5.24 Effects of various particle sizes on the gas-phase temperature for a fully subsonic flow in nozzle N1

Fig. 5.25 Particle size effects on the gas-phase temperature in shocked mixture flow in nozzle N1

Fig. 5.26 Particle material density effects on the mixture pressure distribution for a fully subsonic flow in nozzle N1

Fig. 5.27 Particle material density effects on the mixture pressure distribution for shocked flow in nozzle N1

Fig. 5.28 Particle material density effects on the mixture pressure distribution for supersonic flow in nozzle N1

Fig. 5.29 Particle density effect on the gas-phase velocity for subsonic mixture flow in nozzle N1

Fig. 5.30 Particle size effect on the gas-phase velocity for shocked mixture flow in nozzle N1

Fig. 5.31 Particle material density effects on the gas and particle velocities for supersonic mixture flow in nozzle N1

Fig. 5.32 Particle density effect on the dispersed phase velocity for fully subsonic flow in nozzle N1

Fig. 5.33 Particle density effect on the dispersed phase velocity for shocked mixture flow in nozzle N1

Fig. 5.34 Particle drag force for various particle densities for fully subsonic flow in nozzle N1

Fig. 5.35 Particle drag force for various particle densities for shocked mixture flow in nozzle N1

Fig. 5.36 Particle material density effects on the gas and particle temperatures for fully subsonic flow in nozzle N1

Fig. 5.37 Particle material density effects on the gas and particle temperatures for shocked flow in nozzle N1

Fig. 5.38 Particle material density effects on the gas and particle temperatures for supersonic mixture flow in nozzle N1 (Y_{fi} = 10%)

Fig. 5.39 Pressure distribution for different particle mass flow fractions for fully subsonic mixture flow in nozzle N1

Fig. 5.40 Gas-phase and particle temperatures for different Y_{fi} values for fully subsonic mixture flow in nozzle N1

Fig. 5.41 Gas-phase and particle velocities for various Y_{fi} values for fully subsonic mixture flow in nozzle N1

Fig. 5.42 Y_{fi} effects on the pressure drop across nozzle N1 for fully subsonic mixture flow

Fig. 5.43 Stokes number versus Y_{fi} for fully subsonic mixture flow in nozzle N1

Fig. 5.44 Pressure distribution for different particle mass flow fractions for shocked mixture flow in nozzle N1

Fig. 5.45 Gas and particle temperatures for various Y_{fi} values for shocked mixture flow in nozzle N1

Fig. 5.46 Gas-phase velocity for various particle mass flow fractions for shocked mixture flow in nozzle N1

Fig. 5.47 Particle velocity for various particle mass flow fractions for shocked mixture flow in nozzle N1

Fig. 5.48 Pressure drop across nozzle N1 versus Y_{fi} for shocked mixture flow

Fig. 5.49 Inlet velocity lag effects on the pressure distribution for the fully subsonic mixture flow in nozzle N1

Fig. 5.50 Inlet velocity lag effects on the gas and particle velocities for subsonic mixture flow in nozzle N1

Fig. 5.51 Inlet velocity lag effects on the gas and particle temperatures for fully subsonic flow in nozzle N1

Fig. 5.52 Inlet velocity lag effects on the pressure for shocked mixture flow in nozzle N1

Fig. 5.53 Inlet velocity lag effects on the gas and particle velocities for shocked mixture flow in nozzle N1

Fig. 5.54 Inlet velocity lag effects on the gas and particle temperatures for shocked mixture flow in nozzle N1

Fig. 5.55 Inlet velocity lag effects on the gas and particle velocities for supersonic mixture flow in nozzle N1 (Y_{fi} = 10%)

Fig. 5.56 Inlet temperature lag effects on the pressure for subsonic mixture flow in nozzle N1

Fig. 5.57 Inlet temperature lag effects on the gas and particle velocities for subsonic mixture flow in nozzle N1

Fig. 5.58 Inlet temperature lag effects on the gas and particle temperatures for subsonic mixture flow in nozzle N1

Fig. 5.59 Inlet velocity and temperature lags effect on the pressure for fully subsonic mixture flow in nozzle N1

Fig. 5.60 Inlet and temperature lags effect on the gas and particle temperatures for subsonic mixture flow in nozzle N1

Fig. 5.61 Inlet velocity and temperature lags effect on the gas and particle velocities for subsonic mixture flow in nozzle N1

Fig. 5.62 Relaxation factor effects on the pressure distribution for subsonic mixture flow in nozzle N1

Fig. 5.63 Pressure distribution for different grids for shocked mixture flow in nozzle N1

Fig. 5.64 Area variation for nozzle N2

Fig. 5.65 Comparison of the pressure ratio predictions in nozzle N2 with those of Mobbs *et al.*[66] for $Y_{fi} = 0.091$

Fig. 5.66 Comparison of the gas and particle velocities predicted in nozzle N2 with those of Mobbs *et al.* for $Y_{fi} = 0.091$

Fig. 5.67 Comparison of the gas and particle temperatures predictions with those of Mobbs *et al.* for $Y_{fi} = 0.091$

Fig. 5.68 Comparison of the time-marching model's predictions with those of Mobbs *et al.* for $Y_{fi} = 0.5$ in nozzle N2

Fig. 5.69 Comparison of the gas and particle temperature predictions with those of Mobbs *et al.* for $Y_{fi} = 0.5$ in nozzle N2

Fig. 5.70 Comparison of the predictions of gas and particle velocities for various particle sizes with those of Mobbs *et al.* for $Y_{fi} = 0.5$

Fig. 5.71 Predictions of gas and particle temperatures for different particle sizes as compared with Mobbs *et al.* results

Fig. 5.72 Comparison of predicted gas and particle velocities for different particle material density with those obtained by Mobbs *et al.* in nozzle N2, $Y_{fi} = 0.5$

Fig. 5.73 Comparison of gas and particle temperatures for different particle densities with those of Mobbs *et al.* for $Y_{fi} = 0.5$

Fig. 5.74 Comparison of gas and particle velocities for $VL_i = 0.5$ with those obtained by Mobbs *et al.* for $Y_{fi} = 0.5$

Fig. 5.75 Comparison of pressure ratio predictions along nozzle N2 with Baum's predictions and measurements (shock at x = 14.5 cm)

Fig. 5.76 Comparison of gas Mach number predictions along nozzle N2 with Baum's predictions and experiment (shock at x = 14.5 cm)

Fig. 5.77 Comparison of particle velocity predictions with Baum's predictions and experiment in nozzle N2 (shock at x = 14.5 cm)

Fig. 5.78 Comparison of gas and particle temperature predictions with Baum's predictions in nozzle N2 (shock at x = 14.5 cm)

Fig. 5.79 Comparison of pressure ratio predictions in nozzle N2 with those of Baum (shock at x = 11.75 cm)

Fig. 5.80 Comparison of gas Mach number predictions with Baum's predictions and measurements (shock at x = 11.75 cm)

Fig. 5.81 Comparison of particle velocity predictions with Baum's predictions and measurements (shock at x = 11.75 cm)

Fig. 5.82 Comparison of gas and particle temperature predictions with Baum's predictions in nozzle N2 (shock at x = 11.75 cm)

Fig. 5.83 Comparison of pressure ratio predictions with Baum's predictions and measurements in nozzle N2 (subsonic flow)

Fig. 5.84 Comparison of gas-phase Mach number predictions with Baum's predictions and measurements along nozzle N2 (subsonic flow)

Fig. 5.85 Comparison of particle velocity predictions with Baum's predictions and measurements in nozzle N2 (subsonic flow)

Fig. 5.86 Comparison of gas and particle temperature predictions with Baum's predictions for a subsonic mixture flow

Fig. 5.87 Geometry of the venturi VE2

Fig. 5.88 Pressure drop along the venture VE2 for loading ratio of 0.29

Fig. 6.1 Computational grid for the time-marching, two-dimensional model showing an interior cell and surroundings

Fig. 6.2 Star of mesh points for calculating variables other than pressure

Fig. 6.3 Star of mesh points for pressure approximation

Fig. 6.4 Angles at wall calculation points

Fig. 6.5 Two-dimensional grid for nozzle N1

Fig. 6.6 Axis and wall gas-phase velocity profiles in nozzle N1 (shocked mixture flow)

Fig. 6.7 Axis and wall particle velocity profiles in nozzle N1 (shocked mixture flow)

Fig. 6.8 Axis and wall particle mass fraction distribution in nozzle N1 (shocked mixture flow)

Fig. 6.9 Crosswise variations of particle mass fraction in nozzle N1

Fig. 6.10 Crosswise variations of the gas and particle velocities after the throat in nozzle N1

Fig. 6.11 Calculated flow angles for different particle sizes along quasi-streamlines j=2 and 6

Fig. 6.12 Comparison of the particle mass fraction distribution for different particle sizes in nozzle N1

Fig. 6.13 Crosswise variations of the particle mass fraction for different particle sizes before and after the throat for shocked mixture flow in nozzle N1

Fig. 6.14 Crosswise variations of the particle mass fraction for different particle material densities before and after the throat

Fig. 6.15 Comparison between the gas-phase streamwise velocity along the nozzle (N1) axis as predicted by the one- and two-dimensional models

Fig. 6.16 Comparison between the particulate phase streamwise velocity along the nozzle (N1) axis as predicted by the one- and two-dimensional models

Fig. 6.17 Axial pressure along nozzle N1 as predicted by the one- and two-dimensional models

Fig. 6.18 Axis and wall pressures along nozzle N1 as predicted by the two-dimensional model

Fig. 6.19 Crosswise variation of the pressure in a shocked mixture flow at x = 10.5

Fig. 6.20 Predicted one- and two-dimensional particle mass fractions along nozzle N1

Fig. 6.21 Predicted one- and two-dimensional (axis) gas-phase temperatures along nozzle N1

Fig. 6.22 Predicted axis and wall gas-phase temperatures along nozzle N1

Fig. 6.23 Predicted one- and two-dimensional (axis) particle temperature along nozzle N1

Fig. 6.24 Predicted axis and wall particle temperatures along nozzle N1

Fig. 6.25 Largest relative change of the gas-phase conserved flow variables versus number of time steps for shocked mixture flow

Fig. 6.26 Largest relative change of the particulate phase conserved flow variables versus number of time steps for shocked mixture flow

Fig. 7.1 Arrangement of gas-solids flow rig

Fig. 7.2 Experimental nozzle profile

Fig. 7.3 The experimental test section

Fig. 7.4 Pitot tubes arrangement for gas-phase velocity measurements

Fig. 7.5 Experimental arrangement for pressure measurements

Fig. 7.6 Experimental arrangement for the double flash photography

Fig. 7.7 Electron microscope photograph of the glass beads used in the experiment (each white line represents 1 mm)

Fig. 7.8 Particle size distribution of the glass beads used in the experiment

Fig. 7.9 Double flash photograph (half total area)

Fig. 7.10 Predicted and experimental pressure along the experimental nozzle axis (Y_{fi} = 0.092)

Fig. 7.11 Predicted and experimental pressure along the experimental nozzle axis for Y_{fi} = 0.419

Fig. 7.12 Predicted and experimental gas-phase velocity along the experimental nozzle axis for a mixture with Y_{fi} = 0.092

Fig. 7.13 Predicted and experimental gas-phase velocity along the experimental nozzle axis for a mixture with Y_{fi} = 0.419

Fig. 7.14 Predicted and experimental particle velocity along the experimental nozzle axis (Y_{fi} = 0.092)

Fig. 7.15 Predicted and experimental particle velocity along the experimental nozzle axis (Y_{fi} = 0.419)

NOMENCLATURE

LATIN LETTERS

Symbol	Meaning
A	Control surface area normal to the flow direction. Constant in equation 6.36.
A_L	Control surface area parallel to the flow direction.
A_p	Particle cross section area.
a	Simplifying symbol defined by equation 6.35.
B	Second virial coefficient.
B_1	Time factor used in time step updating (equation 4.63).
B_2	Time factor used in spatially varied time step (equation 4.64).
b	Coefficient in the partial differential equation 1.2.
C_c	Condensation rate on to a droplet.
C_D	Drag coefficient.
C_f	Constant used in evaluating the gas-phase reference dynamic viscosity (equation 4.16).
C_k	Coefficient for parabolic fitting (for variables other than pressure).
$\bar{C}_k$	Coefficient for parabolic fitting (for pressure only).
CON	Simplifying symbol defined by equation 4.46.
c_e	Equilibrium speed of sound.
c_g	Speed of sound in the gas phase.
c_m	Speed of sound in the mixture.

Symbol	Meaning
c_p	Gas-phase specific heat at constant pressure.
c_s	Specific heat of particle material.
c_v	Gas-phase specific heat at constant volume.
D	Self diffusion coefficient (equation 2.20).
	Substantial derivative (equation 2.26).
$\vec{D}_p$	Particle drag force vector referred to a single particle.
D_p	Particle drag force (one-dimensional model) referred to a single particle.
D_p	Substantial derivative for the particulate phase (equation 2.26).
D_t	Nozzle throat diameter (or height).
d	Simplifying symbol (function of x) used in equations 4.14 and 4.28.
d_p	Particle diameter.
E	Total energy per unit mass of mixture.
	Generic variable (equation 2.44).
E_m	Evaporation rate from a single droplet.
e	Internal energy per unit mass of the mixture.
$\vec{e}$	Unit vector.
F	Generic variable (equation 2.44).
Fr	Reference state Froude number.
f	Friction factor.
	Factor = $Re_p C_D/24$ (equation 2.3).

Symbol	Meaning
$f_n(d_p)$	Number frequency of particles of diameter d_p (equation 2.9).
G	Generic variable. Cunningham correction for the drag coefficient.
GF	Gas-phase streamwise smoothing ratio.
g	Acceleration due to gravity.
H	Total enthalpy per unit mass of mixture. Generic variable (equation 2.55).
h	Static enthalpy per unit mass of mixture.
I	Number of crosswise grid lines (two-dimensional model).
i	Crosswise grid line (two-dimensional model).
J	Number of streamwise grid lines (two-dimensional model).
J_i	Nucleation rate expressed as number of nuclei produced per second in a unit mass of mixture.
j	Calculation point (one-dimensional model). Streamwise grid line (quasi-streamline) in the two-dimensional model.
Kn	Knudsen number.
K_1, K_2 C_1, C_2	Constants used in equation 3.56.
k	Number of calculation points (one-dimensional model).
k_g	Gas-phase thermal conductivity.
L	Length of duct. Enthalpy of phase change (equation 2.15).

Symbol	Meaning
M_e	Gas-phase Mach number based on the equilibrium speed of sound (c_e).
M_g	Gas-phase Mach number based on the speed of sound in the gas alone (c_g).
M_m	Gas-phase Mach number based on the speed of sound in the mixture (c_m).
MOM	Mixture momentum.
MOMX	Mixture momentum in x-direction.
m	Mass Mass of gas molecule (equation 2.15).
$\dot{m}$	Mass flow rate.
$\dot{m}_c$	Rate of growth of the droplet (condensation rate).
$\vec{m}_j$	Unit vector in j-direction (equations 3.9 - 3.11). Unit vector tangent to the curve C (equation B.2).
N	Number of particles per unit mass of mixture.
Nu	Nusselt number.
n	Time level (number of time steps). Index of polytropic expansion. Coordinate normal to the wall.
$\vec{n}$	Outward unit vector normal to the control surface.
n_{sm}	Time step when constant smoothing is imposed.
n_p	Number of particles per unit volume (equations 2.9 and 2.10).
P	Pressure

Symbol	Meaning
P_b	Nozzle back pressure.
PF	Particulate phase streamwise smoothing ratio.
Pr	Prandtl number.
q	Heat flux.
q_c	Condensation coefficient.
$\dot{Q}_L$	Rate of heat liberation from a droplet.
Q_p	Heat transfer from a single particle.
Q_w	External heat transfer per unit mass flow per unit length.
R_f	Relaxation factor.
R_g	Gas constant.
Re_g	Gas-phase Reynolds number.
Re_o	Reynolds number at a characteristic velocity V_o (equation 2.12).
Re_p	Particle Reynolds number.
r	Radius of curvature of the wall.
r*	Radius of critical droplet.
r_p	Particle radius.
S	Area.
SC	Fraction used in the streamwise smoothing of the variables (function of Δx).
SF	Streamwise smoothing constant.
St	Stokes number.

Symbol	Meaning
S_f	Flow area.
s	Curvilinear coordinate.
	Entropy.
T	Temperature.
TL	Temperature lag $\left(= \frac{T_p - T_o}{T_g - T_o}\right)$
t	Time.
U_{rel}	Relative velocity between two particle sizes (equation 2.11).
$\vec{U}$, $\vec{u}$	Velocity vector.
U	Velocity.
u	Velocity component in the x-direction.
u_{gi}	Gas velocity in the i-direction.
V	Volume.
V_o	Characteristic velocity (equation 2.12).
VL	Velocity lag $\left(= \frac{u_p}{u_g}\right)$
v	Velocity component in the y-direction.
W	Generic variable.
x	Streamwise or axial Cartesian coordinate.
x_i	Coordinate along the i-direction.
Y	Particle mass fraction
	Wetness fraction
Y_f	Particle mass flow fraction.
y	Crosswise Cartesian coordinate.

Symbol	Meaning
Z	Cartesian coordinate.
	Loading ratio.
	Generic variable.
Z_1, Z_2	Simplifying symbols used in equations 4.40 and 4.43 respectively.

GREEK SYMBOLS

α_{qs}	Angle between the quasi-streamline and the x-axis.
α_r	Heat transfer coefficient.
α_s	Angle between the tangent to a curve and the x-direction.
α_{sm}	Crosswise smoothing constant.
β_1	c_s/c_p
β_2	c_s/c_v
γ	Ratio of gas-phase specific heats (= c_p/c_v).
γ_e	Simplifying symbol defined by equation 2.43.
$\Delta( )$	Change in ( )
ΔG^*	Change in Gibbs' free energy.
Δs	Length of a quasi-streamline segment.
ΔS	Flow face area (two-dimensional model).
$\overrightarrow{\Delta S}_f$	Area vector for flow face f.
Δt	Time step size.
Δt_{max}	Maximum time step for stability.
Δx	Step size in the x-direction.
Δx_i	Step size in the i-direction.

Symbol	Meaning
Δx_j	Step size in the one-dimensional model.
Δy	Step size in the y-direction.
$\Delta\phi$	Correction factor for ϕ
δ_{ij}	Kronecker delta operator.
ϵ	Tolerance Smoothing factor for the pressure.
η	Fraction of particles entering the pitot tube mouth.
θ	Flow angle.
λ	Gas-phase molecular mean free path.
μ	Micron (10^{-6}m)
μ_g	Gas-phase dynamic viscosity.
μ'_g	Gas-phase volumetric (bulk) viscosity.
ν	Simplifying symbol used in equation 2.15.
ρ	Density.
ρ'_p	Particles bulk density.
ρ_p	Particle material density.
σ	Droplet surface tension.
τ_c	Time between collisions for two particles.
τ_g	Gas-phase characteristic time.
τ_{ij}	Viscous stress along the i-direction acting on a surface normal to the j-direction.
τ_p	Particle relaxation time.
τ_w	Wall shear stress.

Symbol	Meaning
ϕ	Generic variable.
ψ	Generic variable.

SUBSCRIPTS

e	Equilibrium mixture flow. Exit.
f	Index (1, 2, 3, 4) for flow face.
fg	Phase transition.
g	Gas-phase.
i	Inlet conditions. Grid-point streamwise index (1,2,----I) for the two-dimensional model. Index (1,2,3) for Cartesian coordinates, i^{th} particle group.
il	Calculated variables at the inlet dummy point (one-dimensional model), inlet face for first flow cell (one-dimensional model).
I	Last crosswise grid line.
j	Calculation point index for the one-dimensional model (j = 1, ---- k). Grid-point crosswise index for the two-dimensional model (1,2, ---- J). Index (1,2,3) for Cartesian coordinates.
J	Last streamwise grid line (upper wall).
k	Index (1,2,3) for Cartesian coordinates. Index for parabolic fitting.
m	Mixture.

Symbol	Meaning
min	Minimum value.
n	Normal to the wall.
p	Particle.
qs	Quasi-streamline.
r	Reference state.
sm	Smoothing.
sub	Subsonic exit and critical mass flow in a nozzle.
t	Nozzle throat or minimum area.
w	Wall.
x	Streamwise direction.
y	Crosswise direction.
o	Stagnation conditions.

SUPERSCRIPTS

f	Final.
i	Initial.
n	Number of time steps.
$t+\Delta t$	Time $t+\Delta t$
*	Critical condition.
	Smoothed variable.
$\rightarrow$	Vector.

ABBREVIATIONS AND IDENTIFIERS

Symbol	Meaning
ANAL•	Analytic solution.
CFL	Courant-Friedrichs-Lewy.
C-L	Centre line.
CPU	Computer processing unit.
CS	Control surface.
N1	Identifier for nozzle shown in Fig. 5.1.
N2	Identifier for nozzle shown in Fig. 5.92.
RHS	Right hand side.
VE2	Identifier for venturi meter shown in Fig. 5.116.
1-D	One-dimensional.
2-D	Two-dimensional.

CHAPTER 1

INTRODUCTION

1.1 THE PROBLEM

The technology of the present engineering world is more conscious of energy, environment, and conservation than it has ever been in the history of human civilization. The sudden awakening of a belligerent consciousness about energy crises and environmental controversies has generated an atmosphere of critical re-evaluation of engineering practices related to energy and industrial systems and processes affecting the environment. The flow of gas conveying particles or droplets is one of the important phenomena from this point of view.

Two-phase flows are of considerable scientific importance and, certainly, of great practical significance; their application is found in mechanical and chemical engineering and in environmental and biological science. The flow of gases with suspended particles is encountered in diverse industrially important energy and environment related applications. The applications range from pulverized coal combustion and gasification, air pollution control systems, pneumatic conveying of granular materials, steam turbines, boilers and condensers to more advanced and unconventional systems for nuclear, geothermal and magnetohydrodynamic power. Furthermore, particulate flows are found in gas turbines. Gas turbine powered aircraft or hovercraft may fly over dusty unimproved land areas or through heavily polluted atmospheres above industrial regions and so encounter suspended particles of dust and dirt as well as water and ice. In the case of industrial gas turbines burning coal directly, ash particles will be present in the products of combustion and some particles may enter the turbine even after filtration between the combustion chamber and turbine. Consequently high velocity particles impact on

engine components, damaging their surfaces, resulting in progressive degradation of engine performance and the reduction of the normal engine overhaul time and life. Similarly, vapour-droplets mixture passing through steam turbine blades causes erosion and corrosion due to droplet deposition on turbine blades and casing.

In all these systems, economy of design, optimization of operating conditions and assessment of safety factors require quantitative information. In most cases, experimental studies are expensive and associated with uncertainties that are contingent on the reliability and accuracy of the measuring techniques; not only are there difficulties in conducting experimental research but also it is sometimes impracticable to simulate environmental problems by laboratory experiment (e.g. fall of rain drops and the precipitation of snow). It is because of these difficulties in obtaining reliable empirical information that a model for predicting such phenomena is particularly to be desired. However, the primary problem in analyzing a gas-droplet or gas-particle flow suspension lies in treating the coupling of mass, momentum and energy between phases. These coupling phenomena comprise a very complex interaction which affects both the gas and particle phases and add a further complication over one-phase flows.

1.2 TWO-PHASE FLOWS

1.2.1 Types of Two-Phase Flow Systems

Two-phase flow is a term which could describe a single- or multi-component system. Single-component systems cover the interacting flow of a single substance in two of its three phases: gas, liquid and solid (e.g. pure liquid and its vapour). The main characteristic of two-phase flows is the existence of an interface. In the case of gas-liquid mixture flowing in a duct several interfacial geometries could be distinguished

(droplets, bubbles, slugs, film....). But this geometry is not always clearly defined, which prevents the flow patterns from being precisely and objectively described. The particular flow pattern depends on the conditions of pressure, flow, heat flux, and duct geometry.

In two-phase flows, the flow patterns must be known in order to model the physical phenomenon as closely as possible. It is obviously impossible to describe bubbly flows and annular flows with a good accuracy by means of the same model. It is far better to adopt two different models, each one fitting the individual flow description. Nevertheless, this approach is still difficult because of the transition zone between two flow patterns and the lack of physical knowledge to describe these buffer zones.

A more general classification takes into account whether the two phases are "well-separated", "well-intermingled" or exist in an "intermediate" state, that is between the two previously defined classes. "Well-separated" flow is found for example when studying the slug flow of gas and liquid along a pipe, while the bubbly flow of a steam-water mixture represents a "well-intermingled" two-phase flow. Furthermore, the annular flow of a steam-water mixture together with entrained droplets is an example of the "intermediate" phenomena. Fig. 1.1 - shows one of many different proposed classifications of gas-liquid flows[1] in a horizontal pipe. In the "bubbly flow" configuration bubbles are moving in the upper part of the pipe. When the gas flow rate is increased bubbles coalesce and a "plug flow" takes place. For low liquid and gas flow rates a "stratified flow" appears with a smooth interface. At higher gas rates waves propagate along the interface ("wavy flow") and can reach the top wall of the pipe giving rise to a "slug flow". Finally at high gas flow rates and low liquid flow rates an "annular flow" can exist with a thicker film in the lower part of the

pipe. It must be emphasized here that the flow patterns in vertical pipes are different to those in horizontal pipes and the horizontal pipe case is chosen here as an illustration to flow patterns in two-phase flow. A more detailed description of two-phase flow patterns in vertical and horizontal pipes can be obtained in many textbooks (e.g. 1,2).

Many other fluid systems are, however, of industrial importance and these include organic liquids, cryogenic liquids (such as oxygen, nitrogen, etc.), liquid metals and gas-solid particle flows. Important applications, particularly in the process chemical industries, involve the use of such multicomponent systems.

1.2.2 Types of Two-Phase Flow Under Consideration

In this work attention is restricted to the flow of gas-particle mixtures which belong to the category of dispersions, that is of media made of a continuous fluid phase and of another phase distributed among discrete volume elements. There exist, a priori, five possible combinations of dispersions according to the nature of the two phases; they can be classified by considering first the fluid phase:

(i) Liquid fluid phase:

- a - Solid dispersed phase: suspension
- b - Liquid dispersed phase: emulsion
- c - Gaseous dispersed phase: foam

(ii) Gaseous fluid phase:

- a - Solid dispersed phase: suspension, smoke, fluidized bed
- b - Liquid dispersed phase: mist, fog, wet steam

The flow of a gas-particle mixture is controlled by the exchange occurring between the two phases; exchange of momentum due to mechanical entrainment of the particles, exchange of heat resulting from thermal non-

equilibrium between the phases, and exchange of mass if there is evaporation, condensation or combustion.

The first type of dispersed flow considered here is the flow of a gas in which small, rigid, and permanent particles are suspended (i.e. gas-solid particle flow). In this type viscous interaction and convective heat transfer between a perfect gas and solid particles are accounted for, while mass transfer by evaporation, condensation or chemical reaction is not considered. Gas-solid particle flow modelling is taken as initial step towards the eventual inclusion and consideration of wet steam flow. Wet steam, especially in turbines, differs from the two-phase system dealt with in equilibrium thermodynamics by the following facts[3]:

(a) The state parameters are subjected to fast changes which may cause supersaturation to occur.

(b) The liquid phase is mostly not bulk liquid, but consists of finely dispersed drops and mist which means that phase boundaries are not plane surfaces.

(c) The vapour phase is not a uniform, monomolecular substance, but also contains submicroscopic-sized clusters of condensed molecules.

(d) There is relative motion between the phases.

(e) There is heat exchange with duct walls.

(f) Spontaneous formation of tiny new droplets (nucleation) may occur in the vapour phase.

(g) Existing droplets grow or evaporate or coagulate with each other or impact on walls and become absorbed in bulk liquid films.

However, the nucleation phenomenon is considered to be outside the scope of the present work and only existing droplet growth will be considered.

1.2.3 Practical Relevance of The Flows Under Consideration

The foregoing section illustrated that gas-particle flows represent one segment of the general class of two-phase flows. It is of interest to know the behaviour of gas-particle flows since they are encountered in many engineering problems and in nature. Such flow problems comprise the conveying of solid particles, dusty gas flow, separation of solid particles, capture of droplets, rocket propulsion, erosion and corrosion of turbine blades caused by deposition and collisison of particles on cascades, ingress of foreign bodies such as sand in aircraft engines, and measurement techniques. For the understanding of such processes, the particle paths in a field of viscous forces, the heat exchange, the attenuation of sound and shock waves must be known.

1.3 PHYSICAL CONSIDERATION OF TURBOMACHINERY FLOWS

In modern turbomachinery cascades, the flow is often characterized by regions containing both supersonic and subsonic flows (i.e. transonic). Transition between supersonic and subsonic regimes in transonic flows can take place smoothly when only moderately supersonic velocities exist, or abruptly when shock waves are formed. The occurrence of mixed supersonic-subsonic flows is common enough so that it is important to be able to predict the behaviour of cascades under these conditions. The interest in the transonic blade-to-blade flow in turbomachinery has increased with the use of more highly loaded gas turbine stages and with the new development in steam turbines to be used in nuclear power plant. Unfortunately, the problem of mixed supersonic-subsonic flow is extremely complex and until recently no generally satisfactory method had been

available for single-phase flows in turbomachines. The essential complication arises out of the fact that in subsonic regions, conditions can be specified on the entire boundary, whereas in supersonic regions these conditions can be specified only on part of the boundary. Mathematically, the character of the subsonic region is said to be elliptic while that of the supersonic region is said to be hyperbolic. In physical terms this means that perturbations in a subsonic flow affect the whole of the flow field whereas perturbations in a supersonic flow affect only the area inside the zone of influence (i.e. changes can not be propagated upstream in a supersonic flow). Any numerical scheme which is used to solve the equations of motion must therefore undergo a change at a Mach number of unity. This leads to further complications as the position of the sonic line is not known a priori. Furthermore, extra complexities arise out of the fact that the flow in modern gas turbines is characterised by being highly three-dimensional, viscous and unsteady. Calculation methods which include the effects of three dimensionality, viscosity and unsteadiness are still far from perfect.

The arguments presented for one-phase flow turbomachinery are also applicable to two-phase flow turbomachinery. The existence of an extra phase in turbines creates additional problems over those experienced in single-phase, resulting in losses of output which are known as wetness losses (in steam turbines). The establishment of an adequate algorithm for predicting two-phase flow in turbomachines has been much delayed for a variety of reasons. The main source of difficulty, in addition to those in gas turbines, is the intricacy of the exchange processes (of mass, momentum and energy) between the phases. The physically complex mechanism of interaction between the phases introduced much perplexity to its mathematical modelling. These exchange processes may involve nucleation, condensation, friction, absorption and dissolution. The laws of such processes are well known only in simple and idealized cases.

Furthermore, when developing a model that takes account of the inter-phase slip, rather than treating the phases as a homogeneous mixture, there are more variables to compute. The problem is not merely quantitative but one of how to produce an economical algorithm for solving the complete set of equations. The foregoing consideration indicates the need for two-phase transonic flow prediction methods capable of dealing properly with the non-equilibrium character of the flow and taking into account inter-phase transfer phenomena.

1.4 TYPES OF PARTIAL DIFFERENTIAL EQUATIONS

Section 1.3 has indicated that care must be taken to its extremes in the choice of a numerical method for the solution of one- and two-phase transonic flows. The main difficulty stems from the fact that small changes in some parameters can lead to large variations in others[4] and alterations in the mathematical nature of the problem. It is perhaps more appropriate to consider the classification and nature of the flow equations in their partial differential form to understand the behaviour of transonic flows in cascades.

A two-dimensional partial differential equation system (PDE) is usually made out of either a set of two first-order equations mainly,

$$\left.\begin{aligned} c_1 \frac{\partial W}{\partial x} + e_1 \frac{\partial W}{\partial y} + c_2 \frac{\partial Z}{\partial x} + e_2 \frac{\partial Z}{\partial y} + g_1 &= 0 \\ c_3 \frac{\partial W}{\partial x} + e_3 \frac{\partial W}{\partial y} + c_4 \frac{\partial Z}{\partial x} + e_4 \frac{\partial Z}{\partial y} + g_2 &= 0 \end{aligned}\right\} \qquad (1.1)$$

or a single second-order equation reducible to a system such as (1.1),

$$a \frac{\partial^2 W}{\partial x^2} + b \frac{\partial^2 W}{\partial x \partial y} + c \frac{\partial^2 W}{\partial y^2} + g = 0 \qquad (1.2)$$

The coefficients of system (1.1) may be functions of x, y, w and z, while those of (1.2) may be functions of x, y, w, $\partial w/\partial x$ and $\partial w/\partial y$. These systems correspond to many classical problems of continuous media[5,6]. At every point (x,y) of the domain there exist two directions, called characteristic directions, along which the integration of the partial differential equation(s) is reduced to an integration involving total differentials only[6]. The equation satisfied by the characteristic directions is a quadratic one in dy/dx called the characteristic equation, whose roots lead to the classification of the partial differential equations. For a hyperbolic system the discriminant of the characteristic equation is positive and there are two real and distinct characteristic directions. Hyperbolic equations describe propagation problems which can be solved in a given region by specifying conditions at only one portion of the boundary, other boundaries remaining open. The hyperbolic system constitutes an initial-value problem[4]. Typical examples of hyperbolic problems, involving inviscid perfect gas, are the unsteady, one-dimensional flow (the characteristics are straight lines in the t-x plane) and the steady, two-dimensional, irrotational, isentropic, supersonic flow.

When there are not real characteristic directions because the discriminant is negative, then the system is elliptic. The steady, two-dimensional, irrotational, isentropic, subsonic flow of a perfect gas is a typical example of an elliptic system. Elliptic equations represent steady processes and can be solved only by specifying the boundary conditions on a complete contour enclosing the whole region, hence an elliptic system is a boundary-value problem. The third type of partial differential equation system is the parabolic system, which occurs when the discriminant of the characteristic equation is equal to zero. This type represents a mixed initial - and boundary-value problem in which the boundary conditions must be closed in one direction but remain open

at one end of the other direction, i.e. this type is a propagation problem. The problem of simple conduction of heat in solid is a typical example of a parabolic system. In propagation problems the solution marches out from the initial state guided and modified in transit by the side boundary conditions[5].

1.4.1 Numerical Techniques For The Treatment of Partial Differential Equations

The numerical treatment of partial differential equations depends strongly on the type of equation or system considered. In the parabolic and hyperbolic cases, which are met in time-dependent problems as well as in steady supersonic flows, a marching procedure may be used. This procedure leads to straightforward explicit computations[7], even in complicated non-linear problems; however, there are usually strong conditions on the stepsize of the progression, if one is to avoid computational instabilities. Steady-state viscous and subsonic inviscid flows lead to elliptic equations, which are much more difficult to solve numerically, because a large system of simultaneous algebraic equations is obtained. Iterations are often used to solve such large algebraic systems. It is interesting to note that many iterative techniques can be interpreted as discretized time-dependent methods, whereby the steady state is obtained asymptotically through a time dependent evolution from arbitrary initial conditions. Standard numerical methods for parabolic and hyperbolic equations may thus be used, as well as the corresponding stability criteria[7].

Problems of mixed type (elliptic - hyperbolic), occurring in the field of transonic inviscid steady flows are even more difficult to treat numerically, since the discretization techniques are very different for elliptic and hyperbolic cases. The difficulty is considerably increased

by the fact that the location of the elliptic and hyperbolic regions is generally not known a priori. Little is known about existence or uniqueness of solutions for such problems and the numerical analyst must therefore hope for the best. Physical intuition itself is not always a reliable guide here[7]. The discretization of partial differential equations can be accomplished through a variety of techniques. The most widely used, at present, are the finite difference methods.

1.5 TRANSONIC ONE-PHASE FLOW CALCULATION METHODS

The ability to deal with mixed subsonic-supersonic flows, in particular with shock waves, is somewhat lacking, and it is in this area that much current research is concentrated. The need to tackle one- and two-phase transonic flows is a very real one, since transonic turbine blading exhausts at modest supersonic velocities, and in highly loaded subsonic impulse sections the flow may become supersonic locally over the blade suction surface. Furthermore, in a high speed compressor rotor-tip section the flow at entry will be supersonic and will shock down to subsonic conditions within the blade.

Most of the research dealing with transonic one-phase flow is concerned with external flows, because of the importance of aeronautical problems. However, internal flows of the mixed nature have been receiving more attention in recent years. Many calculation methods have been developed to deal with transonic flow, they include hodograph methods, relaxation methods, time-dependent methods, the method of characteristics and the finite element method.

1.5.1 Hodograph Methods

These methods make use of the mapping of the physical plane to the hodograph surface. The hodograph surface is defined by the scalar of

the fluid velocity and the flow angle as coordinates. This method is useful as a design tool as the velocity components can be specified to yield x and y as opposed to the analysis method where x and y are specified and the velocity components calculated. The mapping to the hodograph surface would result in a system of linear partial differential equations. However, the hodograph theory cannot be expanded to three-dimensional flows and the possibility of the method to deal with shock waves appears to be very remote[8], but it can be used in the solution of shockless flows[9].

1.5.2 Method of Characteristics

In cases where purely supersonic flows exist the method of characteristics is employed. The term "characteristics" may denote the real solution to any hyperbolic equation[9]. The method uses the fact that for supersonic flow information can only be transmitted along the Mach lines or along the characteristic direction. The initial conditions are given along a curve which is not a characteristic. This curve is approximated by a series of straight lines. The "triangular" network of characteristic lines and their characteristic relationships are built up in a step-by-step manner working outwards from the given curve[9]. In this manner an extremely accurate picture of supersonic flow fields can be built up. The main drawback of the method is that it is necessary to define the position of the sonic line as a starting point for the calculation, which in turn limits the number of cases when it can be used. However, this method has been applied recently by Daneshyar and Glynn[10] in a time-dependent form to one-dimensional steady nozzle flows for any pressure ratio (including shocked conditions) and by Delaney and Kavanagh[11] to solve two-dimensional, steady, transonic cascade flows.

The method of characteristics can be used together with the streamline curvature method for solving mixed subsonic-supersonic flows. The streamline curvature method is terminated on the first completely supersonic quasi-normal, while the method of characteristics starts at the sonic line or on the supersonic quasi-normal.

1.5.3 Streamline Curvature Method

In this method the streamwise velocity gradient along the normal or quasi-normal to the streamline is expressed in terms of an assumed radius of curvature of the streamline. This expression is integrated by marching in the crosswise direction, with the constant of integration given by the continuity equation. When the streamlines are located, a new radius of curvature is determined and the procedure is carried out until convergence. This method has been used by Wilkinson[12] for calculating the flow in the blade-to-blade plane. Transonic solutions can be found by searching for the calculating plane where chocking occurs and then taking subsonic solutions upstream and supersonic solutions downstream of this plane. However, strong shocks cannot be included in the calculation because the inherent discontinuity in streamline slope cannot be obtained, which again limits the number of cases where such a method can be applied.

1.5.4 Relaxation Methods

Relaxation methods are a standard procedure for solving boundary value problems described by elliptic partial differential equations[14]. They cover quite a wide range of techniques and represent an iterative solution of a coupled set of finite difference equations by carrying out successive approximation to a final state that is invariant with further iterations and independent of the initial guess[15]. There are many varieties of relaxation methods (successive point over relaxation, line

relaxation, etc.). From one point of view, relaxation recasts an elliptic equation into a parabolic or hyperbolic equation. Thus in some sense a relaxation method is equivalent to a time-dependent method. These methods are generally applied to potential formulation in order to deal with external inviscid transonic flows. Relaxation methods are quite developed as far as the solution of the transonic small disturbance theory is concerned. However, the small-disturbance formulations are too restrictive and although successful for flow conditions very close to sonic conditions, are inadequate for dealing with strong discontinuities. Furthermore, formulations based on the exact potential flow equation give poor predictions of pressure rises across shocks[4].

1.5.5 Finite Element Method

The finite element method, like the finite difference methods, can be applied to quite arbitrary meshes but its great advantage is that the corresponding discretized equations can be written explicitly, without significant preliminary computation effort[7]. The meshes are arbitrarily shaped polygons, the simplest case using triangles. In each polygon a suitable interpolation formula is used to represent each unknown function in terms of its values at the apices of the polygon. This interpolation is linear in the case of triangular meshes. The equations corresponding to a mesh point P are obtained by differentiating the functional with respect to the value of the functions at P. These values are, therefore, coupled only to values at points which are apices of polygons for which P is an apex. Thus a "local coupling" is obtained between values of unknown functions at neighbouring points, as in the case of finite difference methods[7]. However, finite element method's ability to handle transonic flows is not developed yet[4].

1.5.6 Time-Dependent Techniques

Most of the finite difference approximation methods reviewed so far are generally iterative: one starts with an initial guess of the flow field and tries to correct the errors in successive steps, until the computed values vary from step to step by less than an accepted tolerance. Relaxation techniques applied to the steady state flow equations are a powerful computational tool, which unfortunately may be difficult to use as long as it relies on the skill of the numerical analyst[16]. Time-dependent techniques are based on a different concept: the unsteady flow equations are used to reach a steady flow asymptotically. The difficulties in solving a mixed elliptic-hyperbolic differential equation may be overcome by retaining the time-dependent terms in the governing equations which then become purely hyperbolic. The original boundary value problem is reformulated as an initial value-boundary value problem. If the boundary conditions are time independent (or become so) the solution at large times should represent a steady state solution of the original boundary value problem[14].

By employing the time-dependent approach the numerical analyst is assured of a properly posed problem from a mathematical viewpoint. One can use physically realistic initial conditions and let the flow develop in time much as it would physically. If only a steady state solution is desired the computations need not follow a real time trajectory as the rate of convergence may be increased by using a pseudo-time. The main difference between time-dependent methods and unsteady methods is that the latter refers to techniques solving unsteady flow, which may or may not lead to a steady state and require, among other things, initial conditions according to the flow equations, an accurate treatment of the boundaries, a rigorous treatment of the domain of dependence and high temporal accuracy. Time-dependent methods on the other hand are pseudo-unsteady and the process resulting from the integration of the flow

equations in time is, generally speaking, not truly transient, simply because the boundary conditions are not allowed to adjust themselves to the flow development.

Time-dependent methods may be based on either the integral or the differential form of the flow equations. However, many of these methods employ the differential form of the flow equations; this is mainly because the partial differential equations are familiar to the users and their programming is relatively simple. Furthermore, the analysis of stability and accuracy is much less complicated than for techniques based on the integral form[4]. These on the other hand, can handle arbitrary domains without coordinate transformations and strongly preserve the conservation form on a macroscopic level and not just when the mesh spacing (Δx_i) and the time step (Δt) tend to zero[17]. Some investigators believe that this latter aspect is crucial for stability for sharp boundary curves[4].

1.6 MERITS OF THE TIME-MARCHING METHOD

The foregoing sections have illustrated that the occurrence of mixed supersonic-subsonic flows is common enough so that it is important to be able to predict the behaviour of cascades under these conditions. Moreover, it has been illustrated that time-marching techniques are the most versatile in solving numerically such flows and that the term 'time-marching techniques' comprises those methods which generate intermediate states defining a quasi-unsteady process, leading to the sought steady state. The advantages of time-marching techniques can be summarized as:

(a) The flow has the same mathematical character everywhere.

(b) The technique's extension to three-dimensional cases is comparatively straightforward[18].

(c) Conservation laws are automatically satisfied between two adjacent elements, giving a reasonable accuracy even with a relatively coarse mesh[4,9].

(d) One of the main features of the time-marching method is its simplicity. It is easy to code, debug and modify[4,19].

(e) A quasi-transient behaviour can be examined in a pseudo-real time from some predetermined initial state[4]. This gives a very important physical understanding[19].

(f) Complicated flows may be tackled without prior experimental knowledge of the flow details and pattern which might occur[4,19], for example, location of shocks.

(g) An isentropic relation can be used to treat inviscid weak shocks[9,20] rather than by solving the full energy equation. Furthermore, a constant total enthalpy condition may be employed[21].

(h) The accuracy of the method is better than that of relaxation methods for high Mach numbers[4].

However, the time-marching method does not escape criticism due to some drawbacks which can be summarized as:

(a) Large amount of computer time is needed to obtain a solution[23].

(b) The amount of computer storage is comparatively large[19].

(c) Time step size in the explicit formulation of the method (which is the most common) is limited by the stability consideration. However, a limited success in obtaining larger time steps for implicit formulation have been reported[4].

(d) The introduction of artificial stabilizing "additives" may be needed to ensure stability and convergence[9,24].

(e) Some authors propose the addition of artificial viscosity in order to capture shock waves. This viscosity may exceed that of the real fluid by orders of magnitude[24], this decreases the accuracy for viscous effects at high Reynolds number[4].

(f) Shock smearing may be strong which leads to low resolution in shocked regions[24].

(g) The method is unlikely to become an economic way for solving purely subsonic flows[9].

(h) Relaxation methods require an order of magnitude less computation and can be more attractive for solving external flow problems[4].

1.7 OBJECTIVES OF THE STUDY

The purpose of this study is to develop computational models capable of predicting two-phase flow phenomena in ducts. The study can be thought of as involving the following steps:

(a) To apply the principles behind a certain time-dependent technique, mainly time-marching method, which has successfully tackled one-phase flow in turbomachines, to the solution of inviscid transonic two-phase internal flows.

(b) To investigate the behaviour of gas-solid particle flow in one- and two-dimensions and to establish the credibility of the solution procedure.

(c) To evaluate the conceptual approach of the prediction models by comparison with data obtained by using double flash photography.

(d) To consider the extension of the numerical models to deal with the process of condensation on existing droplets in vapour-droplet flow as well as polydisperse particle size spectra.

1.8 OUTLINE OF THE THESIS

The calculation method developed in this work is for the prediction of fully coupled gas-particle flows. Attention has been focussed on one- and two-dimensional problems in order to examine in depth the foundations of the subject. An overall view of the thesis and its contents is provided below.

Chapter 2 provides a review of the applications of the time-marching method in transonic one-phase flow problems. A review of numerical techniques for the prediction of two-phase flow problems is also included. The mathematical equations governing the transport of mass, momentum and energy of the co-flowing continua are formulated and presented in chapter 3. In chapter 4 the one-dimensional flow equations are transformed to their finite-difference equivalents, and the solution procedure for the resulting one-dimensional model is fully described. The results of the one-dimensional computational model are analyzed in chapter 5.

Chapter 6 contains a full description of the two-dimensional model together with the numerical results obtained from the model. Chapter 7 contains the validation of the one-dimensional model by means of comparison with experimental data obtained from a gas-solid particle rig. The experimental procedure together with the nozzle design, details and performance are also included. Discussion of the results lead to a series of conclusions presented in chapter 8 together with a summary of the achievements of the present study, and suitable directions for future work are recommended.

CHAPTER 2

LITERATURE REVIEW

2.1 INTRODUCTION

The previous chapter has illustrated that gas-particle flows are intended to be a particular class of two-phase flows in which small particles are suspended in a gas. Mass, momentum and energy interchange may occur between the two phases. Mass transfer occur by evaporation and condensation or chemical reactions while momentum and energy transfer occur by viscous interaction and convective heat transfer respectively.

The rapidly increasing capability of computers has led to the development of numerical models for gaseous flows and, in turn, gas-particle and gas-droplet flows. These computational models are a very useful tool for a deeper understanding and a higher level of design in gas-particle flow field, considering both the inability of analytical methods to account for all the complications involved in real problems, and the intrinsic difficulty of experimental investigations and measurement techniques. This chapter reviews the essential features of gas-particle flows from the point of view of model development. Various models that have appeared for one- and two-dimensional flows are discussed. A review of one-phase flow time-marching methods is also included.

2.2 GAS-PARTICLE FLOWS IN GENERAL

Gas-particle mixtures belong to the category of dispersions. In such mixtures the amount of particles may be so small that the gas flow field is not affected by the presence of the particles, while the trajectories of the particles are determined by the motion of the gas. In

such cases the mixture exhibits a "one-way" physical coupling between the two phases (from gas to particles). Moreover, the amount of particles may be large enough to change the gas flow field significantly and resulting in a "two-way" physical coupling between the two phases (from gas to particles and *vice versa*)[25].

In a flowing suspension, the particle mass fraction (wetness fraction in the case of vapour-droplet mixtures), defined as the ratio of the mass flow of particles to that of the mixture, is a very important parameter[26]. Depending on its value, different kinds of gas-particle flows are encountered, ranging from atmospheric dust to fluidized beds. Intermediate conditions between the two extreme cases occur for gas-particle flows in machine ducts, such as turbomachines operating with dusty gases or wet steam, rocket propulsion nozzles with metallic powder and combustion chambers with powdered fuel injection. When the size of the particles and their mass fraction (concentration) are small to the extent that they follow the suspending media (i.e. no slip between the two phases), the flow is of the homogeneous type. The particles in such flows are used as tracers to determine local gas motion. However, because of their inertia, the ability of particles to follow rapid changes of the flow velocity may be inadequate, and it becomes important to analyze the accuracy with which particles of a certain size can be used as tracers in a specific flow[27]. If the particle mass fraction becomes high enough to affect the gas flow, the analysis becomes much more complicated, because both phases of the flow must be considered at the same time. In such cases a very complex interaction takes place, depending on many factors such as the concentration of the particles, the variety of their sizes and shapes, the agglomeration and inter-particle collision and the heterogeneous particle distribution[27,28].

2.2.1 Stokes Number (St)

The Stokes number is an important parameter in classifying special cases for numerical as well as analytic solutions[28]. The Stokes number is defined as the ratio of the particle relaxation time (τ_p) to a gas characteristic time (τ_g)[28,29,30]. The Stokes number, then, is

$$St = \tau_p/\tau_g \tag{2.1}$$

The particle relaxation time (aerodynamic response time) τ_p is the time required for a particle released at zero velocity in a uniform gas flow to achieve $\left(1 - \frac{1}{e}\right)$ or 63.3 percent of the gas velocity. Particle relaxation time can be obtained by integrating the following particle trajectory equation[29,31,32,33]:

$$m_p \frac{d\vec{u}_p}{dt} = C_D \rho_g (\vec{u}_g - \vec{u}_p) |\vec{u}_g - \vec{u}_p| \frac{A_p}{2} + m_p \vec{g} \tag{2.2}$$

where m_p is the particle mass, A_p is the particle area, $\vec{u}_g$ is the gas velocity vector, $\vec{u}_p$ is the particle velocity vector, $\vec{g}$ is the gravity vector, C_D is the drag coefficient and ρ_g is the gas density. Hence, for a spherical particle of density ρ_p and diameter d_p

$$\tau_p = \frac{\rho_p d_p^2}{18 \mu_g f} \tag{2.3}$$

The factor f is the ratio of the actual drag coefficient to the Stokes drag coefficient $24/Re_p$, i.e.

$$f = \frac{Re_p C_D}{24} \tag{2.4}$$

μ_g is the coefficient of gas viscosity and Re_p is Reynolds number based on the slip velocity and particle diameter.

$$Re_p = \frac{\rho_g |\vec{u}_g - \vec{u}_p| d_p}{\mu_g} \tag{2.5}$$

An example of the many proposed relationships between f and Re_p is that used by Crowe[33] and Sharma[29], i.e.

$$f = 1.0 + 0.15\ Re_p^{.687}\ , \tag{2.6}$$

valid for $Re_p < 1000$.

The characteristic time τ_g is the residence time of the gas in the flow duct (nominal length divided by a gas phase velocity). Lee[30,34] in his numerical model for gas-particle flow in a venturi has used the ratio of the throat diameter D_t to the inlet gas velocity to calculate the gas characteristic time, yielding the following expression for the Stokes number:

$$St = \frac{\rho_p\ d_p^2\ u_g}{18\ \mu_g\ D_t} \tag{2.7}$$

If $St << 1$, the particles have ample time to respond to property changes in the conveying gas. In this case, the particle velocities could be taken as equal to those of the conveying gas and the mixture could be treated as a single-phase flow with modified properties. On the other hand, if $St >> 1$, the particles have insufficient time to respond to changes in the gas flow and the mixture may be treated again as a single-phase flow but with distributed resistance and thermal source[28].

2.2.2 Knudsen Number (Kn)

A number of problems of practical importance require knowledge of molecular phenomena in the two-phase medium[35]. To clarify these problems, the molecular-kinetic theory of the structure of the matter is used together with the thermodynamic method. The molecular structure of the gas or vapour phase must be analyzed when the molecular mean free path (λ) is commensurate with the particles or droplets size. Whether the gas behaves with regard to a droplet as a continuum or, at the other extreme, as a free-molecular gas, depends on the value of Knudsen number Kn, which is defined as[3]

$$Kn = \frac{\text{mean free path of gas molecules}}{\text{diameter of particle}} = \frac{\lambda}{d_p} \qquad (2.8)$$

For $Kn < 0.01$ there is continuum flow, while for $Kn > 4.5$ free molecular conditions prevail; in between there is a broad transition regime. Most fog droplets studied in steam turbines fall into the transition regime, especially at low pressure[3]. Knudsen number has been introduced in many expressions for different parameters in two-phase flows like the Nusselt number Nu, heat transfer coefficient of droplets α_r and the drag coefficient C_D, to account for all flow regimes from continuum to free molecule.

2.2.3 Dilute and Dense Gas-Particle Flows

A dilute gas-particle flow is a flow in which particle motion is controlled by local aerodynamic forces; on the other hand, a dense gas-particle flow is a flow in which particle motion is governed by particle-particle interaction and particle collision. The delineation between dilute and dense flows is qualitatively established by the ratio of aerodynamic response time τ_p to the time between collisions (τ_c)[28,33,36].

Crowe[33] has derived the time between collisions for two particles of diameters d_{po} and d_p and velocities $u_p(d_{po})$ and $u_p(d_p)$ respectively as

$$\frac{1}{\tau_c} = \frac{\pi n_p}{4} \int_o^\infty (d_{po} + d_p)^2 \, u_p(d_p) - u_p(d_{po}) \, f_n(d_p) \, d(d_p) \qquad (2.9)$$

where $f_n(d_p)$ is the number frequency of particles of diameter d_p and n_p is the total number of particles per unit volume. The value of n_p can be expressed in terms of the mass of particles per unit volume of mixture (bulk density) ρ_p' as

$$n_p = \frac{6 \, \rho_p' \, \rho_g}{\pi \int_o^\infty d_p^3 \, f_n(d_p) \, d(d_p)} \qquad (2.10)$$

Combining equations 2.3, 2.9 and 2.10, Crowe[33] expressed the ratio τ_p/τ_c as

$$\frac{\tau_p}{\tau_c} = \frac{Z \, Re_o}{12f} \frac{\int_o^\infty \left[1 + \frac{d_p}{d_{po}}\right] \frac{U_{rel}}{V_o} \, f_n(d_p) \, d(d_p)}{\int_o^\infty \left(\frac{d_p}{d_{po}}\right)^3 f_n(d_p) \, d(d_p)} \qquad (2.11)$$

where Z is the loading (mass of particles/mass of gas), U_{rel} is the relative velocity between two particle sizes and V_o is a characteristic velocity. The Reynolds number, Re_o, is defined as

$$Re_o = \frac{\rho_g \, V_o \, d_{po}}{\mu_g} \qquad (2.12)$$

The particle diameter d_{po} should be a diameter representative of the particle flow. A reasonable choice for d_{po} is the mass-averaged or the mass-median diameter (the median diameter is defined as the diameter

for which the cumulative distribution function is equal to one half[30]).

If τ_p is small compared to τ_c, a particle has time to respond to the local gas velocity field before the next collision so its motion is dominated by aerodynamic forces. This condition constitutes a dilute flow. On the other hand, if τ_p is large compared to τ_c, the particle has insufficient time to respond to aerodynamic forces before the next collision so the particle motion is collision-controlled and the flow is dense. In brief

$$\frac{\tau_p}{\tau_c} < 1 \text{ : dilute flow} \tag{2.13}$$

$$\frac{\tau_p}{\tau_c} > 1 \text{ : dense flow} \tag{2.14}$$

The dilute and dense nature of the gas-particle flow depends on particle mass fraction, with decreased particle mass fraction leading to a dilute flow. In addition, particles of the same size in a steady, uniform flow field will have the same velocities and will not collide. However, a distribution of particles subjected to a velocity gradient imposed by the flow field (e.g. flow through a nozzle and a venturi) will accelerate at different rates and collisions will ensue.

When the particles are solid, their collision tends, on the one hand, to limit the velocity differences between particles and, on the other, to ensure their diffusion within the flow. From a theoretical point of view, the movement of each class of particles should be studied by examining the momentum exchanges between that class and all other particles. This interaction term, as seen above, is established by a statistical analysis of the impacts, and this calculation implies a good knowledge of the elementary collisison mechanism. The problem becomes more difficult, but also more important, when liquid particles are

considered[38]. Collisions entail accretions and possibly breakdowns, appearing as a continuous evolution of the condensed phase, particularly unfavourable for aerodynamic predictions. The elementary mechanisms of coalescence are little known, and hence the difficulty in predicting the collision efficiency and the size of the particles formed when accretion is followed by breakdown[38].

2.3 GAS-PARTICLE INTERACTION (COUPLING PHENOMENA)

Compared to modelling single phase flows, modelling multiphase flows is more difficult due to the interfacial coupling phenomena between phases. These coupling phenomena are represented by the exchanges occurring between the phases: exchange of momentum due to mechanical entrainment of the particles, exchange of heat resulting from thermal nonequilibrium between the phases, and exchange of mass if there is evaporation, condensation or combustion. The evaporating or burning droplets/particles will increase the mass of the gas-flow field by effecting a momentum increase in the gas in the direction of the particle's motion (momentum coupling), and heat transfer from particles results in a local increase in the gas thermal energy and changes in local properties such as density and viscosity (thermal coupling)[30]. On the other hand, the effects of condensation are the reverse of those caused by evaporation. These coupling phenomena ultimately influence the entire flow field.

2.3.1 Inter-Phase Mass Transfer

Exchange of mass may take the form of droplet evaporation, condensation, nucleation or burning. The effects of inter-phase mass transfer are usually accounted for in the two phases' continuity equations. However, to account for evaporation and condensation effects, an energy

equation for the individual phase must be introduced, since the process involves the release or absorption of latent heat[27]. The type of mass transfer of interest here is that taking place due to condensation on existing droplets; nucleation is mentioned in this section for the sake of completeness.

From a fundamental viewpoint, condensation may be divided into nucleation, growth and agglomeration. Nucleation is defined as the formation of the least stable (thermodynamically or kinetically) cluster or particle of the new phase. Growth is the molecule-by-molecule disposition of new material onto the nucleus or larger particles. Agglomeration (coagulation) is the coalescence of two colliding particles to form a larger particle. The rate of condensation and also the size distribution of the product particles therefore involve the simultaneous kinetics of a sequence of nucleation, growth and agglomeration reactions. Nucleation is considered here to be outside the scope of this study while coagulation is generally thought to play an unimportant role in nozzle and low-pressure turbine flow. In the high pressure blading of nuclear turbines, coagulation between droplet streams moving at different speeds may possibly be important because of the higher number concentration, but this problem has only recently been receiving attention[39]. Nucleation and coagulation will therefore not be further considered beyond this chapter.

Nuclei that emerge from the nucleation process as stable droplets with radius larger than the critical droplet radius will grow by capturing molecules from the vapour. The formation rate of critical droplets per unit mass of vapour per unit time as used by Bakhtar *et al*[40] is

$$J = \frac{q_c}{1+\nu}\sqrt{\left\{\frac{2\sigma}{\pi m^3}\right\}}\frac{P_s(T_g)}{\rho_p}\exp\left\{\frac{-\Delta G^*}{R_g T_g}\right\} \qquad (2.15)$$

where

$$\Delta G^* = \frac{4\pi r^* \sigma}{3}$$

and

$$\nu = \frac{q_c \rho_g}{\alpha_r} \sqrt{\left(\frac{R_g T_g}{2\pi}\right)} \left(\frac{L^2}{R_g T_g^2} - \frac{L}{2T_g}\right) ;$$

also, q_c is the condensation coefficient, σ is the droplet surface tension, m is mass of one molecule of vapour, T_g is the vapour temperature, $P_s(T_g)$ is the saturation pressure corresponding to T_g, R_g is the gas (vapour) constant, ρ_p is the droplet density, G^* is Gibbs' free energy of the critical droplet, α_r is the heat transfer coefficient, ρ_g is the vapour density and L is the enthalpy of phase change. The Kelvin-Helmholtz relation describing the radius of a critical droplet in metastable equilibrium with a supercooled vapour is(39-44)

$$r^* = \frac{2\sigma}{\rho_p R_g T_g \ln\left\{\frac{P}{P_s(T_g)}\right\}} \qquad (2.16)$$

The condensing molecules give up latent heat to the liquid which has then to be transferred back to the vapour. To obtain an appreciation of what is involved consider the temperature rise of a cluster of molecules when it captures another molecule. The temperature rise of the cluster will so affect the saturation vapour pressure of the droplet that unless the heat is carried away very quickly, the cluster will have to lose the molecule. Thus the rate of condensation on a particle (drop) is governed by the rate at which the latent heat can be carried away from the surface into the cooler vapour. Hence, in order to follow

the growth of the droplet the expressions for heat and mass transfer must be solved simultaneously.

During the droplet growth, condensation rates vary in a broad range. The lowest value is encountered in the free molecular regime where the mean free path of the vapour phase molecules is much larger than the droplet diameter; in this case, the laws of kinetic theory of gases dominate the process. The other extreme refers to the continuum regime where the mean free path is much smaller than the droplet diameter; here, the laws of continuum mechanics can be applied. It is then convenient to define the process relevant to the local conditions by the Knudsen number, which is defined by equation 2.8 as

$$Kn = \frac{\lambda}{2r_p}$$

where r_p is the droplet radius. Considering the case when the particle is small enough to be in the free molecule regime (Kn >> 1), the rate of condensation on to a droplet C_c in mass per unit time can be obtained from the kinetic theory of gases[41,42,45]

$$C_c = \frac{4\pi r_p^2 P q_c}{(2\pi R_g T_g)^{\frac{1}{2}}} \qquad (2.17)$$

Here, there is a possibility that the vapour and liquid are at different temperatures, hence the use of suffix (g) to denote the vapour phase. The gross evaporation rate from the surface of a given droplet is a function of its temperature alone and to calculate this rate it should be noted that this would be equal to the condensation rate if the droplet were in equilibrium. Hence using E_m to denote the evaporation rate,

$$E_m = \frac{4\pi r_p^2 P_s(T_p, r_p) q_c}{(2\pi R_g T_p)^{\frac{1}{2}}} \qquad (2.18)$$

where T_p denotes the droplet temperature and $P_s(T_p,r_p)$ the saturation pressure corresponding to T_p and a surface of radius r_p. Therefore the rate of growth of the droplet can be written as:

$$\dot{m}_c = q_c r_p^2 \left(\frac{8\pi}{R_g}\right)^{\frac{1}{2}} \left[\frac{P}{T_g^{\frac{1}{2}}} - \frac{P_s(T_p,r_p)}{T_p^{\frac{1}{2}}}\right] \tag{2.19}$$

If the particle is large enough to be in the continuum regime (Kn << 1), Jackson[46] suggests the use of the following formula

$$\dot{m}_c = \frac{4\pi r_p D}{R_g} \left[\frac{P}{T_g} - \frac{P_s(T_p,r_p)}{T_p}\right] \tag{2.20}$$

which is the classical diffusion formula originally suggested by Fuchs[47]. In the above equation D is the self-diffusion coefficient appropriate to the gas temperature T_g. At the stages when the droplet is between these extreme ranges equation 2.19 should be modified. However, a relationship due to Young[48],

$$\dot{m}_c = \frac{8}{3} \frac{r_p^2 \, Kn}{\left(1 + \frac{8}{3}\frac{Kn}{q_c}\right)} \left(\frac{8\pi}{R_g}\right)^{\frac{1}{2}} \left[\frac{P}{T_g^{\frac{1}{2}}} - \frac{P_s(T_p,r_p)}{T_p^{\frac{1}{2}}}\right] \tag{2.21}$$

is corrected for variations of vapour temperature in the vicinity of the droplet and is intended to apply for all droplet sizes.

The rate of heat liberation $\dot{Q}_L$ is connected to droplet growth rate,

$$\dot{Q}_L = \Delta h_{fg} \frac{dm_p}{dt} = \Delta h_{fg} \, 4\pi r_p^2 \rho_p \frac{dr_p}{dt} \tag{2.22}$$

while the heat transfer rate Q_p from the droplet to the vapour is given by

$$Q_p = 4\pi r_p^2 \alpha_r (T_p - T_g) \tag{2.23}$$

In the above equation the heat capacity of the droplet (particle) is neglected. The heat balance requires

$$\dot{Q}_L = Q_p$$

i.e.

$$\Delta h_{fg} \frac{dm_p}{dt} = 4\pi r_p^2 \alpha_r (T_p - T_g) \tag{2.24}$$

The behaviour of any wet vapour is dominated by the droplets present within it and the growth or evaporation of droplets is determined by equations 2.19 and 2.24. Thus these two equations are the key to predicting the behaviour of wet steam. However, in the case of solid particles suspended in a gas the importance of inter-phase mass transfer diminishes since the solid particle's mass is constant. The emphasis in such flows is solely based on the importance of inter-phase heat transfer. For gas-solid particle flow equation 2.23 can be written as[49]

$$\frac{\pi d_p^3}{6} \rho_p c_s \frac{dT_p}{dt} = \pi d_p^2 \alpha_r (T_p - T_g) \tag{2.25}$$

where c_s is the specific heat of particle material.

2.3.2 Inter-Phase Momentum Transfer

The density of solid (or liquid) particles is generally much larger than the density of the ambient gas (or vapour). Because of inertial effects, particles cannot follow immediately the motion of the gas but show relaxation[50]. These particles move under the influence of forces

exerted on them by the gas, but if the particle concentration is low enough (dilute mixture), the reaction of these forces affects the gas flow only to a negligible extent. Interactions of particles with wakes of other particles then also are of no consequence. The one-dimensional equation of motion for a spherical particle in a gas flow is given, e.g. Soo[51], Rudinger[49], by

$$\frac{\pi d_p^3}{6}\rho_p \frac{D_p u_p}{Dt} = \text{Viscous Drag} - \frac{\pi d_p^3}{6}\frac{\partial P}{\partial x} + \frac{1}{2}\frac{\pi d_p^3}{6}\rho_g\left(\frac{Du_g}{Dt} - \frac{D_p u_p}{Dt}\right)$$

$$+ \frac{3}{2} d_p^2 (\pi\rho_g\mu_g)^{\frac{1}{2}} \int_0^t \frac{\frac{Du_g}{Dt'} - \frac{D_p u_p}{Dt'}}{(t-t')^{\frac{1}{2}}} dt' \qquad (2.26)$$

where the substantial derivatives must be taken along the trajectories of the gas and of the particles, so that

$$\frac{D}{Dt} = \frac{\partial}{\partial t} + u_g \frac{\partial}{\partial x} \qquad (2.27)$$

and

$$\frac{D_p}{Dt} = \frac{\partial}{\partial t} + u_p \frac{\partial}{\partial x} \qquad (2.28)$$

Lateral forces on the particles may develop as a result of particle rotation, slip in the shear flow of a boundary layer, and other effects[49]. Such forces will not be considered here.

The left-hand side of equation 2.26 represents the product of mass and acceleration, while the right-hand side indicates various forces that act on the particle. The first term represents the viscous drag force which will be discussed below. The second term shows the effect of the pressure gradient in the gas for which the gas acceleration can be substituted by using the gas momentum equation[49]

$$\rho_g \frac{Du_g}{Dt} = - \frac{\partial P}{\partial x} \tag{2.29}$$

However, if the gas flow is affected by the particles, the above relation does not hold, and the substitution then is not permissible (see Rudinger[49]). The third term indicates the force needed to accelerate the added mass which, for a spherical particle, equals one-half of the mass of the displaced fluid. The integral term, which is known as Basset force, accounts for deviation of the flow pattern around the particle from that for steady flow; it represents the influence of the history of the motion on the instantaneous force. The effect of the history of the motion may affect the particle trajectory under extreme conditions. However, under the usual conditions, in which ρ_p is about three orders of magnitude greater than ρ_g, only the viscous drag need to be considered here.

The drag force exerted by a fluid medium on a spherical particle in relative motion depends primarily on the velocity of the gas phase relative to the particle. The drag force for a spherical particle in the x-direction, can be written as

$$\text{Viscous Drag} = C_D \cdot \frac{\pi d_p^2}{4} \cdot \frac{1}{2} \rho_g (u_g - u_p) |u_g - u_p| \tag{2.30}$$

In continuum flow regime, the drag coefficient C_D is a function only of the particle Reynolds number defined in equation 2.5. The "standard drag curve" for a sphere drag coefficient against particle Reynolds number, Fig. 2.1, appears to be used by almost all investigators to evaluate the force on a solid particle being accelerated by the surrounding fluid medium. This drag has been obtained by many workers from measurements of the drag force on a single sphere at constant velocity

in still, isothermal, incompressible fluid of effectively infinite extent. However, when one compares this with conditions in dispersed flows where the particle is present in a moving, often accelerating fluid stream, possibly of temperature different from that of the particle, and in the presence of many other particles, the similarity between the two flow conditions seems to be remote.

Previous workers in theoretical studies of a gas-particle nozzle flows have mainly considered very small particles and have assumed the well known classical Stokes solution where

$$C_D = \frac{24}{Re_p} \tag{2.31}$$

applies. The drag then takes the simple form

$$\text{Stokes Drag} = 3\pi\, d_p\, \mu_g (u_g - u_p) \tag{2.32}$$

The above expression is only valid for very low velocities when the particle Reynolds number $Re_p < 0.1$ and the inertia terms in the equation of motion, of a viscous fluid, are neglected compared with viscous forces. For higher particle Reynolds numbers, the empirical correlation between the drag coefficient and Re_p, over a wide range, proved to be the aim of several analytical treatments of flows beyond the Stokes regime. Many empirical fits to the standard drag curve have appeared in the literature (e.g. Carlson *et al.*[52], Boothroyd[53], Kannapprakasam[54] and Soo[51]). Crowe *et al.*[31], Sharma[29,32] and Lee[30] used equation 2.6 to calculate C_D for gas-particle flow in venturis. For liquid droplets in gas flow: Moore[57] suggested the following expression for C_D (obtained by Churchill and Usagi[58]).

$$C_D = \frac{24}{Re_p}\left[1 + \left(\frac{Re_p}{60}\right)^{5/9}\right]^{9/5},$$

$$0 < Re_p < 3000. \qquad (2.33)$$

If the particles are extremely small, or the gas density is quite low, the molecular mean free path in the gas, λ, may become comparable with the particle dimensions, and it then becomes necessary to introduce a correction to the drag coefficient. This correction, usually called the "Cunningham correction" is a function of the Knudsen number. The corrected drag coefficient is

$$C_D' = \frac{C_D}{G} \qquad (2.34)$$

where

$$G = 1 + Kn(2.492 + 0.84\, e^{-1.74/Kn})$$

The above relationship for G was obtained by Fuchs (as reported by Rudinger[49]).

2.3.3 Inter-Phase Heat Transfer

In compressible flow, any velocity change is accompanied by a temperature change. Thus, both the velocity and the temperature of the suspended particles can lag behind the corresponding gas values[49]. For a particle moving relative to a gas stream the heat exchanged between the gas and the particle is mainly transferred by convection. The rate of heat transfer by convection between the suspended particle and the flowing gas can be expressed by equation 2.23

$$Q_p = (\pi d_p^2)\, \alpha_r (T_p - T_g)$$

where α_r is the heat transfer coefficient, T_p is the particle temperature and T_g is the gas temperature. The heat transfer coefficient α_r can be expressed in terms of the Nusselt number Nu, which is defined as

$$Nu = \frac{\alpha_r d_p}{k_g} \tag{2.35}$$

where k_g is the thermal conductivity of the gas.

Theoretical solutions for heat transfer to a sphere exist only for Reynolds numbers sufficiently low that the symmetrical Stokes flow field prevails. Consequently, for particle Reynolds number greater than 0.1, empirical expressions have to be relied upon. The theoretical solution for heat transfer from a sphere at a given temperature submerged in a fluid at another temperature, can be obtained by equating the rate of heat loss from the sphere by conduction to the rate of heat transfer by convection[59]. The value of $Nu = 2$ applies for pure heat conduction. Additional heat transfer by convection takes place if the particle moves with respect to the gas[49]. The Nusselt number then becomes a function of the particle Reynolds number Re_p. Soo[51] suggests that almost all solutions are given in the series expansion form:

$$Nu = 2 + \frac{1}{2} Re_p Pr + \frac{1}{6} (Re_p\, Pr)^2 + \text{---} \tag{2.36}$$

where Pr is the Prandtl number of the fluid defined as

$$Pr = \frac{c_p \mu_g}{k_g} \tag{2.37}$$

and c_p is the specific heat of the fluid at constant pressure. A frequently used relationship, e.g. Crow *et al.*[31], Johnson[60], Sharma[29,32], Neilson and Gilchrist[61] and Bowers[59], is

$$Nu = 2.0 + 0.6\ Re_p^{0.5}\ Pr^{0.333} \tag{2.38}$$

for $1 < Re_p < 70000$ and $0.6 < Pr < 400$. Other investigators, e.g. Mobbs *et al.*[66], Glazunov and Rychkov[67], Hoglund[68] and Dash and Thorpe[69] have used

$$Nu = 2.0 + 0.459\ Re_p^{0.55}\ Pr^{0.333} \tag{2.39}$$

One of the important assumptions in calculating the thermal energy exchange between particles and gas is that heat transfer occurs by convection only so that equations 2.23 and 2.35 yield the following expression

$$Q_p = (\pi d_p^2)\ \frac{Nuk_g}{d_p}\ (T_p - T_g) \tag{2.40}$$

The foregoing relationships imply that the temperature is uniform throughout the particle, but heat flux into, or out of, the particle requires internal temperature gradients. However, uniform temperature can be assumed if the rate of temperature equalization within the particle is fast compared with the rate of heat transfer between the particle and the gas; this has been shown by Rudinger[49] to be almost always true. In the case of particle clouds, uncertainties arise in evaluating the drag coefficient and the Nusselt number due to the high concentration of particles and particle collisions with each other. The resultant uncertainty of the drag coefficient and the Nusselt number is emphasized by Rudinger[49] and Hoglund[68].

2.4 TWO-PHASE FLOW CALCULATION METHODS

The subject of modelling of two- or multiphase-flows has become increasingly important to a wide variety of engineering applications. Frequently, a viable model for gas-particle flow is needed to complement the design of engineering systems. A first way to face the problem of gas-particle flow modelling is to assume dynamic and thermal equilibrium between the two phases in order to consider the suspensions as a single homogeneous fluid with modified properties with respect to the ambient supporting fluid to account for the presence of the suspended particles. In this approach the suspension is usually assumed to be dilute[25]. However, models employing a more physical assumption of two separate phases have appeared in the literature. One-way coupling models either based on a Lagrangian approach for the trajectories of the particles[70], or based on the Eulerian approach considering the particle as a continuum [71], have been frequently used. Two-way coupling models are also available in the literature although less frequently than the one-way coupling models[25,72]. In such models the reciprocal interaction of the fluid and particles must be considered.

2.4.1 Equilibrium Flow

Equilibrium flow represents an idealised gas-particle flow where the suspended particles are always assumed to be travelling at the same velocity, and to have the same temperature as the neighbouring gas. With such assumption, the particle momentum equation and the particle heat transfer equation are no longer applicable[59]. By making use of the equilibrium flow concept, a number of investigators, e.g. Kliegel[73], Kriebel[74] and Bowers[59], have derived from the basic flow equations a set of relationships similar to the one-dimensional perfect gas flow relationships, except that the Mach number is now the equilibrium Mach

number, and the ratio of the specific heats for a gas is replaced by that for a gas-particle mixture, i.e. $u_p = u_g$, $T_p = T_g$ and

$$M_e = \frac{u_g}{c_e} \tag{2.41}$$

where M_e is the equilibrium Mach number and c_e is the equilibrium sound speed found by Kliegel and Kriebel to be,

$$C_e^2 = \frac{\gamma_e R_g T_g}{\left[1 + \frac{\dot{m}_p}{\dot{m}_g}\right]} \tag{2.42}$$

and $\dot{m}_p$ is the mass flow rate of the particles, $\dot{m}_g$ is the mass flow rate of the gas. γ_e is defined as

$$\gamma_e = \frac{\gamma\left[1 + \left(\frac{\dot{m}_p}{\dot{m}_g}\right)\left(\frac{c_s}{c_p}\right)\right]}{\left[1 + \gamma\left(\frac{\dot{m}_p}{\dot{m}_g}\right)\left(\frac{c_s}{c_p}\right)\right]} \tag{2.43}$$

where γ is the gas specific heats ratio c_v/c_p. Kliegel[73,75] has gone one step further in that he has derived a set of relationships, again similar to the one-dimensional perfect gas flow equations, but the Mach number and ratio of specific heats are those corresponding to there being a constant fractional lag of particle velocity to gas velocity and of particle temperature to gas temperature. The criteria for the "constant fractional lag" flow are that the velocity lag and temperature lag should remain constant throughout the flow. The particle momentum and particle heat transfer equations are also not applicable for this flow. Bowers[59] has included in his thesis a comprehensive derivation for equilibrium and constant fractional lag flow relationships. Kliegel [73,75] and Kriebel[74] have used the above concepts to investigate flows

through nozzles and across normal shock waves of gas-solid particle mixtures

2.4.2 One-Dimensional Steady Flows

One-dimensional and quasi one-dimensional steady gas-particle flows numerical models have been developed to predict performance losses in rocket nozzles with condensed combustion products or to evaluate the effects of the inclusion of metallic powder in solid rockets. In this case, information is restricted to travel in one direction only and solutions can be obtained by integrating the governing equations in this direction[28]. Kliegel[75] has used this approach to model gas-particle flow in a Laval nozzle. The particle and gas equations were integrated explicitly accounting for momentum and thermal coupling. Kliegel found that since the conditions at the sonic point depend on the particle lags at the sonic point, these conditions can be changed by changing the nozzle inlet and throat geometry. This simply means that the upstream velocity must be varied until the solution proceeds smoothly through the sonic region near the throat, since the correct inlet conditions are unknown a priori. This technique was used extensively by other investigators, e.g. Hultberg and Soo[76], Hoglund[68], Neilson and Gilchrist[61], Mobbs *et al.*[66], Ishii[77] and Cole *et al.*[78]. While most investigators[61,68,76] considering gas-particle flow through nozzles have assumed the gas and the particles to be in velocity and temperature equilibrium at the nozzle inlet, Mobbs *et al.*[66] have examined the effects of varying degrees of velocity and temperature disequilibrium at the nozzle inlet on the subsequent flow through the nozzle.

Sharma *et al.*[32] developed a quasi one-dimensional numerical model for analyzing gas-particle flows through venturis, utilizing conservative variables and PSI-cell concept (particle source in cell). In this model

the equations are expressed in conservative form for the gas using mass flow $(\rho_g u_g A)$, momentum flux plus pressure $(\rho_g u_g^2 A + PA)$, and total energy flux $\left(h_g + \frac{u_g^2}{2}\right)\rho_g u_g A$ as the dependent variables. In the above A is the cross-sectional area and h_g is the gas enthalpy. Furthermore, the mass, momentum and energy coupling terms due to the particles appear as source terms to the gas phase. The numerical procedure for each computational cell proceeds by assuming a value for the downstream pressure and setting the particle source terms equal to zero. The new gas velocities and temperatures derived from the conservative variables at the downstream station are used to calculate new particle source terms and the new pressure is used to update the initial guess. The iteration continues until the downstream pressure converges within acceptable limits. When the computation of one cell is complete, the scheme proceeds to the adjacent downstream cell. This scheme is reported by Crowe[28] to be conceptually simple and its results show good agreement with experiment. Baghdadi[27] has used another quasi-one-dimensional numerical model for gas-particle flows. The model is based on a system of equations for the entire field and solved by using relaxation methods. The model was applied to gas-particle flow in a venturi as studied by Sharma[29] and good agreement with experimental data is reported.

Campbell and Bakhtar[45], Yousif *et al.*[79] and Bakhtar *et al.*[80] in predicting nucleation and droplet growth in nozzles have used a system of equations which was originally used by Oswatitsch[81]. With the assumption that the two phases travel with the same velocity and that the flow area occupied by the liquid phase is small, their calculation procedure used in the integration of flow equations over a step length Δx in the condensing zone is as follows:

(i) By using the known properties of steam at entry to Δx, the droplet formation and growth equations (similar to equations 2.15 and 2.16 respectively) are used to calculate the first approximations to the mean values of the change in liquid phase mass flow rate (ΔM_L) and the liquid phase mass flow rate (M_L) over the step. These values are then used to integrate the flow equations over Δx.

(ii) The resulting properties of steam are reapplied as entry conditions to the element resulting in new average values for ΔM_L and M_L. A new mean of the values of ΔM_L and M_L calculated in (i) and this step is then calculated and introduced into the flow equations which are then integrated over Δx and starting from the original initial conditions.

This numerical procedure is reported to be accurate to second order.

Moore *et al.*[82] have developed a method of predicting the fog-drop size in wet steam turbines. Similar to Bakhtar's method, this method assumes that slip between steam and drops is negligible. The flow equations are written as simultaneous differential equations and complemented by a wetness gradient equation and different nucleation theories. The simultaneous differential equations are then integrated using a fourth order Runge-Kutta method. However, the method is reported to have a singularity at the sonic point and a standard iterative procedure is used to locate its position and to determine the critical mass flow so the integration can be restarted at supersonic conditions. This method was shown through comparisons with experimentally measured pressure distributions to be successful in predicting the nucleation and growth of droplets in the supersonic expansion region. Jackson[83] has used the above method to calculate one-dimensional monodispersive flow of wet steam through ducts. However, this model takes into account the

relative motion between the phases. The system of equations used is a steady version of the time-dependent equation derived by Jackson[46]. Puzyrowski and Studzinski[84] in their investigation of condensation phenomena in one-dimensional flow of water vapour through nozzles have also used an iterative procedure between inlet and throat to achieve the correct mass flow rate at the saddle point. Several other investigations of condensing flows have been carried out, e.g. Hill[41], Hill *et al.*[42], Wegener and Parlange[85] and Wegener and Mack[86].

2.4.3 Two-Dimensional Steady Flows

Several two-dimensional computational models for solving steady gas-particle flows have been reported in the literature. Regan *et al.*[87] have developed a model for solving transonic gas-particle flows in axisymmetric nozzles. The method is in two stages, in the first stage, the gas-particle mixture is assumed to be in equilibrium (i.e. there are no particle velocity or temperature lags, and the two-phase mixture is treated as a heavy perfect gas with modified isentropic exponent and modified molecular weight) and an initial flow field is then obtained. Alternatively, a constant fractional lag mixture assumption is used to provide initial estimate of the flow field. The initial flow field data are used as starting values for the second stage which involves a relaxation procedure. The non-equilibrium effects of the two-phase mixture are incorporated in this stage. The partial differential equations governing the gas-particle flow are rewritten as algebraic replacement equations and solved iteratively by using a modified Gauss-Siedel method. This method has also been used by Cousins[88] to predict two-phase flow through a rocket exhaust nozzle.

The trajectory methods have been used to solve subsonic two-dimensional gas-particle flows. This approach (Particle-Source-in-Cell) is based on

treating the particles as sources of mass, momentum and energy to the gaseous phase. Finite-difference equations for mass, momentum and energy conservation are written for each cell, incorporating the contribution due to the condensed phase. Thus, the continuum flow field is analyzed by utilizing the Eulerian approach. The particle trajectories, size and temperature history are obtained by integrating the equations of motion for the particles in the gas flow field and utilizing expressions for the particle-gas mass and heat transfer rates. Thus, solving for the particle velocity, size and temperature along particle trajectories is done using the Lagrangian approach. The solution procedure begins by solving the gas flow field assuming no particles are present. Using this flow field, particle trajectories, and the mass and temperature history on individual trajectories are then calculated through the gas flow field. The particle properties on crossing the boundaries of computational cells yields the mass, momentum, and energy source terms for the gas in each cell. The gas flow field is then recalculated, taking into account these source terms. New trajectories are calculated and source terms re-evaluated. The process is continued until the flow field fails to change with repeated iteration. This method has been used by Crowe and Pratt[89] with the vorticity-stream function formulation to solve for the gas-particle flow in a cyclone separator. This formulation is also used by Crowe and Stock[90] for the solution of gas laden with hot particles issuing into a sudden expansion. Crowe[91] has analysed gas-droplet flow field near an atomizer by using the trajectory method. Furthermore, Lee[30,34] has employed this approach for the solution of gas-particle flow in two-dimensional nozzles.

The method of characteristics is well established and widely used for supersonic solutions of two-dimensional flows. In this method

pairs of characteristic lines are drawn from an initial line. The compatibility conditions between the dependent variables yield the values of the dependent variable at the point where the characteristic lines cross. The particle path constitutes a third characteristic. The integration of the equations for particle properties along the particle path yields the particle compatibility condition which yields the gas and particle properties at the intersection point when combined with the gas-phase compatibility conditions[28]. Kliegel[73] has used this approach to analyse the flow of gas-particles in rocket nozzles. Johnson[60] has also used this method for solving supersonic gas-particle flow in axisymmetric nozzles. Recently, another numerical scheme for two-dimensional supersonic gas-particle flows has been developed by Dash and Thorpe[69]. In this case the two-dimensional flow equations are written in conservative form and represented by

$$\frac{\partial E}{\partial x} + \frac{\partial F}{\partial y} + G = 0 \qquad (2.44)$$

where E and F are variables representing combinations of gas-phase flow properties and x and y are the marching and transverse directions respectively. The effects of the particles are included in the term G (e.g. E and F for the gas continuity equation are the component mass fluxes and G is the mass addition term due to the particles). The momentum and energy equations are written in the same form. The particle cloud equations are also written in conservation form. The system of coupled conservation equations are solved by the two-step MacCormack algorithm which consists of a Predictor step and a corrector step. Via this approach internal shock waves in the flow are numerically captured. Other numerical investigations of two-dimensional gas-particle flows have also been carried out by other investigators, e.g. Blagosklonov and Stusenko[92] and Neilson and Gilchrist[61].

Two-dimensional computational models which include nucleation and droplet growth phenomena have recently been presented. Bratos and Burnat[93] in their model for two-phase flow with phase transition in a Laval nozzle have considered the relative velocity between the phases to be negligible. The conservation equations based on the mixture variables are solved by using a modified Lax scheme. A numerical model which combines the streamline curvature through flow calculation method with one-dimensional wet steam theory has been recently developed by Yeoh and Young[91]. The basis of the numerical scheme for the simultaneous solution of the main conservation equations is that used by Denton[95] to predict one-phase flow in transonic axial-flow turbines. The method has been applied to dry, equilibrium and wet steam in duct and blade flow. In the case of wet or nucleating steam, droplet growth is considered along stream surfaces in order to calculate the change in wetness fraction between quasi-orthogonals.

2.4.4 Two-Phase Flow Through Normal Shock Waves

The flow of suspensions of particles in compressible gases with the possible existence of shock waves has been analyzed by previous investigators, generally for solid particles in air. The work of Carrier[96], Rudinger[49], Marble[36,97] and Kriebel[74] represents the foundation developed in this area. Almost all previous workers have assumed that equilibrium exists between the gas and the particles prior to the gas discontinuity. This is true when a shock wave propagates through a stationary suspension[78]. However, when a shock wave occurs in the rapidly accelerating flow through nozzles, the particles will have a considerable velocity and temperature lag by the time a shock wave is reached. It is perhaps convenient at this stage to consider the nature of shock waves in a mixture of perfect gas and a collection of small, solid, spherical particles of uniform size. So long as the particles

are large with respect to molecular dimensions, the thickness of a gas dynamic shock is negligible in comparison with the momentum and thermal ranges of the particles. Thus, the structure of a normal shock wave in a particle-gas mixture may be thought of as a conventional gas dynamic shock since the solid particles cannot be so quickly decelerated that they could modify the gas shock relations. Behind this conventional shock the velocity of the gas is smaller than that of the particles and the particles will then be decelerated. The particles will also accept heat from the gas since the gas temperature has been increased above that of the ambient mixture by the shock[96]. Hence the shock wave in gas-particle mixtures is followed by a relaxation zone where particles and gas come closer to velocity and temperature equilibrium.

The significant calculations on shock waves in gas-particle flows generally involve the relaxation zone structure and length behind normal shock waves. Carrier[96] analyzed the plane, steady, decelerated flow of gas heavily laden with particles by eliminating the space coordinate (x) between the two lag equations. Kriebel[74] produced an approximate analytical solution for weak shock waves and computer results for strong shocks where three particle sizes were present. Krier and Mozaffarian[63] presented a one-dimensional model for steady, compressible gas flow containing solid propellant particles behind a normal shock. Unlike other investigators Krier and Mozaffarian retained the void volume fraction as a variable in the governing conservation equations. Srivastava and Sharma[98] have also considered the structure of normal shock waves without neglecting the particle volume fraction. All these investigators have considered the particles and the gas to be in velocity and temperature equilibrium upstream and again far downstream of the shock wave. However, Cole *et al.*[78] have considered the changes in the flow variables through the relaxation zone due to varying states of disequilibrium ahead

of the gas shock. They have shown that the extent of the particle velocity and temperature lag have a radical influence on the properties of the relaxation zone. The effects of varying the particle-to-gas mass flow ratio, the particle material density, the particle diameter and the specific heat of the particle material have also been investigated by Cole *et al.* They reported that the variations of pressure, gas velocity, gas temperature, solids velocity and solids temperature in the relaxation zone depend significantly on the degree of thermal and velocity lag existing in the flow prior to the shock.

Modifications of the normal shock analysis for a mixture of liquid droplets in the air have been carried out by Panton and Oppenheim[62], Lu and Chiu[99] and Narkis and Gal-or[65].

2.5 ONE-PHASE FLOW TIME-DEPENDENT METHODS

It has been shown in Chapter 1 that many different methods have been developed to calculate one-phase flow in ducts and turbomachines and that only time-marching is capable of solving for the transonic shocked flow which is characteristic of the flow in low-pressure steam turbines and early compressor stages. The basic principle of the method is to start from arbitrary initial conditions and treat the problem as though it were unsteady, seeking the solution as a function of time. When the solution tends to an asymptotic limit at large times, the limit solution is taken as the solution of the steady physical problem. In dealing with time-dependent methods, these points should be kept in mind if a numerical representation of the mathematical model is needed[16,100].

(i) An overall consistency of the numerical technique with the mathematical model of the flow. The concept of consistency is related to the correctness with which the finite difference equations represent the differential equations, in the limit when the grid size becomes infinitesimally small[4,101].

(ii) A proper treatment of boundary conditions.

(iii) A choice of initial conditions which leads to a natural evolution of the flow to a steady state. In order to ensure that the problem is properly posed, careful attention must be paid to the initial conditions. For mixed problems (initial value, boundary value type), the boundary conditions specified must be necessary and sufficient[101].

2.5.1 Some Standard Finite Difference Schemes

There exist, in the literature, several finite-difference schemes for solving transonic one-phase internal flows. In selecting the difference scheme, two criteria of importance must be considered: the order of accuracy and the stability, which establishes the allowable time step[102]. The accuracy of the scheme is given by the order of the truncation error[4]. The truncation error can be considered as a means of checking the consistency condition for the finite-difference scheme since it is the difference between the differential equations that are actually solved numerically and the original partial differential equations. The truncation error is generally expressed as a function of the temporal and spatial step sizes. On the other hand, the concept of stability is one of the most important in numerical methods. A method is stable if the iterative process converges or if the difference between two successive iterations goes to zero. This implies that the computed values are bounded[101,103]. Courant *et al.*[104] showed that for explicit hyperbolic problems, satisfactory calculations can be made for

$$\frac{\Delta t}{\Delta x} < \frac{1}{a} \tag{2.45}$$

where a is an eigenvalue of the simple linear equation[101]

$$\frac{\partial W}{\partial t} + a \frac{\partial W}{\partial x} = 0 \tag{2.46}$$

Hence, if computations are attempted for $\frac{\Delta t}{\Delta x} > \frac{1}{a}$ troubles can be anticipated in the form of instabilities. This stability condition is known as the Courant-Friedrichs-Lewy (CFL) condition and it establishes a relationship between the spatial grid size and the time step. Physically, it means that a disturbance cannot travel more than one cell length in one time increment, otherwise instabilities may arise.

Different finite difference schemes have been used by different investigators to solve the unsteady one-dimensional equations of motion for inviscid flow[105],

$$\frac{\partial}{\partial t}[F] + \frac{\partial}{\partial x}[G] = 0 \tag{2.47}$$

where,

$$F = \begin{bmatrix} \rho_g \\ \rho_g u_g \\ \rho_g E_g \end{bmatrix} \quad \text{and} \quad G = \begin{bmatrix} \rho_g u_g \\ P + \rho_g u_g \\ \rho_g H_g u_g \end{bmatrix}$$

and ρ_g and u_g are the gas density and velocity respectively. E_g and H_g are the gas specific energy $(c_v T_g + \frac{1}{2} u_g^2)$ and enthalpy $(c_p T_g + \frac{1}{2} u_g^2)$ and P is the pressure. Roache[17], Spurr[105], Damia-Torres[4], Gopalakrishnan[101] and Holst[106] have stated some of these finite difference schemes which are classified as follows:

Lax:

$$[F]_j^{n+1} = \frac{[F]_{j+1}^n + [F]_{j-1}^n}{2} - \frac{([G]_{j+1}^n - [G]_{j-1}^n)\Delta t}{2\,\Delta x} \tag{2.48}$$

Euler:

$$[F]_j^{n+1} = [F]_j^n - \frac{([G]_{j+1}^n - [G]_{j-1}^n)\Delta t}{2\ \Delta x} \tag{2.49}$$

MacCormack:

$$[\tilde{F}]_j^n = [F]_j^n - \frac{([G]_{j+1}^n - [G]_j^n)\Delta t}{\Delta x} \tag{2.50}$$

$$[F]_j^{n+1} = \frac{([\tilde{F}]_j^n + [F]_j^n)}{2} - \frac{([\tilde{G}]_j^n - [\tilde{G}]_{j-1}^n)\Delta t}{2\ \Delta x} \tag{2.51}$$

where $[\tilde{G}]_j^n$ is evaluated using $[\tilde{F}]_j^n$

Two step Lax-Wendroff:

$$[\tilde{F}]_j^n = \frac{([F]_{j+1}^n + [F]_{j-1}^n)}{2} - \frac{([G]_{j+1}^n - [G]_{j-1}^n)\Delta t}{4\ \Delta x} \tag{2.52}$$

$$[F]_j^{n+1} = [F]_j^n - \frac{([\tilde{G}]_{j+1}^n - [\tilde{G}]_{j-1}^n)\Delta t}{2\ \Delta x} \tag{2.53}$$

Leap-Frog:

$$[F]_j^{n+1} = [F]_j^{n-1} - \frac{([G]_{j+1}^n - [G]_{j-1}^n)2\Delta t}{2\ \Delta x} \tag{2.54}$$

Many other schemes have been mentioned in literature, e.g. Du Fort-Frankel [106], Brailovskaya[4] and Hopscotch[17,106]

2.5.2 Time-Dependent Methods In Nozzle Flows

In recent years the time-dependent approach to the solution of the governing equations of steady-state fluid flow has enjoyed considerable popularity in certain areas of computational fluid dynamics. An example

is the analysis of one- and two-dimensional flows in convergent-divergent nozzles, where the solution is difficult with conventional steady-state methods, and yet has been shown to be straightforward when approached *via* the time-dependent method. One-dimensional, one-phase flows in convergent-divergent nozzles have been investigated by Crocco[107], Benison and Rubin[108], Holst[106], Griffin and Anderson[109] and Damia-Torres and Baker[110]. Holst has investigated the relative merits of several explicit finite-difference techniques for solving the compressible time-dependent Navier-Stokes equations. The techniques considered are DuFort-Frankel, MacCormack, Brailovskaya and Hopscotch in a convergent-divergent nozzle with supersonic outlet and with a standing shock. The partial differential equations used are in conservative form, including viscous effects *via* the normal stresses.

Marsh and Merryweather[23] and Merryweather[111] have studied the inviscid subsonic and supersonic flow in convergent-divergent nozzles. The governing partial differential equations used are in conservation form. The basis for the finite difference approximation used is a Taylor series expansion. The spatial derivatives of variables other than pressure are given by 3-point backward differencing, while for pressure a 3-point forward differencing is used. The subsonic and shocked flow results are compared with the analytic solution and good agreement is reported. Damia-Torres and Baker[4,110] have produced a quasi one-dimensional model for viscous, heat-conducting, compressible fluid in ducts. Equations used are of the integral type applied to a control volume which have been used by previous workers (e.g. McDonalds[20] and Denton[18,21]). The method reported is fully explicit. The finite difference scheme used is that used by Denton[18,21] which allows information about the inlet stagnation conditions to travel downstream while pressure waves could propagate upstream. Initial conditions used are those corresponding to a uniform flow, defined by isentropic

expansion from the inlet stagnation conditions to the back pressure. The model is reported to be successful in predicting subsonic, supersonic and shocked flows. Good agreement is obtained when inviscid flow results in convergent-divergent nozzle are compared with the analytic solution. Good predictions are also obtained in the cases of Rayleigh and Fanno flows. Daneshyar and Glynn[10] have proposed a model using a time-marching technique based on the method of characteristics, with a reported advantage of the capability to use large time steps hence the need for fewer iterations for convergence to occur and that the model is stable and will normally converge. The nozzle used is that of Marsh and Merryweather[23]. Results obtained show good agreement with those obtained by Marsh and Merryweather[111].

Two-dimensional nozzle flows have been investigated by a number of workers. Two-dimensional models in nozzle flows are often constructed as an intermediate step towards the solution of cascade flows since it does not suffer from effects of some peculiarities like leading and trailing edges, periodicity in the pitchwise direction and wakes from other blade rows. Merryweather[23,111] has extended his one-dimensional model to two-dimensions. Six points are used to obtain a finite difference approximation to a first derivative with respect to x which is accurate to the order of Δx^2. The finite difference approximations for the derivatives with respect to y used three points only. Damia-Torres[4] has also extended his one-dimensional model to deal with two-dimensional flows in ducts. The grid used is that of Denton[18,21] which is characterized by overlapping in the crosswise direction. The "opposed difference technique" is used to approximate variables in the streamwise direction. Inlet conditions used by Damia-Torres are a constant total pressure, total temperature and the flow direction together with the assumption of zero pressure gradient between the inlet and the first calculation point. Outlet conditions on the other hand are a fixed

back pressure P_b together with zero gradient of all other variables between the last calculation point and the exit. Because of the relevance of Denton's and Damia-Torres' models to this work, extensive details are given in chapters 4 and 6. Other investigators include Cline[113,114] who studied the inviscid shockless flow in a two-dimensional and axisymmetric nozzles by using the MacCormack finite difference scheme for interior mesh points and a characteristic scheme for the boundary points. Brunell[115] has studied inviscid and viscous flows in convergent-divergent nozzles by using two-step, second order finite difference scheme. Good agreement of experimental and numerical results is reported.

2.5.3 Cascade and Turbomachinery Flows

Time-marching methods have long been recognized as the most flexible means of solving the flow in turbomachinery cascades. Gopalakrishnan and Bozzola[116] developed one of the first methods for solving the inviscid unsteady Euler equations of motions, mainly

$$\frac{\partial}{\partial t}[F] + \frac{\partial}{\partial x}[G] + \frac{\partial}{\partial y}[H] = 0. \qquad (2.55)$$

where

$$[F] = \begin{bmatrix} \rho_g \\ \rho_g u_g \\ \rho_g v_g \\ \rho_g E_g \end{bmatrix}, \quad [G] = \begin{bmatrix} \rho_g u_g \\ P+\rho_g u_g^2 \\ \rho_g u_g v_g \\ \rho_g u_g H_g \end{bmatrix} \quad \text{and} \quad [H] = \begin{bmatrix} \rho_g v_g \\ \rho_g u_g v_g \\ P+\rho_g v_g^2 \\ \rho_g v_g H_g \end{bmatrix}$$

where v_g is the velocity component in y direction and all other variables are as defined for equation 2.55. However, Gopalakrishnan's method was limited in accuracy because the differential formulation of

the equations can lead to non-conservation of mass and momentum. Small changes in mass flux may not be significant in a free stream problem but in a blade row or a duct flow they can have very large effects, particularly near the sonic condition[19]. One way of avoiding this problem is to divide the flow field into a finite number of calculating volumes and to apply the conservation equations to each volume. In this way once the steady state is reached the nett flux into each elemental volume is zero so that overall mass and energy flows are conserved and changes in momentum equate to the forces imposed on the boundaries. McDonald[20] was the first to use this finite volume form of time marching for blade-to-blade calculations. He used a grid of hexagonal elements so that six flux terms had to be evaluated for each equation for each element. The numerical scheme involved central differences with spatial smoothing to maintain stability; however, the complicated nature of the grid lead to computer times of several minutes for a two-dimensional flow. Couston[103] improved McDonald's method by reducing the need for the spatial smoothing necessary to maintain stability and produced a second order accurate method. Couston corrected for the effects of smoothing by using a "damping surface technique".

Denton[18,19,21] produced a method which succeeded in reducing computational times by approximately an order of magnitude and the use of a simple grid meant that storage requirements were also less than previous methods. The scheme contains some features of both McDonald's[20] and Marsh and Merryweather's[23] methods plus many of its own. The grid used, Fig. 2.2, is well suited for turbomachinery flow and is characterized by overlapping in the crosswise direction. The basis of the method is that the mass and momentum fluxes crossing any pitchwise face are initially evaluated using values of density and velocity from upstream of the face and pressure from downstream of the face. In this manner an extremely stable, first-order accurate scheme is formulated which is

then corrected by the addition of correction factors such that a second-order accurate scheme results. The correction factors on velocities, pressure etc. are calculated such that the flux crossing any given face is finally obtained by taking upstream or downstream properties and adjusting the values of these properties such that the values are those at the face. The correction factors which are calculated by curve fitting through adjacent points are also upwind or downwind biased. This is the basis for the Opposed Difference Technique. Denton has applied his method to various cases of blade-to-blade cascade flows in two- and quasi three-dimensions.

Bryce and Litchfield[117] have assessed Denton's method and concluded that the method compared favourably with other methods with regard to accuracy and was substantially quicker. They also reported a significant total pressure variations at the nose and trailing edge of the blades. However, Denton[118] suggested that a very fine grid should be used if changes in total pressure are to be avoided. Denton[19,119] also suggested different ways that lead to substantial reductions in computer times, mainly

(i) Spatially varied time step.

(ii) Streamwise smoothing of rates of change.

(iii) Pressure field smoothing.

Other investigators using Denton's opposed difference scheme have tried to improve the convergence rate *via* computing time reductions (e.g. semi-implicit time marching method used by Spurr[120]). Singh[121] has coupled Denton's inviscid flow method with a boundary layer calculation to account for boundary layer interactions. Furthermore, extensions of Denton's time-marching method to fully three-dimensional flows have been developed by Spurr[105,122,123] and Singh[124] while Mitchell[125] has studied the two-dimensional unsteady flow in a blade passage by using

Denton's approach. Other workers who have studied turbomachinery flow by time-dependent techniques include Bosman and Highton[126,127] and Oliver and Sparis[128].

2.5.4 Initial And Boundary Conditions

In formulating time-dependent techniques, often the initial conditions are specified arbitrarily, and the boundary conditions are specified without reference to the true physical features of the boundaries. These procedures are not always unsatisfactory because the initial conditions do not affect the final solution due to the hyperbolicity of the formulation, and the effect of approximate boundary conditions is not always catastrophic[129]. Initial conditions can be considered as a large perturbation of the final solution, giving rise to perturbation waves. Convergence is reached when these perturbation waves have died out. The flow field must be completely specified at the start of the computation. The total time taken to reach convergence would depend upon how far from the true solution, the initial conditions were. However, some instabilities have been reported, if the initial adjustment is too severe[112]. These instabilities can occur during the first part of the calculation, when large temporal changes can occur[4]. The disadvantage of choosing arbitrary initial conditions is that until convergence is reached, all the intermediate solutions have no physical meaning. Some investigators[110] believe that even if the initial conditions represent an actual physical situation, the intermediate results do not give the development of a steady flow. This is because the boundary conditions imposed on the flow do not represent, in a general sense, a transient flow. Various types of initial conditions have been used by previous investigators. For one-dimensional flows, a uniform flow defined by an isentropic expansion from the inlet stagnation conditions to the back pressure has been used for inviscid

cases[110], while viscous flows can be started from inviscid analytical solutions, linear variations or even numerical solutions[106]. Van Hove and Arts[130] compared the effect of different initial conditions on rate of convergence and concluded that it is more important to have smooth initial conditions than spending computer time for the calculation of a sophisticated first guess. One-dimensional, inviscid, analytical solutions are quite common as initial conditions for multi-dimensional problems[4].

The importance of boundary conditions in time-dependent techniques lies in their guidance for the flow towards a steady state along a pseudo-temporal path. In order to do this, the boundary conditions have to exchange information with the flow. Different types of flows require different types of boundary conditions; overspecified or underspecified boundary conditions can result in instabilities. Boundaries include rigid walls (impermeable boundaries) and arbitrary permeable boundaries of the computational domain (inlet and outlet). Shock waves can also be considered as boundaries especially when using shock fitting techniques.

(i) Inlet and outlet boundaries

The treatment of the inlet and outlet boundary conditions have been covered by most investigators (e.g. Moretti[100,131], Gopalakrishnan and Bozzola[129], Van Hove and Arts[130] and Griffin and Anderson[109]). Moretti[100] outlined features of the inlet and outlet boundaries by the following:-

(a) If the flow enters the computational domain through an arbitrary boundary with a normal velocity component which is supersonic, no signal from inside can reach the boundary. Therefore, the values on the boundary can be prescribed arbitrarily. However, such values must be consistent with some physical pattern upstream

(a) continued

of the computational region to give physical sense to the results.

(b) If the flow is subsonic at the boundary, all arbitrariness in the choice of the boundary values sends arbitrary signals inside the computational region. The results in the latter then show the effects of such arbitrariness. In other words, the numerical model is inconsistent with the physical problem. Furthermore, any change in the computational region will send waves upstream through the boundary. These waves modify the upstream flow and values at the boundary. At the next computational step, one should assume updated values on the boundary. This implies bringing in the influence of the upstream flow.

Moretti[100] suggested that for subsonic boundaries, the computational region should be extended to where the physical values are well defined and unaffected by travelling waves. This amounts to extending the region to infinity with the consequential mapping of the infinite physical domain into a finite computational domain.

In the formulation of permeable boundaries, it is important to establish the number of boundary conditions to be specified. Van Hove and Arts[130] have shown, by a characteristic analysis for one-dimensional nozzles, that if the inlet velocity is subsonic ($u_g < c_g$) then two variables have to be fixed at the inlet while the third is allowed to float and can be computed as a function of time. On the other hand, if the inlet velocity is supersonic ($u_g > c_g$) then three variables have to be fixed at the inlet. By using the same analysis, Van Hove showed that for subsonic inlet only one variable needs to be fixed at the outlet while for supersonic inlet no variables need to be

fixed at the outlet. Usually, for one-dimensional flows with subsonic inlets, total pressure and total temperature are fixed at the inlet while static pressure or density can be fixed at the outlet[4,130]. Allowing all variables to change with time (float) at outlets, with supersonic inlets, is an advantage from the point of view of convergence speed as no boundary condition can be imposed and the perturbation waves can leave freely the computational domain, i.e. the "flush out" is more rapid. All other boundaries are constrained and reflect the perturbation waves back into the domain. This reflection can be neutral or can damp or even amplify the waves[130].

Boundary conditions for inlets and outlets in two-dimensional flows have also been analysed by Van Hove[130] and Gopalakrishnan[129]. For two-dimensional subsonic inlets it is convenient to specify the total pressure, total temperature, and relative flow angle at the inlet and static pressure at the exit. For compressor rotors with supersonic inlet relative velocity (but subsonic axial velocity) the absolute inlet angle can be specified[4,129]. However, if the inlet axial velocity is supersonic, all variables at the inlet can be specified while the outlet boundary need no fixed variables at all. Griffin and Anderson[109] have shown that for nozzles it is not necessary to take the upstream "reservoir" point to infinity to yield a well-behaved solution. They predicted that placing the boundary "reservoir" point a distance of ten throat heights upstream from the nozzle throat gives excellent results. They also have shown that provided the inlet is well upstream of the throat, the inlet to throat area ratio is not crucial as far as instabilities are concerned.

One of the problems facing the numerical analyst when treating the boundaries is how to calculate the variables which change with time (floating variables). Methods used to evaluate floating variables

range from extrapolations, one-sided differences to constant gradients. For subsonic inlets some workers specify the whole set of variables (e.g. Gopalakrishnan and Bozzola[116]). McDonald[20] fixes the pressure and flow angle while the momentum variables are continually adjusted until the average axial pressure gradient approaches zero. Denton[21] fixes the total pressure and total temperature together with the flow direction while the pressure gradient along the quasi-streamlines is set to zero (see Fig. 2.2) and the pressure at the first crosswise line is equated to that calculated at the same quasi-streamline on the second crosswise line. For subsonic outlets the fixed variable is usually the static pressure while floating variables are found by different means:- zero gradients[108], one-sided differencing[20] or zero velocity gradient along the quasi-streamlines[21]. For supersonic outlets all values can be determined by different extrapolation techniques from the inside of the computational domain[4,112]. Fully supersonic inlets are dealt with by the complete specification of the boundary[4]. However, for supersonic inlets with an axial Mach number less than one, the relative flow direction is not allowed to float[4].

(ii) Wall boundaries

For inviscid flows, the important condition to be satisfied at every point on a rigid wall is the vanishing of the normal velocity component to the wall (u_n)[4,100,112], i.e.

$$u_{gn} = 0 \tag{2.56}$$

In treating wall boundary conditions researchers have used various approaches; these include reflection techniques, extrapolation from interior points and averaging. Reflection techniques[17,131] utilize the idea

that across a wall, flow properties are reflected (i.e. the wall acts as a mirror). Extrapolation from interior points make use of the fact that increments in a physical variable ϕ at the wall depends on derivatives such as $\partial\phi/\partial n$ and $\partial^2\phi/\partial n^2$. These derivatives depend on the geometrical nature of the fitting curve and not on the physical properties[4]. McDonald[20] used a one-sided differencing. A condition of no mass transport is imposed, while the momentum transport depends only on the wall static pressure. Denton[18,21] has used a one-sided differencing by applying the conservation equations to a half element on the solid wall (Fig. 2.2) and assumed a linear variation of the flow properties between the centre of the first interior element, the centre of the half element and the boundary. The same equations were also obtained by extending the half element at the wall beyond the boundary to form an element and obtaining the fluxes through the surface beyond the boundary by parabolic extrapolation from the boundary point and first two interior points.

Gopalakrishnan[112] has used a technique in which the static pressure at the wall is computed directly from the curvature of the wall. In his method the gradient of the static pressure normal to the wall is equated to the centrifugal force, produced by the local radius of curvature of the wall (r),

$$\left(\frac{\partial P}{\partial n}\right)_w = \frac{\rho_g U_g^2}{r} \qquad (2.57)$$

where n is the direction normal to the wall. Equation 2.56 has also been used by Damia Torres[4] to predict values of the pressure at the solid walls of two-dimensional nozzles.

2.6 TWO-PHASE FLOW TIME-DEPENDENT METHODS

Several computational models employing time-dependent techniques have recently been presented to solve for gas-particle flows. One of the approaches used in time-dependent methods is the "two-fluid" model. The "two-fluid" approach is to regard the conveying and particulate phase as two interactive fluids. The two-fluid equations are obtained by averaging the conservation equations over a volume and expressing the equations in differential form[28]. In his review of numerical models for gas-particle flows, Crowe[28] has defined the two-fluid equations to be similar to those for the flow of a single phase with the exception of source terms which represent the exchange phenomena between the phases (such equations will be discussed and presented in the next chapter). By retaining the time derivatives the two-fluid equations form a good basis for time-dependent models in two-phase flows. One of the advantages of applying the two-fluid models to dilute gas-particle flows is the use of numerical procedures already established for single-phase flow[28]. However, two-fluid models do not escape criticism; Crowe[28] summarized the drawbacks of these models as:

(i) The use of upwind differencing introduces numerical diffusion which requires the use of finer grid spacing for control.

(ii) The use of fine grid spacing would be more costly.

(iii) When treating more than one particle size, one must regard each size category as a separate fluid which demands more computer storage.

(iv) Prohibitively small time steps must be used when strong gas-particle momentum coupling is encountered[132].

Recently Chang[132] has used time-dependent two-fluid equations in conservative partial differential equations to predict gas and particle

fields in planar and axisymmetric nozzles. The solution method includes the use of a body-fitted coordinate system and the MacCormack finite difference scheme. The gas phase initial conditions are the results obtained from a converged pure gas flow while the particle velocity and temperature are taken to be equal to those of the gas phase. A characteristics formulation is used at the inlet to compute the horizontal inflow boundary conditions while at the exit a simple linear extrapolation is used. The solid wall boundaries are calculated by using a linear extrapolation from two adjacent interior points and then modified by the local tangency condition. The calculations were used for single size particles and solutions were obtained for submerged nozzles and nozzles with small radii of curvature.

Di Giancinto *et al.*[25] have presented a numerical model for dilute gas-particle flow through a constriction (like an orifice) based on the two-fluid equations. Two sets of non-conservative partial differential equations are solved simultaneously by a time marching implicit technique. The particle volume fraction is omitted from the gas equations. Gas phase pressures were determined by an iteration over relaxation routine which updates the pressure, modifying at the same time the velocity components towards the satisfaction of the continuity equations. At the inlet boundary identical velocity profiles for both phases and a uniform value of the particle volume fraction have been used while at the solid wall a condition of zero velocity for the gas, slip condition for the particle velocity and zero flux for the particle volume fraction have been assumed. For the exit boundary first or second derivatives of the variables have been assumed to be zero. The calculations were performed with a single particle size. Another two-dimensional two-fluid model has been presented by Kopchenov and Kraiko[133] in which two sets of conservative integral equations have been used. The new values for the conservative variables are calculated by using old values of the variables

in the integration of the flow equations over the elementary cells used. The inlet boundary conditions used are equal velocities and temperatures along the x-axis while the cross-stream components of the phases' velocities are taken to be zero. Moreover, the total enthalpy and the entropy at the inlet are fixed. At the nozzle wall the condition of zero normal velocity is applied while at the exit the variables were allowed to float since the exit flow is taken to be supersonic.

Other numerical models have employed different formulations to obtain steady state solutions by time-dependent methods for two-phase flows. Comfort *et al.*[134,135] have produced a quasi one-dimensional model which combines the time-dependent (hyperbolic) Eluerian equations for continuity, momentum and energy for the two-phase mixture with the droplet Lagrangian equation of momentum and the continuity equation for the droplet phase. The Eulerian equations are integrated by the MacCormack scheme while the Lagrangian droplet equation is integrated by an implicit form of the trapezoidal rule. The model can only deal with ducts of constant inlet and outlet areas. Boundary conditions include subsonic and supersonic specifications. The concept that inlet vapour and droplet velocities retain a constant ratio (slip) is also introduced. Good agreement with experimental data is reported. Although the phase velocity nonequilibrium and phase change are considered, the temperature nonequilibrium between phases is not included in Comfort's model.

More recent numerical models for nucleating and wet steam flows using Denton's[18,21] time-marching approach have appeared in the literature. Bakhtar and Mohammadi Tochai[40] have presented a two-dimensional model to predict nucleating and wet steam flow with no inter-phase slip. The model's continuity and momentum equations are those used by Denton for his one-phase flow approach (equation 2.55) with the replacement of the gas density (ρ_g) by the mixture density

(ρ_m). The mixture flow is assumed to take place at constant total enthalpy. The solution procedure adopted in Bakhtar's numerical model is basically the same as Denton's. However, for regions where the flow is dry, Newton-Raphson method is used to find the vapour temperature in order to satisfy the constant total enthalpy condition. In the zones where the flow is nucleating or wet, Newton-Raphson method is also used to calculate the liquid terms at downstream points along a streamlines. The iterative procedure in nucleating or wet zones makes use of equations describing nucleation and droplet growth together with other two-phase relations (e.g. the wetness fraction and the mixture density formulae). Additional boundary conditions are added to those used by Denton to account for the droplet phase at the inlet. These are specified inlet stagnation conditions which include enthalpy, degree of supercooling, wetness fraction and size of the existing droplets. The inlet and outlet sections are extended to achieve uniform flow. Initially, linear variation of the static pressure between the inlet and outlet planes is assumed and the flow is taken to be isentropic for the case of dry steam. Initial conditions for the case when the steam is wet at inlet are, droplet radius and wetness fraction in the entire flow field to be equal to those specified at the inlet while the degree of supercooling of the vapour phase is assumed. The numerical model's predictions are reported to be in good agreement with experimental data and those obtained by other investigators in different ducts.

Snoeck[136] has presented a one-dimensional model for condensing steam flow which also neglects inter-phase slip between the two phases. Snoeck's method combines a time-marching solution procedure for the vapour phase equations with an analytical solution of the droplet growth. The time-dependent Eulerian equations for the vapour phase are expressed in a way so as to include terms to account for the effects of phase change as sources and sinks. The liquid phase is represented by the classical

nucleation theory and Gyarmathy's model. The vapour phase equations are integrated by the artificial viscosity scheme initially proposed by McDonald[20]. Boundary conditions for subsonic inlet flow are the assumption of dry vapour flow between the settling chamber and the nozzle inlet where the variables are evaluated by assuming conservation of total enthalpy and entropy and equal mass flow rates through the first two planes. For subsonic outlets, the back pressure is fixed and balances of momentum and energy are considered between the last two planes. In the case of supersonic outlet flow, the full information is provided from the computational domain by the conservation laws of mass, momentum and energy. Good agreement is shown between numerical results of Snoeck's model and experimental results obtained by other investigators in nozzles (e.g. Moore *et al.*[82]). Other numerical models[137] using a time marching method based on Denton's approach are also reported to be under development. These models consider the flow of nucleating and wet steam with negligible inter-phase slip velocity.

2.7 CLOSURE TO CHAPTER 2

The following summary can be made based on the review of the literature. Different approaches to deal with gas-particle flows, with or without inter-phase mass transfer, have been introduced. Many of the available numerical techniques suffer from various limitations. The assumption of zero interphase slip velocity has appeared in the various techniques dealing with condensing wet steam flow. Furthermore, the inability of the various techniques to deal with transonic gas-particle flow and the need for an easy but effective calculation method to deal with fully coupled two-phase flow have made the two-phase flow investigators turn to time-dependent techniques. These techniques have enjoyed tremendous popularity with one-phase flow numerical analysts for their simplicity, effectiveness to deal with mixed flows, and ability for

automatic shock capture. The few two-phase time-dependent models available in the literature are reported to be successful. However, the majority of these do not consider the two-phase mixture within the scope of the "two-fluid" approach with distinct velocities and temperatures for each phase.

CHAPTER 3

MATHEMATICAL FORMULATION OF TWO-PHASE TIME DEPENDENT EQUATIONS

3.1 INTRODUCTION

This chapter describes the mathematical formulation of the time-dependent two-phase flow equations used in the present work. The conservation laws of mass, momentum and energy are derived for each phase. The problem specification is completed by the choice of auxiliary relations already reviewed in Chapter 2. The resulting equations describe the motion of the gas and particles as though they were interpenetrating continua. Finally the one- and two-dimensional sets of equations are normalized by using a set of reference values and presented in their time-marching form. In order to keep lucidity, the case of ordinary single phase flow is explained first.

3.2 ONE-PHASE FLOW TIME-DEPENDENT EQUATIONS

3.2.1 One-Phase Viscous, Heat Conducting Flow Equations

The basic equations for one-phase flow arise from the conservation of mass, momentum and energy. Neglecting body forces and sources, the unsteady flow of a viscous, heat conducting, compressible fluid may be described by the following set of partial differential equations written in cartesian tensor form:

Continuity

$$\frac{\partial \rho_g}{\partial t} \quad \frac{\partial}{\partial x_j} (\rho_g u_{gj}) = 0 \qquad (3.1)$$

Momentum

$$\frac{\partial}{\partial t}(\rho_g u_{gj}) + \frac{\partial}{\partial x_j}(\rho_g u_{gi} u_{gj}) = \frac{\partial}{\partial x_j}(-P\delta_{ij} + \tau_{ij}) \qquad (3.2)$$

Energy

$$\frac{\partial}{\partial t}(\rho_g E_g) + \frac{\partial}{\partial x_j}(\rho_g E_g u_{gj}) = \frac{\partial}{\partial x_j}\left[u_{gj}(-P\delta_{ij} + \tau_{ij}) - q_j\right] \qquad (3.3)$$

If the working fluid is a perfect gas (say, air), the equation of state can be written as:

$$P = \rho_g R_g T_g \qquad (3.4)$$

Here, t and x_j $(j = 1,2,3)$ are the time- and space-coordinates, while ρ_g, u_{gj}, E_g and P are the density, velocity components, total (internal and kinetic) energy per unit mass and pressure, respectively. Also τ_{ij} is the viscous stress tensor, q_j is the heat flux vector, and δ_{ij} is the Kronecker delta operator which is unity for $i = j$ and zero otherwise. The viscous stress tensor for a Newtonian fluid is a linear function of the rates of strain, namely:

$$\tau_{ij} = \mu_g\left[\frac{\partial}{\partial x_j} u_{gj} + \frac{\partial}{\partial x_i} u_{gj}\right] + \delta_{ij}\left[\mu_g' - \frac{2}{3}\mu_g\right]\frac{\partial}{\partial x_k} u_k \qquad (3.5)$$

Where μ_g amd μ_g' are the dynamic (molecular) and volumetric (bulk) viscosity coefficients respectively.

The heat flux vector is proportional to the temperature gradient, i.e. :-

$$q_j = -k_g \frac{\partial T_g}{\partial x_j} \qquad (3.6)$$

k_g is the thermal conductivity and T_g is the temperature. The total specific energy is:

$$E_g = c_v T_g + \frac{1}{2} u_{gi} u_{gi} \tag{3.7}$$

where the specific heat at constant volume c_v is constant. In the above set of equations, it must be noted that in the cartesian index notation, repeated indices mean summation over the whole index range. It is customery to consider the dynamic viscosity and thermal conductivity as functions of the gas temperature only, while the volumetric viscosity is constant and equal to zero, i.e. :-

$$\begin{aligned} \mu_g &= \mu_g(T_g) \\ k_g &= k_g(T_g) \\ \mu'_g &= 0. \end{aligned} \tag{3.8}$$

Equations 3.1 to 3.3 can be solved for two scalar unknowns (ρ_g and $\rho_g E_g$) and one vectorial unknown ($\rho_g u_{gj}$). Dividing the flow field into a finite number of fixed, non-deformable calculating volumes, then for each volume V and time step Δt the flow equations can be obtained either by applying the Divergence (Gauss) theorem to the partial differential system (3.1 - 3.3) or by using the conservation laws directly on each control volume V. The latter technique gives:

$$\frac{\partial}{\partial t} \int_V \rho_g dV + \int_{CS} \rho_g u_{gj} \vec{m}_j \cdot \vec{n} \, dS = 0 \tag{3.9}$$

$$\frac{\partial}{\partial t} \int_V \rho_g u_{gj} dV + \int_{CS} (\rho_g u_{gi} u_{gj} + \delta_{ij} P - \tau_{ij}) \vec{m}_j \cdot \vec{n} dS = 0 \tag{3.10}$$

$$\frac{\partial}{\partial t} \int_V \rho_g E_g dV + \int_{CS} (\rho_g E_g u_{gj} + \delta_{ij} P u_{gj} - \tau_{ij} u_{gj} + q_j) \vec{m}_j \cdot \vec{n} dS = 0 \tag{3.11}$$

where dV is an elementary volume of the control volume V, dS is an elementary surface of the control surface surrounding V, $\vec{m}_j$ is the unit vector in j-direction (j = 1,2,3) and $\vec{n}$ is the unit outward normal vector to dS.

3.3 MULTIPHASE FLOW

There are several methods of attempting to describe multiphase flow, mostly two-phase flow. We consider here flows with changes of phase, due to physical reasons. Hence neither mass, nor accompanying momentum nor energy of a single phase are conserved. Only the sum of the respective source terms over all phases is possibly zero. There are difficulties in formulating a tractable and properly determined mathematical model of a flow field impregnated with particles undergoing interphase transfer. Wundt[138] states that "most relevant papers which deal with establishing conservation laws for multiphase flows finally give unequal numbers of equations and dependent variables", and further Crowe[139] remarks that "comparing the various equations which have been proposed, one finds few discrepancies in those for disperse-phase solid particles. However, serious inconsistencies occur in those for liquid, reacting droplets.". The basic complication in treating such flow arises from the exchange of mass, momentum and energy between the phases. These complex interactions between the particulate phase and gas (or vapour) phase are called coupling phenomena. Consider, for example, slowly moving particles in an accelerating gas flow field. Momentum is transferred from the gas to the particles through the drag force interaction, and consequently, there is a corresponding decrease in momentum in the gas. The decrease in momentum of the gas alters the gas flow field and changes the trajectories of particles. In this way, there is a

momentum coupling effect. Mass coupling and thermal coupling become important when evaporation (or condensation) and thermal nonequilibrium between the phases are significant.

Although, the mathematical formulation of two-phase flow is still debated, most of the researchers have recognized the need to express each conservation law by a pair of differential equations pertaining to each phase. Two different conceptual approaches have been reported in the literature for handling the pair of governing equations. The first approach is based on the concept of two superimposed continua. It is confined to dispersed flow situations only, the conservation equations of the suspending continuum are modified to include extra source terms that take into account the presence of the dispersed phase. This method was proposed by Migdal and Agosta[140] and used by Crow *et al.*[31], Sharma[32] and Lee[30,34]. While the conveying, or gaseous, phase is treated as a fluid with additional terms which account for sources of mass, momentum and energy from the particulate phase. The particle field, in turn, is obtained by following the motion of many particles through the gas field. These trajectories yield the sources of mass, momentum and energy to the gas in each computational volume. The second approach is more general than the first one in that its applicability is not restricted to dispersed flows. It considers the coexistence of the two continua with different concentration at different locations in the flow domain. This approach solves the governing equations simultaneously by regarding each phase as a continuous fluid and accounts for the coupling between phases. This approach introduces the "average" particle properties concept. Models employing this type have been described by Jackson[46,83], Anderson and Jackson[141], Soo[51] and Murray[142].

All schemes for calculation of vapour-droplet flow accompanied by interphase mass transfer (e.g. homogeneous condensation of water vapour in expanding flow) can be divided in three basic parts:

(i) Equations of conservation and thermodynamic description of the condensing gas.

(ii) An expression for the nucleation rate.

(iii) Equations for droplet growth.

The above stated parts together with expressions for the drag force and heat transfer between the phases would form a solid starting point for any numerical scheme for solving nucleating and condensing two-phase flow systems. Two-phase flows with no interphase mass transfer (e.g. gas-solid particles) are somehow simpler since nucleation and condensation phenomena are absent.

3.3.1 Eulerian Two-Phase Flow Time-Dependent Equations

In principle the motion of a system of particles suspended in a fluid is completely determined by the Navier-Stokes equations, to be satisfied at each point of the fluid, and the Newtonian equations of motion, to be satisfied by each particle. However, when the system of interest comprises a large number of closely spaced particles, the problem is far too complicated to permit direct solution when stated in these terms, and for practical purposes it is necessary to seek some method of simplifying it so that it can be described by a relatively small number of equations. The literature contains several attempts (Van Deemter and Van der Laan[143], Hinze[144], Murray[142], Anderson and Jackson[141], for gas-solid particles, and Jackson[46] and Crowe [139,145] for vapour-droplet cloud) to simplify the problem in this way, all of which replace the point mechanical and fluid mechanical variables

by smoothed variables obtained by averaging over regions large compared with the particle (droplet) spacing but small compared with the complete system. The resulting equations, therefore, describe the motion of the fluid and particles as though they were interpenetrating continua. This approach in modelling gas-particle flows is called the "two-fluid" approach in which the two-phase flow equations are similar to those for the flow of a single phase with the exception of mass, momentum and energy source terms which represent the inter-phase interaction between the phases. In the two-fluid approach the mixture is represented by two continuity, two momentum and two energy equations. Also, there is no equation of state for the particle cloud as there is for the conveying gas phase. In fact, the particle cloud is analogous to compressible fluid with no equation of state[28]. Crowe[139,145] derived a set of equations describing the conservation of mass, momentum and energy of a flowing gas with suspended particles by using the Reynolds transport theorem. Crowe has included in his derivation the boundary-droplet effects. Consequently, his derivation shows that droplets intersected by the control surface give rise to a term in the momentum equations. Crowe states that "strictly speaking one cannot define droplet density at a point in the flow. The only meaningful definition of droplet density is bulk density or mass of droplets per unit volume of mixture. Thus, the mixture volume which one considers must contain many droplets in order to define an "average".". As a result Crowe's equations are expressed in terms of the void fraction and the particle (or droplet) and gas bulk densities. Other derivations using the particle void fraction include those by Van Deemter and Van der Laan[143] and Hinze[144]. The resulting equations differ in various ways such as the formulation for the pressure gradient term and the nature of the momentum source terms[28]. Arguments over the correct form of the derived equations persist in the literature.

Jackson[46] presented a set of two-fluid, two-phase flow, time-dependent equations by using the control volume approach. The derived equations are presented in their integral and differential form and expressed in terms of the particle mass fraction Y (defined as the mass of particles (or droplets) per unit mass of the mixture). The equation set is proposed by Jackson to deal with fog droplet flows within turbomachinery. Thus, equations derived by Jackson are thought to be suitable for the present project since its eventual aim is the prediction of condensing flows in turbomachinery. Next, these equations are presented and discussed.

3.4 TWO-PHASE TIME-DEPENDENT EQUATIONS PROPOSED FOR THE MODEL

The particular two-phase flow of concern here consists of a continuous vapour- or gas-phase containing a distribution of liquid droplets or solid particles of varying sizes and velocities, which may be (in the case of vapour-droplet flow) in the process of nucleation, condensation or evaporation. Jackson's mathematical presentation for such flows involves a "smoothing operation" in which the particle properties are treated as field variables, i.e. they are thought of as continuous and differentiable functions of space and time. Jackson remarks that "reasonable results may be expected by using such smoothing operation so long as the far field gas properties do not change significantly over distances of the order of a droplet diameter.". Jackson's approach starts with the "two-fluid" equations which regards the conveying and particulate phase as two interactive fluids in much the same way as one would regard the two species of a flowing binary mixture.

The droplets are taken to be incompressible and spherical, the viscous forces in the gas phase are ignored (i.e. inviscid) while the drag and heat interactions between the drops and gas are included. The

liquid phase is subdivided into droplet groups designated by the subscript (i) and distinguished by the size of the member droplets at some specific spatial position. A droplet once so labelled remains in the same group throughout its flow history. The equation set derived is three-dimensional time variant, describing multiphase gas-liquid continuum flow. The equations are relevant to a number of multiphase problems including gas-solid suspensions and liquid-bubble systems, as well as the gas-droplet system. A brief description of the derivation is given in this section and further details can be found in Jackson[46]. Consider an elemental volume δV_m of the vapour-droplet mixture comprising a volume of δV_g occupied by the vapour and δV_p occupied by the droplets, where

$$\delta V_p = \sum_i \delta V_{pi} \tag{3.12}$$

and δV_{pi} is the volume occupied by the i^{th} droplet group. Thus,

$$\delta V_m = \delta V_g + \delta V_p \tag{3.13}$$

Similarly for the component masses

$$\delta m_m = \delta m_g + \delta m_p = \delta m_g + \sum_i \delta m_{pi} \tag{3.14}$$

also, $\delta m_m = \rho_m \delta V_m$, $\delta m_g = \rho_g \delta V_g$ and $\delta m_{pi} = \rho_{pi} \delta V_{pi}$, where δm_m, δm_g and δm_{pi} are the mixture, gas, and the i^{th} droplet group masses respectively. The i^{th} droplet group mass fraction Y_i is :

$$Y_i = \frac{\delta m_{pi}}{\delta m_m} = \frac{\rho_{pi} \delta V_{pi}}{\rho_m \delta V_m} \tag{3.15}$$

Also, total mass fraction of the droplets is :

$$Y = \sum_i \frac{\delta m_{pi}}{\delta m_m} = \sum_i Y_i \tag{3.16}$$

Hence,

$$\frac{\delta m_g}{\delta m_m} = 1 - \sum_i \frac{\delta m_{pi}}{\delta m_m} = (1 - Y) = \frac{\rho_g \delta V_g}{\rho_m \delta V_m} \tag{3.17}$$

i.e.

$$\rho_m(1 - Y) = \frac{\rho_g \delta V_g}{\delta V_m} \tag{3.18}$$

The term $\rho_m(1 - Y)$ is the gas phase partial density, while the i^{th} droplet group partial density can be found from equation 3.15 as

$$\rho_m Y_i = \frac{\delta m_{pi}}{\delta V_m} \tag{3.19}$$

and the total droplets partial density from equation 3.16 as

$$\rho_m Y = \sum_i \frac{\delta m_{pi}}{\delta V_m} \tag{3.20}$$

The mixture density ρ_m can be found by combining equations 3.13, 3.18 and 3.19 and expressed as

$$\frac{\rho_m(1 - Y)}{\rho_g} + \sum_i \frac{\rho_m Y_i}{\rho_{pi}} = 1 \tag{3.21}$$

Considering the mass flows through a small surface $\vec{\delta S}$. The i^{th} droplet group particles with a velocity vector $\vec{U}_{pi}$ would sweep out a volume of $\vec{U}_{pi} \cdot \vec{\delta S}\, \delta t$ in a time increment δt. The mass of the i^{th} droplet group contained in the swept volume is $\rho_m Y_i \vec{U}_{pi} \cdot \vec{\delta S}\, \delta t$ so that,

$$i^{th} \text{ droplet group flux} = \rho_m Y_i \vec{U}_{pi} \cdot \vec{\delta S}$$

$$\text{gas phase flux} = \rho_m(1 - Y) \vec{U}_g \cdot \vec{\delta S}$$

where $\vec{U}_g$ is the gas velocity vector. If the total surface $\vec{\delta S}$ is assumed to be divided into individual sub-surfaces passing each phase alone, i.e.

$$\vec{\delta S} = \vec{\delta S}_g + \sum_i \vec{\delta S}_{pi} \tag{3.22}$$

then the following continuity relationships must be satisfied :

$$\rho_{pi} \vec{U}_{pi} \cdot \vec{\delta S}_{pi} = \rho_m Y_i \vec{U}_{pi} \cdot \vec{\delta S}$$

and

$$\rho_g \vec{U}_g \cdot \vec{\delta S}_g = \rho_m (1 - Y) \vec{U}_g \cdot \vec{\delta S}$$

Hence,

$$\vec{\delta S}_{pi} = \frac{\rho_m Y_i}{\rho_{pi}} \cdot \vec{\delta S} \tag{3.23}$$

and

$$\vec{\delta S}_g = \frac{\rho_m (1 - Y)}{\rho_g} \cdot \vec{\delta S} \tag{3.24}$$

The two-phase conservation equations are derived by following the motion of a given assembly of matter and by evoking the "material" or "substantive" differential operator

$$\frac{D}{Dt} = \frac{\partial}{\partial t} + \vec{U} \cdot \nabla \tag{3.25}$$

for each phase.

Continuity equations

For the motion of a surface threading elements of the gas phase in a time increment δt and in the presence of nucleation and condensation a

mass equal to

$$\sum_i \int_V (N_i \dot{m}_{ci} + J_i m_i)\rho_m \, dV \, \delta t$$

is lost by the gas-phase in the volume enclosed by the surface due to nucleation and condensation of the droplet groups included in the volume, where N_i is the number of i^{th} group droplets per unit mass of mixture, $\dot{m}_{ci}$ is the condensation rate on the droplet surface, J_i is the nucleation rate defined as the number of nuclei produced per second in a unit mass of mixture and m_i is the mass of the i^{th} group droplet. Hence,

$$\frac{D}{Dt} \int_V \rho_m (1 - Y) dV = - \sum_i \int_V (N_i \dot{m}_{ci} + J_i m_i)\rho_m dV \qquad (3.26)$$

By using relationship 3.25 and remembering that for a small volume δV

$$\frac{D}{Dt} (\delta V) = \int_{\delta S} \vec{U} \cdot d\vec{S} \qquad (3.27)$$

and

$$\lim_{\delta V \to o} \int_{\delta S} \frac{\vec{U} \cdot d\vec{S}}{\delta V} = \nabla \cdot (\vec{U}) \qquad (3.28)$$

also by invoking Gauss's theorem, equation 3.26 yields the integral form of the continuity equation for the gas phase as

$$\int_V \frac{\partial}{\partial t} [\rho_m (1-Y)] dV + \int_{CS} \rho_m (1-Y) \vec{U}_g \cdot d\vec{S} = - \sum_i \int_V (N_i m_{ci} + J_i m_i)\rho_m dV \qquad (3.29)$$

Repeating the process for a surface threading droplets of the i^{th} group, by using equations 3.25, 3.27 and 3.28, the resulting droplet phase continuity equation is

$$\int_V \frac{\partial}{\partial t}(\rho_m Y_i)dV + \int_{CS}(\rho_m Y_i)\vec{U}_{pi}\cdot d\vec{S} = \int_V (N_i\dot{m}_{ci} + J_i m_i)\rho_m dV \qquad (3.30)$$

where CS refers to the control surface.

Momentum equations

The sum of applied forces acting on the gas phase within the volume V is

$$-\int_{CS} P d\vec{S}_g - \sum_i \int_V N_i \vec{D}_{pi}\, \rho_m\, dV$$

where $\vec{D}_{pi}$ denotes the drag vector acting on a droplet of i^{th} droplet group as a result of its relative motion with respect to the gas. Also in a time increment δt the amount of momentum transferred from the gas to the liquid phase is

$$\sum_i \int_V (N_i\dot{m}_{ci} + J_i m_i)\, \vec{U}_g\, \rho_m\, dV\, \delta t$$

The rate of momentum change for the original mass of gas is

$$\frac{D}{Dt}\int_V \rho_m(1 - Y)\vec{U}_g dV + \sum_i \int_V (N_i\dot{m}_{ci} + J_i m_i)\vec{U}_g\rho_m dV$$

By equating the rate of momentum change with the applied forces and by using equations 3.24 and 3.25 and invoking Gauss's theorem the integral form of the gas-phase momentum equation can be expressed as

$$\frac{\partial}{\partial t}\int_V \rho_m(1-Y)\vec{U}_g dV + \int_{CS}\rho_m(1-Y)\vec{U}_g(\vec{U}_g\cdot d\vec{S}) = -\int_{CS}\frac{\rho_m(1-Y)}{\rho_g}P\, d\vec{S} - \sum_i\int_V N_i\vec{D}_{pi}\rho_m dV$$

$$-\sum_i\int_V (N_i\dot{m}_{ci} + J_i m_i)\vec{U}_g\rho_m dV \qquad (3.31)$$

Applying the same procedure for the droplets of the i^{th} group and using equation 3.23 instead of 3.24, the integral form of the momentum equation for droplets of the i^{th} group can be expressed as

$$\frac{\partial}{\partial t}\int_V (\rho_m Y_i \vec{U}_{pi})dV + \int_{CS} \rho_m Y_i \vec{U}_{pi}(\vec{U}_{pi}\cdot d\vec{S}) = -\int_{CS} \frac{\rho_m Y_i}{\rho_{pi}} P\, d\vec{S}$$

$$+ \int_V N_i \vec{D}_{pi}\rho_m dV + \int_V (N_i \dot{m}_{ci} + J_i m_i)\vec{U}_g \rho_m dV \qquad (3.32)$$

Energy equations

In a time δt, the amount of energy transferred from a moving volume V of gas to the liquid phase is,

$$\sum_i \int_V (N_i \dot{m}_{ci} + J_i m_i)\left[e_g + \frac{U_g^2}{2}\right]\rho_m dV\delta t$$

where, for the two-dimensional case, $U_g^2 = u_g^2 + v_g^2$, and e_g is the gas-phase specific internal energy.

The work done by surface pressure forces $= -\int_{CS} P\vec{U}_g \cdot d\vec{S}_g$

The work done by droplet drag $= -\sum_i \int_V N_i \vec{D}_{pi}\cdot\vec{U}_{pi}\rho_m dV$

The work done at the phase boundary

$$= \sum_i \int_V P\left[(N_i \dot{m}_{ci} + J_i m_i)(V_{pi} - V_g) + N_i m_i \frac{DV_{pi}}{Dt_i}\right]\rho_m dV$$

Note that work done due to surface tension effects is not included in the last term.

The heat added to the gas phase $= \sum_i \int_V N_i Q_{pi}\rho_m dV$

where Q_{pi} is heat transfer from a single droplet. The rate of energy change of the gas-phase is,

$$\frac{D}{Dt}\int_V \rho_m(1 - Y)\left[e_g + \frac{U_g^2}{2}\right]dV + \sum_i \int_V (N_i\dot{m}_{ci} + J_i m_i)\left[e_g + \frac{U_g^2}{2}\right]\rho_m dV$$

By equating the sum of heat and work input with the energy change and by using equations 3.24 and 3.25 and evoking Gauss's theorem as well as regrouping to introduce the gas-phase enthalpy, the integral form of the gas-phase energy equation can be expressed as

$$\frac{\partial}{\partial t}\int_V \rho_m(1-Y)E_g dV + \int_{CS} \rho_m(1-Y)H_g\vec{U}_g\cdot d\vec{S} = \sum_i \int_V N_i Q_{pi}\rho_m dV - \sum_i \int_V N_i\vec{D}_{pi}\cdot\vec{U}_{pi}\rho_m dV$$

$$- \sum_i \int_V (N_i\dot{m}_{ci} + J_i m_i)\left[H_g - \frac{P}{\rho_{pi}}\right]\rho_m dV \qquad (3.33)$$

where H_g is gas-phase total enthalpy which can be expressed as:

$$H_g = h_g + \frac{U_g^2}{2} \qquad (3.34)$$

while h_g is the enthalpy. E_g can be found by using equation 3.7. Note that the term $N_i m_i \frac{DV_{pi}}{Dt_i}$ has been set to zero since the droplets are assumed to be incompressible. The same procedure can be repeated to produce the energy equation for the i^{th} group droplets as:

$$\frac{\partial}{\partial t}\int_V \rho_m Y_i E_{pi} dV + \int_{CS} \rho_m Y_i H_{pi}\vec{U}_{pi}\cdot d\vec{S} = -\int_V N_i Q_{pi}\rho_m dV$$

$$+ \int_V N_i\vec{D}_{pi}\cdot\vec{U}_{pi}\rho_m dV + \int_V (N_i\dot{m}_{ci} + J_i m_i)\left[H_g - \frac{P}{\rho_{pi}}\right]\rho_m dV \qquad (3.35)$$

where H_{pi} and E_{pi} are the i^{th} group droplet total enthalpy and energy respectively. H_{pi} and E_{pi} can be expressed as follows:

$$H_{pi} = e_{pi} + \frac{U_{pi}^2}{2} + \frac{p}{\rho_{pi}} \tag{3.36}$$

$$E_{pi} = e_{pi} + \frac{U_{pi}^2}{2} \tag{3.37}$$

and e_{pi} is the internal energy of the i^{th} group droplet.

The derived set of equations is self consistent in that no equation is in contradiction of the original model assumptions. The individual phase equations sum exactly to give the mixture equations which are known with certainty. Checks on the validity of the equations as can be made are satisfied, such as, they collapse correctly to the single-phase forms when Y is set to zero or unity. The equations are suitable for quite wide applications being appropriate, for example, to describe the propogation of sound waves in two-phase media where the inclusion of distinct phase velocities is essential. They allow for interphase slip which is an important feature for large droplets (normally > 10 μm). They are immediately applicable to non-reacting suspensions (gas-solid particles).

The main source of difficulty encountered in the study of two-phase flow lies in the lack of information permitting a proper modelling of the field coupling terms. To minimize the complexity of the study, attention is restricted to the one- and two-dimensional forms of the governing equations. The purpose of this strategy is to concentrate on the physical aspects of the flow, without distraction from the variations in lateral directions. In this work, nucleation rate is considered to be outside the scope of the present study since the main aim of the study

is to investigate the behaviour of two-phase systems with existing large droplets such as arise in final stage steam turbine blading; however, droplet growth term is included in the flow equations. The introduction of interphase drag force (i.e. slip) increases the number of equations and solution complexity so that the current study has been initially restricted to the treatment of monodispersive flows, i.e. the radii of all particles in any given plane are equal. For a monodispersive flow with constant density droplets, i.e.

$$\rho_p = \rho_{p1} = \rho_{p2} \text{ ----- } = \rho_{pi}$$

the mixture density (equation 3.21) can be expressed as:

$$\rho_m = \frac{\rho_g}{(1-Y) + Y\frac{\rho_g}{\rho_p}} \tag{3.38}$$

and where $\rho_p >> \rho_g$ (e.g. low-pressure wet steam),

$$\rho_m \simeq \frac{\rho_g}{(1 - Y)} \tag{3.39}$$

3.4.1 Supplementary equations

In order to complete the mathematical formulation of the problem, supplementary relationships are needed to define some of the variables used in the flow equations.

Number of droplets per unit mass of the mixture (N)

$$N = \frac{Y}{\rho_p V_p} \tag{3.40}$$

where V_p is volume of a single droplet.

Droplet mass flow rate fraction (Y_f)

Where the phase velocities are not equal, the droplet mass fraction Y can be replaced by another which is based on mass flow rates Y_f. For a unit volume of mixture

$$Y_f = \frac{1}{\left(1 + \frac{\rho_g u_g A}{N m_p u_p}\right)} \tag{3.41}$$

where m_p is mass of a single droplet and A is the flow area. The droplet mass fraction Y is

$$Y = \frac{1}{\left(1 + \frac{\rho_g A}{N m_p}\right)} \tag{3.42}$$

hence,

$$Y_f = \frac{Y u_p}{(1-Y)u_g + Y u_p} \tag{3.43}$$

Droplet phase total enthalpy and energy

$$H_p = c_s T_p + \frac{1}{2}(u_p^2 + v_p^2) + \frac{p}{\rho_p} \tag{3.44}$$

$$E_p = c_s T_p + \frac{1}{2}(u_p^2 + v_p^2) \tag{3.45}$$

Mixture total enthalpy

$$H_m = (1 - Y_f)H_g + Y_f H_p \tag{3.46}$$

3.5 NORMALIZED FORM OF THE FLOW EQUATIONS

The numerical model equations are written on the basis of normalized (dimensionless) values. The basic set of reference values is given by a length L_r, a pressure P_r, a temperature T_r and a velocity U_r corresponding to the speed of sound in pure gas at the reference temperature. A list of the most important reference values is presented in table 3.1. The reference value for constants (e.g. c_p) is unity. The same applies to variables given by a sum of terms, one of which is constant. All the variables in the rest of this work are dimensionless unless otherwise stated.

3.5.1 One-dimensional two-phase flow equations

Making the appropriate one-dimensional reductions to the two-dimensional equations 3.29 - 3.35 in section 3.4 and normalizing yields the flow equations for the one-dimensional model. It must be noted here that extra terms have been added to the normalized one-dimensional equations used in the model, mainly

(i) Wall shear stress acting on the gas phase only.

(ii) External heat transfer through the wall to the gas phase only.

(iii) Gravity effects on both phases.

Taking into account the above extra terms, the normalized one-dimensional equations are given by,

gas-phase,

$$\frac{\partial}{\partial t}\int_V C_1 dV = \sum [C_1 u_g S] + \int_{CS} F_1 dA - \int_V Z_1 dV + I_1 \qquad (3.47)$$

where the column vectors are defined as

$$C_1 = \begin{bmatrix} \rho_m(1-Y) \\ \rho_m(1-Y)u_g \\ \rho_m(1-Y)E_g \end{bmatrix}, \quad F_1 = \begin{bmatrix} 0 \\ \frac{\rho_m(1-Y)}{\rho_g}\left(\frac{P}{\gamma} - \tau_w\right) \\ 0 \end{bmatrix}$$

$$Z_1 = \begin{bmatrix} \dot{Nm}_c\rho_m \\ \dot{Nm}_c\rho_m u_g - ND_p\rho_m + \frac{\rho_m(1-Y)}{Fr^2} \\ \gamma\dot{Nm}_c\rho_m\left(H_g - \frac{\gamma-1}{\gamma}\frac{P}{\rho_p}\right) - \gamma(\gamma-1)ND_p u_p\rho_m - \frac{\gamma}{Re_r Pr} NQ_p\rho_m \end{bmatrix}$$

and

$$I_1 = \begin{bmatrix} 0 \\ 0 \\ \sum\left[(\gamma-1)\frac{\rho_m(1-Y)}{\rho_g} Pu_g S\right] + \int_i^e Q_w\rho_m(1-Y)u_g S dx \end{bmatrix}$$

droplet phase,

$$\frac{\partial}{\partial t}\int_V C_2 dV = \sum[C_2 u_p S] + \int_{CS} F_2 dA + \int_V Z_2 dV + I_2 \qquad (3.48)$$

where

$$C_2 = \begin{bmatrix} \rho_m Y \\ \rho_m Y u_p \\ \rho_m Y E_p \end{bmatrix}, \quad F_2 = \begin{bmatrix} 0 \\ \frac{\rho_m Y}{\rho_p}\frac{P}{\gamma} \\ 0 \end{bmatrix}, \quad I_2 = \begin{bmatrix} 0 \\ 0 \\ \sum\left[(\gamma-1)\frac{\rho_m Y}{\rho_p} Pu_p S\right] \end{bmatrix}$$

$$Z_2 = \begin{bmatrix} N\dot{m}_c\rho_m \\ N\dot{m}_c\rho_m u_g - ND_p\rho_m + \dfrac{\rho_m Y}{Fr^2} \\ \gamma N\dot{m}_c\rho_m \left[H_g - \dfrac{\gamma-1}{\gamma}\dfrac{P}{\rho_p}\right] - \gamma(\gamma-1)ND_p u_p \rho_m + \dfrac{\gamma}{Re_r Pr} NQ_p\rho_m \end{bmatrix}$$

and

$$\sum [\ ] = [\ ]_i - [\ ]_e$$

i and e refer to the inlet and exit flow face of a flow cell of volume V, whose contours define a control surface CS (Fig. 3.1). Fr is the reference state Froude number defined as

$$Fr = \frac{U_r^2}{L_r g} \tag{3.49}$$

where g is acceleration due to gravity. Also,

S = flow area

dA = area element, either normal or parallel to the flow direction

τ_w = wall shear stress

Q_w = external heat transfer rate per unit mass flow of the gas-phase per unit length and it is assumed to be known.

The dimensionless wall shear stress is defined as

$$\tau_w = f\frac{\rho_g u_g^2}{2} \tag{3.50}$$

while the friction factor f is either constant or a function of the gas Reynolds number based on the duct hydraulic diameter.

Equation of state

$$P = \rho_g T_g \tag{3.51}$$

Supplementary equations

Total enthalpies:

$$H_g = T_g + \frac{\gamma-1}{2} u_g^2 + \frac{\gamma-1}{Fr^2} x \tag{3.52}$$

$$H_p = \beta_1 T_p + \frac{\gamma-1}{2} u_g^2 + \frac{\gamma-1}{\gamma} \frac{P}{\rho_p} + \frac{\gamma-1}{Fr^2} x \tag{3.53}$$

where

$$\beta_1 = \frac{c_s}{c_p} \tag{3.54}$$

Total energies:

$$E_g = T_g + \frac{\gamma(\gamma-1)}{2} u_g^2 + \frac{\gamma(\gamma-1)}{Fr^2} x \tag{3.55}$$

$$E_p = \beta_2 T_p + \frac{\gamma(\gamma-1)}{2} u_p^2 + \frac{\gamma(\gamma-1)}{Fr^2} x \tag{3.56}$$

where

$$\beta_2 = \frac{c_s}{c_v} \tag{3.57}$$

Inter-phase heat transfer (equation 2.40):

$$Q_p = 2\pi r_p k_g (T_p - T_g) Nu \tag{3.58}$$

where

$$Nu = 2.0 + 0.6\ (Re_p Re_r)^{\frac{1}{2}}\ Pr^{0.333} \tag{3.59}$$

Drag force (equation 2.30) :

$$D_p = \frac{1}{2} C_D \rho_g (\pi r_p^2)\ \ (u_p - u_g)|u_p - u_g| \tag{3.60}$$

where

$$C_D = \left(\frac{24}{Re_p Re_r}\right)\left[1 + \left(\frac{Re_p Re_r}{60}\right)^{5/9}\right]^{9/5} \quad \text{for } 0 < Re_p Re_r < 3000 \tag{3.61}$$

and

$$Re_p = \frac{2 r_p \rho_g |u_p - u_g|}{\mu_g} \tag{3.62}$$

with

$$\mu_g = \mu_g(T_g)$$

$$k_g = k_g(T_g)$$

It must be emphasized here that since D_p is taken as a function of $(u_p - u_g)$, the drag force sign in the flow equations 3.47 and 3.48 have been changed.

3.5.2 Two-dimensional two-phase flow equations

The two-dimensional coupled system of gas-phase and droplet-cloud conservation equations 3.29 - 3.35 in normalized form is as follows.

Gas-phase:

$$\frac{\partial}{\partial t}\int_V C_3 dV = \sum[C_3 u_g \Delta S_x + C_3 v_g \Delta S_y] - \int_V Z_3 dV + I_3 \qquad (3.63)$$

where the column vectors are defined as

$$C_3 = \begin{bmatrix} \rho_m(1-Y) \\ \rho_m(1-Y)u_g \\ \rho_m(1-Y)v_g \\ \rho_m(1-Y)E_g \end{bmatrix}, \quad I_3 = \begin{bmatrix} 0 \\ \sum\left[\frac{\rho_m(1-Y)}{\rho_g}\frac{P}{\gamma}\Delta S_x\right] \\ \sum\left[\frac{\rho_m(1-Y)}{\rho_g}\frac{P}{\gamma}\Delta S_y\right] \\ \sum\left[(\gamma-1)\frac{\rho_m(1-Y)}{\rho_g}P(u_g\Delta S_x + v_g\Delta S_y)\right] \end{bmatrix}$$

$$Z_3 = \begin{bmatrix} \dot{N}m_c\rho_m \\ \dot{N}m_c u_g\rho_m - ND_{px}\rho_m \\ \dot{N}m_c v_g\rho_m - ND_{py}\rho_m \\ \gamma\dot{N}m_c\rho_m\left(H_g - \frac{\gamma-1}{\gamma}\frac{P}{\rho_p}\right) - \gamma(\gamma-1)N\rho_m(u_pD_{px} + v_pD_{py}) - \frac{\gamma}{Re_r Pr}NQ_p\rho_m \end{bmatrix}$$

droplet-cloud:

$$\frac{\partial}{\partial t}\int_V C_4 dV = \sum[C_4u_p\Delta S_x + C_4v_p\Delta S_y] + \int_V Z_3 dV + I_4 \qquad (3.64)$$

where

$$C_4 = \begin{bmatrix} \rho_m Y \\ \rho_m Yu_p \\ \rho_m Yv_p \\ \rho_m YE_p \end{bmatrix}, \quad I_4 = \begin{bmatrix} 0 \\ \sum\left[\frac{\rho_m Y}{\rho_p}\frac{P}{\gamma}\Delta S_x\right] \\ \sum\left[\frac{\rho_m Y}{\rho_p}\frac{P}{\gamma}\Delta S_y\right] \\ \sum\left[(\gamma-1)\frac{\rho_m Y}{\rho_p}P(u_p\Delta S_x + v_p\Delta S_y)\right] \end{bmatrix}$$

The summations are made over the four faces of the element and ΔS_x and ΔS_y are the projections of the faces in the x and y directions respectively (see Fig. 3.2). The above equation sets together with the following supplementary equations form the basis for the two-dimensional two-phase flow model:

$$H_g = T_g + \frac{\gamma-1}{2}(u_g^2 + v_g^2) \qquad (3.65)$$

$$H_p = \beta_1 T_p + \frac{\gamma-1}{2}(u_p^2 + v_p^2) + \frac{\gamma-1}{\gamma}\frac{p}{\rho_p} \tag{3.66}$$

$$E_g = T_g + \frac{\gamma(\gamma-1)}{2}(u_g^2 + v_g^2) \tag{3.67}$$

$$E_p = \beta_2 T_p + \frac{\gamma(\gamma-1)}{2}(u_p^2 + v_p^2) \tag{3.68}$$

$$D_{px} = \frac{1}{2} C_D(\pi r_p^2)\, \rho_g (u_p - u_g)|u_p - u_g| \tag{3.69}$$

$$D_{py} = \frac{1}{2} C_D(\pi r_p^2)\, \rho_g (v_p - v_g)|v_p - v_g| \tag{3.70}$$

$$Re_p = \frac{2 r_p \rho_g [(u_p - u_g)^2 + (v_p - v_g)^2]^{\frac{1}{2}}}{\mu_g} \tag{3.71}$$

while expressions for C_D, Q_p, $\dot{m}_c$, Kn and the state equation are the same as those stated in section 3.5.1 for the one-dimensional case.

3.6 CLOSURE TO CHAPTER 3

The governing equations describing the two-phase flow motion, as two interpenetrating continua, were presented in this chapter. Because of the concern with relative motion of the two phases, separate sets of equations were written for each phase. It was shown that the extension of the standard single-phase conservation equations to analyze two-phase (gas/particle) flow in the nonequilibrium limit involves the introduction of gas/particle interaction terms which account for the exchange of mass, momentum and energy between the gas and particles; it also involves the

solution of a system of integral equations for the particles based on a "continuum particle cloud" assumption where the continuous distribution of particle sizes at each point in the flow is modelled by several groups of representative "constant size" particles. The mathematical equations can be adopted to the solution of different types of two-phase flow problems. However, in the coming chapters these equations are applied to the solution of gas-solid particles flow.

CHAPTER 4

ONE-DIMENSIONAL MODEL

4.1 INTRODUCTION

A one-dimensional computational model for gas-particle flow in ducts is proposed and analyzed, making use of a control volume approach for solving numerically the time-dependent, two-phase flow equations. It has been constructed in order to assess the capability of the basic method and various modifications in dealing with two-phase flows having velocity slip, in a more economical way than a two-dimensional version, and to enable comparisons with other one-dimensional predictions. The one-dimensional flow model can provide a rigorous test case for time-marching methods in solving one-and-two-phase flows, especially if a convergent-divergent nozzle is considered. High flow property gradients, the product of area changes or irreversibilities or both, can easily be simulated. This should provide a suitable foundation for the two-dimensional model which is the goal of this project; a description of the two-dimensional model is left until chapter 6 because its essential features are more easily understood without the complications of wall friction, wall heat transfer, etc.

The equations used are those presented in the previous chapter for the one-dimensional flow case. Numerical schemes proposed and used by Denton (18, 19) and Damia-Torres (4, 110) for one-phase flows are employed. The model incorporates the effects of varying degrees of velocity and temperature disequilibrium at the duct inlet on the subsequent flow through the duct. Furthermore, it includes other features such as the capability to deal with external heat transfer and wall friction. Although the finite difference form of the flow equations contains inter-phase mass transfer terms, no attempt has been made to solve for cases where inter-phase mass tranfer occurs.

In the present chapter the physical - mathematical features of the one-dimensional model are described. The exact equations are translated into finite - difference approximations. A full description of boundary and initial conditions are included together with other important numerical aspects. All equations are in non-dimensional form unless otherwise stated.

4.2 PHYSICAL FEATURES AND ASSUMPTIONS

The test case under consideration is a duct along which gas-particle mixture flows from a reservoir. The flow is physically determined by the characteristics of the duct, the conditions in the inlet reservoir and the back pressure. Moreover, the nature of the flow is also dependent on the particle size, particle material density and particle mass fraction. The assumptions on which the model is based are as follows:

(1) The flowing gas is assumed to be perfect, while its dynamic viscosity and heat conductivity are proportional to its temperature (constant Prandtl number).

(2) The specific heats of the gas and the particles are constants.

(3) The gas is inviscid apart from the drag it exerts on the particles and the duct walls.

(4) The particles are spherical and of uniform diameter.

(5) Drag forces are the only forces accelerating or decelerating the particles.

(6) The particles do not collide with each other (this assumption is satisfied rigorously for the case of a monodisperse suspension and steady flow) and are uniformly distributed.

(7) Brownian motion of the particles does not contribute to the pressure of the system.

(8) The particles have a large thermal conductivity and small mass and in consequence have a uniform temperature.

(9) Thermal energy exchange between the particles and the gas occurs by convection.

(10) There are no mass or energy losses from the system.

(11) There are no phase transitions or coagulation.

(12) In the case where there is heat transfer from an external agent at the duct walls, the external heat transfer is assumed to occur by conduction to the gas phase. The external heat transfer rate per unit mass flow of gas phase per unit length is assumed to be known.

For a one-dimensional flow cell of volume V, whose contours define a control surface CS (Fig. 3.1), the time gradients of the mass, momentum and energy of each phase of the mixture occupying the control volume (cell) at a time t are determined by: (a) the nett transport rate of these quantities through the flow faces denoted by i and e, (b) the surface forces acting on CS, (c) the flow work rate due to these forces, (d) the overall heat transfer rate through CS and, (e) the interaction phenomena between the phases within the control volume V. The flow equations describing the two-phase system in the flow cell are those derived in the previous chapter (i.e. equations 3.72 and 3.73). Flow variables are averaged over the cross-sections so that they only depend on the streamwise coordinate x. Thus, it is assumed that the rate of change of the component phases properties normal to the streamline direction is negligibly small compared with the rate of change along the streamline. Furthermore, the crosswise velocity is assumed to be small compared to the total velocity.

4.3 FINITE DIFFERENCE APPROXIMATIONS

4.3.1 Mesh Configuration

The grid for the one-dimensional model is formed by a succession of flow cells similar to that illustrated in Fig. 3.1. Considering a convergent-divergent nozzle as shown in Fig. 4.1, where the centreline of the nozzle lies along the x-axis, the grid is formed by dividing the nozzle by a series of vertical lines. Any two adjacent vertical lines form a flow cell. The vertical lines (crosswise lines) need not be evenly spaced, thus different cells may have different widths. Calculation points are taken to be at the centres of the cells. The first vertical line (i.e. inlet face for the first cell) is taken at the nozzle inlet ($x = 0$) while the last vertical line (i.e. outlet face of the last cell) is taken at the nozzle outlet ($x = L$). Fig. 4.1 shows a nozzle divided into k cells which define k calculation points, spaced in such a way that $x_1 > 0$ and $x_k < L$. The width of the cell j (i.e. the grid size at point j) is denoted by Δx_j. The model's grid is formed in such a way so as to deal with rectangular and circular ducts. When the wall contour is a curve, it is approximated by a straight line. Thus it is recommended to pack the grid (i.e. use small Δx_j) in areas where large area changes are expected.

4.3.2 Finite Difference Equations

The various terms in equations 3.47 and 3.48 are approximated by finite differences based on the centre points j of the flow cells (Fig. 3.1), assuming that the values of the different variables at j represent the space averages of the respective variables in the cell under consideration. The time derivative terms are approximated by a simple forward difference

$$\frac{\partial}{\partial t}\int_{V_j} C\, dV = V_j \frac{C_j^{t+\Delta t} - C_j^t}{\Delta t} \tag{4.1}$$

where C is a column vector containing the variables $\rho_m(1-Y)$, $\rho_m(1-Y)u_g$ and $\rho_m(1-Y)E_g$ for the gas-phase, while for the particle-phase it contains the variables $\rho_m Y$, $\rho_m Y u_p$ and $\rho_m Y E_p$. Δt is the time step size. In order to evaluate $C_j^{t+\Delta t}$, equations 3.47 and 3.48 are expressed as follows.

Continuity equations:

$$[\rho_m(1-Y)]^{t+\Delta t} = \rho_m(1-Y) - \frac{\Delta t}{V}\left\{\sum_{CS}[\rho_m(1-Y)u_g S] + \dot{Nm}_c \rho_m V\right\} \tag{4.2}$$

$$[\rho_m Y]^{t+\Delta t} = \rho_m Y - \frac{\Delta t}{V}\left\{\sum_{CS}(\rho_m Y u_p S) - \dot{Nm}_c \rho_m V\right\} \tag{4.3}$$

Momentum equations:

$$[\rho_m(1-Y)u_g]^{t+\Delta t} = \rho_m(1-Y)u_g - \frac{\Delta t}{V}\left\{\sum_{CS}\left[\frac{\rho_m(1-Y)}{\rho_g}\frac{P}{\gamma} + \rho_m(1-Y)u_g^2\right]S + \frac{\rho_m(1-Y)}{\rho_g}\tau_w A_L + V\left[\dot{Nm}_c \rho_m u_g - ND_p\rho_m + \frac{\rho_m(1-Y)}{Fr^2}\right]\right\} \tag{4.4}$$

$$(\rho_m Y u_p)^{t+\Delta t} = \rho_m Y u_p - \frac{\Delta t}{V}\left\{\sum_{CS}\left[\frac{\rho_m Y}{\rho_p}\frac{P}{\gamma} + \rho_m Y u_p^2\right]S - V\left[\dot{Nm}_c \rho_m u_g - ND_p\rho_m + \frac{\rho_m Y}{Fr^2}\right]\right\} \tag{4.5}$$

Energy equations:

$$[\rho_m(1-Y)E_g]^{t+\Delta t} = \rho_m(1-Y)E_g - \frac{\Delta t}{V}\left\{\sum_{CS}[\gamma\rho_m(1-Y)H_g u_g S]\right.$$

$$+ V\left[\gamma\dot{N}m_c\rho_m\left(H_g - \frac{\gamma-1}{\gamma}\frac{P}{\rho_p}\right) - \gamma(\gamma-1)ND_p u_p\rho_m\right.$$

$$\left.\left. - \frac{\gamma}{Re_r Pr}NQ_p\rho_m\right] + Q_w\rho_m(1-Y)u_g A\,\Delta x\right\} \qquad (4.6)$$

$$[\rho_m YE_p]^{t+\Delta t} = \rho_m YE_p - \frac{\Delta t}{V}\left\{\sum_{CS}(\gamma\rho_m YH_p u_p S)\right.$$

$$- V\left[\gamma\dot{N}m_c\rho_m\left(H_g - \frac{\gamma-1}{\gamma}\frac{P}{\rho_p}\right) - \gamma(\gamma-1)ND_p u_p\rho_m\right.$$

$$\left.\left. - \frac{\gamma}{Re_r Pr}NQ_p\rho_m\right]\right\} \qquad (4.7)$$

where

$\sum_{CS}\{\phi\}$ = the summation of ϕ over the control surface CS.

The drag force D_p is expressed as a function of the slip velocity (equation 3.60) and it carries the same sign as that of $(u_p - u_g)$, while Q_p is evaluated by using equation 3.58. No superscripts means that the flow variables are evaluated at time t and no subscripts indicate that the flow variables refer to point j. The total enthalpies H_g and H_p per unit mass of the mixture are introduced in the energy equations 4.6 and 4.7 for computational purposes by using the following relationships

$$H_g = \frac{E_g}{\gamma} + \frac{\gamma-1}{\gamma}\frac{P}{\rho_g} \tag{4.8}$$

$$H_p = \frac{E_p}{\gamma} + \frac{\gamma-1}{\gamma}\frac{P}{\rho_p} \tag{4.9}$$

which are derived from equations 3.52 - 3.57 and the gas (one-phase) equation of state.

$\rho_m(1-Y)$, $\rho_m(1-Y)u_g$, $\rho_m(1-Y)E_g$, $\rho_m Y$, $\rho_m Yu_p$ and $\rho_m YE_p$ are taken as conserved variables. Also, the following groups of variables are treated as single variables: $\rho_m(1-Y)u_g^2$, $\rho_m Yu_p^2$, $\rho_m(1-Y)H_g u_g$ and $\rho_m YH_p u_p$. To provide a fully explicit system for determining the conserved variables at the new time $(t + \Delta t)$ the right hand sides of equations 4.2 - 4.7 are evaluated at time t. These equations in conjunction with the correct time step-cell size ratio $(\Delta t/\Delta x)$, initial conditions and inlet and outlet boundary conditions provide a numerical solution for the two-phase steady flow under study.

4.3.3 Variables Approximations

Most of the terms on the right hand side of equations 4.2 - 4.7 have to be evaluated at the flow faces i (inlet) and e (exit) of the cells. The finite difference scheme chosen to evaluate the different variables at the inlet and exit faces of each cell is one used by Denton[21] and known as the "opposed difference technique". From a physical viewpoint, this scheme acts in such a way that information about the inlet stagnation conditions could travel downstream and that pressure waves could propagate upstream. According to the opposed difference technique, the pressure at the calculation point plus a correction factor acts on the inlet flow face (i); on the other hand the velocity at the same point plus another correction factor controls

the mass and momentum fluxes through the exit flow face (e) (Fig. 3.1). These correction factors are obtained by using curve fitting techniques and their time variation is damped. Based on this scheme, all the flow variables other than pressure are evaluated at the flow faces of interior cells $(2 \leq j \leq k-1)$ by

$$\phi_{i,j} = \phi_{j-1} + \Delta\phi_{j-1} \tag{4.10}$$

where $\phi_{i,j}$ represents the value of the variable at the inlet face of the flow cell j and

$$\Delta\phi_j = (1-R_f)\Delta\phi_j^{t-\Delta t} + R_f \left(\frac{\partial\phi}{\partial x}\right)_j \frac{\Delta x_j}{2} \tag{4.11}$$

On the other hand, the pressure is given by

$$P_{i,j} = P_j - \Delta P_j \tag{4.12}$$

and ΔP_j is given by

$$\Delta P_j = (1-R_f)\Delta P_j^{t-\Delta t} + R_f \left(\frac{\partial P}{\partial x}\right)_j \frac{\Delta x_j}{2} \tag{4.13}$$

However, as far as the one-dimensional model is concerned, the space derivatives at point j in equations 4.11 and 4.13 are evaluated by using a second order central difference to the values of the variable under consideration at points $j-1$, j and $j+1$. Consequently, at the flow faces, all the variables but pressure are given by biased backward finite differences, while the pressure is calculated using biased forward finite differences. By using a Taylor's series expansion, the space derivatives for all variables including the pressure can be shown to be

$$\left(\frac{\partial\phi}{\partial x}\right)_j = \frac{-d_{j+1}^2\phi_{j-1} + (d_{j+1}^2 - d_j^2)\phi_j + d_j^2\phi_{j+1}}{d_j\, d_{j+1}\, (d_j + d_{j+1})} \qquad (4.14)$$

where

$$d_j = x_j - x_{j-1}$$

When the relaxation factor R_f in equations 4.11 and 4.13 is unity, the change in the variable is just its space gradient times the distance. This is also true when the numerical scheme has adequately converged, irrespective of the value of R_f. However, the relaxation factor can be a constant value (usually less than unity) throughout the calculation or it can be set to zero (maximum damping) during the initial time steps and increased to a certain value (0.1 is recommended) during the rest of the calculations. Setting the relaxation factor to zero during the initial time steps would help smooth any large changes which may occur during these time steps due to the initial conditions.

4.3.4 Inter-Phase Interaction

Inter-phase coupling terms present in the flow equations 4.2 - 4.7 are expressed by their values at the calculation points. The gas coefficients of dynamic viscosity (μ_g) and thermal conductivity (k_g) are assumed to be proportional to the first power of the gas temperature, i.e.

$$\mu_g = k_g = T_g \qquad (4.15)$$

Furthermore, the reference dynamic viscosity of the gas is taken to be[4]

$$\mu_r = C_f T_r \qquad (4.16)$$

where $C_f = 5.65314 \times 10^{-8}$, also μ_r is in (kg/m.s) and T_r in (°K).

However, the reference thermal conductivity (k_r) is evaluated from the assumption of a constant Prandtl number Pr of 0.707 for the gas phase. Thus, the particle Reynolds number (equation 3.62) is expressed as

$$Re_p = \frac{\rho_g |u_p - u_g| d_p}{T_g} \tag{4.17}$$

where d_p is the particle diameter, while inter-phase mass transfer $\dot{m}_c$ is set to zero throughout the calculations.

4.3.5 Wall Friction and Heat Transfer

Wall shear stress τ_w and wall heat transfer are also expressed by their values at the calculation points. Wall shear stress is expressed by equation 3.50. The friction factor f is either a constant throughout the calculation or, for more realistic values, it can be made to depend on the gas Reynolds number Re_g. For example[4]

$$f = \frac{16}{Re_g}, \quad Re_g < 2300. \tag{4.18}$$

$$f = \frac{0.255}{(\log_{10} Re_g)^{2.5}}, \quad Re_g > 2300. \tag{4.19}$$

where the gas Reynolds number Re_g is based on the hydraulic diameter at the calculation point. External heat transfer per unit mass per unit length to the gas phase is supplied as input data at each calculation point.

4.3.6 Numerical Procedure

The procedure for both the one-and two-dimensional versions depends on having a set of values of $\rho_m (1-Y)$, $\rho_m Y$, $\rho_m(1-Y)u_g$, $\rho_m Y u_p$, etc. at each calculating point in the mesh at time t. The values of the flow variables at each calculating point at time $t + \Delta t$ are calculated from the governing equations in the following steps.

Step 1. New values of $\rho_m(1-Y)$ and $\rho_m Y$ are calculated from equations 4.2 and 4.3 respectively by using old values of ρ_m, Y, u_g and u_p.

Step 2. New values of $\rho_m (1-Y) E_g$ and $\rho_m Y E_p$ are calculated from equations 4.6 and 4.7 respectively by using old values of ρ_m, Y, H_g, H_p, u_g, u_p, $N.D_p$, $N.Q_p$ and P.

Step 3. New values of P are calculated by using the gas equation of state 3.51, employing new values of densities and the gas energy per unit volume together with old values of the gas velocity. Pressure gradients based on new pressures are also calculated at this step.

Step 4. New values of $\rho_m(1-Y)\, u_g$ and $\rho_m Y u_p$ are calculated from equations 4.4 and 4.5 respectively by using new values of P and old values of ρ_m, Y, u_g, u_p, $N.D_p$ and τ_w.

Step 5. New values of ρ_m and Y are calculated by using new values of $\rho_m(1-Y)$ and $\rho_m Y$.

Step 6. New values of u_g and u_p are calculated from new values of $\rho_m(1-Y)u_g$, $\rho_m Y u_p$, $\rho_m(1-Y)$ and $\rho_m Y$.

Step 7. New values of E_g and E_p are calculated from new values of $\rho_m(1-Y)\, E_g$, $\rho_m Y E_p$, $\rho_m(1-Y)$ and $\rho_m Y$.

Step 8. New values of T_g and T_p are found from the new E_g, E_p, u_g and u_p using equations 3.55 and 3.56.

Step 9. New values of D_p and Q_p are calculated using new values of u_g, u_p and ρ_g, via equations 3.60 and 3.58.

Step 10. New values of variables' gradients are then evaluated and steps 1 to 10 are then repeated.

4.4 BOUNDARY CONDITIONS

In order to reach a steady solution, the boundary conditions are kept constant. They determine the nature of the final flow. The flow under consideration is that of a gas-particle mixture coming from a reservoir, flowing along a duct and being discharged into another reservoir. The boundary conditions discussed are those corresponding to subsonic inlets only.

4.4.1 Inlet Cell

New values of the flow variables (time = t + Δt) at the centre of the first flow cell are calculated by using the finite difference form of the flow equations 4.2 - 4.7. However, fluxes through the inlet face of that cell (i.e. duct inlet) are used directly in the flow equations after being evaluated by imposing the inlet boundary conditions. The specified boundary conditions at the inlet plane of the duct are as follows.

(1) The inlet stagnation conditions determined by Pressure (P_o), temperature (T_o) and particle mass flow rate fraction (Y_o).

(2) The possibility of inlet thermal and dynamic disequilibrium between the phases is also considered. This is represented by the specified velocity and temperature lags at the duct inlet. Velocity lag (VL_i) and temperature lag (TL_i) are defined by[59,66,78]

$$VL_i = \left(\frac{u_p}{u_g}\right)_{il} \tag{4.20}$$

and

$$TL_i = \left(\frac{T_p - T_o}{T_g - T_o}\right)_{il} \tag{4.21}$$

respectively, where the subscript (il) indicate values at the inlet plane of the duct. The values of (VL_i) and (TL_i) range between zero to unity.

(3) The particle mass flow rate fraction (Y_{fi}), which is the ratio of the particle mass flow rate to the total mass flow rate of the mixture, i.e.

$$Y_{fi} = \left(\frac{\dot{m}_p}{\dot{m}_m}\right)_{il} \tag{4.22}$$

where $\dot{m}_m = \dot{m}_g + \dot{m}_p$, is also specified.

(4) The size of the particles, represented by their radius at the duct inlet (r_{pi}).

The gas phase is assumed to undergo an isentropic expansion from the upstream stagnation conditions. Furthermore, in order to calculate the static pressure at the inlet plane of the duct (P_{il}), the two-phase mixture is assumed to have a constant total momentum between the duct inlet and the first calculation point. This assumption is necessary since the pressure gradient between these two points can not be set to zero due to the possible existence of inter-phase heat and momentum transfer, i.e. from equation 4.12.

$$\Delta P_{il-1} \neq 0. \quad \text{and} \quad P_{il} \neq P_1$$

However, the assumption of constant total momentum of the mixture would in turn require a condition of constant flow area between the inlet and the first calculation point. This condition is not a drawback since most researchers employing time-marching methods in one- and two-phase flows recommend the use of a long constant-area duct at the inlet of the computational domain (e.g. Damia Torres[4], Marsh and Merryweather [23] and Bakhtar and Mohammadi Tochai[40].). This facilitates the

damping of high-pressure waves moving towards the inlet from within the passage. Moreover, this long straight inlet introduces the physical idea of the flow starting at infinity[4].

The mixture's total momentum can be found by adding the momentum equations 4.4 and 4.5 and neglecting the unsteady terms (steady state condition). The condition is then

$$MOM_{i1} = MOM_1 \tag{4.23}$$

where for a particular time step MOM_{i1} can be expressed as a function of (P_{i1}) by imposing the inlet boundary conditions and MOM_1 is constant, then

$$MOM_{i1} - MOM_1 = G(P_{i1}) \tag{4.24}$$

The value of P_{i1} can be calculated by using the Newton-Raphson method to solve equation 4.24. The actual procedure for determining P_{i1} is as follows.

(1) Using the old values of the flow variables (e.g. P, $\rho_m Yu_p^2$ and $\rho_m(1-Y)u_g^2$) the total momentum at the first calculation point (MOM_1) is calculated from equation A1 (see appendix A). However, new versions of the model employ new values of the pressure $P_1^{t+\Delta t}$ in conjunction with old values of the other variables. This will be explained in more detail later in the chapter.

(2) Using an initial value for the inlet static pressure as $P_{i1} = P_1$, equation 4.24 is solved by using the Newton-Raphson method to find the correct value of P_{i1}. The condition for the completion of the iterative procedure is set by specifying a value for $|\Delta P/P|_{i1}$ of, say, 0.0001.

(3) Using the calculated value of P_{il}, all other variables at the inlet are calculated by using the specified boundary conditions and the isentropic expansion relationships for the gas phase, together with the definition of the total enthalpy of the mixture, i.e.

$$H_{mo} = (H_m)_{il} \tag{4.25}$$

where H_{mo} is the mixture's stagnation enthalpy given by

$$H_{mo} = \left[(1-Y_o) + Y_o \left[\beta_1 + \frac{\gamma-1}{\gamma} \frac{P_o}{\rho_p T_o}\right]\right] T_o \tag{4.26}$$

A detailed derivation of $G(P_{il})$ and other inlet relationships are given in Appendix A.

4.4.2 Outlet Cell

Similar to the inlet region, the outlet region of the duct is recommended to be of constant area. This type of outlet introduces the concept of the flow ending at infinity and helps in damping the pressure waves. The only specified property at the duct exit is the static pressure P_b (known as the back pressure). The back pressure controls the resulting flow régime in the duct.

At the last calculation point (k), the space derivatives of all flow variables except pressure are calculated by using a second order upwind difference and their time variation is damped, i.e.

$$\Delta\phi_k = (1-R_f)\Delta\phi_k^{t-\Delta t} + R_f\left(\frac{\partial\phi}{\partial x}\right)_k \frac{\Delta x_k}{2} \tag{4.27}$$

and

$$\left(\frac{\partial\phi}{\partial x}\right)_k = \frac{d_k^2\phi_{k-2} - (d_{k-1}+d_k)^2\phi_{k-1} + (2d_{k-1}d_k + d_{k-1}^2)\phi_k}{d_{k-1}\, d_k\, (d_{k-1}+d_k)} \tag{4.28}$$

The specified back pressure is introduced at a distance Δx_k after the point k. This is equivalent to setting a dummy point $(k+1)$ with

$$d_{k+1} = \Delta x_k \quad \text{and} \quad P_{k+1} = P_b$$

The pressure at the inlet face of flow cell k is calculated by using equations 4.12 and 4.13. Furthermore, the pressure at the outlet face of the cell (i.e. duct outlet plane) is evaluated by using equation 4.12, i.e.

$$P_{e,k} = P_b - \Delta P_{k+1} \tag{4.29}$$

where the subscript (e,k) represents the exit plane of the last flow cell k. However, ΔP_{k+1} is calculated by using equations 4.27 and 4.28 with the replacement of k by $k+1$.

4.5 INITIAL CONDITIONS

In order to initialise the numerical procedure, the conditions of the flow at $t = 0$ must be specified at all calculation points. Due to the hyperbolic nature of the flow equations, the initial conditions do not affect the steady state solution and therefore completely arbitrary initial conditions can be used for the flow variables. However, the initial conditions affect the number of time steps needed for reaching the final solution and could create stability problems characterised by high pressure waves travelling towards the upstream end of the flow region. Moreover, the closer the initial conditions are to the steady solution the faster is the convergence rate. Intermediate results do not represent the real development of the steady flow even if the initial conditions represent an actual physical flow and R_f of unity is used. This is because the boundary conditions do not represent a real transient flow.

Different sets of initial conditions can be employed in the one-dimensional model. In all the sets of the different initial conditions employed the initial spatial gradients of the flow variables (e.g. $\partial P/\partial x$, $\partial[\rho_m(1-Y)]/\partial x$, $\partial(\rho_m Y)/\partial x$, $\partial[\rho_m(1-Y)u_g^2]/\partial x$, $\partial(\rho_m Y u_p^2)/\partial x$ ------- .) are set to zero at all calculation points. The different schemes used to evaluate the flow variables at $t = 0$ are as follows.

4.5.1 Scheme One

Initial conditions correspond to uniform gas-particle flow, defined by a constant pressure equal to that specified at the exit of the duct, P_b, at all calculation points. The gas phase is assumed to undergo an isentropic expansion from the inlet stagnation conditions to the back pressure. The gas velocity is evaluated by assuming conservation of total enthalpy of the mixture. However, the particle-phase is assumed to be travelling with velocity and temperature lags equal to those specified at the inlet boundary, i.e.

$$(u_p)_j = (u_g\ VL)_j \tag{4.30}$$

and

$$(T_p)_j = TL_j(T_g - T_o)_j + T_o \tag{4.31}$$

where

$$VL_j = VL_i \quad \text{and} \quad TL_j = TL_i \tag{4.32}$$

Moreover, the particle mass flow rate fraction $(Y_f)_j$ is taken to be equal to that specified at the inlet boundary (Y_{fi}). The particle mass fraction Y_j is calculated by using equation 3.68 which can be expressed as

$$Y_j = \left[\frac{Y_f}{(1-Y_f)\ VL + Y_f}\right]_j \tag{4.33}$$

The mixture density is calculated by using equation 3.44.

4.5.2 Scheme Two

The flow is initially taken to be that of a mixture with constant mass flow rate, as well as constant total conditions, i.e.

$$\dot{m}_m = [\rho_m(1-Y)u_g + \rho_m Y u_p]A = \text{constant} \tag{4.34}$$

Furthermore, effects of the particle velocity and temperature lags on the compressible flow index of the gas-phase are considered. Also considered are their effects on the speed of sound in the two-phase mixture. Bowers[59] has derived the following expressions for a dilute gas-particle flow with constant temperature and velocity lags

$$\frac{P}{\rho_g^n} = \text{constant} \tag{4.35}$$

$$\frac{P_o}{P} = \left(1 + \frac{n-1}{2} M_m^2\right)^{\frac{n}{n-1}} \tag{4.36}$$

$$\frac{T_o}{T_g} = 1 + \frac{n-1}{2} M_m^2 \tag{4.37}$$

$$\frac{A}{A_t} = \frac{1}{M_m}\left(\frac{T_{gt}}{T_g}\right)^{\frac{n+1}{2(n-1)}} \tag{4.38}$$

where the subscript t refers to variables at the throat, M_m is the gas Mach number based on the speed of sound c_m in the mixture, i.e.

$$M_m = \frac{u_g}{c_m} \tag{4.39}$$

and

$$c_m = \left[\frac{nR_g T_g}{1+Z_1 VL}\right]^{\frac{1}{2}} \tag{4.40}$$

$$\beta_2 = \frac{c_s}{c_v} \tag{4.41}$$

$$Z_1 = \frac{Y_f}{1-Y_f} \tag{4.42}$$

Also,

$$n = \frac{(\gamma+Z_1\beta_2 TL)(1+Z_2 VL^2)}{(\gamma+Z_1\beta_2 TL)(1+Z_2 VL^2) - (\gamma-1)(1+Z_1 VL^2)} \tag{4.43}$$

where

$$Z_2 = \frac{Y}{1-Y} \tag{4.44}$$

By using equations 4.35 - 4.44 the mixture mass flow rate defined by equation 4.34 can be expressed as

$$\dot{m}_m = CON \cdot \frac{A \frac{P_o}{\sqrt{T_o}} M_m \left[1 + \frac{n-1}{2} M_m^2\right]^{-\frac{n+1}{2(n-1)}}}{\left[\rho_p + Z_2 \frac{\gamma P_o}{T_o}\left[1 + \frac{n-1}{2} M_m^2\right]^{\frac{1}{n-1}}\right]} \tag{4.45}$$

where

$$CON = \rho_p(1+Z_2 VL)\sqrt{\frac{n}{\gamma(1+Z_1 VL)}} \tag{4.46}$$

Equations 4.20 and 3.38 are also used in deriving equation 4.45.

In order to determine the type of the mixture flow in the duct caused by the specified back pressure P_b, the ratio of the exit area A_e of the duct to the minimum area A_t is expressed, by using equation 4.38, as

$$\frac{A_e}{A_t} = \frac{b_1}{(M_m)_{sub}} \left[\frac{1 + \frac{n-1}{2} (M_m^2)_{sub}}{\left(\frac{n+1}{2}\right)} \right]^{\frac{n+1}{2(n-1)}} \tag{4.47}$$

with

$$b_1 = \left[\rho_p + Z_2 \frac{\gamma P_o}{T_o} \left[1 + \frac{n-1}{2} (M_m^2)_{sub} \right]^{\frac{1}{n-1}} \right] \Bigg/ \left[\rho_p + Z_2 \frac{\gamma P_o}{T_o} \left[\frac{n+1}{2} \right]^{-\frac{1}{n-1}} \right]$$

where $(M_m)_{sub}$ is the exit Mach number corresponding to subsonic exit and critical mass flow. Equation 4.47 can be solved to determine $(M_m)_{sub}$ by the Newton-Raphson method. Hence, the exit pressure (P_{sub}) corresponding to $(M_m)_{sub}$ can be calculated and used to define the initial flow field. In order to avoid fast changing gradients and supersonic flows, which can limit the time step size and may lead to instabilities at the first stages of the calculation, the following criterion is adopted for the initial exit pressure $(P_e^{t=o})$.

If $P_b \geq P_{sub}$, then $P_e^{t=o} = P_b$, (4.48a)

or if $P_b < P_{sub}$, then $P_e^{t=o} = P_{sub}$. (4.48b)

The mixture mass flow rate at the duct exit is then calculated by using the calculated initial exit pressure $(P_e^{t=o})$ and the total conditions defined by equations 4.35 - 4.37 into equation 4.45. The calculated mixture mass flow rate is then kept constant throughout the duct, i.e.

$$(\dot{m}_m)_j = (\dot{m}_m)_{exit} \tag{4.49}$$

The Mach number (M_m) is then calculated throughout the duct by using the Newton-Raphson method on equation 4.49. The rest of the gas-phase

flow properties are calculated by using the isentropic relations with n as the compressible flow index. The particle-phase flow variables are evaluated by setting the constant temperature and velocity lags equal to those specified at the inlet boundary of the duct and by assuming constant stagnation enthalpy of the mixture.

4.5.3 Other Schemes

Other schemes employed in the model are those corresponding to the inviscid analytical solution of a single-phase gas flow while the particle-phase properties are determined by using temperature and velocity lags equal to those specified at the inlet together with the constant mixture stagnation enthalpy assumption. Constant velocities and temperatures for the particle-phase with the inviscid analytical solution of the gas-phase are also considered.

4.6 SMOOTHING

Time-dependent techniques are usually characterized by instabilities occurring due to the amplification of short wavelengths to magnitudes beyond physical reality. These high-frequency components lead to strong oscillations in the steady-state solution resulting in a slower rate of convergence or the collapse of the numerical procedure. The instabilities could also act as obstacles to larger time steps[4]. High pressure gradients occurring in a strong shocked flow are the usual cause of non-linear instabilities in the streamwise direction[4]. This can lead to overshoot and undershoot around the shock wave which in turn can be smoothed out by mesh refinement. Mesh refinement can be impractical so that it is recommended to control the instabilities by the use of a pseudo-viscosity term introduced by the smoothing[4].

4.6.1 Pressure Field Smoothing

Pressure field smoothing has been reported (Denton[119]) to be an effective way of avoiding instabilities resulting from the interaction of changes in pressure with changes in velocity. By freezing the pressure field and allowing other flow variables to convect freely then the upwind differencing on these variables gives, in principle, complete stability for any size of time step[119]. Hence, in order to delay the onset of instabilities the pressure field is damped out by spatial smoothing after each time step as follows:

$$P_{js}^{t+\Delta t} = (1-\varepsilon)P_j^{t+\Delta t} + \frac{\varepsilon}{2}\left[P_{j+1}^{t+\Delta t} + P_{j-1}^{t+\Delta t}\right] \qquad (4.50)$$

where the subscript s indicates a smoothed value of P ε is a constant smoothing factor with a recommended value of 0.0 - 0.5[119]. Furthermore, the effect of smoothing on the final solution can be reduced by basing the pressure correction factors on the unsmoothed pressure field whilst using the smoothed pressure field in the two-phase flow momentum equations.

4.6.2 Flow Variables Smoothing

Smoothing of the conserved variables as applied in the one-dimensional model is that used by Holst[106] and Damia-Torres[4] for one-phase flows. The "corrections" are applied at the end of each time step. Consider three calculation points $j-1$, j and $j+1$ and let ϕ be the variable to be smoothed and ϕ_{js} its value at j if there were a linear variation of ϕ between $j-1$ and $j+1$, i.e.

$$\phi_{js} = \phi_{j+1} + (\phi_{j-1} - \phi_{j+1})SC_j \qquad (4.51)$$

where

$$SC_j = \frac{\Delta x_j + \Delta x_{j+1}}{\Delta x_{j-1} + 2\Delta x_j + \Delta x_{j+1}} \tag{4.52}$$

and Δx_j is the width of the cell whose centre is the point j. For $\Delta x_j = \Delta x_{j-1} = \Delta x_{j+1} = \Delta x$, $SC_j = 0.5$. If $\Delta\phi_{js}$ is the difference between ϕ_{js} and the actual value of ϕ at point j, then

$$\Delta\phi_{js} = SC_j\ \phi_{j-1} + (1-SC_j)\ \phi_{j+1} - \phi_j \tag{4.53}$$

Smoothing is carried out by correcting ϕ_j by adding to its calculated value a fraction of $\Delta\phi_{js}$ as given by equation 4.53. $\Delta\phi_{js}$ is multiplied by a factor which is formed by an arbitrary smoothing constant (SF) multiplied by another factor which is a function of the partial mass of each phase. Thus for the gas-phase

$$\phi_j^* = \phi_j + SF \cdot GF_j\ [SC_j\ \phi_{j-1} + (1-SC_j)\phi_{j+1} - \phi_j] \tag{4.54}$$

where ϕ represents any one of the flow variables $\rho_m(1-Y)$, $\rho_m(1-Y)u_g$ and $\rho_m(1-Y)E_g$ while ϕ_j^* is the smoothed value of ϕ_j. Also,

$$GF_j = \frac{|SC_j\ W_{j-1} - W_j + (1-SC_j)W_{j+1}|}{[SC_j\ W_{j-1} + W_j + (1-SC_j)W_{j+1}]} \tag{4.55}$$

where $W = \rho_m(1-Y)$.

The particle-phase flow variables are smoothed as follows

$$\psi_j^* = \psi_j + SF \cdot PF_j\ [SC_j\ \psi_{j-1} + (1-SC_j)\psi_{j+1} - \psi_j] \tag{4.56}$$

where ψ represents any one of the flow variables $\rho_m Y$, $\rho_m Yu_p$ and $\rho_m YE_p$ while ψ_j^* is the smoothed value of ψ_j. Also,

$$PF_j = \frac{\left|SC_j(\rho_m Y)_{j-1} - (\rho_m Y)_j + (1-SC_j)(\rho_m Y)_{j+1}\right|}{\left[SC_j(\rho_m Y)_{j-1} + (\rho_m Y)_j + (1-SC_j)(\rho_m Y)_{j+1}\right]} \qquad (4.57)$$

GF_j and PF_j are positive fractions formulated in such a way that they are small in regions where the flow is smooth and where the variations of $\rho_m(1-Y)$ and $\rho_m Y$ are more linear. Furthermore, GF_j and PF_j are dimensionless, less than unity (since the denominator is always larger than the numerator) and have the magnitudes of $\rho_m(1-Y)$ and $\rho_m Y$ respectively as controlling factors.

This smoothing introduces a pseudo-viscosity which is only significant in regions of high density oscillations. However, smoothing is not applied to the flow variables at the first and last calculation points. A constant value in the range 0.1 - 0.15 is recommended for SF.

4.7 OTHER COMPUTATIONAL ASPECTS

The order of solution of the flow equations 4.2 - 4.7 is as follows.

(1) For calculation points $1 < j < k$ solve the flow equations in the following order.

a - Continuity equations

b - Momentum equations

c - Energy equations

(2) For the inlet cell solve the flow equations in the same order as for interior points. The new values (at time = $t+\Delta t$) of fluxes through the inlet plane of the duct are then calculated.

(3) The flow equations are then solved in the same order as in (1) for the last calculation point ($j = k$).

The above solution procedure is fully explicit in the sense that the new variables are not used in the time step in which they are calculated. Furthermore, the procedure solves the energy equations of the component phases instead of assuming constant stagnation enthalpy for the mixture throughout the flow.

4.7.1 Pressure Updating

New versions of the one-dimensional model employ a pressure updating procedure where the new values of the pressure are used in the momentum equations in conjunction with old values of all other variables. Although pressure updating is not indispensable for a successful convergence, it is thought to be necessary for the effectiveness of the opposed difference technique (Denton[21]). The order of solution of the flow equations when pressure updating is used is as follows.

(1) For interior points $1 < j < k$, solve the following flow equations

a - Continuity equations.

b - Energy equations.

c - Update the pressure by using the gas equation of state, using new values of densities and the gas energy per unit volume together with old value of the gas kinetic energy per unit mass, i.e.

$$\rho_g^{t+\Delta t} = \frac{[\rho_m(1-\bar{Y})]^{t+\Delta t}}{\left[1 - \frac{(\rho_m Y)^{t+\Delta t}}{\rho_p}\right]} \tag{4.58}$$

$$p^{t+\Delta t} = \rho_g^{t+\Delta t}\left[E_g^{t+\Delta t} - \frac{\gamma(\gamma-1)}{2}u_g^2 - \frac{\gamma(\gamma-1)}{Fr^2}x\right] \tag{4.59}$$

d - Evaluate pressure gradients using new values of the pressures.

(2) For the inlet cell (j = 1), similar steps are used as a, b and c in (1). Furthermore, the total momentum of the mixture is calculated by using new values of the pressure and old values of $(\rho_m Y)$, $\rho_m(1-Y)$, u_g and u_p. The inlet plane variables are then calculated by using the new value of P_1 and old values of all other variables.

(3) For the last flow cell (j = k), similar steps to a, b, c and d in (1) are used.

(4) The momentum equations are solved for the new values of $\rho_m(1-Y)u_g$ and $\rho_m Y u_p$ by using the new values for pressure and old values for all other variables.

Pressure updating has proved to be very useful in increasing the convergence rate and avoiding instabilities. This will be clear in the following chapters.

4.7.2 Convergence Criterion

In order to decide whether the steady state has been reached, a comparison of two consecutive values of each of the main flow variables $\rho_m(1-Y)$, $\rho_m(1-Y)u_g$, $\rho_m(1-Y)E_g$, $\rho_m Y$, $\rho_m Y u_p$ and $\rho_m Y E_p$ is made at every calculation point. The convergence criterion employed in the one-dimensional model is

$$\left| \frac{\phi_j^{t+\Delta t} - \phi_j}{\phi_j} \right| < 0.0001 \ , \quad j = 1 \text{ to } k \tag{4.60}$$

where ϕ_j represents the main flow variables at point j. The convergence test is applied every certain number of time steps (typically 100 time steps) and intermediate results are printed out. Furthermore, if

a variable is very large, very small or would produce a complex result, the calculation is stopped. It is also stopped when the number of time steps carried out exceeds a maximum number of time steps which is specified.

4.7.3 Time Step Updating

Time step size used in solving the finite difference equations is a very important factor in maintaining stability and achieving rapid convergence rates. The aim of the various stability criteria employed by different investigators is to use the maximum possible time step for maintaining stability. The stability criterion used in the one-dimensional model is that recommended by Denton[21], i.e. in dimensional form,

$$\Delta t \leq \frac{\Delta x}{c_g(1 + M_g)} \tag{4.61}$$

which is the well known (CFL) condition. The above condition is based on the gas-phase variables only. c_g and M_g are the speed of sound in the gas phase and the gas phase Mach number respectively. No attempts have been made to introduce the effects of the dispersed phase on the stability condition. The stability condition can be expressed in a non-dimensional form as

$$\Delta t \leq \frac{\Delta x}{T_g^{\frac{1}{2}}(1 + M_g)} \tag{4.62}$$

The model employs three different schemes for determining the time step.

(1) Constant Time Step

The time step size can be kept constant throughout the calculation. This scheme has also been used by one-phase flow investigators (e.g.

Damia-Torres[4]). The size of the maximum time step for a gas-particle flow in a particular grid is determined by using the stability condition (4.62) for the analytical solution of a pure gas flow in the same grid and under the same boundary conditions (i.e. P_b, T_o and P_o). However, the maximum time step for stability of the solution in a gas-particle flow Δt_{max} is usually less than that predicted by equation 4.62 for the gas flow analytical solution. This has limited the scheme in such a way that the maximum value of the time step for a stable solution in gas-particle flow has to be determined by numerical tests. This scheme, although implemented in the model, has not been used intensively since it requires an optimization procedure for different grids.

(2) The CFL Condition

This scheme makes use of the (CFL) condition (4.62) which is implemented in the model. Because the CFL condition is a necessary condition for stability, it gives the maximum allowable time step for any explicit finite-difference scheme. The (CFL) condition (4.62) is a local condition to be fulfilled at every calculation point. For this scheme, the stability condition is expressed as

$$\Delta t_{max} = B_1 \frac{(\Delta x)_{min}}{T_g^{\frac{1}{2}}(1 + M_g)} \tag{4.63}$$

where $(\Delta x)_{min}$ is the minimum value of Δx. In practice this scheme calculates the limiting time step at every calculation point using the local values of T_g, M_g and Δx and the most restrictive time step is then selected and used throughout the grid. B_1 is the time factor which is usually less than unity. In this scheme the time step calculated from (4.63) is updated every certain number of time steps (typically 50 time steps). The initial time step used in the calculation is part of the data input to the model.

(3) Spatially Varied Time Step

The previous scheme for determining the time step indicates that in only one calculation point does the time step equal the maximum permissible value and in all other points (for a non-uniform grid) the time step is often considerably smaller than allowed. In these points the stability of the finite-difference scheme is underestimated which means that the perturbation waves do not propagate as far as they might and the convergence is slowed down. Since the nett fluxes of mass, momentum and energy are conserved when the steady state is reached, then the steady state solution will be correct even if different time steps are taken at different points in the flow. Furthermore, since the maximum stable time step is determined by the local grid spacing it is highly recommended (see Denton[119] and Van Hove[130]) when using a non-uniform grid to use larger time steps in regions where the grid spacing is high. However, this procedure involves throwing away all pretence of following the time evolution of the flow, but provided stability is maintained it will give exactly the same steady state solution as uniform time steps[119]. The CFL condition (4.62) is expressed as

$$\Delta t_j = B_2 \left[\frac{\Delta x}{T_g^{\frac{1}{2}} (1 + M_g)} \right]_j \tag{4.64}$$

where B_2 is a time factor which is usually less than unity and different from B_1. In this scheme the time step Δt_j at each calculation point is updated every certain number of time steps (typically 50 time steps). This is different from the scheme used by Denton[119] in that his method updates the effective volume of the elements instead of the time step.

The merits of each of the above schemes in reducing the number of time steps necessary to achieve convergence will be discussed in the next chapter.

4.7.4 Organization of the Model

The model is constructed using the non-dimensional variables. The geometrical data of the duct are calculated in a separate program and read in as part of the data to the model. The maximum number of time steps is specified (say 1000) and when this limit is reached, the two-phase flow variables are printed out for subsequent study. At the end of each time step values of $\rho_m(1-Y)$, $\rho_m(1-Y)u_g$, $\rho_m(1-Y)E_g$, $\rho_m Y$, $\rho_m Y u_p$ and $\rho_m Y E_p$ are stored. Checks for convergence as well as for the limit of maximum number of time steps are performed every certain number of time steps (say 100). Convergence test is carried out in a subroutine (ERROR) which contains the inequality (4.60). The largest relative changes are then calculated and compared with the specified tolerance. When the steady state solution is reached the flow variables are then printed out and stored in a permanent file for subsequent study and use.

The damping is initially taken to be maximum ($R_f = 0$). However, after a certain number of time steps (usually 200) the relaxation factor is increased to 10%. Thus the R_f-t relation is a step function. The updating of the time step can take place as often as the convergence test or more frequently. The choice of initial conditions and time step updating schemes are read as part of the input data to the model. The model contains the following subroutines.

(1) INITIAL, calculates the initial flow field ($t = 0$) according to the initial flow scheme chosen.

(2) TRANSFER, calculates the inter-phase heat transfer and the drag force as well as the particle Reynolds number Re_p and other relevant parameters.

(3) STAT1, calculates the static pressure and fluxes at the inlet plane of the duct and hence imposes the boundary conditions.

(4) ERROR, for convergence test.

Fig. 4.2 shows a flowchart containing the main features of the one-dimensional model.

CHAPTER 5

ONE-DIMENSIONAL MODEL'S PREDICTIONS

5.1 INTRODUCTION

In the previous chapter an outline of the one-dimensional model was presented. In the present chapter, a number of illustrative tests are presented. These tests are intended to show how the model can be applied to the solution of gas-solid particle flows in ducts. They have been chosen to demonstrate and assess the capabilities and versatility of the one-dimensional model. In order to show effects caused by the presence of the particulate phase on the gas flow, the inviscid analytical solution of the latter is presented in most cases. Effect of the particle size, density, mass flow rate fraction and specific heat capacity on the flow are presented. The effects of the inlet velocity and temperature lags are also discussed. Furthermore, discussions on the effects of various aspects of the numerical scheme are presented.

5.2 MIXTURE FLOW IN CONVERGENT-DIVERGENT NOZZLE

In order to quantify the effects of inter-phase coupling phenomena, the flow through a horizontal, convergent-divergent nozzle is considered. The nozzle chosen is one with a sinusoidal area variation (nozzle N1). It is composed of four parts (Fig. 5.1): (1) a duct of constant area A_1, (2) a sinusoidal contraction from area A_1 to the throat area A_t, (3) a sinusoidal expansion from the throat to an area A_2 and (4) a duct of constant area A_2. The non-dimensional length of each part is taken to be 5.0 and $A_1 = A_2 = 1.5$, $A_t = 1.0$. Unless otherwise stated, the grid used is one made up by 23 calculation points (cells) with a variable flow cells width. The distribution and width of the flow cells are as follows:

number of cells	width
5	1.0000
3	0.7916
7	0.7500
3	0.7916
5	1.0000

In all test cases, unless otherwise stated, the nozzle is assumed to have smooth walls, i.e. $f = 0$, while a perfect gas with $\gamma = 1.4$, $R_g = 287.1$ J/kg°K and a constant Prandtl number (Pr) of 0.707 is considered. The solid particles have $\rho_p = 1057$ kg/m^3 and $c_s = 1340$ J/kg°K (polystyrene). Reference state parameters are taken to be $L_r = 1.0$ m, $T_r = 600$°K and $P_r = 1.5 \times 10^6$ N/m^2, while the dimensionless stagnation pressure and temperature are taken to be unity, i.e. $T_o = T_r$ and $P_o = P_r$, and $Y_o = Y_{fi}$. Thus the ratio P_b/P_o is expressed simply as P_b throughout the chapter. Convergence tests, for all cases, were carried out every 100 time steps and all figures show non-dimensional variables.

5.2.1 Subsonic Flow

A fully subsonic flow can be obtained along the nozzle N1 by setting the back pressure P_b to 0.9. The mixture considered is one containing solid particles with $d_p = 200$ μm and $Y_{fi} = 10\%$. The mixture is assumed to be in equilibrium at the nozzle inlet, i.e. $VL_i = TL_i = 1.0$. The initial reduction in nozzle area (convergent part) results in an acceleration of the gas-phase accompanied by a fall in static pressure and gas temperature (see Figs. 5.2, 5.3 and 5.4). Since the solids velocity and temperature are unable to keep pace with these changes, velocity and temperature lags soon develop. The particle drag force (D_p), in the convergent section, acts in such a way

so as to slow the gas velocity, while the particle heat transfer (Q_p) affects the flow by raising the gas-phase temperature slightly. These effects become more apparent when comparing the gas-phase velocity and temperature with those of the clean gas flow (Figs. 5.3 and 5.4). However, the mixture static pressure, between the nozzle inlet and throat region, as depicted in Fig. 5.2 displays a slight increase above that predicted in the clean gas only. It is also indicated that the minimum static pressure in the mixture occurs downstream of the geometrical throat. In the divergent section of the nozzle the gas-phase velocity starts to decelerate while the particle velocity is still increasing. When the gas velocity becomes less than that of the particles, the reversal in the action of the drag force causes the particles to decelerate. A reversal in the action of the particle heat transfer also occurs in this section. These reversals bring the velocity and temperature of the two phases closer to equilibrium near the nozzle exit. The total pressure P_o shows a slight decrease in the second half of the nozzle caused by the presence of the particles (Fig. 5.2).

Results presented in the above mentioned figures can be obtained by using the basic solution method, i.e. no pressure updating, with a constant relaxation factor (R_f) of 0.1. The initial state is one defined by "scheme one" described in the previous chapter. The number of time steps required to achieve convergence is 1000. However, this number can be reduced to 900 time steps by setting the relaxation factor to zero for the first 200 time steps and afterwards to 0.1. This illustrates the effectiveness of using strong damping at the beginning of the calculation to smooth out large changes which may arise during the first time steps. A further reduction in the number of time steps to 700 can be obtained by employing the pressure updating scheme and initial conditions corresponding to that described by "scheme two" of

the initial conditions. The steady state solution can be reached even faster (600 time steps) by using a spatially varied time step, i.e. equation 4.64. Effects of the various schemes will be discussed later in this chapter.

5.2.2 Shocked Flow

Transonic flows of gas-particle mixtures are of particular interest here. They emphasize the capability of time-marching methods in calculating flows of the mixed elliptic-hyperbolic nature. A normal shock in the divergent part of nozzle N1 can be obtained by setting the back pressure P_b to 0.7. The mixture considered is that containing solid particles (200 μm) in diameter and mass flow rate fraction (Y_{fi}) of 10%. The mixture is considered to be in thermal and dynamic equilibrium at the nozzle inlet, i.e. $TL_i = VL_i = 1.0$. For $Y_{fi} = 0.1$ the deviation of the mixture static and total pressures from those predicted analytically for clean gas flow is negligible (Fig. 5.5) except in the vicinity of the shock wave. This is due partly to the presence of the particles; also the step discontinuity in the flow cannot be entirely described by equations which assume a continuous variation of properties[110], so that the shock is smeared over the cells adjacent to it. Shock smearing can be reduced by choosing a finer grid around the shock. The deviation of the mixture static and total pressures is expected to increase by increasing the mass flow rate fraction (Y_{fi}) as will be seen later in this chapter.

Fig. 5.6 shows the velocity distribution of the two phases and that of the clean gas flow under the same conditions. Effects on the gas phase velocity due to the particles' presence seem to be small everywhere except in the shock vicinity when the slip velocity is at a maximum. The particle velocity reaches a maximum at the shock while the gas phase

velocity is undergoing a sharp discontinuity. The particles cannot be rapidly decelerated, resulting in a relaxation zone behind the shock. In this zone, gas-phase velocity is smaller than that of the particles which causes the slip to change its direction and hence a gradual deceleration of the particles. The particles will also accept heat from the gas phase since the gas temperature has been increased above that of the particles (Fig. 5.7). The particles and the gas approach velocity and temperature equilibrium at nozzle exit.

Converged solutions for the shocked gas-particle mixture can generally be obtained at a faster convergence rate than that in a fully subsonic flow ($P_b = 0.9$) for the same grid, R_f and Δt. The number of time steps needed for convergence in the shocked flow, when there is no pressure updating and $B_1 = 0.5$ is 800 compared with 900 for the subsonic case. However, the number of time steps for convergence when $P_b = 0.7$ can be reduced to 700 when the pressure is updated at every time step. Further reductions can be obtained by using spatially varied time steps with $B_2 = 0.8$. This reduces the number of time steps for convergence to 500. The phenomenon of faster convergence rates in shocked flows than in subsonic flows is believed by some investigators (e.g. Damia-Torres[4]) to show the suitability of the opposed-difference technique to hyperbolic flows. The shocked flow moves from hyperbolic to mixed hyperbolic-elliptic (when the steady state is reached)[4].

Fig. 5.8, shows the particle mass fraction distribution along the nozzle for subsonic and shocked mixture flows. In the inlet straight section, the gas and particles are in velocity equilibrium ($u_g = u_p$), hence the particle mass fraction Y is equal to the particle mass flow rate fraction (Y_f) (see equation A.8). Moreover, in the convergent part,

$$VL < 1.0 \quad \text{so} \quad Y > Y_f$$

while for the divergent part,

$$VL > 1.0 \quad \text{so} \quad Y < Y_f \ .$$

The particle mass fraction in the shocked flow shows steeper variations in the convergent and divergent parts of the nozzle compared to those in the subsonic case. This is due to the higher slip velocity present in the shocked flow.

5.2.3 Flows with Supersonic Outlets

Flows with supersonic outlets in nozzle N1 can be obtained by setting the back pressure to 0.16. The clean gas analytical solution corresponds to fully supersonic flow in the divergent part of the nozzle. Figs. 5.9 and 5.10 show profiles for a mixture with $P_b = 0.16$, $d_p = 200$ μm and $Y_{fi} = 10\%$. The mixture is assumed to be in velocity and temperature equilibrium at the nozzle inlet. The gas phase initial conditions are those corresponding to the clean gas analytical solution for the same back pressure. The particle phase initial parameters are derived by using the condition of constant mixture enthalpy and assuming temperature and velocity lags equal to those specified at the nozzle inlet (in this case, TL = VL = 1.0). In order to allow the back pressure to float with time rather than being fixed, the back pressure is assumed to be equal to the pressure at the nozzle exit face throughout the calculations. Furthermore, to avoid any instabilities caused by the initial conditions during the first time steps, a small constant value of the time step ($\Delta t = 0.1$) coupled with strong constant damping ($R_f = 0.1$) are employed. Convergence can be achieved within 800 time steps; however, this number can be much less for different particle parameters (e.g. 500 time steps for $d_p = 20$ μm).

Fig. 5.9 shows the total and static pressures in the mixture as well as the gas and particle velocities. Fig. 5.10 shows the gas and particle temperature fields. The onset of the deviation of the gas phase profiles from those of the clean gas flow starts after the mixture has passed through the geometrical throat. Fig. 5.11 shows the gas-phase Mach number in the mixture and the analytically-obtained clean gas Mach number. The figure show that the introduction of the solid particles in the flow makes necessary a slight reduction of the inlet Mach number[66].

5.3 PARAMETRIC STUDY

For nozzle N1, this study investigates, firstly, the influence of particle size, material density, specific heat and mass flow fraction on the pressure, velocity and temperature fields in the nozzle; secondly, effects of varying values of inlet temperature and velocity lags between the particles and the gas on the subsequent flow in the nozzle are considered. In all the following test cases, unless otherwise stated, a perfect gas with properties similar to those used in section 5.2 is considered. The reference and stagnation parameters are also taken to be the same as those in section 5.2. Convergence tests for all cases are carried out every 100 time steps with a tolerance of 0.01% and all figures show the non-dimensional variables. The study is carried out for the subsonic, shocked and supersonic exit flow.

5.3.1 Particle Size Effects

The effects of varying the particle size are investigated while other parameters are kept constant as follows:

$TL_i = VL_i = 1.0$, $Y_{fi} = 10\%$, $c_s = 1340$ J/kg°K and $\rho_p = 1057$ kg/m^3

For a given particle mass fraction Y and particle density, the number of particles per unit mass of the mixture N can be calculated by

$$N = \frac{Y}{\pi\, d_p^3\, \rho_p / 6} \tag{5.1}$$

An increase in particle diameter results in a reduction in the number of particles per unit mass of the mixture. Particle sizes ranging between 2 and 300 μm are investigated in the subsonic ($P_b = 0.9$), shocked ($P_b = 0.7$) and supersonic exit ($P_b = 0.16$) cases.

(i) Effects on the pressure field

Figs. 5.12 , 5.13 and 5.14 show the static pressure profiles in the nozzle for different particle sizes. For smaller size particles, the pressure follows more closely the behaviour of that in the clean gas flow. This is clearly illustrated in the throat region for the subsonic and shocked flow cases. The figures also indicate that the smaller particles produce larger pressure drops between the inlet and the throat.

(ii) Effects on the velocity fields

Results presented in Figs. 5.15 , 5.16 and 5.17 show that for the three different back pressures, the smaller particles respond quicker to the flowing gas stream than larger particles. Consequently, near the nozzle exit, smaller particles and the gas phase approach velocity

equilibrium at faster rates. However, while lower gas speed is observed in the two-phase flow field than that in the gas-only one-phase (Figs. 5.18 - 5.20), the small-sized particles act more effectively to slow down the gas-phase expansion (for P_b = 0.16) than that of the large-sized particles for the same particle mass flow fraction. This is also evident in the convergent section of the nozzle in the shocked case (P_b = 0.7). Fig. 5.18 shows gas-phase velocity for particle size of 2 and 200 μm in the subsonic mixture flow case (P_b = 0.9). In order to avoid instabilities due to high particle velocities in regions of fast area changes, care must be taken in the case of very small-sized particle flows (d_p < 5 μm). Thus, it is recommended to use a very small constant time step for small-sized particle flows to achieve a stable solution.

The concept of lower gas-phase velocity for small-sized particles is physically correct, since for the same particle mass fraction the total surface area (and total projected area) effective for momentum exchange between gas and particles is greater in a two-phase involving smaller diameter particles[66,132].

(iii) Effects on the temperature fields

Figs. 5.21 - 5.25 show the gas and particulate phase temperatures for various particle size for the three different back pressures (P_b = 0.9, 0.7 and 0.16). The temperature of the small-sized particles follows more closely the gas-phase temperature than the large-sized

particles temperature. Also, the temperature of the smaller particles equilibrates rapidly to the gas temperature in the second half of the nozzle (divergent and straight sections).

5.3.2 Particle Density Effects

Effects of varying the particle material density are investigated for particles 200 μm in diameter. The inlet boundary conditions, particle specific heat and mass flow fraction are kept constant and correspond to those in the previous subsection. Particle density is varied inside the range of 1057 - 10000 kg/m^3. It must be emphasized here that some of the chosen densities do not represent any known physical material, this is carried out in a random way to assess the effects of increasing values of particle density on the subsequent mixture flow in the nozzle.

Further consideration of equation 5.2 shows that for the same particle mass fraction and particle size, an increase in the particle density reduces the number of particles per unit mass of the mixture with a consequent reduction in the total particle heat transfer ($N \cdot Q_p$) and total particle drag ($N \cdot D_p$). Thus, the effects of such variations are expected to produce a similar trend of behaviour as that produced by reducing the particle size.

(i) Effects on the pressure field

Figs. 5.26 - 5.28 show the total and static pressures for different particle densities in the cases of P_b = 0.9, 0.7 and 0.16 respectively. In the fully subsonic (P_b = 0.9) and shocked flow (P_b = 0.7) cases, particles having smaller densities tend to produce slightly bigger pressure drops between the inlet and the throat region. This is also reflected in the total pressure behaviour along the nozzle. In the supersonic exit case (Figs. 5.28), particles having smaller densities appear to produce larger deviations of both the static and total pressures towards the nozzle exit when compared to the gas-only one-phase analytical case.

(ii) Effects on the velocity fields

Effects of varying the particle material density on the gas-phase and particle velocities are illustrated in Figs. 5.29 - 5.33. Figs. 5.29 - 5.31 show the gas-phase velocity in the mixture for P_b = 0.9, 0.7 and 0.16 respectively. While lower gas speed is observed in the two-phase flow field than that in the analytical one-phase flow, particles with lower densities act more effectively to slow down the gas-phase than that of the high density particles for the same particle mass flow fraction. Effects of different particle density on the gas-phase velocity are more evident in the supersonic exit case (Fig. 5.31) while for the fully subsonic flow (Fig. 5.43) such effects are almost negligible. Effects of changing the particle density on the particle velocity are illustrated in Figs. 5.31 - 5.33 which show particle velocities for P_b = 0.16, 0.9 and 0.7 respectively. The results indicate that lower density particles respond quicker to the flowing gas stream than higher density particles. Consequently, low density particles achieve higher velocities and, in the case of subsonic and shocked flow, approach equilibrium with the gas velocity in the exit

straight section quicker than particles with high densities. Figs. 5.34 and 5.35 show the particle drag force D_p as a function of $(u_p - u_g)$ for different particle densities for $P_b = 0.9$ and 0.7 respectively.

(iii) Effects on the temperature fields

Figs. 5.36 - 5.38 show effects of various particle densities on the gas and particle temperature fields. Generally, after the inlet constant area section, while higher gas temperatures are observed in the two-phase flow field than those of the clean gas analytical solution, the lower density particles act more effectively to raise the gas-phase temperature than higher density particles. This is due to the increase in the total inter-phase heat transfer caused by an increase in the number of particles per unit mass of the mixture. Moreover, these figures show that lower density particles respond quicker to changes in the gas-phase temperature than particles of higher density.

5.3.3 Effects of The Particle Mass Flow Rate Fraction

Effects of the particle mass flow rate fraction Y_{fi} are investigated only when equilibrium conditions $(TL_i = VL_i = 1.0)$ exist at the nozzle inlet. By increasing the particle mass flow rate fraction while keeping the particle diameter and density constant, the number of particles present per unit mass of the mixture N must increase (equation 5.1) with a consequent rise in the total particle drag ND_p and the particle heat transfer rate NQ_p. An investigation of the

effect of varying the particle mass flow rate fraction at the inlet is made for particles 200 μm in diameter. In all test cases Y_o is set equal to Y_{fi}, thus H_{mo} varies as Y_{fi} is varied.

(i) Subsonic mixture flow

Effects of varying Y_{fi} on the pressure, temperature and velocity fields in nozzle N1, when a fixed back pressure of 0.9 is used, are shown in Figs. 5.39, 5.40 and 5.41 respectively. As depicted in Fig. 5.39, increasing Y_{fi} results in a pressure increase at the nozzle inlet while the position of the minimum pressure is observed to move further inside the divergent section. The pressure in the divergent section is seen to increase less rapidly when Y_{fi} is large. Fig. 5.40 shows that the increase in the total particle heat transfer as Y_{fi} increases causes the gas temperature to rise and in consequence a reduction in the temperature difference between the two phases is also indicated as Y_{fi} increases. In general, the indicated pattern shows an upward shift in temperature profiles for increasing values of Y_{fi}. This is due to the fact that H_{mo} increases as Y_o (since $Y_o = Y_{fi}$) and the inlet temperatures are product of the calculation (i.e. not fixed). Fig. 5.41 summarises several velocity profiles for different Y_{fi} values. Lower inlet velocities are observed for high particle mass flow fractions resulting in a downward shift of the corresponding velocity profiles. The computed velocity profiles indicate a decrease in the maximum velocity difference between the two phases, as Y_{fi} is increased, due to the increase of the total particle drag force.

Fig. 5.42 shows that the pressure drop for the entire length of the nozzle ΔP_N is with good approximation linearly dependent on the particle mass flow fraction Y_{fi}. Fig. 5.43 shows variations of Stokes number with the particle mass flow fraction. Stokes number is defined as:

$$St = \frac{\rho_p \, u_{gi} \, r_p^2}{18 \, \mu_g \, D_t} \cdot \left(\frac{24}{Re_p C_D} \right)_i \qquad (5.2)$$

where the subscript i indicates the nozzle inlet. Fig. 5.43 shows that higher Stokes numbers are associated with low particle mass flow fractions. This indicates that for low Y_{fi} values the gas flow behaves as though the particles were essentially absent.

(ii) Shocked mixture flow

Figs. 5.44 and 5.45 show the pressure and temperature fields respectively, in the nozzle when $P_b = 0.7$, for various particle mass flow fractions while Figs. 5.46 and 5.47 show the gas and particles velocity fields respectively. In this case, the pressure fields behaviour follows a similar pattern to that indicated for the fully subsonic case. While the inlet pressure increases as Y_{fi} is increased, a high particle mass flow fraction ($Y_{fi} \geq 0.5$) produces an entirely subsonic flow. It is then possible to obtain a fully subsonic flow from a shocked clean gas flow by introducing high amounts of dispersed particles in it. An upward shift of the temperature fields accompanied by a reduction in the maximum temperature difference is also observed. The computed gas and particle velocities indicated in Figs. 5.46 and 5.47 show that a reduction of particle mass flow fraction immediately reduces the total particle drag effect resulting in higher gas and particle velocities. Fig. 5.48 shows that the pressure drop for the entire length of the nozzle ΔP_N is linearly dependent on the particle mass flow fraction.

5.3.4 Particle Specific Heat Effects

Effects of varying the particle specific heat c_s are not presented graphically. In subsonic and shocked nozzle flows higher values of c_s seem to produce larger pressure drop, between the nozzle inlet and the throat, together with higher velocities. Also when c_s is high, variations in T_g have little effect on Tp. In the supersonic exit mixture flow, variations of c_s appear to produce little change in the flow in the nozzle.

5.3.5 Inlet Velocity and Temperature Lags Effects

Effects of varying the inlet temperature and velocity lags between the solid particles and the gas are investigated next. The assumptions are Y_{fi} = 10%, d_p = 200 μm, c_s = 1340 J/kg°K and ρ_p = 1057 kg/m^3. Total and reference conditions are those stated in section (5.2). Effects of different VL_i values are investigated while TL_i is kept constant and equal to 1.0 and *vice versa*. Effects of varying both VL_i and TL_i are also considered.

(i) Effects of varying VL_i

In order to investigate the effect of varying values of VL_i on the subsequent flow in nozzle N1, TL_i is kept constant and corresponding to temperature equilibrium at the inlet (i.e. TL_i = 1.0).

Results presented here are those corresponding to $VL_i = 1.0$ and 0.3. Figs. 5.49, 5.50 and 5.51 show the pressure, velocity and temperature fields respectively for the cases of $VL_i = 1.0$ and $VL_i = 0.3$. Both cases correspond to back pressure of 0.9 (i.e. fully subsonic flow). When compared with the case of inlet velocity equilibrium, the pressure profile for $VL_i = 0.3$ shows a slight increase at the inlet and the throat regions, while lower gas and particle velocities are observed in the subsequent flow in the nozzle. The gas and particle temperature fields, on the other hand, indicate higher values than those for $VL_i = 1.0$ throughout the nozzle. It is believed that the increase in the pressure at the inlet section is due to the increase in the mass of particles per unit mass of the mixture (Y) at the inlet caused by the lower particle velocity (equation A.8).

Figs. 5.52, 5.53 and 5.54 show the pressure, velocity and temperature fields respectively for the same values of VL_i (1.0 and 0.3) in the shocked flow case (i.e. $P_b = 0.7$). The effects of decreasing the inlet velocity lag on the subsequent shocked flow of the mixture are very slight especially in the convergent section of the nozzle. However, these slight effects are magnified in the shock region. Fig. 5.55 shows the gas phase and particle velocities for the case of supersonic exit flow with $VL_i = 1.0$ and 0.3. In this case, due to the high acceleration of the mixture, the effects of reducing VL_i are almost negligible beyond the inlet straight section. Effects of changing VL_i values on the pressure and temperatures of the two phases in this case are also very small. Thus the pressure and temperature fields for $VL_i = 0.3$ in the supersonic exit flow can be represented by Figs. 5.9 and 5.10 respectively.

(ii) Effects of varying TL_i –

Figs. 5.56 , 5.57 and 5.58 show the pressure, velocity and temperature fields respectively for $P_b = 0.9$, comparing the cases of $TL_i = 0.5$ and $TL_i = 1.0$ (inlet temperature equilibrium). The static pressure for $TL_i = 0.5$ shows higher values in the throat region than those of $TL_i = 1.0$, and lower velocities are also observed throughout the nozzle. Considerations of the gas and particle temperatures show that due to the higher inlet particle temperature for the case of $TL_i = 0.5$ there will be an increase in the inter-phase heat transfer resulting in higher gas temperatures than those observed for $TL_i = 1.0$.

Variations of the inlet temperature lag in the shocked ($P_b = 0.7$) and supersonic exit flow produced only a very small effect in the subsequent flow. For this reason, these results are not presented here.

(iii) Effects of varying VL_i and TL_i –

Effects of varying both the inlet velocity and temperature lags are considered next. Figs. 5.59 , 5.60 and 5.61 show the pressure, temperature and velocity fields respectively for the fully subsonic flow. These figures present a comparison between a mixture flow with $VL_i = TL_i = 1.0$ and one with $VL_i = 0.3$ and $TL_i = 0.5$. The combined effects of thermal and dynamic inlet disequilibrium on the pressure are indicated by a slight increase in the pressure at the inlet section and a lower pressure drop, between the inlet and the throat, than that in the inlet equilibrium case. Consequently, lower velocities and higher temperatures are also observed. Effects of using both $VL_i = 0.3$ and $TL_i = 0.1$ in the shocked flow case do not offer any significant change to those produced by $VL_i = 0.3$ and $TL_i = 1.0$. Hence the pressure, velocity and temperature field for $VL_i = 0.3$ and

$TL_i = 0.1$ in the shocked case can be represented by Figs. 5.51 , 5.52 and 5.53 respectively. Similarly, the supersonic exit case with $VL_i = 0.3$ and $TL_i = 0.5$ is not presented here since results obtained are similar to the case of $VL_i = 0.3$ and $TL_i = 1.0$ represented in Figs. 5.9 and 5.55 .

5.4 NUMERICAL ASSESSMENT OF THE MODEL

In order to evaluate their potential, several aspects of the numerical procedure have been tested. The effects of initial conditions, relaxation factor, time step updating, pressure updating and other numerical features, on the stability and convergence rate of the model are discussed.

5.4.1 Effects of Initial Conditions

Intuitively one would expect that the initial conditions can affect, to a considerable extent, the number of time steps for convergence. The initial conditions can play a detrimental role by affecting the stability of the numerical procedure since, generally speaking, the initial flow does not obey the conservation laws. The influence of the initial conditions can be tested numerically by considering the different initial conditions schemes discussed in chapter 4. The main restriction caused by some initial conditions schemes is a high pressure wave moving from the throat region towards the nozzle inlet which could cause negative pressures especially at the nozzle inlet face. This could be due to a combination of large area changes and the choice of initial conditions. The choice of uniform set of constant values of the initial conditions ICl could in some cases, where fast area changes are present, lead to mass accumulation. Numerical tests show that high pressure waves may develop in cases where $Y_{fi} \geq 90\%$. Tests have also

shown that the number of time steps needed for convergence, when IC1 is used, is rather high (e.g. 1000 for the case of $P_b = 0.9$, $Y_{fi} = 10\%$, $B_1 = 0.5$ and constant relaxation factor of 0.1). The number of time steps needed for convergence is even higher when higher values of Y_{fi} are used (e.g. 1100 for $P_b = 0.9$, $B_1 = 0.5$ and $Y_{fi} = 80\%$).

Scheme two (IC2) of the initial conditions has proved to be good for reducing the number of time steps needed for convergence. Numerical tests employing initial conditions corresponding to IC2 show that while high pressure waves also appear for $Y_{fi} \geq 90\%$, the reduction in the number of time steps needed for convergence can be substantial, e.g. for the case of $P_b = 0.9$, $B_1 = 0.5$ and $Y_{fi} = 10\%$ a 30% reduction (from 1000 to 700). Other initial conditions could involve the clean gas analytical solution while the particle velocity and temperature lags throughout the flow field are taken to be equal to those specified at the nozzle inlet. Such schemes have proved to be unreliable and could cause problems during the initial time steps due to combination of large area changes and high velocities. It is recommended when using the clean gas analytical solution in the initial conditions to use strong damping and small initial time steps.

Further schemes used are those corresponding to scheme two (IC2) with the exception that the particle velocity and temperature are taken to be constant throughout the nozzle and equal to those at the inlet. However, this scheme has produced further reductions in the number of time steps for convergence from that of IC2 only in cases where very small inlet velocities are involved.

5.4.2 Effects of Relaxation Factor

Flow variables calculated at the flow faces of calculation cells are influenced by the value of the relaxation factor R_f, through

equations 4.10 and 4.11. The method employed in the one-dimensional model is basically of first-order accuracy when $R_f = 0$. However, the accuracy of the flow face-to-calculation point change (equation 4.11) is increased for $R_f > 0$. Fig. 5.62 shows the effects of constant R_f values on the pressure field in nozzle N1 with $P_b = 0.9$, $Y_{fi} = 10\%$, $d_p = 200$ μm and $TL_i = VL_i = 1.0$. Consider the two extreme values of R_f ($R_f = 0$ and 1.0). When $R_f = 1.0$, the effect of the initial values of the gradients is very small since their time variation is not damped. On the other hand, for $R_f = 0$ (maximum damping) the gradients are constant throughout the calculations and equal to their initial values. Hence, the accuracy of the final solution will be very poor unless the initial gradients are chosen correctly. Fig. 5.62 , shows that the accuracy and the final solution do not depend on the relaxation factor for $0.1 < R_f \leq 1.0$. The number of time steps for convergence for $R_f = 0.0$, 0.1, 0.5 and 1.0 are 600, 700, 600 and 700 time steps respectively. A relaxation factor of 0.1 has already been established by one-phase flow investigators (e.g. Damia-Torres[4]) to yield the fastest rate of convergence while giving second-order accuracy in the steady state. The scheme adopted here is that employed by Damia-Torres[4] in which R_f is set to zero (maximum damping) during the initial time steps and increased to 0.1 during the rest of the calculation. This has proved to be very effective in smoothing any large changes which may occur during the first time steps.

5.4.3 Effects of Time Step Updating

Time step updating has proved to be an extremely effective tool in speeding up the convergence rate of the calculation. For the mixture flow in nozzle N1 with $P_b = 0.9$, $Y_{fi} = 10\%$, $d_p = 200$ μm and $TL_i = VL_i = 1.0$, while using an optimum constant time step of 0.32

yields the steady state solution in 800 time steps, updating the time step according to the CFL condition (equation 4.63), with $B_1 = 0.8$, reduces the number of time steps for convergence to 700. A further reduction to 600 time steps can be achieved when a spatially varied time step, with $B_2 = 0.8$, is employed. The number of time steps for convergence when using spatially varied time step can be as low as 500 in many cases, especially where $VL_i \neq 1.0$ and/or $TL_i \neq 1.0$. Numerical tests show that for $B_1 = B_2$ a spatially varied time step gives the highest rate of convergence. Table 5.1 shows the convergence rate for different values of B_1 and B_2. The CPU time per time step per calculation point (including initial conditions computation and solution input/output is 3.7×10^{-3}s on a CDC Cyber 174 computer.

5.4.4 Effects of Grid Size

Numerically, it is expected that the use of finer grid will produce more accurate predictions in regions where fast changing gradients may occur, due, for example, to large area changes in a short distance, shocks and transonic flow regions. The grid size may be increased in regions where variation in the variables is gradual. Thus, a fine grid of constant cell size taken throughout the nozzle is not always necessary due to high cost and storage requirements needed. Fig. 5.63, displays a comparison of the pressure fields obtained for three different grids in nozzle N1 with $P_b = 0.7$, $Y_{fi} = 10\%$, $d_p = 200$ μm and $TL_i = VL_i = 1.0$. The grids considered are: (1) a constant cell size grid of 20 points with $\Delta x_j = 1.0$, (2) a constant cell size grid of 40 points with $\Delta x_j = 0.5$ and, (3) a variable cell size grid of 23 points corresponding to the grid distribution used in section 5.1 with $\Delta x_{min} = 0.75$. The main difference in the predictions occurs in the shock

region. While pressure fields computed for the 40 point and 23 point grids vary very little, that predicted for the 20 point grid shows a slight deviation in the shock region. The number of time steps for convergence for the 20 points, 40 points and 23 points are 700, 800 and 700 respectively. Consequently, the variable cell size grid of 23 calculation points with $\Delta x_{min} = 0.75$ is considered best for the present study.

5.4.5 Effects of Pressure Updating and Smoothing

As described in the previous chapter, for Denton's scheme to be effective, pressure updating is recommended. It can increase the rate of convergence. Consider the case of the mixture flow in nozzle N1 with $P_b = 0.9$, $Y_{fi} = 10\%$, $d_p = 200$ μm, $TL_i = VL_i = 1.0$ and $B_1 = 0.5$. A reduction in the number of time steps for convergence from 1000 to 900 can be obtained by employing the pressure updating scheme. Similarly, a reduction from 800 to 700 can be made for the shocked case with $P_b = 0.7$. Further consideration of this scheme shows that it helps maintain stability and smooth out any time oscillations of the pressure. The advantage of this scheme becomes apparent in cases where the mixture has small inlet velocity (i.e. $0.99 < P_b < 1.0$). Convergence rates for such flows are very slow and often a steady state solution is not achieved even after an appreciable number of time steps, e.g. for the experimental nozzle (see chapter 7) no convergence can be achieved after 4000 time steps for the following data: $P_b = 0.9972$, $Y_{fi} = 0.2563$, $c_s = 878.6$ J/kg°K and $\rho_p = 2700$ kg/m^3. This is one of the reasons why some investigators believe that time-marching methods are not suitable for fully subsonic flows. Applying pressure field smoothing does not further reduce the number of time steps for convergence, while instability occurs when a pressure smoothing factor ε of 0.5 is used.

5.5 COMPARISON WITH OTHER WORK

Baum[147] investigated subsonic and shocked flow of a gas-particle mixture in a convergent-divergent nozzle. His investigation included experimental measurements of the pressure, gas Mach number and particle velocities, which were compared with the numerical predictions of his steady gas-particles model. This model was also used to predict other cases of gas-particle flows in nozzles with supersonic exists and these latter predictions were also published by Mobbs *et al.*[66]. The model uses the same procedure as that outlined in section 2.4.2 in chapter 2. The nozzle used in Baum's model and experiment is one designed by Bowers[59] by using the constant fractional lag theory (Nozzle N2). The nozzle is designed to accelerate an air-solids flow to a mixture Mach number of 2.1 at the nozzle exit, with an exit to inlet pressure ratio of approximately 9.1. The throat area of the nozzle is 2.206 cm^2 (0.342 sq. in.) and the aspect ratio of the nozzle exit is 5 to 1. The width and height dimensions of the nozzle exit area are 1.016 cm (0.4 in.) and 5.08 cm (2 in.) respectively. The nozzle inlet and exit areas and aspect ratios are equal while its length is 20.32 cm (8 in.). Fig. 5.64 shows the nozzle area variations. In the present time-marching model constant area sections are added to the nozzle. A constant area section at the inlet 2.032 cm long is added while that at the exit is 1.016 cm. The grid used is a coarse one containing 23 points of constant width (Δx = 1.016 cm). The solid particles have material density of 1057 kg/m^3 and specific heat capacity of 1340 J/kg°K (polystyrene). The gas mass flow rate is 0.127 kg/s and the stagnation temperature is 297°K, while the reference temperature is set equal to the stagnation temperature. Results presented here are of the following non-dimensional variables: P/P_i, u_g, u_p, T_g and T_p, where P_i is the inlet pressure. Comparison cases considered are as follows.

(i) Supersonic exit flow

By following the procedure outlined in section 5.2.3 a supersonic exit flow solution for the gas-particle mixture in nozzle N2 can be obtained. The back pressure is allowed to float from an initial value of 0.07158 while a constant time step of 0.001 is used together with constant relaxation factor of 0.1. Gas-phase initial conditions used are those corresponding to the clean gas analytical solution for the same back pressure while those of the particulate phase are derived from constant velocity and temperature lags throughout the nozzle. Results obtained by the time-marching model are compared with those predicted by Mobbs *et al.*[66]. Comparison cases considered are those of varying Y_{fi}, d_p, ρ_p and VL_i. Unless otherwise stated, $VL_i = TL_i = 1.0$ for all comparison cases considered.

Y_{fi} variations

Two different values of Y_{fi} are considered, $Y_{fi} = 0.091$ (loading ratio of 0.1) and 0.5 (loading ratio of 1.0). Particles used are those with 60 μm diameter. Figs. 5.65, 5.66 and 5.67 provide a comparison for $Y_{fi} = 0.091$ for the pressure ratio, velocities and temperatures respectively. Comparisons for $Y_{fi} = 0.5$ are presented in Figs. 5.68 and 5.69. Generally, good agreement is observed, for the two values of Y_{fi}, in the pressure and gas and particle velocities. However, gas-phase temperature for $Y_{fi} = 0.091$ (Fig. 5.67) as predicted by the time-marching model show slightly higher values, in the divergent part of the nozzle, than those predicted by Mobbs *et al.*

d_p variations

For a constant value of Y_{fi}, namely 0.5, particle diameters considered by Mobbs *et al.*[66] are 30 and 300 μm. Fig. 5.70 shows the gas and particle velocities for the two different sizes considered.

The figure shows that the velocities of the component phases as predicted by the two models are very close. This also applies for the temperatures predictions as made by the two models (Fig. 5.71).

ρ_p variations

For a mixture with $Y_{fi} = 0.5$ and $d_p = 60$ μm, two particle densities are employed for comparison purposes. Particle densities of 1000 and 4000 kg/m^3 are used. Fig. 5.72 compares gas and particle velocities, for the different particle densities, as predicted by the two models while Fig. 5.73 compares the temperature predictions. Good agreement is shown in these figures between results obtained by the present time-marching model and those predicted by Mobbs *et al.* [66].

VL_i variations

For a flow with $Y_{fi} = 0.5$, $d_p = 60$ μm, $TL_i = 1.0$ and $VL_i = 0.5$, Fig. 5.74 represents a comparison between the two models' predictions for the gas and particle velocities. Reasonable agreement is also shown in this case. Comparison cases for P/P_i, T_g or T_p are not presented here since these parameters change very little from the case of $VL_i = 1.0$, the predictions being almost identical to those in Figs. 5.68 and 5.69 .

(ii) Shocked flow

In his thesis, Baum [147] presented experimental measurements of the pressure ratio P/P_i, gas-phase Mach number at the nozzle inlet and exit and the particle velocity (measured by streak photography technique) along the axis of nozzle N2. His measurements were taken in shocked and subsonic mixture flow in the nozzle. For a mixture with a standing normal shock in the divergent part, Baum also obtained numerical predictions by supplying the position of the shock as data

to the model. A comparison is presented here between the present time-marching model's predictions and those predicted and measured by Baum. Particles used in Baum's experiment are polystyrene particles with d_p = 270 μm and Y_{fi} = 0.5. Baum also estimated that the inlet particle velocity lag was about 0.8. Comparison cases presented are those for a flow with a normal shock at x = 14.5 and 11.75 cm from the nozzle inlet. For a normal shock at x = 14.5 cm, a back pressure of 0.52 is estimated and used in the present model. This value of P_b corresponds to that predicted by Baum's model. Inlet velocity lag used in the present model is 0.85. Figs. 5.75 - 5.78 show results for P/P_i, gas-phase Mach number, particle velocity and gas and particle temperatures respectively. Generally, predictions made by the present time-marching model show good agreement with those made by Baum's model. Fig. 5.75 indicates that pressure measurements as made by Baum show reasonable agreement with predictions made by both models. However, behind the shock Baum's pressure measurements show lower pressures than those predicted by the two models. Baum attributed this to wall friction effect which was not included in his model. By applying an estimated back pressure corresponding to Baum's experimental back pressure (P_b = 0.375) and using equations 4.18 and 4.19 to account for wall friction effect, the present time-marching model predicts a deviation in the shock position towards the nozzle exit as shown in Fig. 5.75 . Mach number predictions (Fig. 5.76) show good consistency with Baum's and with his measured inlet and exit values. Predictions of the present model for the particle velocity (Fig. 5.77) show reasonable agreement with Baum's predictions and measurements. His measurements show higher particle velocities, behind the shock, than those predicted by the two models. Fig. 5.78 shows a comparison of the gas and particle temperatures as predicted by the present model with those of Baum.

Comparisons for the mixture flow with normal shock at $x = 11.75$ cm are shown in Figs. 5.79 - 5.82 . These figures represent P/P_i, gas-phase Mach number, particle velocity and gas and particle temperatures respectively. Predictions of P/P_i (Fig. 5.79) are consistent with Baum's predictions (experimental measurements are not supplied in Baum's thesis for P/P_i for this case). This consistency is also indicated in the two models' predictions and the experimental data for M_g, u_p, T_g and T_p. The value of back pressure used in this case is 0.72 and $VL_i = 0.8$.

(iii) Subsonic flow

Subsonic mixture flow measurements and predictions are also presented by Baum for polystyrene particles with $d_p = 270$ μm and $Y_{fi} = 0.333$ (loading ratio of 0.5). Figs. 5.83 - 5.86 show the present time-marching model's predictions as compared to those measured and predicted by Baum. Back pressure of 0.934 is used for the time-marching predictions with $VL_i = 0.8$. Good agreement is shown for the predicted values of P/P_i, M_g, T_g and T_p. However, Baum's measurements of P/P_i in the divergent part of the nozzle are lower than those predicted by the two models. By using an estimated back pressure corresponding to Baum's experimental back pressure (P_b = 0.814), the present time-marching model predicts lower values of P/P_i at the nozzle throat (approximately 0.4) than those shown in Fig. 5.83 . The time-marching predictions for the particle velocity (Fig. 5.85) show more consistency with the experimental values than those predicted by Baum.

Further comparisons are also obtained with a case presented by Sharma[29] for subsonic mixture flow with small inlet velocities. His investigation included the experimental measurements of the pressure drop along a circular vertical venturi meter as well as the numerical

predictions of his quasi one-dimensional model CONVAS (Conservative VAriables and Source) which is based on the Eulerian-Lagrangian approach. Fig. 5.87 shows the nozzle configuration (venturi VE2) used by Sharma. Particles used in his experiment and predictions are glass beads with material density of 2480 kg/m^3 and a mass median diameter of 30 μm. Pressure drop results presented by Sharma show that CONVAS predictions show an appreciable disagreement with his experimental measurements in the divergent part of the venturi. Sharma attributed this to two-dimensional effects (channelling) which causes the particles to concentrate about the centreline in the throat and beyond. Fig. 5.88 shows a comparison of the pressure drop predictions made by the time-marching model with those of CONVAS and the experimental measurements made by Sharma. The figure also shows predictions made by Baghdadi[27] for the same venturi by using different correlations to represent the inter-phase drag force. These correlations are: (i) one used by Harlow and Amsden[72] and given as a function of the void fraction and (ii) a correlation allowing for the virtual mass effects. More details of these correlations can be found in reference 27.

Predictions presented in Fig. 5.88 are obtained for the following data:

inlet static pressure	=	26.92 cm of alcohol, specific gravity of 0.79
atmospheric pressure	=	705 mmHg
room temperature	=	26.7°C
loading ($\dot{m}_p/\dot{m}_g$)	=	0.29
particle specific heat	=	878.6 J/kg°K
gas-phase mass flow-rate	=	0.01083 kg/s

The above data are those measured experimentally by Sharma. The back pressure used is 0.99982, while the inlet gas-phase density is taken to be that corresponding to the atmospheric pressure and room temperature. The grid used is a coarse one with 22 cells distributed as follows:

Number of cells	Width (mm)
3	16.71
6	25.40
5	6.10
6	25.40
2	25.47

Fig. 5.88 shows the pressure drop along the venturi in cms of alcohol (sp.Gr. = 0.79) as predicted by the different models and experimentally measured by Sharma. The present model predicts similar pressure drops at the throat as those measured by Sharma. By using a back pressure corresponding to the experimental back pressure the present time-marching model predictions show a higher pressure drop at the throat than those shown in Fig. 5.88 (the pressure drop at the throat being approximately 3.0 cms of alcohol).

CHAPTER 6

TWO-DIMENSIONAL TWO-PHASE TIME-MARCHING MODEL

6.1 INTRODUCTION

In this chapter, the development of a two-dimensional time-marching model for gas-particle flow through nozzles is proposed and discussed. The two-dimensional, two-phase conservation equations are changed into the finite-difference equations and solved by the time-marching method. Numerical schemes used by Denton[18,21] and Damia-Torres[4], mainly the opposed difference technique, are employed. Physical features and assumptions on which the two-dimensional model is based are basically the same as those used for the one-dimensional model (section 4.2, numbers 1-11). No attempt is made to include effects caused by external heat transfer, wall friction or gravity. The predicted results are compared with those obtained by the one-dimensional time-marching model. In all test cases, no attempt has been made to solve for cases where inter-phase mass transfer occurs.

6.2 FINITE-DIFFERENCE DISCRETIZATION

6.2.1 Mesh Configuration

The computational grid in the flow region of interest, illustrated in Fig. 6.1, is one used by Denton[18,21] and Damia-Torres[4] in their one-phase time-marching models. The calculation cells are formed by the intersection of a series of quasi-streamlines which are evenly spaced in the y direction and a series of crosswise lines which are parallel to the y-axis and need not be evenly spaced in the x direction. The quasi-streamlines are generated by evenly dividing the crosswise lines into the same number of segments. Calculation points

are located on the quasi-streamlines and half way between any two consecutive crosswise lines. Calculation points having the same value of x are connected by broken lines which are also termed crosswise lines. The crosswise lines are identified by the index i, while the quasi-streamlines are identified by j. The basic elemental control volume used to evaluate the flow properties at the calculating point (i,j) is a trapezium whose vertices are the points $(i-1, j+1)$, $(i-1, j-1)$, $(i+1, j-1)$ and $(i+1, j+1)$. These vertices are called secondary points and are identified by $\bullet$ (see Fig. 6.1). The cells overlap in the y direction so that the upper and lower flow faces of each cell contain the calculating points for the cells preceding and following in the y direction. The first and last crosswise lines, denoted by $i = 1$ and $i = I$ respectively, contain secondary points. Hence secondary points are located on odd i-lines while calculating points (identified by x) are located on even i-lines.

The quasi-streamlines extend from $j = 1$ to $j = J$. The geometry considered here is that of symmetrical ducts so that the line $j = 2$ is taken to be a straight line representing the duct centre-line and from now on only the upper wall will be mentioned. For curved walls, only the secondary points on the quasi-streamline $j = J$ are located on the wall. Thus, a grid well packed in the x-direction is necessary to reduce the deviation of the calculating points, at this line, from the wall.

6.2.2 Finite Difference Form of the Flow Equations

In order to replace the two-dimensional two-phase flow equations 3.63 and 3.64 by their finite difference form, a flow cell with its four sides represented by flow area vectors $\overrightarrow{\Delta S}_f$ (Fig. 3.2) is considered. The flow area vectors $\overrightarrow{\Delta S}_f$ are given by:

$$\overrightarrow{\Delta S}_f = (\vec{n}\,\Delta S)_f \quad , \quad f = 1,2,3,4 \tag{6.1}$$

where $\vec{n}$ is the outward unit vector normal to the control surface and ΔS is the flow face area. The left and right crosswise flow faces are identified by setting the subscript f to 1 and 3 respectively, while the upper and lower streamwise flow faces are represented by f equals 2 and 4 respectively. It is assumed that the values of the different variables at point (i,j) represent the space average of the respective variables over the flow cell and that the properties at points (i-1,j), (i,j-1), (i+1,j) and (i,j+1) represent the space average over the flow faces 1,2,3 and 4 respectively. If the time derivative terms are approximated by a simple forward difference (equation 4.1), then equations 3.63 and 3.64 can be expressed as

Continuity equations:

$$[\rho_m(1-Y)]^{t+\Delta t} = \rho_m(1-Y) - \frac{\Delta t}{V}\left\{\sum_1^4 [\rho_m(1-Y)u_g\Delta S_x + \rho_m(1-Y)v_g\Delta S_y]_f + \dot{Nm}_c\rho_m V\right\} \tag{6.2}$$

$$[\rho_m Y]^{t+\Delta t} = \rho_m Y - \frac{\Delta t}{V}\left\{\sum_1^4 [\rho_m Y u_p\Delta S_x + \rho_m Y v_p\Delta S_y]_f - \dot{Nm}_c\rho_m V\right\} \tag{6.3}$$

Momentum equations:

$$[\rho_m(1-Y)u_g]^{t+\Delta t} = \rho_m(1-Y)u_g - \frac{\Delta t}{V}\left\{\sum_1^4 \left[\rho_m(1-Y)\left[u_g^2 + \frac{P}{\gamma\rho_g}\right]\Delta S_x + \rho_m(1-Y)u_g v_g\Delta S_y\right]_f + \dot{Nm}_c u_g\rho_m V - ND_{px}\rho_m V\right\} \tag{6.4}$$

$$[\rho_m(1-Y)v_g]^{t+\Delta t} = \rho_m(1-Y)v_g - \frac{\Delta t}{V}\left\{\sum_1^4 \left[\rho_m(1-Y)v_g u_g \Delta S_x + \rho_m(1-Y)\left(v_g^2 + \frac{P}{\gamma\rho_g}\right)\Delta S_y\right]_f + N\dot{m}_c v_g \rho_m V - ND_{py}\rho_m V\right\} \quad (6.5)$$

$$[\rho_m Y u_p]^{t+\Delta t} = \rho_m Y u_p - \frac{\Delta t}{V}\left\{\sum_1^4 \left[\rho_m Y\left(u_p^2 + \frac{P}{\gamma\rho_p}\right)\Delta S_x + \rho_m Y u_p v_p \Delta S_y\right]_f - N\dot{m}_c u_g \rho_m V + ND_{px}\rho_m V\right\} \quad (6.6)$$

$$[\rho_m Y v_p]^{t+\Delta t} = \rho_m Y v_p - \frac{\Delta t}{V}\left\{\sum_1^4 \left[\rho_m Y v_p u_p \Delta S_x + \rho_m Y\left(v_p^2 + \frac{P}{\gamma\rho_p}\right)\Delta S_y\right]_f - N\dot{m}_c v_g \rho_m V + ND_{py}\rho_m V\right\} \quad (6.7)$$

Energy equations:

$$[\rho_m(1-Y)E_g]^{t+\Delta t} = \rho_m(1-Y)E_g - \frac{\Delta t}{V}\left\{\sum_1^4 \left[\rho_m(1-Y)\left(E_g + \frac{\gamma-1}{\rho_g}P\right)u_g \Delta S_x + \rho_m(1-Y)\left(E_g + \frac{\gamma-1}{\rho_g}P\right)v_g \Delta S_y\right]_f - \gamma(\gamma-1)N\rho_m V(u_p D_{px} + v_p D_{py}) - \frac{\gamma}{Re_r Pr} NQ_p \rho_m V + \gamma N\dot{m}_c \rho_m V\left(H_g - \frac{\gamma-1}{\gamma}\frac{P}{\rho_p}\right)\right\} \quad (6.8)$$

$$[\rho_m Y E_p]^{t+\Delta t} = \rho_m Y E_p - \frac{\Delta t}{V}\left\{\sum_1^4 \left[\rho_m Y\left(E_p + \frac{\gamma-1}{\rho_p} P\right)u_p \Delta S_x + \rho_m Y\left(E_p + \frac{\gamma-1}{\rho_p} P\right)\right.\right.$$

$$\left. v_p \Delta S_y\right]_f + \gamma(\gamma-1)N\rho_m V(u_p D_{px} + v_p D_{py}) + \frac{\gamma}{Re_r Pr} NQ_p \rho_m V$$

$$\left. - \gamma N\dot{m}_c \rho_m V\left(H_g - \frac{\gamma-1}{\gamma}\frac{P}{\rho_p}\right)\right\} \qquad (6.9)$$

No superscripts indicates that the flow variables are evaluated at time t while no subscripts means that the flow variables refer to point (i,j). ΔS_x and ΔS_y denote the area projections of the flow area vector for a flow face, along the x- and y-coordinates, respectively, so that

$$(\Delta S_x)_f = \overrightarrow{\Delta S}_f \cdot \vec{e}_x \,, \qquad (6.10)$$

$$(\Delta S_y)_f = \overrightarrow{\Delta S}_f \cdot \vec{e}_y \,. \qquad (6.11)$$

$\rho_m(1-Y)$, $\rho_m(1-Y)u_g$, $\rho_m(1-Y)v_g$, $\rho_m(1-Y)E_g$, $\rho_m Y$, $\rho_m Y u_p$, $\rho_m Y v_p$ and $\rho_m Y E_p$ are taken as conserved variables. The use of equation 4.1 leads to a first-order temporal accuracy. The flow variables at the flow faces are evaluated according to the following scheme

f	i	j
1	i-1	j
2	i	j-1
3	i+1	j
4	i	j+1

Hence the y-derivatives are approximated by second-order central differences[4].

The finite difference scheme chosen to evaluate the different flow properties at points (i-1,j) and (i+1,j) is one employed by Denton[21] and Damia-Torres[4] (opposed difference technique). All variables but pressure are approximated by upwind differencing, i.e.

$$\phi_{i-1,j} = \phi_{i-2,j} + \Delta\phi \tag{6.12}$$

$$\Delta\phi = (1-R_f)\,\Delta\phi^{t-\Delta t} + R_f \sum_{k=0}^{2} C_k\,\phi_{i-2k,j} \tag{6.13}$$

where $\Delta\phi$ is a correction factor, calculated from a parabolic fitting of points (i-4,j), (i-2,j) and (i,j). The term under the summation sign represents a quantity that when added to $\phi_{i-2,j}$ would interpolate ϕ at point (i-1,j) entirely from the parabolic fitting. C_k (k = 0,1,2) are the fitting coefficients with $\sum_{k=0}^{2} C_k = 0$. The star of mesh points employed for variables other than pressure is shown in Fig. 6.2.

The pressure is approximated by a downwind differencing as follows:

$$P_{i-1,j} = P + \Delta P \tag{6.14}$$

$$\Delta P = (1-R_f)\Delta P^{t-\Delta t} + R_f \sum_{k=-1}^{1} \bar{C}_k\,P_{i+2k,j} \tag{6.15}$$

The pressure parabolic fitting is through points (i-2,j), (i,j) and (i+2,j) and $\bar{C}_k$ (k = -1,0,1) are fitting coefficients. Fig. 6.3 shows the star of mesh points employed for pressure approximation. In a similar fashion as in the one-dimensional model, the relaxation factor R_f can be set to zero during the initial time steps and increased to a certain value (0.1 is recommended) during the rest of the calculation. By reducing the damping (i.e. increasing R_f) the correction factors in equations 6.12 and 6.14 increase the spatial accuracy in the streamwise

direction[4] . Thus, the two-dimensional model is first-order accurate in time and second-order accurate in the steady state.

In solving the two-phase flow equations (6-2 - 6.9) the continuity and energy equations are solved first. The pressure is then updated by using new values of the densities and the gas-phase energy per unit volume and old values of the kinetic energy per unit mass, i.e.

$$p^{t+\Delta t} = \rho_g^{t+\Delta t}\left[E_g^{t+\Delta t} - \frac{\gamma(\gamma-1)}{2}U_g^2\right] \qquad (6.16)$$

where $\rho_g^{t+\Delta t}$ is found by using equation 4.58 and U_g is the gas velocity ($U_g^2 = u_g^2 + v_g^2$). Finally, the momentum equations are solved using new values of the pressure and old values for all other variables. In addition to the conserved variables mentioned earlier in this section, the pressure P and the two phases component velocities u_g, v_g, u_p and v_p are also considered as computational variables. Thus, terms like $\rho_m(1-Y)u_g^2$ and $\rho_m Y v_p u_p$ are evaluated as $[\rho_m(1-Y)u_g]u_g$ and $(\rho_m Y v_p)u_p$ respectively.

6.2.3 Inter-Phase Interaction

Particle drag and heat transfer terms present in the two-dimensional, two-phase flow equations are calculated at the centre of each flow cell. Variations of the gas-phase dynamic viscosity μ_g with temperature are calculated by using the Sutherland's law[4,148], which can be expressed in the following dimensional form:-

$$\frac{\mu_g}{\mu_{su}} = \left(\frac{T_g}{T_{su}}\right)^{\frac{3}{2}} \frac{T_{su} + S_{su}}{T_g + S_{su}} \qquad (6.17)$$

where T_{su} = 283.1°K, μ_{su} = 0.1716 mP and S_{su} = 110.6°K for air. The temperature range for a ±2% error is 167 - 1900°K. The thermal conductivity of the gas-phase is evaluated from the condition of constant Prandtl number Pr of 0.707. In order to save computer time in calculating the gas viscosity from equation 6.17 the viscosity is updated only every certain number of time steps (25 is recommended).

Particle Reynolds number and drag coefficient are calculated by using equations 3.71 and 3.61 respectively, while the particle drag force components are evaluated from equations 3.69 and 3.70 respectively. The particle Nusselt number and particle heat transfer are calculated by using equations 2.38 and 2.40 respectively.

6.3 BOUNDARY CONDITIONS

6.3.1 Inlet Plane

The geometrical arrangements considered in the model consist of convergent-divergent nozzles. As in the case of the one-dimensional model, the upstream region of the duct is extended so that it has a constant area inlet. The specified boundary conditions at the inlet plane of the duct are the stagnation pressure P_o, temperature T_o and particle mass flow fraction Y_o. The inlet velocity and temperature lags are also specified. Velocity lag ($VL_{1,j}$) and temperature lag ($TL_{i,j}$) are defined by

$$VL_{1,j} = \left(\frac{U_p}{U_g}\right)_{1,j} \tag{6.18}$$

and

$$TL_{1,j} = \left(\frac{T_p - T_o}{T_g - T_o}\right)_{1,j} \tag{6.19}$$

respectively, where $j = 1,2 \text{ --- } J$ and $U_p = (u_p^2 + v_p^2)^{\frac{1}{2}}$. Further inlet data specified are the particle mass flow fraction $(Y_f)_{1,j}$, the particle size and the flow direction.

The gas-phase is assumed to undergo an isentropic expansion from the upstream stagnation conditions and the inlet static pressure is evaluated from the assumption of constant total x-momentum between secondary points on the inlet plane (i = 1 and j = 1,2,---J) and the first column of calculation points. The total x-momentum can be evaluated by adding the steady form of the x-momentum equations 6.4 and 6.6, so that

$$MOMX = \sum_1^4 \left\{ \left[\rho_m (1-Y) u_g^2 + \rho_m Y u_p^2 + \frac{P}{\gamma} \right] \Delta S_x + \left[\rho_m (1-Y) u_g v_g + \rho_m Y u_p v_p \right] \Delta S_y \right\}_f \tag{6.20}$$

The inlet static pressure $P_{1,j}$ can be calculated by employing the Newton-Raphson method to solve the following function

$$MOMX_{1,j} - MOMX_{2,j} = F(P_{1,j}) \tag{6.21}$$

while the rest of the inlet variables are evaluated from the definition of total conditions. However, in the present study cases where the inlet mixture flow is parallel to the x-axis only are considered, so that v_p and v_g are both zero at the nozzle inlet and the calculation procedure followed is similar to that shown in appendix A.

6.3.2 Exit Plane

Similar to the inlet, the outlet region is extended to become straight in order to damp any existing pressure waves. The only specified property at the duct exit is the static pressure (back pressure P_b) which is assumed to be uniform. The back pressure is introduced at

a column of dummy points (I+1) situated downstream of the exit plane. This is believed to be beneficial in cases where the back pressure corresponds to either over-expansion or under-expansion. The pressure at the exit plane (crosswise line i = I) is given by equation 6.14 with ΔP evaluated from a parabola fitted through points (I-3,j), (I-1,j) and (I+1,j). Other flow variables, e.g. $\rho_m(1-Y)$, $\rho_m Y$, $\rho_m(1-Y)u_g$, $\rho_m Y u_p$, u_p, u_g----etc., are evaluated at the exit plane by using equation 6.12 with $\Delta\phi$ evaluated from a parabola fitted through points (I-5,j), (I-3,j) and (I-1,j).

6.3.3 Solid Wall Boundary

One of the important variables to be determined at the wall is the static pressure. The method adopted here to evaluate the wall pressure is one used by Gopalakrishnan[112] and Damia-Torres[4] in their one-phase time-marching models. The method involves the use of the radial equilibrium equation by equating the static pressure gradient normal to the wall to the "centrifugal force" produced by the local radius of curvature (see section 2.5.4). The radial equilibrium equation for the mixture is expressed as follows:

$$\left(\frac{\partial P}{\partial n}\right)_w = \frac{\rho_m(1-Y)U_g^2 + \rho_m Y U_p^2}{r} \qquad (6.22)$$

In order to evaluate the wall pressure equation 6.22 is expressed in a finite-difference form involving five calculation points, three of which are situated at the wall (see Fig. 6.4). Consequently, the wall pressure is given implicitly by equation 6.22. Appendix B shows how the wall pressure evaluation is reduced to the solution of a tri-diagonal matrix. The partial densities of the two phases at the wall are evaluated from a linear extrapolation along the crosswise lines, i.e.

$$\phi_{i,J} = 2\,\phi_{i,J-1} - \phi_{i,J-2} \tag{6.23}$$

where ϕ represents $\rho_m(1-Y)$ or $\rho_m Y$. Damia-Torres[4] has recommended such an approximation in his one-phase model. However, while the gas-phase energy at the wall is evaluated from euqation 3.96, the particulate phase energy is found by applying equation 6.23 with ϕ representing $\rho_m Y E_p$.

The momentum components $\rho_m(1-Y)u_g$, $\rho_m(1-Y)v_g$, $\rho_m Y u_p$ and $\rho_m Y v_p$ at the wall are linearly extrapolated[4] (equation 6.23). Consequently, first estimates of u_g, v_g, u_p and v_p are obtained by dividing first estimates of $\rho_m(1-Y)u_g$ and $\rho_m(1-Y)v_g$ by $\rho_m(1-Y)$ and first estimates of $\rho_m Y u_p$ and $\rho_m Y v_p$ by $\rho_m Y$. The resulting velocity components normal to the wall are then set to zero while only the tangential components of the first estimates of u_g, v_g, u_p and v_p are kept. The resulting new values of u_g and v_g are combined with $\rho_m(1-Y)$ to give the new values of $\rho_m(1-Y)u_g$ and $\rho_m(1-Y)v_g$ at the wall, while u_p and v_p are combined with $\rho_m Y$ to give the new values of $\rho_m Y u_p$ and $\rho_m Y v_p$ at the wall.

6.3.4 Symmetry Conditions

The quasi-streamline $j = 2$ is the symmetry line. Across the line of symmetry the following relationship holds:

$$\left(\frac{\partial \phi}{\partial y}\right)_{i,2} = 0 \,, \tag{6.24}$$

so that

$$\phi_{i,1} = \phi_{i,3} \tag{6.25}$$

where ϕ represents P, $\rho_m(1-Y)u_g$, $\rho_m(1-Y)E_g$, u_g, $\rho_m Y u_p$, $\rho_m Y E_p$ and u_p. Similarly,

$$\psi_{i,1} = -\psi_{i,3} \tag{6.26}$$

which, indirectly, leads to

$$\psi_{i,2} = 0 , \tag{6.27}$$

where ψ represents v_g, $\rho_m(1-Y)v_g$, v_p and $\rho_m Y v_p$.

6.4 INITIAL CONDITIONS

The initial conditions are basically the same as those described in "scheme two" used in the one-dimensional model (chapter 4). Every row of cells is assumed to act as a channel and the flow direction is taken to be the same as the direction of the quasi-streamlines. A quasi-one-dimensional mixture flow is considered along each channel, with its properties given by the central quasi-streamline. The mixture mass flow rate in each channel is assumed constant as well as the total conditions. For each row of cells, the ratio of the exit area ΔS_I to the minimum area ΔS_t can be expressed as

$$\frac{\Delta S_I}{\Delta S_t} = \frac{b_1 \cos(\alpha_{qs})_t}{(M_m)_{sub} \cos(\alpha_{qs})_I} \left[\frac{1 + \frac{n-1}{2} (M_m^2)_{sub}}{\left(\frac{n+1}{2}\right)} \right]^{\frac{n+1}{2(n-1)}} \tag{6.28}$$

where b_1 is that used in equation 4.47.
The ratio of the cosines of the quasi-streamlines angles appears in the above equation since, in general, the quasi-streamlines are not straight lines parallel to the x-axis. For one-dimensional flow, where the flow is parallel to the x-axis, the above equation reduces to equation 4.47.

The constant mixture mass flow rate in each row of cells can be expressed as

$$\dot{m}_m = CON \cdot \frac{\frac{P_o}{\sqrt{T_o}} \Delta S \cos \alpha_{qs} \; M_m \left(1 + \frac{n-1}{2} M_m^2\right)^{-\frac{n+1}{2(n-1)}}}{\left[\rho_p + Z_2 \frac{\gamma P_o}{T_o} \left(1 + \frac{n+1}{2} M_m^2\right)^{-\frac{1}{n-1}}\right]} \qquad (6.29)$$

where Z_2 and CON are defined by equations 4.44 and 4.46 respectively. Equation 6.28 can be solved for $(M_m)_{sub}$ by the Newton-Raphson method and subsequently the exit pressure P_{sub} corresponding to $(M_m)_{sub}$ can be calculated from equation 4.36 and used to define the initial flow according to the conditions 4.48a and 4.48b. The Mach number M_m at every other point in the channel can then be calculated by solving equation 6.29 by the Newton-Raphson method. Other gas-phase variables can be calculated by using the isentropic relations with n as the compressible index (see section 4.5.2). The particulate phase flow variables are evaluated by setting the constant temperature and velocity lags equal to those specified at the inlet plane of each row of cells and by assuming constant stagnation enthalpy of the mixture. Finally, the wall pressure is evaluated by linear extrapolation from interior points while the rest of the gas- and particle-phase properties on the wall are calculated in the same manner as for the interior points.

6.5 OTHER COMPUTATIONAL FEATURES

6.5.1 Smoothing

Streamwise smoothing of the conserved variables adopted in the two-dimensional model is basically the same as that employed in the one-dimensional model discussed in section 4.6.2. Corrections due to the streamwise smoothing are introduced while equations 6.2 - 6.9 are being solved. For any three calculation points i-2,i and i+2 in a stream-

wise line (all the j indices are dropped) the analogous expression to equation 4.51 is

$$\phi_{is} = \phi_{i+2} + (\phi_{i-2} - \phi_{i+2})SC_i \tag{6.30}$$

where

$$SC_i = \frac{\Delta x_i + \Delta x_{i+2}}{\Delta x_{i-2} + 2\Delta x_i + \Delta x_{i+2}} \tag{6.31}$$

Thus similar expressions to those in section 4.6.2 (equations 4.53 - 4.57) can be used to smooth variables at point i by employing their values at points $i-2, i$ and $i+2$.

Smoothing in the crosswise direction is also applied. Consider three points $j-1$, j and $j+1$ (all the i-indices are dropped) in a crosswise line. If ψ is the variable to be smoothed and ψ_{js} its value at j if there were a linear variation of ψ between $j-1$ and $j+1$, then

$$\psi_{js} = \frac{1}{2}(\psi_{j-1} + \psi_{j+1}) \tag{6.32}$$

Let $\Delta\psi_j^*$ be the difference between ψ_{js} and the actual value of ψ at j,; thus

$$\Delta\psi_{js} = \psi_{js} - \psi_j = \frac{1}{2}(\psi_{j-1} - 2\psi_j + \psi_{j+1}) \tag{6.33}$$

and smoothing in the crosswise direction is carried out by adding a fraction α_{sm} of $\Delta\psi_{js}$ to the value of ψ_j, i.e.

$$\psi_j^* = \psi_j + \frac{1}{2}\alpha_{sm}(\psi_{j-1} - 2\psi_j + \psi_{j+1}) \tag{6.34}$$

where ψ_j^* is the smoothed ψ_j. Such smoothing has been applied by Denton and Singh[19] for the streamwise smoothing of the pressure field and the changes with time of the conserved variables. Damia-Torres[4]

has applied equation 6.34 to smooth P, ρ_g, $\rho_g u_g$ and $\rho_g v_g$ in the crosswise direction. The latter approach is adopted here by applying equation 6.34 to smooth P, $\rho_m(1-Y)$, $\rho_m Y$, $\rho_m(1-Y)u_g$, $\rho_m(1-Y)v_g$, $\rho_m Y u_p$ and $\rho_m Y v_p$. In order to avoid one-sided smoothing, variables at points on the wall and the lower boundary as well as on the symmetry line are not smoothed. Pressure and density smoothing is applied at the end of the pressure updating.

The smoothing constant α_{sm} can be varied with time between the first-time step and a specified number of time steps n_{sm} [4] as follows:

$$\alpha_{sm} = \alpha_{sm}^{i} - a\left(\alpha_{sm}^{i} - \alpha_{sm}^{f}\right) \tag{6.35}$$

where α_{sm}^{i} and α_{sm}^{f} are the initial and final values of α_{sm}, while

$$a = A\, e^{n \ln\left(1 + \frac{1}{A}\right)/n_{sm}} \qquad 1 \leq n \leq n_{sm} \tag{6.36}$$

$$a = 1.0 \qquad n \geq n_{sm} \tag{6.37}$$

and A is taken to be 1%. Typical values for α_{sm}^{i}, α_{sm}^{f} and n_{sm} are 0.15, 0.12 and 226 respectively.

6.5.2 Convergence Criterion

The convergence criterion adopted in the two-dimensional model is similar to that used in the one-dimensional model. The condition for the completion of the solution is set by specifying a value for $|\Delta\phi/\phi|$ of, say 0.01% - 0.05%, where ϕ represents any one of the conserved variables $\rho_m(1-Y)$, $\rho_m Y$, $\rho_m(1-Y)E_g$ and $\rho_m Y E_p$ and $\Delta\phi$ is the change in ϕ between two consecutive time steps. However, the condition for convergence applied for the momentum components is as

follows:

$$\left.\begin{aligned} \left| \frac{\Delta[\rho_m(1-Y)u_g]}{\rho_m(1-Y)U_g} \right| &< \varepsilon \\ \left| \frac{\Delta[\rho_m(1-Y)v_g}{\rho_m(1-Y)U_g} \right| &< \varepsilon \end{aligned}\right\} \qquad (6.38)$$

$$\left.\begin{aligned} \left| \frac{\Delta(\rho_m Y u_p)}{\rho_m Y U_p} \right| &< \varepsilon \\ \left| \frac{\Delta(\rho_m Y v_p)}{\rho_m Y U_p} \right| &< \varepsilon \end{aligned}\right\} \qquad (6.39)$$

and $\varepsilon = 0.01\% - 0.05\%$. This is applied mainly due to the fact that small values of $\rho_m(1-Y)v_g$ and $\rho_m Y v_p$, although having little influence on the flow, can lead to misleading changes[4]. Convergence tests are applied at all calculation points except those on the lower and upper boundaries, since variables at these boundaries are not strictly calculated but approximated, extrapolated or assumed.

6.5.3 Time Step Updating

In order to use a time step as large as possible, the size of the time step is updated after the convergence criterion is applied. The stability criterion employed here is one used by MacCormack and Warming [149] and Damia-Torres[4] in their one-phase flow models, namely

$$\Delta t = B_1 \left[\frac{|u_g|}{\Delta x} + \frac{|v_g|}{2\Delta y} + c_g \left(\frac{1}{\Delta x^2} + \frac{1}{4\Delta y^2} \right)^{\frac{1}{2}} \right]^{-1} \qquad (6.40)$$

which is recommended[4], since for most time-dependent techniques, the crosswise grid size influences the onset of instabilities. Δx and $2\Delta y$ are the widths of the flow cell in the streamwise and crosswise directions respectively, while the term raised to the $\frac{1}{2}$ power represents a characteristic length for the cell and B_1 is a constant which is usually less than unity. It must be noted here that equation 6.40 is an extension of the one-dimensional CFL condition (equation 4.61).

6.6 PREDICTIONS OF THE TWO-DIMENSIONAL MODEL

The two-dimensional flow of a gas-particle mixture in a horizontal, rectangular convergent-divergent nozzle has been investigated. The sinusoidal nozzle, N1, employed in the previous chapter was also used here. Fig. 6.5 shows the two-dimensional grid used in the predictions. The grid is composed of 20 cell columns with a uniform length (Δx) distribution and 7 quasi-streamlines evenly spaced in the crosswise direction. In order to investigate the two-dimensional effects on the behaviour of the mixture in the nozzle a comparison is presented with results obtained by the two-phase one-dimensional model. Consequently, gas and particle properties employed in the two-dimensional predictions are those stated in section 5.2. Reference state parameters are represented by a reference length of 1.0m, temperature of 600°K and pressure of 1.5×10^6 N/m^2, while the dimensionless stagnation pressure and temperature are taken to be unity. Inlet velocity and temperature lags are also taken to be unity. Convergence tests for the two-dimensional model are performed every 75 time steps. Unless otherwise stated, all variables represent non-dimensional variables.

One of the main features of two-dimensional gas-particle flows in nozzles is the fact that small particles have a tendency to follow the gas-phase streamlines even near the curved region of the throat, whereas the larger particles show a tendency to maintain their original trajectories. Therefore, large particles tend to accumulate near the axis of the throat region and a high local concentration of particles results. Consequently, in the nozzle divergence the solid particles do not remain fully dispersed across the flow. More gas-phase momentum is lost near the axis of the throat region in order to accelerate the relatively dense concentration of particles at the throat axis. Thus, for a fixed pressure gradient in the flow direction near the nozzle throat the relatively particle-free region (near the wall) will experience a larger acceleration compared to the particle-laden region (at the throat axis); thereby, the gas near the throat wall is expected to exhibit the maximum velocity. This is more evident for high particle mass flow fractions, Y_f, where the magnitude of the streamwise velocity of both phases near the wall becomes significantly higher than that near the axis. This trend is shown in Figs. 6.6 and 6.7 which show the gas and particle velocities respectively. These figures clearly show the increase in the gas and particle velocities near the wall in regions slightly downstream of the nozzle throat. Figs. 6.6 and 6.7 represent a gas-particle mixture with d_p = 20 μm, Y_f = 50% and P_b = 0.7. The fact that the particles do not follow the gas streamlines but travel through the divergence concentrated on the nozzle axis is well illustrated in Fig. 6.8 which shows the behaviour of the particle mass fraction Y along the nozzle. The figure shows that, in the divergence, while the particle mass fraction increases along the nozzle axis (centreline) it decreases drastically near the nozzle wall. This is also demonstrated in Fig. 6.9 which shows the crosswise variations

of the particle mass fraction before and after the nozzle throat. Figs. 6.8 and 6.9a indicate that prior to the throat the particles accumulate near the nozzle wall resulting in an increase in Y in the wall region. The dramatic change in the gas-phase streamwise velocity profile as particles are introduced in the flow is shown in Fig. 6.10. The figure shows the crosswise variations of the streamwise velocities of a clean gas flow and that of the gas-particle mixture at a non-dimensional distance of 12.5 from the nozzle inlet, i.e. in the nozzle divergence.

The behaviour of different particle sizes in the two-phase flow can be visualized best by comparison of the calculated particle flow angles θ_p for the small (d_p = 20 μm) and the large (d_p = 200 μm) particles depicted in Fig. 6.11. The figure indicates that since larger particles cannot effectively turn around the throat corner, their flow direction lags behind that of the gas phase. However, smaller particles follow more closely the gas-phase flow direction. Fig. 6.12 emphasizes the above argument by comparing the particle mass fractions along the centreline and near the wall for large and small particles, while Fig. 6.13 shows the crosswise variations of the particle mass fractions for the small and large particles in the convergence (x = 7.5) and the divergence (x = 12.5) of the nozzle. Fig. 6.13a shows that in the nozzle convergence a region of high particle mass fraction is indicated near the wall for the larger particles (d_p = 200 μm). This indicates that larger particles are likely to impinge on the steep wall in the nozzle convergence. The present model does not incorporate any particle impingement calculations to evaluate the particle energy transfer caused by such impingement. Effects of the particle material density on its behaviour in the crosswise direction can be observed in Fig. 6.14. For a certain particle

size, denser particles tend to cluster near the throat axis, thus provoking the same behaviour as that of large sized particles already discussed. Fig. 6.14 shows the crosswise distribution of the particle mass fraction in the nozzle convergence and divergence for particle densities of 1057 and 2000 kg/m^3.

The above predictions highlight the fact that the major difference between one-dimensional and axially symmetrical gas-particle nozzle flow calculations is the change in the particle mass distribution in the nozzle due to the inability of the particles to follow the gas-phase streamlines directions. Consequently, in the nozzle convergence and divergence, the streamwise velocities of both phases along the centreline is lower than the one-dimensional estimate. This results because of the high particle concentration on the nozzle axis (and hence higher total particle drag force). Figs. 6.15 and 6.16 show such behaviour for 200 μm particles for the gas and particles respectively. Fig. 6.17 shows the two-dimensional model's pressure predictions compared to that predicted by the one-dimensional model, while Fig. 6.18 shows the wall and the axis pressures as predicted by the model for 20 μm particles. In regions prior to the shock, the wall pressure shows lower values than those of the axis pressure. However, the reduction in the pressure at the nozzle wall is only of small magnitude. Numerical tests in different nozzles (e.g. the experimental nozzle, described in the next chapter, with $P_b = 0.9$) show higher reductions in the pressure at the wall (approximately 6%) when compared with the pressure at the nozzle axis in the throat region. Fig. 6.19 shows the crosswise variation of the pressure in nozzle N1 at a non-dimensional distance of 10.5 from the nozzle inlet.

Fig. 6.20 compares the particle mass fraction distribution on the centreline and near the wall to that in the one dimensional nozzle.

Comparison of the gas-phase temperature along the centreline with that estimated by one-dimensional model shows that generally temperatures on the centreline have higher values than those predicted by the one-dimensional model. Once again, this is because the high concentration of particles along the nozzle axis and hence high total particle heat transfer (see Fig. 6.21). The increase in the particle concentration along the nozzle axis would also result in the axis gas temperature being slightly higher than that near the wall in the nozzle convergence and divergence (Fig. 6.22). A similar trend is also exhibited by the particle temperature in Figs. 6.23 and 6.24. Fig. 6.23 shows the centreline particle temperature as compared to the one-dimensional model's estimate while Fig. 6.24 shows the particle temperatures along the centre line and near the nozzle wall. Figs. 6.25 and 6.26 show the largest relative change of the conserved variables for the gas and particles respectively.

Converged solutions, for the two-dimensional two-phase flow model for the 41X7 mesh with $P_b = 0.7$ (shocked flow), require between 500 - 1000 time steps. The number of time steps for convergence depends on various parameters, e.g. P_b, Y_f, d_p, $TL_{l,j}$, $VL_{l,j}$, smoothing factors and the initial time step size. A typical two-phase run involving 525 time steps (for $d_p = 20$ μm and $Y_f = 0.1$) takes approximately 1 minute execution time on the CDC 6600 computer.

6.7 DEPOSITION AND COLLISIONS

There are a number of practically important flow situations in which it is undesirable for the particles to collide with a flow boundary. For example, in turbomachinery applications the collision of airborne particles with the blade surface could lead to the deposition of particles on the surface with the possibility of impairing the aerodynamic performance, or the collision, in the case of sand or other abrasive particles, could lead to serious erosion. Particle impingement on the walls is caused by their deviation from the gas streamlines during changes in gas flow direction. For the same reason the particles may also move away from the wall thereby forming a particle-free region between the so called limiting particle streamline and the wall.

Two-dimensional numerical tests in nozzle N1 for a back pressure of 0.7 (i.e. shocked flow) show a region of high particle concentration at the nozzle wall. This high concentration region develops at the start of the convergent portion of the nozzle (i.e. $x = 5.0$) and reaches a maximum at an axial distance of about 8.0 (See Fig. 6.8). These results show that for 20 μm diameter particles the increase in the particle mass fraction Y in this region is 25% of that at the centre line of the nozzle at the same cross section. This indicates the increase in the number of particles per unit volume of mixture near the wall in that region, thus increasing the number of particles likely to impinge on unit area of the wall per unit time, as well as increasing the likelihood of particle-particle collison. Furthermore (Fig. 6.12), the smallest particles (20μm) are so influenced by the air stream that their increase in concentration at the nozzle convergence wall is

small compared to that of the larger particles (200 μm). Large particles are less influenced by the air stream and more liable to strike the nozzle wall. For the 200 μm diameter particles results show that the increase in the particle mass fraction at the nozzle convergence wall above that at the nozzle axis is about 35%. The tendency of particles to strike the convergence wall of the nozzle is also shown by numerical tests to increase for heavier particles (ρ_p = 4000 kg/m^3). Heavier particles show higher concentrations at the nozzle wall (x = 8.5) than lighter particles for the same Y_{fi} and d_p.

In the diverging portion of the nozzle, numerical tests show that particles tend to congregate in a dense central core and that there is a considerable wall region behind the throat which does not suffer particle attack. This is indicated by the decrease in the wall particle mass fraction behind the throat (Fig. 6.12), reaching a minimum at about x = 14.0. Fig. 6.12 also shows that, for larger particles, the particle mass fraction at the wall of the divergent section drastically decreases to a small value but it does not vanish exactly. This shows that the majority of the large particles fail to approach the diverging of wall of the nozzle. Further tests show that in the divergent section, the location of the minimum value of the wall particle mass fraction moves downstream of the throat as d_p is increased, indicating that the length of the so-called particle-free region increases as d_p increases. For 200 μm particles a reduction of about 70% in the value of Y at the diverging wall from that at the centre line is indicated.

These results highlight the behaviour of particles suspended in inviscid laminar flow of gas in nozzle N1 and show that the most

likely region of particle deposition on the wall is in the convergent portion. However, in real flows, the possibility of deposition and particle-particle collisions is increased by the turbulence; particle-particle collisons, if resulting in stable agglomerates, can further increase the likelihood of deposition.

As mentioned above, particle-wall collsion may be caused by the particle deviation from the gas stream lines during changes in gas flow direction, i.e. due to particle inertia. This type of deposition is determinded by the Stokes number St. Well established methods, e.g. Sharma and Crowe [32], assume a known gas flow field and compute particle trajectories by integrating the particle velocity/time relationship. Thus most of these methods consider one-way momentum coupling only, i.e. they are good for dilute mixtures only. However, computing particle trajectories is not a feature of the present method and a simple estimate of inertial deposition rate cannot easily be made.

Deposition can also occur due to fluctuations in the gas flow, i.e. in turbulent flows. Turbulent motion of the gas can penetrate very close to the wall [53] and whereas gas can be transferred across the "laminar" sub-layer by molecular diffusion, there is no such mechanism for transport of the particles, unless they are very small. Thus on moving towards the wall, the particles may overshoot the surrounding eddy owing to their inertia and hit the wall. The heavily damped region of the boundary layer close to the wall will inhibit deposition of small particles, but large particles will "coast" through it. The rate of turbulent flow of particles deposited on the wall is determined by the deposition velocity k_d where

$$k_d = \frac{\text{No. of particles deposited on unit area in unit time}}{\text{No. of particles per unit volume in the core flow}}$$

k_d is usually normalized by the friction velocity u_* and plotted against dimensionless relaxation time τ_*, where

$$\tau_* = u_*^2 \tau_p \rho_g / \mu_g \qquad (6.41)$$

Graphs of k_d/u_* versus τ_* are presented by many investigators, e.g. Crane et. al. (165), and may be applied to the present results as illustrated by the following example.

Numerical results based on the one-dimensional flow of 20 μm diameter particles suspended in a gas through nozzle N1 with P_b = 0.7 and Y_{fi} = 0.1, show that at the throat the value of Re_g based on the throat height D_t is of the order of 10^6. The resulting value of τ_*, with equation 4.19 used to calculate the friction factor, is of the order of 10^3. Graphical representation in ref. 165 shows that for this value of τ_* the corresponding value of k_d/u_* is in the range 0.1 — 0.2. This indicates a deposition velocity at the nozzle throat in the range of 1.3 — 2.6 m/s, which implies that 0.6 % of particles entering the throat region are likely to be deposited by turbulence in a distance Δx = 0.75 m.

Particle-particle collision may occur owing to inertial effects or turbulence. Inertial particle-particle collison affects two differently sized particles when the gas accelerates or decelerates. Thus, particle-particle collison is often largely a consequence of polydispersion in the suspension. Particles of different diameters d_p and d_{po} will collide with an average frequency as given in equation 2.9. The collision frequency can be used to determine whether the mixture is dilute or dense. If the

particle obeys Stokes' law, it will tend to regain the velocity it would have in the absence of collision in an interval of the same order as its relaxation time. Thus if $\tau_p/\tau_c << 1$, particles of size d_{po} will tend to return to the velocity they would have in the absence of collisions, before they suffer a further collision with a particle of size d_p. Turbulent particle-particle collision on the other hand can occur for monodispersions if particle diameter is less than the Kolmogorov microscale, i.e.

$$d_p < \left[\frac{\mu_g^3}{\epsilon \rho_g^3}\right]^{1/4} \tag{6.42}$$

where ϵ is the turbulent energy dissipation rate, given by

$$\epsilon \approx \frac{4\, u_*^3}{D} \tag{6.43}$$

and D is the duct's height. If the particles are sufficiently small to follow the turbulent motion exactly and be entrained completely by the smallest, energy-dissipating eddies, the collision rate C_{12}, determined from the relative motion of two adjacent particles is (166, 167)

$$C_{12} \approx 0.4\, d_p^3 \left[\frac{\epsilon \rho_g}{\mu_g}\right]^{1/2} \tag{6.44}$$

so that the number of collisions per second per unit volume of space is $C_{12}N_p^2$, where N_p is number of particles per unit volume. (The likelihood of a stable particle being formed from a collision depends on surface properties, impact velocity, etc., and its estimation is beyond the scope of this work.) Another illustrative example follows.

Calculations based on two-dimensional numerical results at x = 11.5 (the nozzle divergence) along the centre line for d_p = 20 μm, P_b = 0.7 and Y_{fi} = 0.1 show that d_p is well within the Kolmogorov microscale (~ 70 μm for this case). By using equation 4.19 to calculate the friction factor with Re_g based on D, the collision rate C_{12} can be shown to be of the order of 10^{-11} while the number of collisions per second per unit volume ($C_{12}N_p^2$) at x = 11.5 along the nozzle axis is of the order of 10^9. This implies that approximately 1% of the particles entering this centreline cell are likely to suffer collision within the cell axial length Δx = 1.0 m.

While estimates of the significance of each deposition and collision mechanism should be made for each time-marching result, the examples above suggest that inertial deposition is likely to be the dominant effect. A separate particle tracking computation would indicate the extent of the problem, but means of incorporating the effects of deposition into the two-dimensional time marching procedure should be investigated.

CHAPTER 7

GAS-SOLID PARTICLES EXPERIMENT

7.1 INTRODUCTION

This chapter provides a description and discussion of all aspects of an experiment to provide data for the evaluation of the one-dimensional model. The initial objective was to provide a near-one-dimensional transonic gas-particle flow. However, modification of the existing rig to provide the required gas flow rate proved to be too costly and the comparison is therefore limited to fully subsonic gas-particle flow. The discussion of the different experimental aspects is presented in two parts. Firstly, a fully detailed description of the layout, geometry and instrumentation of the rig is presented. Secondly, a comparison between experimental measurements and the one-dimensional model's predictions is presented. The performance of the rig is examined in detail and the errors in the different measurements are discussed.

7.2 PREVIOUS WORK

The velocity and behaviour of particles in the flow of gas-particle mixtures, through convergent-divergent nozzles, were investigated by several workers. Various particle velocity measurement techniques are reported in the literature. They include double-flash photography, streak cameras and laser Doppler anemometer. Double-flash photography was used by Okuda and Choi[153] to measure particle velocities in different nozzles. Their measurements were based on taking photographs for the whole flow domain. The particles were introduced at the throat and their behaviour was investigated in the divergent part only. This technique has also been used by Neilson

and Gilchrist[61] to measure velocities of spherical iron shot and glass beads in converging nozzles. Other workers employing this technique include Ow[154], who used it to study the behaviour of two-phase turbulent pipe flow, and Farwagi[155]. Streak camera photography has also been widely used to measure particle velocities in nozzle flows. Baum[147] used this technique to measure particle velocities in shocked and subsonic nozzle flows. His results show good consistency with his one-dimensional model's predictions (see chapter 5). Warda[156] has also used streak camera photography to measure particle velocities in different nozzles while Bowers[59] used it ot investigate turbulent gas-particle flow in pipes. Other workers using streak camera techniques include Kramer[157,158] and Wakstein[159]. Recently laser Doppler anemometry has been used to measure particle velocities and size distribution as well as their concentrations by Durst[160]. Duckworth[161] states that "the relatively new technique of laser-Doppler anemometry appears to offer the prospect of measuring both the particle and fluid velocity distributions and the particle concentration distribution". This technique has also been used and developed at the Von Karman Institute to measure particle velocities in low and high speed gas-particle flows.

Gas velocity measurements in two-phase flow have been carried out mainly by using conventional methods. One of the popular methods to measure the gas-phase velocity is the use of a pitot tube. This probe has been modified by various investigators to account for the presence of the particles in the flow. The presence of solids may confuse the measurement by increasing the measured pressure. A pitot tube with pinched mouth was used by Kramer[157] while Dussourd and Shapiro[162] used a probe with a vent at the downstream end of the pitot's head. This was done to scavenge trapped particles out of the

probe. Other probes used were purged pitot tubes and pitot tubes with capped mouth to avoid clogging with particles. Further experimental studies of gas-solids flow include those of Farbar[163] and Lee[30]. However, their work did not include the measurement of particle velocity and was mainly concerned with metering the flow of gas with solid particles by measuring and predicing pressure drops across venturi meters.

7.3 DESCRIPTION OF EXPERIMENTAL APPARATUS

7.3.1 The Existing Rig

The existing closed loop gas-solids rig employed in the work is one designed and used by Wakstein[159] for his study of the behaviour of solid particles suspended in turbulent air flow in vertical pipes. The rig is made up of (a) means to circulate the air, (b) a means of feeding the particles into the air flow, (c) the test section, (d) a means of separating the particles from the air flow and (e) gas and particle flow measurement devices. The only section varied in the present experiment was the test section.

The arrangement of the rig is shown in Fig. 7.1. Air is circulated by a Roots-type blower of approximately 0.08 m^3/s at the standard conditions (20°C and 760 mmHg). The blower is followed by a check valve and silencer. Following the silencer there is a pressure relief valve and an aftercooler. The flow rate is controlled by a throttling valve in a by-pass line. The solid particles are introduced into the gas flow from a pressurized feed hopper supported on a platform scale. The solid particles are injected through a 12.7 mm diameter tube at the start of a vertical section pipe of 50.8 mm diameter and 3.048 m in length. The test section is situated at the end of this acceleration section. Next there is a 0.1524 m diameter

cyclone separator, designed to remove particles from the flow, with a collection efficiency of 99.3% for 30 μm particles[159]. The separated solids fall into a collector hopper connected to the base of the cyclone separator. The collector hopper is situated above the feed hopper and connected to it *via* a diaphram valve. Thus, solid particles can be transferred into the feed hopper as needed by simply pressurising the collector hopper and then opening the connecting valve. The air and any particles not removed in the cyclone separator are then led to a large pocket-type fabric filter unit with a fabric area of approximately 14 m^2. This filter unit can collect essentially all particles above a size of 3 μm once an initial coating of particles has formed on the fabric[159]. The filter unit is surrounded by a pressure vessel in order to protect it in case of pressurized operation of the rig. The pressure vessel has a conical bottom so that solids can drain into a smaller collector hopper. In order to protect the blower, primarily against damage resulting from the accidental tearing of the fabric in the pocket filter unit, a commercial compressor pipe line filter is installed as an emergency filter. The air flow rate is measured in the return line to the blower by means of an orifice plate designed in accordance with the recommendations of B.S. 1042.

7.3.2 Rig's Performance

According to Wakstein[164] the rig was designed so that it can be pressurised to a maximum pressure of 2.069×10^5 N/m^2. Furthermore, the pressure drop for the maximum air flow rate of 0.08 m^3/s including the acceleration pressure drop for the solids, taken from the injection point to the cyclone separator, is about 0.48×10^5 N/m^2. Also pressure drops across the cyclone separator, the pocket filter unit and the clean emergency filter are 0.048×10^5 N/m^2, 0.0689×10^5 N/m^2 and

0.0276×10^5 N/m^2 respectively, while the Roots-type blower can develop 0.786×10^5 N/m^2. Preliminary calculations showed that, while the rig is under the maximum pressure and with the maximum air flow rate, the total pressure at the inlet of the existing circular pipe is approximately 2.6063×10^5 N/m^2. If a total temperature of 293°K is assumed and simple one-dimensional theory is used, the corresponding throat area for a proposed nozzle to be choked was estimated to be less than 1:0 cm^2. Such throat area is considered to be impractical since it would lead to the possibility of flow distortions resulting from the insertion of any mechanical probes in the nozzle. Furthermore, the use of alternative means of recirculating the air or substituting a "once-through" air flow driven by a vacuum pump were considered to be too costly in terms of money and technician efforts. Further considerations of the rig performance showed that in the existing test section (pipe with a diameter of 50.8 mm) the maximum velocity while the rig is fully pressurized is about 15 m/s with the ratio of the exit pressure to inlet total pressure being about 0.96.

7.3.3 The Experimental Nozzle

As mentioned in the previous subsection the experimental rig's performance lacked the necessary power to achieve shocked flow in a nozzle of reasonable size. Also by using a nozzle of moderate cross sectional area the air inlet velocity would be small (in the range 10-20 m/s). This indicates that any numerical solution to be obtained by using the one-dimensional model for any proposed experimental nozzle would be hindered by a slow rate of convergence or by instabilities (see section 5.5.5). To avoid any numerical instabilities it was decided to select a nozzle profile with a relatively long and gentle curvature and relatively moderate throat area. Other criteria for selecting a

nozzle profile included the exclusion of any fast area changes as well as a relatively distant throat position from the inlet plane. The selected nozzle profile is a modified and scaled down version of a convergent-divergent nozzle reported by Bratos and Burnat[93] to have been used at the Gottingen Max Planck Institute to investigate the behaviour of moist air. The scaled down profile used in the present experiment is given in table 7.1 while Fig. 7.2 shows the nozzle profile. The exit to throat area ratio for the nozzle is 2.0314. The nozzle has constant area portions at both the inlet and the outlet, with the inlet area being equal to that of the exit.

The experimental nozzle is designed to have a rectangular cross-section with a constant depth of 77.4 mm and a total length of 340 mm. The nozzle is arranged to be part of a pipe of square cross section (77.4×77.4 mm^2). This pipe is incorporated in the rig to replace part of the accelerating section. The transition from the 50.8 mm diameter pipe to the designed square section pipe is achieved by a 152.4 mm long diffuser with a divergence angle of 5°. This diffuser is followed by a 1466.9 mm long pipe of square cross section which precedes the nozzle section. After the nozzle section there is a 381 mm long pipe of square cross section which leads to the diffuser prior to the cyclone separator.

The basic structure of the nozzle is shown in Fig. 7.3, and consists mainly of two blocks which represent the upper and lower wall profiles. These blocks are made of aluminium alloy with the profiles made smooth by hand and polished. One of the early objectives of the present design of the test section was to enable static pressure measurements to be made along the nozzle axis, simultaneously with gas and particle velocity variation measurements in the axial flow direction. To accomplish this objective two pairs of removable side plates were

designed to form the opposite lateral walls of the nozzle. Both pairs are 127 mm wide and 387.4 mm long. The first pair of side plates are made of 19.1 mm thick perspex. The two perspex plates are used in conjunction with the double flash photography system to measure the particles' velocity along the nozzle axis. The second pair of side plates are made of aluminium alloy 19.1 mm in thickness and are associated with pressure measurements. One of these aluminium plates has along its centre 14 static pressure tappings for measurements along the central plane of the nozzle. The second aluminium plate incorporates a system of retractable pitot tube probes. In order not to obstruct the flow, the inside surface of this plate has, along its longitudinal axis, a number of grooves designed to accommodate the head of each retracted pitot tube while the probe is not in use. Fig. 7.4 shows the aluminium plate with the pitot tubes arrangement. The side plates (perspex or aluminium) can be fixed to the nozzle profile blocks by means of aluminium clamping plates 4.8 mm thick. These clamping plates are designed to hold the side plates in position by means of 8 screws (on each side of the side plate) and are made to clear the viewing section when the perspex plates are mounted. Thus, the clamping plates are machined to have a similar profile to that of the nozzle. It was desired for safety that the test section should withstand an internal pressure of at least 3 atmospheres. However, on assembly, sealing of the edges of the nozzle blocks against the surface of the side plates appeared to be difficult. A satisfactory seal was achieved by using Hermetite, a liquid compound which when applied between the surfaces sets like rubber in a few minutes. The compound was poured between the surfaces which were then clamped together. The material flowed into areas of non contact between the edges of the side plates and the nozzle blocks and subsequently set.

7.4 INSTRUMENTATION AND MEASUREMENTS

During the course of the experimental procedure presented here, measurements of air and solids flow rates, air and particle velocities as well as static and total pressures along the nozzle centre line were obtained. All these measurements and their instrumentation will be discussed under headings of air velocity and particle velocity measurements.

7.4.1 Air Velocity Measurements

Air velocity was calculated from the measured difference in total and static air pressure. Total pressure was measured with a conventional pitot tube placed at different stations in the flow stream (see section 7.3.3). Due to limitations on the size of the pitot tubes, it was necessary to use wall taps to measure static pressure of the stream. Static pressure tap holes of 0.5 mm diameter were drilled normal to the aluminium side wall, to meet a bigger hole which was drilled perpendicular to the small hole. The bigger holes accommodated 3 mm pipe fittings and were connected to a manometer bank *via* polythene tubing. The manometer bank contained coloured water and its reading was arranged to give a differential estimate against the tapping nearest to the nozzle exit which was connected to a 1m long water U-tube manometer. Pitot tubes were constructed of hypodermic tubing with an inside diameter of 1.5 mm. The mouth of each pitot tube was pinched to form a slit 0.5 mm wide. The pitot tube opening was made small to keep the majority of impacting particles from entering and eventually clogging the tube. Even so, clogging did occasionally occur. For this reason, the pitot tubes were purged with high pressure air before and after each measurement. The use of pitot tubes with pinched mouths has also been reported by Baum[147] and Kramer[157]. Each pitot tube

had a 115 mm long stem and a 10 mm long head and was kept aligned with the flow direction. Inlet total pressure was also measured by means of a pitot tube having similar specification as those described above. However, the inlet total pressure tube was fixed to the upper wall of the nozzle. All pitot tubes were inserted through brass guide bushes and sealed with rubber "O" rings. The pitot tubes were connected to a digital pressure transducer registering the absolute pressure at each measuring station (Shape Instruments Limited type TPI 600). Two pressure transducers were available for use with ranges of 0 - 0.1 MPa and 0.1 - 1.0 MPa. The connection of the probes to the pressure transducer was made *via* a Mercury Instruments switching gate unit. This unit has 10 pneumatic channels which can be connected in sequence manually or automatically. Ten probes were connected to the digital pressure transducer *via* the switching gate while the rest were connected to the static pressure manometer bank (see Fig. 7.5). Pitot tubes mouths and static pressure tappings were placed at the following distances from the nozzle inlet, x = 0, 15, 55, 85, 105, 125, 155, 175, 195, 215, 235, 255, 285 and 325 mm respectively.

When low pressures were applied on the feed hopper the solid particles feeding was intermittent. This in turn caused pressure pulsations which were evident from the pressure manometer bank. Pressure pulsations occurred for feed hopper pressures of less than 0.3447×10^5 N/m^2. Thus, measurements for feed hopper pressures less than 0.3447×10^5 N/m^2 were not taken. Higher feed hopper pressures produced a continuous stream of particles which in turn reduced the pulsations to a minimum. Blockage of the particles feeding system did occur occasionally due to the formation of larger masses caused by particles adhering together. This was probably caused by humidity in the air. For this reason the solid particles were cleaned by using a sieve

every few runs to get rid of large masses of particles. Further difficulty was encountered due to the clogging of the pitot tubes which was more frequent at higher particle flow rates.

Initially the rig was operated while under pressure; however, on pressurising the rig it was found that preventing air leakage from the various bends and joints as well as the test section proved to be an impossible task. The main difficulty was to keep the pressure in the rig constant and steady. Various attempts were made to detect and seal the different leaks in the loop. Although many leaks were detected and sealed, a constant pressure was never achieved due to undetected leaks. As a result it was decided to run the rig under atmospheric conditions. This was done by having two openings immediately before the blower's inlet to act as input and output ports. This in turn helped to reduce pressure unsteadiness in the rig. Leaks in the test section kept developing in its various joints and a constant check had to be made to detect and seal the leaks. Other measurements carried out were of air total temperatures at the nozzle inlet and outlet. This was achieved by using retractable copper-constantan thermocouples which can be positioned on the nozzle centre line and retracted to grooves in the wall when not in use. These thermocouples were positioned in the pipes immediately before and after the nozzle. It was hoped that temperatures measured by these thermocouples would give a qualitative indication of the overall heat transfer to the gas. These thermocouples were connected to digital voltimeters and a cold junction. No attempt was made to measure the gas temperature along the nozzle centre line, while the gas density was assumed to be constant and equal to that at the nozzle inlet. This assumption was made since for the maximum air flow rate and a temperature of 293°K, the gas-phase Mach number was estimated to reach a

maximum value of about 0.1. The solids mass flow rate was measured by recording the time (using a stop watch) for a certain amount of solids to be fed into the system, while the gas mass flow rate was measured by the pressure drop across the orifice plate.

7.4.2 Solids Velocity Measurements

Double-flash photography is the technique used to obtain a measurement of the velocity of the solid particles. This is basically done by exposing the passing particles twice to a light source within a predetermined time interval while their images are recorded on an exposed film. By measuring the distance between the two images the velocity of the particle could then be determined. The solids velocity measurement required the use of the perspex side walls. In order to measure the solids velocity, the following instruments are used.

Camera

This is an MPP Photographic Products Limited monorail technical camera (see Fig. 7.6) with a maximum bellows extension of approximately 762 mm. It houses a standard 5 inch by 4 inch (127 mm × 102 mm) double-sided black slide at its back plate whilst the lens is at its front plate. The maximum distance separating the focussing screen at the rear and the nodal plane of the lens in front is approximately 902 mm. A magnification of up to 14X can easily be met when using a 59 mm focal length lens. At a magnification of approximately 10X the 5 inch × 4 inch format captures a two-dimensional field of view measuring about 13 mm × 10 mm[154]. This camera has 25 double-sided cut-film holders enabling a total of 50 cut-films to be exposed in any one job. The camera also has a heavy-duty tripod.

Spark Source

This is a double-electrode spark unit manufactured by Pulse (Instrumentation and Controllers) Limited. The design of the Pulse unit is such that the power pack is separated from the flash head. This permits the light-weight flash head to be moved around during alignment. The flash head and the power pack are housed in a cylindrical container. In order to increase the light intensity produced by the Pulse unit a large condenser lens is located in front of the electrode assembly. The spark unit is operated under a continuous supply of argon gas at a delivery pressure of approximately 5 psig.

The Pulse Generator

This is a Malden Electronics Limited Model 738 pulse generator. It provides the firing pulse for the spark unit. It has two separate signal channels, each is capable of delivering consecutive triggering pulses set at various combinations of pulse widths, frequencies and amplitudes. It also has a manual operation facility which delivers a single or a pair of consecutive pulses (with adjustable delay periods) each time a switch is operated. Each channel has independently adjustable delayed triggering facilities, the delay periods may be varied from microseconds up to a maximum of one second.

Counter-Timer

A Racal Universal counter-timer was used to register the interval between two consecutive flashes (because the interval was not necessarily equal to that set by the pulse generator). The start and stop signals to the counter were provided by a photodiode detector which generates a pulse with each detected flash. The leading edge of each pulse was used to start and stop the timer. The light from the spark source is transmitted to each photodiode *via* two lengths of optical fibre.

The Optical Bench

An optical bench was used on which the spark source and the monorail camera may be mounted to slide as an integral unit. The optical bench was initially designed by Ow[154] for photographing and studying two-phase turbulent pipe flow. It houses the Pulse flash head at one end and the monorail camera at the other and it allows for the horizontal movements of both units separately. The total length of the bench is approximately 2m. While the optical bench makes the alignment of the flash head and the camera relatively easy, it does not allow for vertical traverses which are essential for the present experiment. This was overcome by means of two car jacks placed underneath each end of the bench together with a number of wooden blocks of different known heights to increase the vertical reach of the two jacks. The optical bench was placed in such a way that the flow pipe passed between its main base beams while the camera and the spark source were placed on opposite sides of the test section. Fig. 7.6 shows the optical arrangement of the experiment. It also shows the pulse generator and the counter-timer.

The Solid Particles

Solid particles used in the experiment were white glass beads of spherical shape. Their apparent density (defined as the ratio of the mass of particles to the volume of particles) was measured in the following manner. First, the mass of the particles was measured using a balance. Next, the particles were mixed with a known volume of distilled water and the total volume was measured using a graduated cylinder; the increase in volume is attributed to the volume of particles. Finally, the apparent density was determined using the measured mass and volume of the particles. The measured particles apparent density was found to be approximately 2700 kg/m^3.

Accurate information on particle size is also important in dispersed flows. In general, the size of a spherical particle is uniquely defined by its diameter. However, the size of irregularly shaped particles can not be defined uniquely and depends on the method of measurement[30]. There are many different methods for measuring particle size such as sieving, microscopy and electrical sensing zone method (the coulter counter), to mention a few. The particles used in the experiment have a nominal diameter (as supplied by the manufacturers) of 250 μm. In order to check their size, samples of the particles were placed under an electron microscope (JSM-T200 Scanning Microscope, manufactured by JEOL-Technics Co. Limited) with photographic and measurement facilities. Fig. 7.7 is a photograph of particles in one of the samples. It shows that generally the particles are of spherical shapes. Few irregular shapes are evident. Three different photographic samples were analysed and the particle mass mean diameter d_{pm} defined by

$$d_{pm} = \left[\frac{\sum_i N_i d_{pi}^3}{\sum N_i} \right]^{1/3} \tag{7.1}$$

was calculated and found to be 250.9, 252.9, and 253.5 μm respectively. Fig. 7.8 shows the number distribution of two analysed samples. It must be emphasized here that the number of particles in each photographic sample was in the range 40 - 60 particles. The assumed particle size used in the numerical predictions for comparison with the experimental results was 250 μm.

Experimental Procedure

For particle velocity measurements the perspex side plates were placed into position. Vertical traversing of the optical bench was performed by using the two car jacks and the wooden blocks. A vertical

scale was fixed near the bench in order to determine its position. Photographs were taken at 7 fixed positions (stations) at x = 15, 90, 140, 190, 240, 280 and 315 mm from the inlet respectively. All photographs were taken along the nozzle centre line. The lens used was an 80 mm f/5.6 Sneider-Componon. The lens magnification was determined by focussing the lens on a pitot tube head (the inlet total pressure probe) placed at the centre line and by photographing the head, the lens magnification was determined and found to be approximately 9X. The test section, camera and spark source were surrounded by a small chamber made out of dark cloth to keep the test section in complete darkness. Feed hopper pressures were adjusted to correspond to those used for air velocity measurements to ensure similar solids flow rates. At each photographic station 3-4 photographs were taken. Choice of the delay between flashes was a compromise between low accuracy but easy matching of first and second images at small delay, and high accuracy but difficult matching with large delay; values in the range 0.05 - 0.08 ms were used. After film development, the negatives were projected on a scaled screen using an Aldis projector and the distance between any two positions of the same particle was measured. The main difficulty in particle velocity measurements was caused by the erosion of the perspex plates which prompted the need to polish the plates after each complete traverse. The need to dismantle the plates and to reseal the gaps when placed back in position slowed progress. The need to polish the plates increased when increasing the solids flow rate (e.g. for $Y_f > 0.4$, the plates were polished 3 times). Beyond $Y_f = 0.45$, photographing the particles through the perspex plates proved to be very difficult. This in turn limited the maximum Y_f value to around 0.4. Fig. 7.9 shows a double flash photograph taken at x = 280 mm for a flow with $Y_f = 0.419$.

7.5 EXPERIMENTAL RESULTS

The flow of a gas-solid suspension through the experimental convergent-divergent nozzle was investigated for different values of Y_f. In all test cases the air flow rate was set to a maximum by closing the throttling valve in the by-pass line. This was done in order to ensure an optimum behaviour of the blower. When solids are introduced into an air flow, the pressure is altered, and this results in a change in the air mass flow rate compared with that for pure air flow with the same control valve setting. As a result, it is extremely difficult to ensure that the pressure drop measurements taken for varying solids loading ratios are all made with the same value of air flow or back pressure. Instead, therefore, of trying to ensure absolutely comparable air flow rates or fixed back pressure for every solids flow rate fraction, the air flow rate and back pressure were allowed to vary. Thus, comparison cases presented do not represent a mixture flow with a fixed back pressure or fixed air flow rate.

As mentioned in section 7.4.1, initially the rig was run while pressurized. This was abandoned since steady pressures could not be maintained; this was attributed to leakage from different parts of the rig. Leakage was kept to a minimum by inspecting the different joints in the rig and sealing detected leakage. However, any possible inaccuracies resulting in the air flow measurements due to air leakage was ignored in the experimental calculations. Another source of error was due to solids flow rate measurements. Weight of particles was measured to within ±0.2 lb while small fractions of the particles failed to separate in the cyclone separator thus giving rise to a small error of about 0.5%. Percentage error in Y_f due to particles' weight measurement was estimated to be around 0.3%.

Numerical predictions

The one-dimensional model's predictions were obtained by using the measured back pressure together with the total inlet pressure and temperature as well as the particulate phase data (d_p = 250 μm and ρ_p = 2700 kg/m^3). Particle specific heat capacity used in the numerical predictions is that of glass which was also used by other investigators[27,29], i.e. c_s = 878.6 J/kg K. Other data used are a gas-phase Prandtl number of 0.707 and gas constant of 287.1 J/kg K. The grid used is one with 34 calculation cells with a constant cell width (Δx) of 10 mm. In order to ensure stability and convergence, the CFL condition (equation 4.63) is used with small values of B_1, mainly 0.25. This in turn resulted in a high number of time steps for convergence, in the range of 2000 - 4000. The use of higher values of B_1 resulted in instabilities or a higher number of time steps (> 4000) with no convergence achieved. This is believed to be due to the high back pressure to inlet total pressure ratio which results in a small velocity range in the nozzle causing a slow rate of "flushing out" of any perturbations present in the coupled flow. Instabilities were in the form of time oscillations of inlet pressure. These instabilities were eliminated by using the pressure updating scheme coupled with small values of B_1. However, depending on the value of Y_f and P_b, inlet pressure oscillations persisted in some cases. In all numerical results presented for comparison with those obtained experimentally, wall friction (equations 4.18 and 4.19) and gravity effects are included in the solution. Two cases of comparisons are presented, for Y_f = 0.092 and 0.419. In both cases numerical predictions are obtained with $VL_i = TL_i = 1.0$, i.e. inlet velocity and temperature equilibrium.

Static Pressure Results

Figs. 7.10 and 7.11 show a comparison between the experimental static pressure and that predicted by the time-marching method (one-dimensional model). These figures show pressure behaviour along the nozzle for Y_f = 0.092 and 0.419 respectively. The experimental pressure readings are shown as vertical bars. This is due to the fact that pressure curves tended to drift. Initially, the pressure was noted to increase, which was probably caused by the solids pressurised feeding. However, after this initial rise the pressure showed a tendency to decline at a slow rate. Towards the end of each run (5 - 10 min) the rate of pressure changes seemed to reach a minimum. Drifts in experimental pressure measurements have also been reported by other investigators. Baum[147] in his thesis states that "with solids present in the flow the pressure curves tended to drift and consistent readings were not possible until after 400 lbs of solids had passed through the nozzle.". Pressure changes have also been reported by Wakstein[164]. As a result of the drift in the pressure, three sets of pressure readings were taken for each experimental run. Numerical solutions, shown in Figs. 7.10 and 7.11, correspond to the average of the experimental back pressures recorded for the three sets. The average back pressure for each run was nearer to the bottom of the pressure vertical bar due to the fact that the pressure changes were small towards the end of the run.

Pressure results show that, at the throat, numerical predictions indicate lower pressures than those obtained experimentally. This could be a result of the measured back pressures as used in the model, being less than would be expected for a one-dimensional flow. Reductions of experimental pressures in the divergent part were reported by Sharma[29] and attributed to channelling effects. Comparisons of

Sharma's experimental results with those obtained by the time-marching method, when the back pressure used was that of Sharma's experiment, showed higher pressure drops at the throat than those measured experimentally. Similar behaviour is also obtained when using Baum's [147] experimental back pressure for the subsonic case (see section 5.6). Thus, for fixed inlet conditions, any reduction in the back pressure measurements due, probably, to two-dimensional effects, would result in lower throat pressures in the one-dimensional model's predictions.

Pressure manometer readings were recorded within ±1 mm. Corrections to the pressure readings based on the hole size, internal diameter of the pressure connection and Mach number are usually neglected, and they are not introduced in the present readings. The effects of the hole size on the wall pressure measurements could lead to a maximum overestimate of about 0.3 - 0.4%. The heads of the pitot tubes were estimated to be parallel to the nozzle centre line within ±0.5°. There was uncertainty of about ±0.01 mV in the reading of the digital voltmeter connected to the total temperature thermocouple wires. When the thermocouples were calibrated to measure atmospheric temperature there was a difference of about 0.5 - 1.0°C with that measured by mercury-in-glass thermometer. This could lead to total temperature estimation with an error in the range 2 - 4%. The total temperature probes placed before and after the nozzle showed an overall increment in the gas-phase total temperature of approximately 0.3 - 0.5% indicating very small and negligible heat transfer to the gas phase.

Air velocity results

Air velocity along the nozzle centreline is calculated by using the measured total and static pressures. When taking total pressure readings in gas-particles flow, consideration has to be given to the interpretation to be placed on such readings. The presence of the particles in the flow introduces an additional term into the momentum equation, i.e. the particles' momentum. In the pitot mouth the gas is stagnant and if a particle enters the stagnant region, it is slowed down by the drag forces exerted on it. Thus, a particle entering the pitot mouth will lose some of its momentum as it is slowed down by the drag forces, i.e. its momentum is transferred to the gas resulting in an increase in the stagnation pressure. The rest of the particle momentum will be absorbed in collisions with the pitot wall. Boothroyd [53] has proposed the following relationship for total pressure P_o calculations in gas-particles flow:

$$P_o = P + \frac{1}{2} \rho_g' u_g^2 + \eta \rho_p' u_p^2 \qquad (7.1)$$

where ρ_g' is bulk density of the gas (defined as mass of the gas in unit volume of the flowing suspension), ρ_p' is the dispersed density of the particles (mass of particles in unit volume of suspension) and η is a fraction of the particles entering the probe with a maximum possible value of 1.0. In practice, a fraction of the particles entering the pitot will hit the inside wall of the probe, so that P_o will be less than that in equation 7.1 [53]. The actual pitot tubes used in the present work are "L" shaped with pinched mouths to reduce the contribution made by the particles to the total pressure measurements. A further precaution taken was the purging of the probes before the measurement was taken. In this way it was hoped that the contribution made by the particles to the total pressure measurements

would be reduced to negligible proportions. A sample calculation shows that for the case of $Y_f = 0.419$ with particle velocity ranging between 17 and 24 m/s and with the maximum value of η (i.e. $\eta = 1$), the contribution made by the particles to the total pressure is in the approximate range of 5 - 9%. However, in the present work all air velocity calculations are carried out with the assumption that the particles' contribution to the total pressure is negligible, i.e. equation 7.1 reduces to

$$P_o = P + \frac{1}{2} \rho_g u_g^2 \qquad (7.2)$$

and ρ_g is taken to be constant and equal to the gas density at the nozzle inlet. A further difficulty in measuring total pressure is the disturbance to the flow caused by the pitot tubes in small cross sectional areas.

Figs. 7.12 and 7.13 show a comparison between the experimental calculation of the gas-phase velocity and that predicted by the time-marching method (one-dimensional model). The figures represent mixture flow with $Y_f = 0.092$ and 0.419 respectively. All experimental calculations of the gas-phase velocity were based on the average pressure measurements. Generally, time-marching predictions for the gas-phase velocity show higher values than those obtained experimentally. The discrepancy between measured and predicted gas velocity increases in the throat region due to the pressure discrepancy in that region. Results indicate that by increasing Y_f from 0.092 to 0.419 the percentage reduction in the gas phase velocity in the throat region is approximately 1.5%. This in turn indicates that $Y_f = 0.419$ is not high enough to give any significant effect of the particles on the gas flow. Consequently, the flow of the mixture for the experimentally obtained range of Y_f values could be considered as a flow with one-way

coupling effects (from gas to particles only). Percentage error in gas velocity measurements is estimated to be in the range 0.5 - 1.0% (due to pressure readings only).

Particle velocity results

Fig. 7.9 shows an example of the double flash photographs obtained for the particle velocity measurements. Figs. 7.14 and 7.15 show a comparison between the experimental and theoretical particle velocity for the cases of $Y_f = 0.092$ and 0.419 respectively. Fig. 7.14 also shows the average particle velocity obtained at each position while Fig. 7.15 shows a histogram of the number of particles for each velocity range to give a clearer picture of the velocity range at each measuring station. The number of measurements on each photograph varies with the number of particles present in each photograph. This number increases as Y_f increases. Thus, for small values of Y_f the number of particles on a photograph is about 5. This increases to 10 - 15 particles for high values of Y_f. A feature of the particle velocity measurements made is a reasonable agreement between the measured and predicted values in the nozzle convergence. However, in the nozzle divergence, due to two-dimensional effects, the solid particles tend to be concentrated on the nozzle axis and are thus travelling near the peak of the velocity profile. The resulting higher drag forces cause the solids on the centre line to reach velocities higher than those predicted by the one-dimensional analysis as shown in Figs. 7.14 and 7.15. Further discrepancy could also arise from the assumption that the particle drag coefficient used in the numerical model is correct. Considerable doubts exist about the true value of particle drag coefficients in multiparticle flows. The use of the standard drag law for a sphere may not be correct. Generally, as shown in Figs. 7.14 and 7.15 a similar trend is indicated in both the numerical and the

measured values of the particle velocity in the nozzle.

Discussions

The measured static pressure, gas-phase velocity and particle velocity in the experimental nozzle show similar trends to those predicted by the one-dimensional model. The main deviation in the gas-phase parameters occurs in the throat region due to two-dimensional effects. Two-dimensional behaviour of the mixture flow was visible in the experiment. A dense central core in the throat and the diverging section where particles tended to congregate was observed through the perspex plates. As a result, pitot tubes in the nozzle divergence tended to clog more often than those in other parts of the nozzle. Comparisons between numerical and experimental results were limited by various factors. Limitations on the particle loadings due to clogging of pitot tubes and perspex plates' scratching caused the comparisons to be for dilute mixture flows only. This was indicated by the small changes in the maximum velocity of the gas-phase showing that the experiment did not allow for two-way coupling effects. Effects of particles impact on the side plates can be seen in Fig. 7.4 where the dark areas on the Aluminium plate show impact areas. Other limitations in the comparisons was the fact that the experimental mixture flow was one with small inlet subsonic velocities. This has caused problems in terms of numerical method's convergence and stability. Pressure drift due to solids pressurised feeding could probably be avoided by use of gravity assisted solids feeding where particles are introduced into the air flow assisted by their gravity to avoid the effects of external pressures on the flow system. Ideally an alternative means of recirculating the air through the flow loop should be used to produce larger pressure drops across the test section and to obtain

proper comparisons with the one-dimensional model's predictions and to investigate the two-way coupling effects in the mixture.

It must be emphasized here that experimental measurements of gas velocity and the one-dimensional model's predictions did not take into account any two dimensional effects, such as the effects of the boundary layer and its possible separation at the wall in the divergent section of the nozzle. Separation of the boundary layer greatly affects the flow as a whole. In particular the formation of a "wake" of disturbed fluid downstream, in which the pressure is approximately constant, radically alters the pattern of flow. The effective boundary of the flow is then not the divergent section solid surface but an unknown dividing streamline. Effects of the boundary layer and its separation should be included for any two-dimensional experiment and calculations. Boundary layer separation in the experimental nozzle is consistent with results in Figs. 7.12 and 7.13, where the measured velocity is higher than that predicted by the one-dimensional model due perhaps to reduction in the actual flow area near the nozzle exit caused by separation of the boundary layer. It would have been a useful addition to the experimental work to have traversed the flow between the curved walls to detect any separation, but this would have involved constructional difficulties.

CHAPTER 8

FURTHER DISCUSSIONS AND CONCLUSIONS

8.1 INTRODUCTION

A study has been made of one- and two-dimensional two-phase transonic duct flows and, in this chapter, further discussions are presented, conclusions are drawn from the results and suggestions are made for areas where future work is needed.

8.2 THE COMPUTATIONAL WORK

The numerical models presented for one- and two-dimensional two-phase transonic duct flows employ the time-marching method based on the opposed difference technique. The extension of the technique to deal with dispersed gas-particle flows shows the versatility of the time-marching method and demonstrates its capability to solve for two-phase flows. The models incorporate coupling phenomena into the unsteady Eulerian two-phase flow equations. The solution of a wide range of one-dimensional gas-particle flows, including the effects of wall friction, wall heat transfer, gravity and inlet thermal and dynamic inequilibrium between the phases, shows the ability of the model to deal with these phenomena as well as varying values of particle parameters (e.g. ρ_p, d_p, Y_f and c_s). Effects of the initial conditions in reducing the number of time steps are also emphasised while the use of variable time steps is shown to be highly beneficial in speeding up convergence. While the model shows very satisfactory convergence rates for most cases considered, numerical results indicate that the time-marching method is not very economical for mixture flows with small subsonic inlet velocities ($P_b/P_{oi} > 0.99$). Solutions for such flow fields tend to have slow convergence rates resulting in a high number

of time steps for convergence. Consequently, more work is needed to establish the possibility of reducing the number of time steps for convergence for such mixture flow fields. Furthermore, care must be taken when dealing with small inlet velocity flows when there is inlet dynamic inequilibrium between the phases. For such cases, with positive VL_i, instabilities could arise during the flow evolution due to the fact that at the inlet the mixture flow tends to be rather dense (depending on the value of VL_i). However, other methods (e.g. Sharma [29] and Lee [30]) could prove to be less costly to solve for mixture flows with small inlet velocities. A further source of instabilities leading to the collapse of the method is the use of small sized particles ($d_p < 1$ μm). In such cases the particulate phase tends to have high velocities at the early stages of the calculations resulting in instabilities in the throat region. The use of a new set of initial conditions (for the particulate phase) coupled with initially small time steps could prove to be beneficial in this case.

The predictions of the one-dimensional time-marching model have been compared with those obtained numerically and experimentally by other investigators, notably with those obtained by Baum [147], Mobbs *et al.* [66] and Sharma [29]. Comparisons represented a wide range of flow regimes, mainly supersonic exit, shocked, subsonic flows and flows with small inlet velocities. These comparisons show that predictions made by the time-marching method are in good agreement with those made by other numerical methods and by experiments. They also focus on the versatility of the time-marching method to treat complex mixture flows and the feasibility of employing the Eulerian formulation of the two-phase flow equations to solve for dispersed flows.

Numerical tests for the case of two-dimensional, two-phase flow in axisymmetric nozzles show that similar instabilities as those

encountered in the one-dimensional model (e.g. for $d_p < 1$ μm and $P_b/P_{oi} > 0.99$) can also arise in the two-dimensional model. Further instabilities could also arise at the solid wall boundaries. Such instabilities occur due to regions of fast nozzle wall divergence where zones of low particle concentrations can develop and appear in the form of negative or zero particulate phase density. This phenomenon appears only in nozzles with sharp divergent sections and can be reduced by applying crosswise smoothing at points adjacent to the wall. However, extending the grid beyond the solid boundaries and solving the flow equations at the wall calculation points (see Denton[19,21]) could be of interest here and is presently classified as work for the immediate future. Comparisons of the two-dimensional model's predictions with those obtained by the one-dimensional model show a good consistency. They also emphasise the fact that in regions where area changes are present, the mixture flow can no longer be considered as fully dispersed due to channelling effects. Consequently, one-dimensional predictions in areas where channelling is strong, should be treated with caution. Comparisons with other investigators' two-dimensional data have proved to be rather difficult. No detailed experimental or numerical results on two-dimensional transonic gas-particle flows are available in the literature and to the author's knowledge the available literature on two-dimensional gas-particle flows does not contain the necessary data for a comparison to be made (e.g. nozzle geometry, back pressures, inlet total conditions and pressure and velocity profiles). It is obviously undesirable that this situation should continue and further experimental work is necessary in this field in both to obtain a two-dimensional understanding of the mixture flow and to gain proper comparisons with numerical results of the two-dimensional model.

The possibility of extending the one-dimensional model to deal with polydisperse flow have also been given some attention. A version of the one-dimensional model dealing with polydisperse mixture flow has already been formulated and coded by the author, however its results are still under examination and are not presented in this work. In the polydisperse model, while the gas-phase flow equations are solved once every time step, the particulate phase flow equations are solved for each particle size group separately. The inter-phase interaction parameters of each size group are included in the gas-phase flow equations in the summations $\sum_i N_i \dot{m}_{ci}$, $\sum_i N_i D_{pi}$ and $\sum_i N_i Q_{pi}$, where i represents the i^{th} particle size group. At the inlet, velocity and temperature lags for each particle size group are considered separately, so that different particle sizes can enter the duct with different velocities and temperatures. The mixture total enthalpy is calculated as

$$H_m = \left(1 - \sum_i Y_{fi}\right) H_g + \sum_i (Y_{fi} H_{pi}) \qquad (8.1)$$

where

$$Y_{fi} = \frac{Y_i u_{pi}}{\left(1 - \sum_i Y_i\right) u_g + \sum_i (Y_i u_{pi})} \qquad (8.2)$$

and H_{pi} is calculated from equation 3.42.

8.3 THE EXPERIMENTAL WORK

The available flow loop has restricted the experimental work. It only provided data for very small inlet velocities which in turn has obstructed the course of the investigation. Measurements were restricted to a maximum Y_f value of 0.419. The range of loadings used did

not provide a test of the two-way coupling effects and measured flows were considered to be dilute. The use of a different particle feeding system is desirable. It is believed that gravity assisted particle feeding could prove beneficial. Such systems have been used by other investigators (e.g. Warda[156]) where particles are introduced into the flow assisted by gravity and fully mixed with the gas in a mixing chamber before passing through the test section. This could reduce any drift in pressure experienced in the present work. The possibility of using an alternative to the perspex plates is also recommended here due to the difficulty in obtaining photographs through the plates at high particle concentrations due to surface scratching. On the whole, double flash photography proved to be adequate for particle velocity measurements. Comparison between the predicted and measured parameters showed similar trends of pressure and velocities. Effects of electrostatic forces on the particles caused by the particle-duct wall collisions are not considered in the experimental or numerical results. These forces could have strong effects in flows with small velocity range and small drag forces on the particles. Consequently, effects of electrostatic force should be investigated further.

8.4 SUGGESTIONS FOR FUTURE WORK

Some areas where future work is necessary have already been outlined. For computational work, these can be summarised as the investigation of the possibility of obtaining a faster convergence rate for flows with high back pressure ratio ($P_b/P_{oi} > 0.99$). It is also worth improving the structure of the models and reducing (where possible) the amount of computer memory required. The advancement of the one-dimensional polydisperse model and a full investigation of its results is also recommended here. The inclusion of the inter-phase mass transfer effects in both the one- and two-dimensional models would also

be a useful extension. This could be achieved by using equations already stated in this work (e.g. 3.76, 3.85 and 3.86) together with the appropriate changes in the inlet conditions. Furthermore, the improvement of the two-dimensional model in obtaining faster convergence rates and reducing instabilities is also recommended. No detailed experimental results on the two-dimensional transonic gas-particle flow are available. This emphasizes the need for a comprehensive experiment designed to investigate the behaviour of gas-particle flow in nozzles and to obtain a good comparison with the two-dimensional model's predictions.

APPENDIX A

DERIVATION OF INLET BOUNDARY RELATIONS

As stated in chapter four the inlet boundary conditions treatment has needed the assumption of constant mixture momentum between the inlet plane and the first calculation point. The mixture momentum is evaluated by adding the momentum equations of the component phases of the two-phase mixture. Hence, at any point

$$MOM = A\left[\frac{P}{\gamma} + \rho_m(1-Y)u_g^2 + \rho_m Y u_p^2 - \frac{\rho_m(1-Y)}{A\rho_g}\tau_w A_L - \frac{\rho_m V}{A \cdot Fr^2}\right] \qquad (A.1)$$

where A_L is the lateral area of the flow cell. The assumption of constant mixture momentum yields

$$MOM_{il} - MOM_1 = G(P_{il}) \qquad (A.2)$$

where MOM_1 is assumed to be constant. The specified boundary conditions are Y_{fi}, TL_i, VL_i and the stagnation state parameters. The assumption of isentropic expansion of the gas phase yields

$$(\rho_g)_{il} = C_1 P_{il}^{\frac{1}{\gamma}} \qquad (A.3)$$

and

$$(T_g)_{il} = C_2 P_{il}^{\frac{\gamma-1}{\gamma}} \qquad (A.4)$$

where

$$C_1 = \frac{P_o^{\frac{\gamma-1}{\gamma}}}{T_o} \qquad (A.5)$$

and

$$C_2 = 1/C_1 \qquad (A.6)$$

The mixture density ρ_m at the inlet can be evaluated by using equations 3.38 and A.3

$$(\rho_m)_{il} = \frac{\rho_p C_1 P_{il}^{\frac{1}{\gamma}}}{\rho_p (1-\gamma)_{il} + Y_{il} C_1 P_{il}^{\frac{1}{\gamma}}} \tag{A.7}$$

while Y_{il} is evaluated by equation (4.33) as

$$Y_{il} = \frac{Y_{fi}}{(1-Y_{fi})\ VL_i + Y_{fi}} \tag{A.8}$$

Furthermore, an expression for the velocity of the gas-phase $(u_g)_{il}$ can be obtained by using the conservation of the total enthalpy of the mixture, i.e. equation (4.25), so that

$$(1-Y_{fi})\left[T_g + \frac{\gamma-1}{2} u_g^2\right]_{il} + Y_{fi}\left[\beta_1 T_p + \frac{\gamma-1}{2} u_p^2 + \frac{\gamma-1}{\gamma\rho_p} P\right]_{il} + \frac{\gamma-1}{Fr^2} x_{il} = H_{mo} \tag{A.9}$$

where $\beta_1 = \frac{c_s}{c_p}$ and H_{mo} is the stagnation enthalpy of the mixture defined by equation 4.26. Also by using equations A.4, 4.20 and 4.21 the particle-phase temperature and velocity at the inlet can be expressed as

$$(T_p)_{il} = TL_i\left[C_2 P_{il}^{\frac{\gamma-1}{\gamma}} - T_o\right] + T_o \tag{A.10}$$

and

$$(u_p)_{il} = (u_g)_{il}\ VL_i \tag{A.11}$$

By substituting the above expressions for $(T_p)_{il}$ and $(u_p)_{il}$ into equation A.9 the gas-phase velocity can be expressed as a function of the static pressure at the inlet

$$(u_g)_{il} = \frac{C_3 - C_4 P_{il}^{\frac{\gamma-1}{\gamma}} - C_5 P_{il}}{C_6} \tag{A.12}$$

where

$$C_3 = H_{mo} - \frac{\gamma-1}{Fr^2} x_{il} - Y_{fi}\beta_1 T_o(1 - TL_i) \tag{A.13}$$

$$C_4 = C_2[(1-Y_{fi}) + Y_{fi} \cdot TL_i \cdot \beta_1] \tag{A.14}$$

$$C_5 = Y_{fi} \frac{\gamma-1}{\gamma \rho_p} \tag{A.15}$$

and

$$C_6 = \left(\frac{\gamma-1}{2}\right)[(1-Y_{fi}) + Y_{fi}\ VL_i] \tag{A.16}$$

When equations A.7, A.11 and A.12 in conjunction with an expression for the wall friction, i.e. equations 3.50, 4.18 and 4.19, are substituted into A.1 the pressure function $G(P_{il})$ is then obtained.

APPENDIX B

WALL PRESSURE EVALUATION

Consider a property ϕ whose derivative normal to a wall is known at all calculation points on the wall, i.e.

$$\frac{\partial \phi}{\partial n} = G \tag{B.1}$$

where n is measured along the normal to the wall and considered to be positive in the direction of the mixture. While the values of ϕ are known at interior points, the problem is to evaluate it at the solid wall boundary. The directional derivative of ϕ with respect to a curvilinear coordinate s is[4,150]

$$\frac{\partial \phi}{\partial s} = \vec{m} \cdot \vec{\nabla} \phi \tag{B.2}$$

where $\vec{m}$ is the unit vector tangent to the curve C along which the coordinate s is measured, so that

$$\vec{m} = \vec{e}_x \cos\alpha_s + \vec{e}_y \sin\alpha_s \tag{B.3}$$

where α_s is the angle between the tangent to the curve C (orientated in the s direction) and the x-direction. Combining equations B.2 and B.3 and performing the scalar product, then

$$\frac{\partial \phi}{\partial s} = \frac{\partial \phi}{\partial x} \cos\alpha_s + \frac{\partial \phi}{\partial y} \sin\alpha_s \tag{B.4}$$

Since the quasi-streamlines are not continuous curves, but successions of straight lines with the calculation points at the centre of each line, the length Δs of any of these lines is

$$\Delta s = \frac{\Delta x}{\cos\alpha_{qs}} \tag{B.5}$$

where α_{qs} is the angle between the quasi-streamline segment and the x-axis and Δx is the cell size in the x-direction. The rate of change of ϕ along a segment of quasi-streamline with respect to s can be expressed as

$$\frac{\Delta\phi}{\Delta s} = \left(\frac{\Delta\phi}{\Delta x}\right)_{qs} \cos\alpha_{qs} \tag{B.6}$$

where $(\Delta\phi/\Delta x)_{qs}$ is the rate of change of ϕ along the segment of the quasi-streamline with respect to x. Consequently, by combining equations B.4 and B.6 and replacing subscript s by qs, then

$$\frac{\partial\phi}{\partial x} = \left(\frac{\Delta\phi}{\Delta x}\right)_{qs} - \frac{\partial\phi}{\partial y} \tan\alpha_{qs} \tag{B.7}$$

where $\tan\alpha_{qs}$ is an average value, since $(\Delta\phi/\Delta x)_{qs}$ is evaluated by finite differences[4].

At the wall, $\partial\phi/\partial n$ can be written as a function of the derivatives along the grid lines by using equations B.4 and B.7, so that

$$\frac{\partial\phi}{\partial n} = \left(\frac{\Delta\phi}{\Delta x}\right)_{w} \cos\alpha_{n} - \frac{\partial\phi}{\partial y} (\tan\alpha_{w} \cos\alpha_{n} - \cos\beta_{n}) \tag{B.8}$$

where the angles and coordinates are defined by Fig. 6.4 and $(\Delta\phi/\Delta x)_{w}$ is the rate of change of ϕ along the wall with respect to x. Equation B.8 can be rewritten, by using trigonometric relations, in the following form

$$\frac{\partial\zeta}{\partial n} = \mp \left(\frac{\partial\phi}{\partial x}\right)_{w} \sin\alpha_{w} \pm \frac{\partial\phi}{\partial y} \frac{1}{\cos\alpha_{w}} \tag{B.9}$$

where the signs depend whether the lower or upper wall, is considered, respectively. In calculating the gradients three points are used, and while $\partial\phi/\partial y$ is evaluated by one-sided differences, $(\Delta\phi/\Delta x)_w$ is calculated by centred differences for interior wall calculation points, and by one-sided differences if the calculation points are at either end of the duct. Following the above, equations B.1 and B.9 form a linear system of algebraic equations for each wall, namely

$$\begin{vmatrix} B_2' & C_2' & E & & & & & & \\ A_4 & B_4 & C_4 & & & & & & \\ & A_6 & B_6 & C_6 & & & & & \\ & & & A_i & B_i & C_i & & & \\ & & & & & & A_{I-5} & B_{I-5} & C_{I-5} \\ & & & & & & & A_{I-3} & B_{I-3} & C_{I-3} \\ & & & & & & F & A'_{I-1} & B'_{I-1} \end{vmatrix} \begin{vmatrix} \phi_2 \\ \phi_4 \\ \phi_6 \\ \phi_i \\ \phi_{I-5} \\ \phi_{I-3} \\ \phi_{I-1} \end{vmatrix} = \begin{vmatrix} R_2' \\ R_4 \\ R_6 \\ R_i \\ R_{I-5} \\ R_{I-3} \\ R'_{I-1} \end{vmatrix} \tag{B.10}$$

where i is the index for the wall calculation points (the j index is dropped). The elements of the coefficient (rectangular) matrix and the column matrix on the RHS are functions of $(\alpha_w)_i$ and the grid geometry adjacent to the wall. The latter matrix is also a function of G_i. The above system of equations B.10 can be transformed into one with a tridiagonal coefficient matrix. The first equation can be replaced by a linear combination of itself and the second equation, and a similar procedure is also performed on the two last equations, hence

$$
\begin{vmatrix}
B_2 & C_2 & & & & & & \\
A_4 & B_4 & C_4 & & & & & \\
 & A_6 & B_6 & C_6 & & & & \\
 & & A_i & B_i & C_i & & & \\
 & & & A_{I-5} & B_{I-5} & C_{I-5} & & \\
 & & & & A_{I-3} & B_{I-3} & C_{I-3} & \\
 & & & & & A_{I-1} & B_{I-1}
\end{vmatrix}
\begin{vmatrix} \phi_2 \\ \phi_4 \\ \phi_6 \\ \phi_i \\ \phi_{I-5} \\ \phi_{I-3} \\ \phi_{I-1} \end{vmatrix}
=
\begin{vmatrix} R_2 \\ R_4 \\ R_6 \\ R_i \\ R_{I-5} \\ R_{I-3} \\ R_{I-1} \end{vmatrix}
\tag{B.11}
$$

Due to the fact that the gradient calculations are based on parabola fittings, the angle α_w in equation B.9 is taken as the angle whose tangent is the arithmetic average of the wall slopes at the three calculation points involved in evaluating $(\Delta\phi/\Delta x)_w$. This implies that $(\alpha_w)_4 = (\alpha_w)_2$ and $(\alpha_w)_{I-1} = (\alpha_w)_{I-3}$, which avoids infinite values for C_2 and R_2 or A_{I-1} and R_{I-1}, when $(\alpha_w)_4$ or $(\alpha_w)_{I-3}$ are equal to zero, respectively. Equations B.11 can be solved by using Gaussian elimination (known as tri-diagonal matrix algorithm). The procedure outlined above is employed to calculate the wall pressure with G is taken as $[\rho_m(1-Y)U_g^2 + \rho_m Y U_p^2]/r$.

REFERENCES

1. DELHAYE, J.M.

Two-phase flow patterns.

In, Two-phase flow and heat transfer in the power and process industries, Bergles, A.E. *et al.*, Hemisphere (McGraw-Hill), 1981, pp. 13-40.

2. COLLIER, J.G.

Convective boiling and condensation.

McGraw-Hill, 1972.

3. GYARMATHY, G.

Basic notions.

In, Two-phase steam flow in turbines and separators.

Moore, M.J. and Sieverding, C.H., Hemisphere, McGraw-Hill, 1976.

4. DAMIA TORRES, J.A.

Time-marching solution of transonic duct flows.

Ph.D. Thesis, University of London, 1980.

5. AMES, W.F.

Numerical methods for partial differential equations.

2nd Edition, Academic Press, New York, 1977.

6. SMITH, G.D.

Numerical solution of partial differential equations.

Oxford University Press, London, 1975.

7. SMOLDEREN, J.J.

Introductory remarks, numerical methods in fluid dynamics.

AGARD-LS-48, paper 1, May, 1972, p.6.

8. TAYLOR, T.D. and YAGGY, P.F.

Numerical methods for predicting subsonic, transonic and supersonic flow.

AGARD-AG-187, January, 1974, p.48.

9. GOSTELOW, J.P.

Review of compressible flow theories for airfoil cascades.

J. Eng. Power, Trans. ASME (A), 95, 4, October 1973, pp. 281-292.

10. DANESHYAR, H. and GLYNN, D.R.

The calculation of flow in nozzles using a time-marching technique based on the method of characteristics.

Int. J. Mech. Sci. vol. 15, 1973, pp. 921-934.

11. DELANEY, R.A. and KAVANAGH, P.

Transonic flow analysis in axial-flow turbomachinery cascades by a time-dependent Method of Characteristics.

J. Eng. Power, Trans. ASME (A), 98, 3, July, 1976, pp. 356-364.

12. WILKINSON, D.H.

Calculation of blade-to-blade flow in a turbomachine by streamline curvature.

A.R.C. Reports and Memoranda No. 3704, December, 1970.

13. ADAMSON, T.G. Jnr. and PLATZER, M.F.

Transonic flow problems in turbomachinery.

Hemisphere, Washington, 1977.

14. MURMAN, E.M.

Computation of transonic potential flows in turbomachinery.

In Ref. 13, pp. 115-133.

15. LOMAX, H. and STEGER, J.L.

Relaxation methods in fluid mechanics.

Ann. Rev. Fluid Mech., vol. 7, 1975, pp. 63-88.

16. MORETTI, G.

Initial conditions and embeded shocks in the numerical analysis of transonic flows.

Lecture Notes in Physics 8, Springer-Verlag, Berlin, 1971.

17. ROACHE, P.J.

Computational fluid dynamics.

Revised printing, Hermosa, Albequerque (USA), 1976.

18. DENTON, J.D.

Extension of the finite area time-marching method to three dimensions.

VKI Lecture Series 84, Brussels, February 2-6, 1976, p.44.

19. DENTON, J.D. and SINGH, U.K.

Time-marching methods for turbomachinery flow calculations.

Part I - basic principles and two-dimensional applications.

VKI Lecture Series 79-7, 1979, p.27.

20. McDONALD, P.W.

The computation of transonic flow through two-dimensional gas turbine cascades.

ASME Paper 71-GT-89, March, 1971, p.7.

21. DENTON, J.D.

A time-marching method for two- and three-dimensional blade-to-blade flows.

ARC R & M 3775, October, 1974, p.24.

22. A SYMPOSIUM ON INTERNAL FLOW.

University of Salford (in collaboration with the NPL and the Inst. Mech. Engrs.), UK, April 20-22, 1971.

23. MARSH, H. and MERRYWEATHER, H.

The calculation of subsonic and supersonic flow in nozzles.

In Ref. 22, Paper 22, p.9.

24. PERKINS, H.J. and HORLOCK, J.H.

Aerodynamic analysis of turbomachinery.

GEC J. Sci. Technol., vol. 41, No. 2 and 3, 1974, pp. 43-52.

25. DI GIACINTO, M., SABETTA, F. and PIVA, R.
Two-way coupling effects in dilute gas-particle flows.
J. Fluids Eng., Trans. ASME, vol. 104, 4, Sept. 1982, pp. 304-312.

26. GINOUX, J. and RIETHMULLER, M.
Flow of solid particles in gases - Activities at the Von Karman Institute for fluid dynamics.
In, Flow of solid particles in gases.
Rudinger, G. AGARD-AG-222, 1976.

27. BAGHDADI, A.H.
Numerical modelling of two-phase flow with inter-phase slip.
Ph.D. Thesis, University of London, 1979.

28. CROWE, C.T.
Review - Numerical models for dilute gas-particle flows.
J. Fluids Eng., Trans. ASME, vol. 104, 4, Sept. 1982.

29. SHARMA, M.P.
Numerical and experimental study of gas-particle flows in orifices and venturis: Application to flow meter design.
Ph.D. Thesis, Washington State University, 1977.

30. LEE, J.
Scaling laws for metering the flows of gas-particle suspensions through venturis.
Ph.D. Thesis, Washington State University, 1980.

31. CROWE, C.T., SHARMA, M. and STOCK, D.
The particle-source-in-cell (PSI-Cell) model for gas-droplet flows.
ASME paper 75-WA/HT-25, 1975.

32. SHARMA, M. and CROWE, C.T.

A novel physico-computational model for quasi-one-dimensional gas-particle flows.

J. Fluids Eng. ASME, vol. 100, Sept. 1978.

33. CROWE, C.T.

On the relative importance of particle-particle collisions in gas-particle flows.

Paper C78-81, conf. on Gas-Borne Particles, Inst. of Mech. Engr. Oxford, England, 1981, pp. 135-137.

34. LEE, J. and CROWE, C.T.

Gas-particle flow in a venturi: a numerical study.

Paper C77-81, conf. on Gas-Borne Particles, Inst. of Mech. Engr. Oxford, England, 1981, pp. 129-133.

35. KIRILLOV, I. and YABLONIK, R.M.

Fundamentals of the theory of turbines operating on wet steam.

Leningrad Press, translated as NASA TT F-611, 1968.

36. MARBLE, F.E.

Dynamics of a gas containing small solid particles.

Combustion and Propulsion, Fifth AGARD Colloquium (High Temperature Phenomena), April 1962.

37. RUDINGER, G.

Flow of solid particles in gases.

AGARD-AG-222, 1976.

38. KUENTZMANN, P.

French contribution to aerodynamics of gas-particle mixtures.

In Ref. 37, pp. 1-17.

39. MOORE, M.J. and SIEVERDING, C.H.
Two-phase steam flow in turbines and separators.
Theory, instrumentation, engineering
VKI Book, Hemisphere, McGraw-Hill, 1976.

40. BAKHTAR, F. and MOHAMMADI TOCHAI, M.
An investigation of two-dimensional flows of nucleating and wet-steam by the time-marching method.
Int. J. Heat and Fluid Flow, vol. 2, No.1, 1980.

41. HILL, P.G.
Condensation of water vapour during supersonic expansion in nozzles.
J. Fluid Mech., vol. 25, part 3, 1966, pp. 593-620.

42. HILL, P.G., WITTING, H. and DEMETRI, E.P.
Condensation of metal vapours during rapid expansion.
J. Heat Transfer, ASME, vol. 85, 1963, pp. 303-316.

43. KIRILLOV, I. and AMELYUSHKIN, V.N.
A method for calculating wet-steam condensation process.
Heat Transfer - Soviet Research, vol. 2, No.3, May 1970, pp. 102-110.

44. MOSES, C.A. and STEIN, G.D.
On the growth of steam droplets formed in a Laval nozzle using both static pressure and light scattering measurements.
J. of Fluids Eng., Trans. ASME, vol. 100, Sept. 1978, pp. 311-322.

45. CAMPBELL, B.A. and BAKHTAR, F.
Condensation phenomena in high speed flow of steam.
Proc. Instn. Mech. Engrs. vol. 185, 25/71, 1970-71, p.395.

46. JACKSON, R.

A self-consistent equations set for a multiphase flow.

Central Electricity Research Laboratories, Lab. Note No. RD/L/N 176/76, 1976.

47. FUCHS, N.H.

Evaporation and droplet growth in gaseous media.

Pergamon Press, New York, 1959.

48. YOUNG, J.B.

Nucleation in high pressure steam and flow in turbines.

Ph.D. Thesis, University of Birmingham, 1973.

49. RUDINGER, G.

Fundamentals and applications of gas-particle flow.

In Ref. No. 37, pp. 55-86.

50. WUEST, W.

Gas flows with solid particles, research and development in Germany.

In Ref. No. 37, pp. 19-31.

51. SOO, S.L.

Fluid dynamics of multiphase systems.

Blaisdell Publishing Company, 1976.

52. CARLSON, D.J. and HOGLUND, R.F.

Particle drag and heat transfer in rocket nozzles.

AIAA Journal, vol. 2, No.11, Nov. 1964, pp. 1980-84.

53. BOOTHROYD, R.G.

Flowing gas-solids suspensions.

Chapman and Hall Ltd., 1971.

54. KANNAPPRAKASAM, B. and BROWN, A.
A review of the bases for predicting gas-particle flows with particular reference to turbo-machinery.
Int. J. Heat and Fluid Flow, 1983.

55. LOW, S.C. and BARUAH, P.D.
Liquid fuel droplets entrained in the transient unidimensional gas flow in a pipe.
Int. J. Multiphase Flow, vol. 7, 1981, pp. 293-309.

56. WARNER, C.F. and NETZER, D.W.
An investigation of the flow characteristics of two-phase flow in converging-diverging nozzles.
ASME Paper 63-WA-192, 1964.

57. MOORE, M.J.
Gas dynamics of wet steam and energy losses in wet-steam turbines.
In Ref. 39, pp. 59-126.

58. CHURCHILL, S.W. and USAGI, R.
A general expression for the correlation of rates of transfer and other phenomena.
AIChE Journal, vol. 18, No.6, 1972.

59. BOWERS, H.M.
A study of gas-solids flows at very high speeds.
Ph.D. Thesis, Leeds University, 1966.

60. JOHNSON, G.R.
Supersonic gas-solid particle flow in an axisymmetric nozzle by the method of characteristics.
VKI, Technical Note 78, Aug. 1971.

61. NEILSON, J.H. and GILCHRIST, A.
An analytical and experimental investigation of the velocities of particles entrained by the gas flow in nozzles.
J. Fluid Mech., vol. 33, part 1, 1968, pp. 131-149.

62. PANTON, R. and OPPENHEIM, A.K.
Shock relaxation in a particle-gas mixture with mass transfer between phases.
AIAA Journal, vol. 6, part 11, 1968, p.2071.

63. KRIER, H. and MOZAFFARIAN, A.
Two-phase reactive particle flow through normal shock waves.
Int. J. Multiphase Flows, vol. 4, 1978, pp. 65-79.

64. OTTERMAN, B. and LEVINE, A.
Analysis of gas particle flows in shock tubes.
AIAA Journal, vol. 12, No.5, May 1974, pp. 579-580.

65. NARKIS, Y. and GAL-OR, B.
Two-phase flow through normal shock wave.
J. of Fluids Engng., Trans. ASME, vol. 94, Sept. 1975, pp. 361-365.

66. MOBBS, F., BAUM, M. and COLE, B.
A theoretical investigation of the effect of initial velocity and temperature lag on the flow of a gas-solid suspension through a convergent-divergent nozzle.
Proc. I. Mech. E., vol. 189, 37/75, 1975, pp. 375-382.

67. GLAZUNOV, A.A. and RYCHKOV, A.D.
Investigation of non-equilibrium two-phase flows in axisymmetric Laval nozzles.
Fluid Dynamics, vol. 12, part 6, 1977, pp. 887-892.

68. HOGLUND, R.F.

Recent advances in gas-particle nozzle flows.

J. of the American Rocket Society, vol. 32, 1962, p.662.

69. DASH, S.M. and THORPE, R.D.

Shock-capturing model for one- and two-phase supersonic exhaust flow.

AIAA Journal, vol. 19, No.7, July 1981, pp. 842-851.

70. MORSI, S.A. and ALEXANDER, A.J.

An investigation of particle trajectories in two-phase flow systems.

J. Fluid Mech., vol. 55, part 2, 1972, pp. 193-208.

71. HAMED, A. and TABAKOFF, W.

Solid particle demixing in a suspension flow of viscous gas.

J. of Fluids Engng. Trans. ASME, vol. 97, 1975, p.106.

72. HARLOW, F.H. and AMSDEN, A.A.

Numerical calculation of multiphase fluid flow.

Journal of Computational Physics, vol. 17, 1975, pp. 19-52.

73. KLIEGEL, J.R.

Gas-particle nozzle flows.

Ninth (Int'l) Symposium on Combustion, Academic Press, 1963, pp. 811-826.

74. KRIEBEL, A.R.

Analysis of normal shock waves in particle laden gas.

J. of Basic Engng., Trans. ASME, Dec. 1964, pp. 655-665.

75. KLIEGEL, J.R.

One-dimensional flow of a gas-particle system.

Paper No. 60-S, IAS 28th meeting, New York, 1960.

76. HULTBERG, J.A. and SOO, S.L.
Two-phase flow through a nozzle.
Astronautica Acta, vol. 11, No. 3, 1965, p.207.

77. ISHII, R.
Nonequilibrium nozzle flows of gas-particle mixtures.
Trans. Japan Soc. Aero. Space Sci., vol. 18, No. 39, March 1975, pp. 29-40.

78. COLE, B.N., BAUM, M.R. and JOBBS, F.R.
The influence of initial velocity and temperature lag on the relaxation zone behind a shock wave in a gas solid flow.
Int. J. Heat and Fluid Flow, I. Mech. E., vol. 5, No. 2, 1975, pp. 110-116.

79. YOUSIF, F., CAMPBELL, B. and BAKHTAR, F.
Stability in condensing flow of steam.
Proc. of Instn. Mech. Engrs., vol. 186, 37/72, 1972, pp. 439-448.

80. BAKHTAR, F., RYLEY, D.J., TUBMAN, K. and YOUNG, J.B.
Nucleation Studies in flowing high-pressure steam.
Proc. of Instn. Mech. Engrs., vol. 189, 41/75, 1975, pp. 427-435.

81. OSWATITSCH, K.
Kondensationsercheinungen in Uberschalldusen.
Z. Angew. Math. u. Mech., 1942, vol. 22, No. 1, p.1.

82. MOORE, M.J., WALTERS, P., CRANE, R.I. and DAVIDSON, B.J.
Predicting the fog-drop size in wet-steam turbines.
Instn. Mech. Engrs., conference publication 3, C37/73, 1973, pp. 101-109.

83. JACKSON, R.
SLIPFLO - A computer program for one dimensional wet-steam flow with distinct phase velocities.
Central Electricity Research Laboratories, RD/L/N 3/77, June 1977.

84. PUZYREWSKI, R. and STUDZINSKI, W.
One-dimensional water vapour expansion with condensation at higher pressures.
Int. J. Multiphase Flow, vol. 6, 1980, PP.425-439.

85. WEGENER, P. and PARLANGE, J.
Non-equilibrium nozzle flow with condensation.
AGARD Conf. Proc. No. 12, "Recent advances in aerothermochemistry", vol. 2, 1967.

86. WEGENER, P. and MACK, L.
Condensation in supersonic and hypersonic wind tunnels.
Advances in Applied Mechanics, vol. 5, 1958, pp. 307-447.

87. REGAN, J., THOMPSON, H. and HOGLUND, R.
Two-dimensional analysis of transonic gas-particle flows in axi-symmetric nozzles.
J. Space Craft, vol. 8, No. 4, April 1971, pp. 346-351.

88. COUSINS, J.
Two-dimensional, two-phase flow through a rocket exhaust nozzle: A progress report.
Rocket Propulsion Establishment, Memorandum No. 685, Aug. 1976.

89. CROWE, C.T. and PRATT, D.T.
Analysis of the flow field in cyclone separators.
J. of Computers and Fluids, vol. 2, 1974, pp. 249-260.

90. CROWE, C.T. and STOCK, D.E.
A computer solution for two-dimensional fluid-particle flows.
Int. J. for Numerical Methods in Engineering, vol. 10, 1976, pp. 185-196.

91. CROWE, C.T.

A numerical model for the gas-droplet flow field near an atomizer.

Proceeding of The First International Conference on Liquid Atomization and Spray Systems.

The Fuel Society of Japan,

Tokyo, Aug. 27-31, 1978, pp. 378-383.

92. BLAGOSKLONOV, V. and STASENKO, A.

Two-dimensional nozzle and jet flows of a multiphase mixture.

Fluid Mechanics - Soviet Research, vol. 8, No.2, March 1979, pp. 157-168.

93. BRATOS, M. and BURNAT, M.

Two-dimensional, two-phase transition in a de Laval nozzle.

Archives of Mechanics, vol. 26, No. 6, 1974, pp. 965-979.

94. YEOH, C. and YOUNG, J.B.

Nonequilibrium streamline curvature throughflow calculations in wet-steam turbines.

J. of Engng. for Power, Trans. ASME, vol. 104, April 1982, pp. 489-496.

95. DENTON, J.

Throughflow calculations for transonic axial flow turbines.

J. of Engng. for Power, Trans. ASME, vol. 100, April 1978, pp. 212-218.

96. CARRIER, G.F.

Shock waves in a dusty gas.

J. Fluid Mech., vol. 4, 1958, p.376.

97. MARBLE, F.E.

Dynamics of dusty gases.

Annual Review of Fluid Mechanics, vol. 2, 1970, pp. 397-446.

98. SRIVASTAVA, R. and SHARMA, J.

Structure of normal shock waves in a gas-particle mixture.

J. of Applied Maths, and Physics (ZAMP), vol. 33, Nov. 1982, pp. 819-825.

99. LU, H. and CHIU, H.

Dynamics of gases containing evaporable liquid droplets under a normal shock.

AIAA Journal, vol. 4, N-. 6, 1966, pp. 1008-1011.

100. MORETTI, G.

The choice of a time-dependent technique in gas dynamics.

In, Numerical methods in fluid dynamics

AGARD-LS-48, May 1972.

101. GOPALAKRISHNAN, S.

Fundamentals of time-marching methods.

In, Transonic flows in turbomachinery, vol. I, Theory, part 1, VKI-LS-59, May 21-25, 1973.

102. YOSHIHARA, H.

Finite difference procedure for unsteady transonic flows: A review.

In, Flow problems in turbomachinery, Adamson, T. and Platzer, M., Hemisphere, Washington, 1977, p.139.

103. COUSTON, M.

Time marching finite area method.

VKI-LS-84, vol. I, Feb. 1976, p.43.

104. COURANT, R., FRIEDRICHS, K. and LEWY, H.
On the partial difference equations of mathematical physics.
IBM J., Vol. 11, No. 2, March 1967, pp. 215-234.

105. SPURR, A.
A computational and experimental study of fully three dimensional transonic flow in turbomachinery.
Ph.D. Thesis, University of Southampton, 1980.

106. HOLST, T.L.
The relative merits of several numerical techniques for solving the compressible Navier-Stokes equations.
In, Advances in Engineering Science, vol. 4, NASA-CP-2001, Nov., 1976, pp. 1467-81.

107. CROCCO, L.
A suggestion for the numerical solution of the steady Navier-Stokes equations.
AIAA J., Vol. 3, No.10, Oct. 1965, pp. 1824-32.

108. BENISON, G. and RUBIN, E.
A time-dependent analysis for quasi-one-dimensional, viscous, heat conducting, compressible Laval nozzle flow.
J. Eng. Math., Vol. 5, 1, Jan. 1971, pp. 39-49.

109. GRIFFIN, M. and ANDERSON, J.D. Jr.
On the application of boundary conditions to time-dependent computations for quasi one-dimensional fluid flows.
Computers and Fluids, vol. 5, No. 3, 1977, pp. 127-37.

110. DAMIA TORRES, J. and BAKER, R.C.
A time-marching, finite area calculation of general quasi-one-dimensional flows.
Computers and Fluids, Vol. 7, No. 3, Sept. 1979, pp. 177-190.

111. MERRYWEATHER, H.

The calculation of subsonic and supersonic flow in ducts.

Ph.D. Dissertation, Department of Engineering, Cambridge University, July, 1969.

112. GOPALAKRISHNAN, S.

Application of the time-dependent technique to turbomachinery cascades

In, Transonic Flows in Turbomachinery, part 1, Vol. I (Theory), VKI Lecture Series 59, Brussels, May 21-25, 1973.

113. CLINE, M.C.

The computation of two-dimensional, viscous nozzle flow.

(Back-up document for AIAA Synoptic schedule published in the AIAA J., Vol. 14, No. 3, March 1976, pp. 295-296), June 27, 1975, p.15.

114. CLINE, M.C.

Computation of steady nozzle flow by a time-dependent method.

AIAA J., Vol. 12, No. 4, April 1974, pp. 419-420.

115. BRUNELL, R.D.

Numerical solutions for compressible flow in planar converging-diverging ducts.

Ph.D. Thesis, University of Notre Dame, June 1970.

116. GOPALAKRISHNAN, S. and BOZZOLA, R.

A numerical technique for the calculation of transonic flows in turbomachinery cascades.

ASME Paper 71-GT-42, March 1971, p.9.

117. BRYCE, J.D. and LITCHFIELD, M.R.

Experience of Denton blade-to-blade time marching computer programs.

ARC, CP 1373, Sept. 1976, p.23.

118. DENTON, J.D.

Change of total pressure in time marching calculations.
Unpublished material, Central Electricity Generating Board, UK, Oct. 1976.

119. DENTON, J.D.

Improvements to time marching methods of flow calculation.
Marchwood Engineering Laboratories, Central Electricity Generating Board, UK, Memorandum MM/MECH/TG/27, March 1977.

120. SPURR, A.

A semi-implicit time marching method.
Marchwood Engineering Laboratories, Central Electricity Generating Board, UK., Memorandum MM/MECH/TF88, March 1978.

121. SINGH, U.K.

Computation of transonic flow in cascade with shock and boundary layer interaction.
In, Numerical methods in laminar and turbulent flows, Pentech, London, 1978, pp. 697-707.

122. SPURR, A.

Progress in the development of a time marching method for through-flow calculations.
Marchwood Engineering Laboratories, Central Electricity Generating Board, UK, Memorandum MM/MECH/TG/9, Sept. 1976.

123. SPURR, A.

The prediction of 3D transonic flow in turbomachinery using a combined throughflow and blade-to-blade time marching method.
Int. J. Heat and Fluid Flow, Vol. 2, No. 4, 1980, pp. 189-199.

124. SINGH, U.K.

A computation and comparison with measurements of transonic flow in an axial compressor stage with a shock and boundary layer interaction.

J. of Engng. for Power, Trans. ASME, Vol. 104, April 1982, pp. 510-515.

125. MITCHELL, N.A.

A time marching method for unsteady two-dimensional flow in a blade passage.

Int. J. Heat and Fluid Flow, Vol. 2, No. 4, 1980, pp. 205-220.

126. BOSMAN, C. and HIGHTON, J.

A calculation procedure for three-dimensional time-dependent, viscous, compressible flow through turbomachine blades of any geometry.

ARC 36969 Ae. Th. 40, Oct. 1976, p. 47.

127. BOSMAN, C. and HIGHTON, J.

A calculation procedure for three-dimensional, time-dependent, inviscid, compressible flow through turbomachine blades of any geometry.

J. Mech. Eng. Sc., Vol. 21, No.1, 1979, pp. 39-49.

128. OLIVER, D.A. and SPARIS, P.

A computational study of three-dimensional transonic shear flow in turbomachine cascades.

AIAA Paper 71-83, Jan. 1971, p.10.

129. GOPALAKRISHNAN, S. and BOZZOLA, R.

Numerical representation of inlet and exit boundary conditions in transient cascade flow.

ASME Paper 73-GT-55, April 1973, p.5.

130. VAN HOVE, W. and ARTS, A.
Comparison of several finite difference schemes for time marching methods as applied to one-dimensional nozzle flow.
VKI Technical Note 132, June 1979, p.45.

131. MORETTI, G.
Importance of boundary conditions in the numerical treatment of hyperbolic equations.
Phys. Fluids, Vol. 12, No. 12, part 2, Dec. 1969, pp. II-13 - II-20.

132. CHANG, I.
One- and two-phase nozzle flows.
AIAA J., Vol. 18, No.12, Dec. 1980, pp. 1455-61.

133. KOPCHENOV, V.I. and KRAIKO, A.N.
Solution of the direct problem of two-phase flow in a Laval nozzle within the scope of the two-fluid model.
Fluid Mechanics - Soviet Research, Vol. 6, No. 2, March 1977, pp. 16-30.

134. COMFORT, W., CROWE, C.T., ALGER, T. and GIEDT, W.
Calculation of two-phase dispersed droplet-in-vapour flows including normal shock waves.
ASME Paper 76-WA/FE-31, 1977.

135. COMFORT III, W. and CROWE, C.T.
Dependence of shock characteristics on droplet size in supersonic two-phase mixtures.
J. of Fluids Engng., Trans. ASME, Vol. 102, March 1980, pp. 54-58.

136. SNOECK, J.
Calculation of mixed flows with condensation in one dimensional nozzles.
In, Aero-Thermodynamics of Steam Turbines, ASME Book No. H00203,

136. continued

presented at The Winter Annual Meeting of the ASME, Washington, D.C., Nov. 15-20, 1981.

137. MOHEBAN, M.

Private communication.

Cambridge University Engineering Department, 1982.

138. WUNDT, H.

On the structure of consistent equation sets to describe multi-phase flow.

Euratom symp. on Two-Phase Flow Dynamics, Eindhoven, September 1967.

139. CROWE, C.T.

Conservation equations for vapour-droplet flows.

Proceedings of 1976 Heat Transfer and Fluid Mechanics Institute.

140. MIGDAL, D. and AGOSTA, V.D.

A source flow model for continuum gas-particle flow.

J. Applied Mech., Trans. ASME, Dec. 1967, p.860.

141. ANDERSON, T. and JACKSON, R.

A fluid mechanical description of fluidized beds.

I and EC Fundamentals, Vol. 6, 4, Nov. 1967.

142. MURRAY, J.D.

On the mathematics of fluidization, Part 1 : Fundamental equations and wave propogation.

J. Fluid Mech., Vol. 21, part 3, 1965.

143. VAN DEEMTER, J. and VAN DER LAAN, E.

Momentum and energy balances for dispersed two-phase flow.

Appl. Sci. Res., Section A, Vol. 10, 1960, p.102.

144. HINZE, J.

Momentum and mechanical-energy balance equations for a flowing homogeneous suspension with slip between the two phases.

Appl. Sci. Res., Section A, Vol. 11, 1962.

145. CROWE, C.T.

On dispersed phase flow equations.

In, Two-Phase Momentum, Heat and Mass Transfer

In Chemical, Process, and Energy Engineering Systems.

By Durst, F., Tsilklauri, G. and Afgan, N. volume 1, Hemisphere, 1979.

146. SHAPIRO, A.H.

The dynamics and thermodynamics of compressible fluid flow.

Volumes 1 and 2.

Ronald Press Company, New York, 1954.

147. BAUM, M.R.

A study of gas-solids flows with special reference to convergent-divergent nozzles.

Ph.D. Thesis, University of Leeds, 1968.

148. WHITE, F.M.

Viscous fluid flow.

McGraw Hill, New York, 1974.

149. MacCORMACK, R.W. and WARMING, R.F.

Survey of computational methods for three-dimensional supersonic inviscid flows with shocks.

AGARD-LS-64, Paper 5, February, 1973, p.20.

150. KREYSZIG, E.

Advanced engineering mathematics.

Wiley International Edition, third edition, 1972.

151. DAMIA-TORRES, J.

Private communication.

Mechanical Engineering Department, Imperial College, 1981.

152. DENTON, J.D.

Private communication.

Wittle Laboratories, Cambridge University.

153. OKUDA, S. and CHOI, W.S.

Gas-particle mixture flow in various types of convergent-divergent nozzle.

J. Chemical Eng. of Japan, Vol. 11, N.6, 1978.

154. OW, C.S.

Studies of two-phase turbulent pipe flow.

Ph.D. Thesis, Imperial College, Mechanical Engineering Department, 1980.

155. FARWAGI, S.

Private Communication.

Imperial College, Mechanical Engineering Department, 1982.

156. WARDA, H.A.

A study of gas-solids flow in supersonic nozzles.

Ph.D. Thesis, University of Leeds, 1975.

157. KRAMER, T.J.

A study of the mean flow characteristics of gas-solid suspensions flowing in vertical tubes.

Ph.D. Thesis, University of Washington, 1970.

158. KRAMER, T.J. and DEPEW, C.A.

Experimentally determined mean flow characteristics of gas-solid suspensions.

ASME Paper 72-FE-29, 1972.

159. WAKSTEIN, S.C.

The motion of small particles suspended in turbulent air flow in a vertical pipe.

Ph.D. Thesis, Queen Mary College, London, 1966.

160. DURST, F.

Review - combined measurements of particle velocities, size distribution, and concentrations.

J. Fluids Eng. ASME, Vol. 104, Sept. 1982.

161. DUCKWORTH, R.A.

A review of research in the United Kingdom in the field of multiple flows of solids and gases.

In, Ref. 37, pp. 33-42.

162. DUSSOURD, J.L. and SHAPIRO, A.H.

A deceleration probe for measuring stagnation pressure and velocity of a particle-laden gas stream.

Jet Propulsion, vol. 28, 1958.

163. FARBAR, L.

Metering of powdered solids in gas-solids mixtures.

Industrial and Engineering Chemistry, Vol. 44, N.12, Dec. 1952, p.2947.

164. WAKSTEIN, S.C.

The behaviour of particles in a turbulent flowing fluid.

Progress Report No. 2, Queen Mary College, London, 1961.

165 - CRANE, R.I., FARWAGI, S.M. and WILLIAMS, J.J.E.
Numerical modelling of deposition from vertical turbulent gas flow.
Paper D1, International Conference on the Physical Modelling of Multi-Phase Flow, Coventry, U.K., April 19-21, 1983.

166 - WILLIAMS, J.J.E. and CRANE, R.I.
Particle collision rate in turbulent flow.
Int. J. Multiphase Flow, Vol. 9, No. 4, pp. 421 - 435, 1983.

167 - DELICHATSIOS, M.A. and PROBSTEIN, R.F.
Coagulation in turbulent flow: theory and experiment.
J. Colloid Interface Sci. 51, 1974, pp.394 - 405.

TABLE 3.1

REFERENCE VALUES

Variable	Reference Value
Length	L_r
Temperature	T_r
Pressure	P_r
Velocity	$U_r = (\gamma R T_r)^{\frac{1}{2}}$
Energy	$c_v T_r$
Enthalpy	$c_p T_r$
Time	L_r/U_r
Density	$\rho_r = P_r/R_g T_r$
Reynolds number	$Re_r = \rho_r U_r L_r/\mu_r$
Viscosity	$\mu_r = \mu_r(T_r)$
Thermal conductivity	$k_r = k_r(T_r)$
Drag force	$L_r^2 \rho_r U_r^2$
Wall heat flux	$k_r T_r/L_r$
Particle heat transfer	$L_r k_r T_r$
Number of particles	$(\rho_r L_r^3)^{-1}$

TABLE 5.1

EFFECTS OF B_1 AND B_2 ON THE CONVERGENCE RATE

Time step based on the minimum CFL condition		Spatially varied time step	
B_1	Number of time steps for convergence	B_2	Number of time steps for convergence
0.25	1600	0.25	1300
0.50	1000	0.50	700
0.70	700	0.70	600
0.80	700	0.80	600
0.90	No convergence	0.90	Unstable

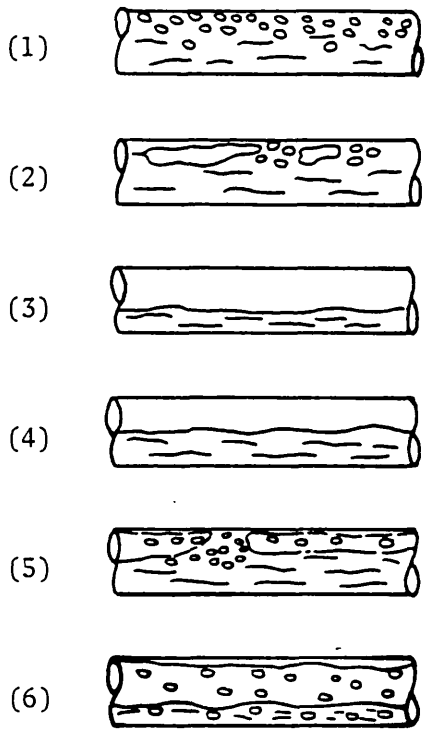
TABLE 7.1

PROFILE OF THE EXPERIMENTAL NOZZLE

(see Fig. 7.2)

x	y	x	y
0.0	38.7	180	19.24
10.0	38.7	190	19.05
20.0	38.7	200	19.24
30.0	37.68	210	19.79
40.0	36.37	220	20.68
50.0	35.05	230	21.87
60.0	33.73	240	23.31
70.0	32.41	250	24.96
80.0	31.10	260	26.77
90.0	29.78	270	28.73
100.0	28.46	280	30.79
110.0	27.15	290	32.95
120.0	25.83	300	35.17
130.0	24.51	310	37.46
140.0	23.31	320	38.70
150.0	21.87	330	38.70
160.0	20.68	340	38.70
170.0	19.79		

(All dimensions are in mm)



(1) Bubbly flow, (2) Plug flow,

(3) Stratified flow, (4) Wavy flow,

(5) Slug flow, (6) Annular flow

Fig. 1.1: Flow patterns in a horizontal pipe (from Ref. 1.)

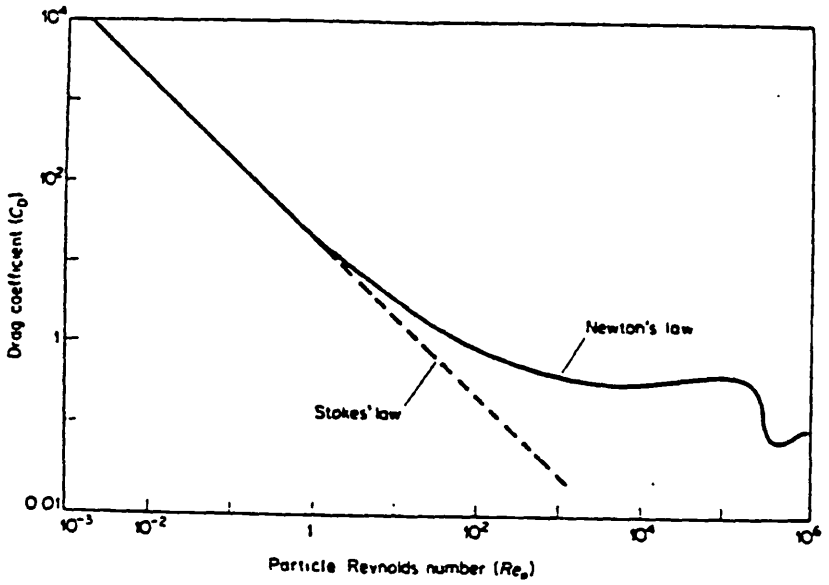


Fig. 2.1: Drag coefficient/Reynolds number relationship for spherical particle moving at uniform relative velocity (ref. 53)

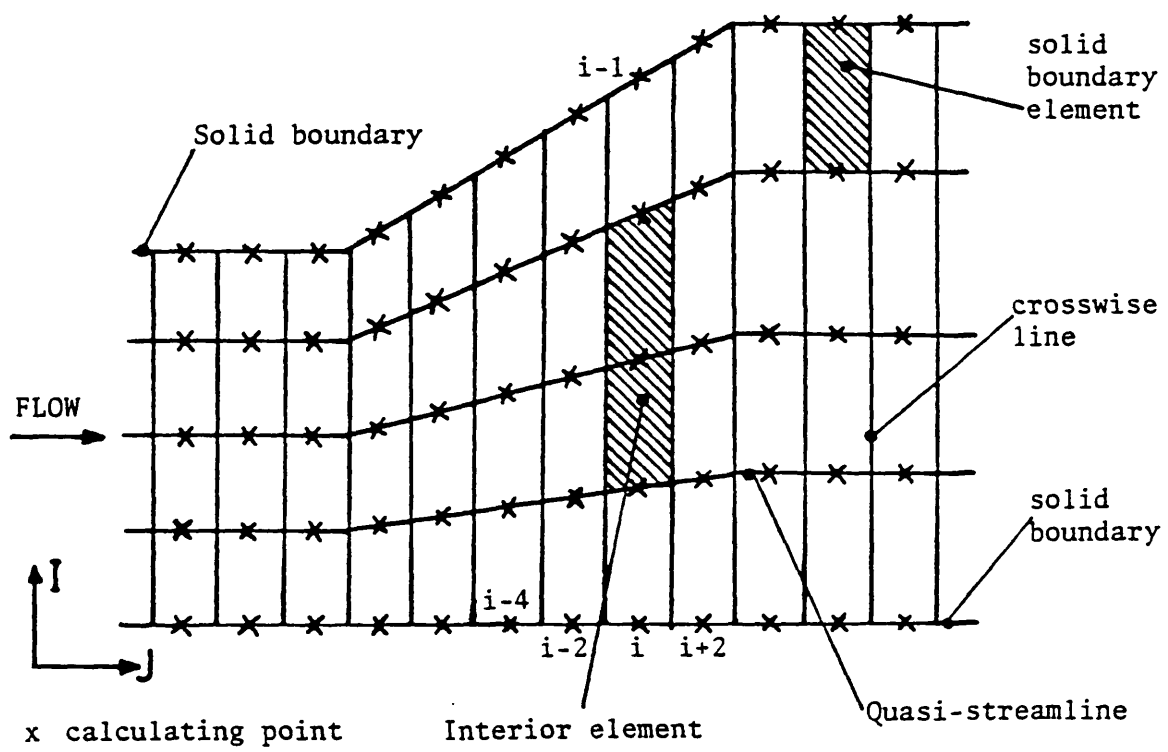


Fig. 2.2: Grid used in Denton's time-marching method

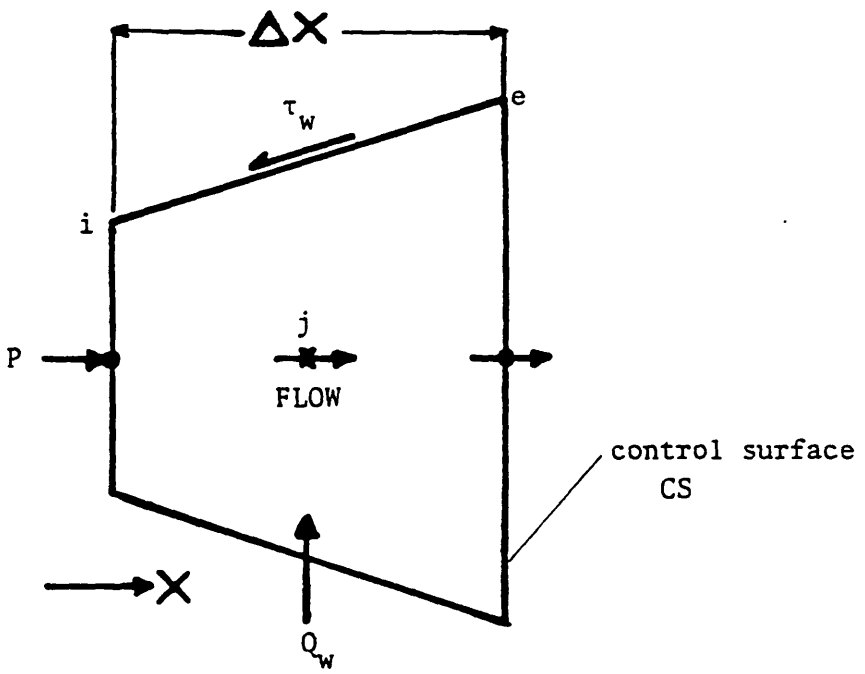


Fig. 3.1: Flow cell for one-dimensional flow

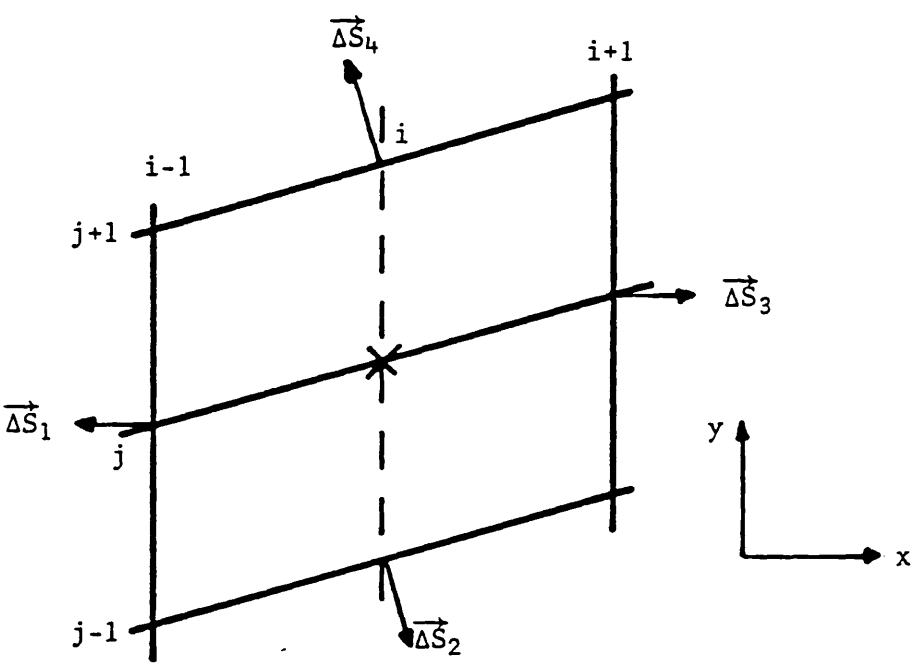


Fig. 3.2: Flow cell showing flow area vectors

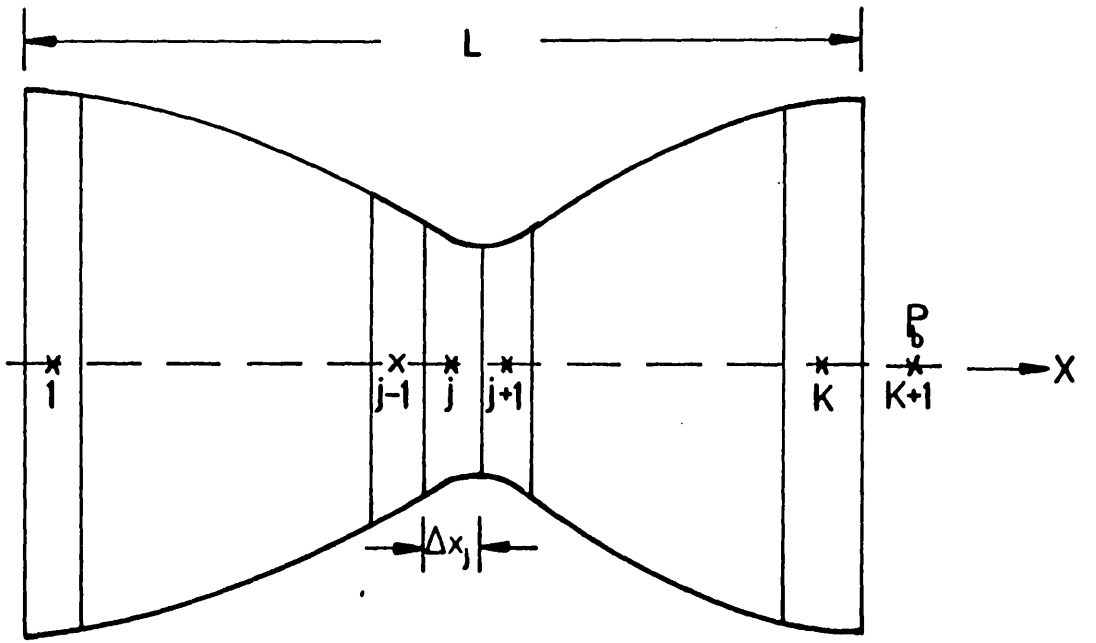


Fig. 4.1: Mesh for the one-dimensional model

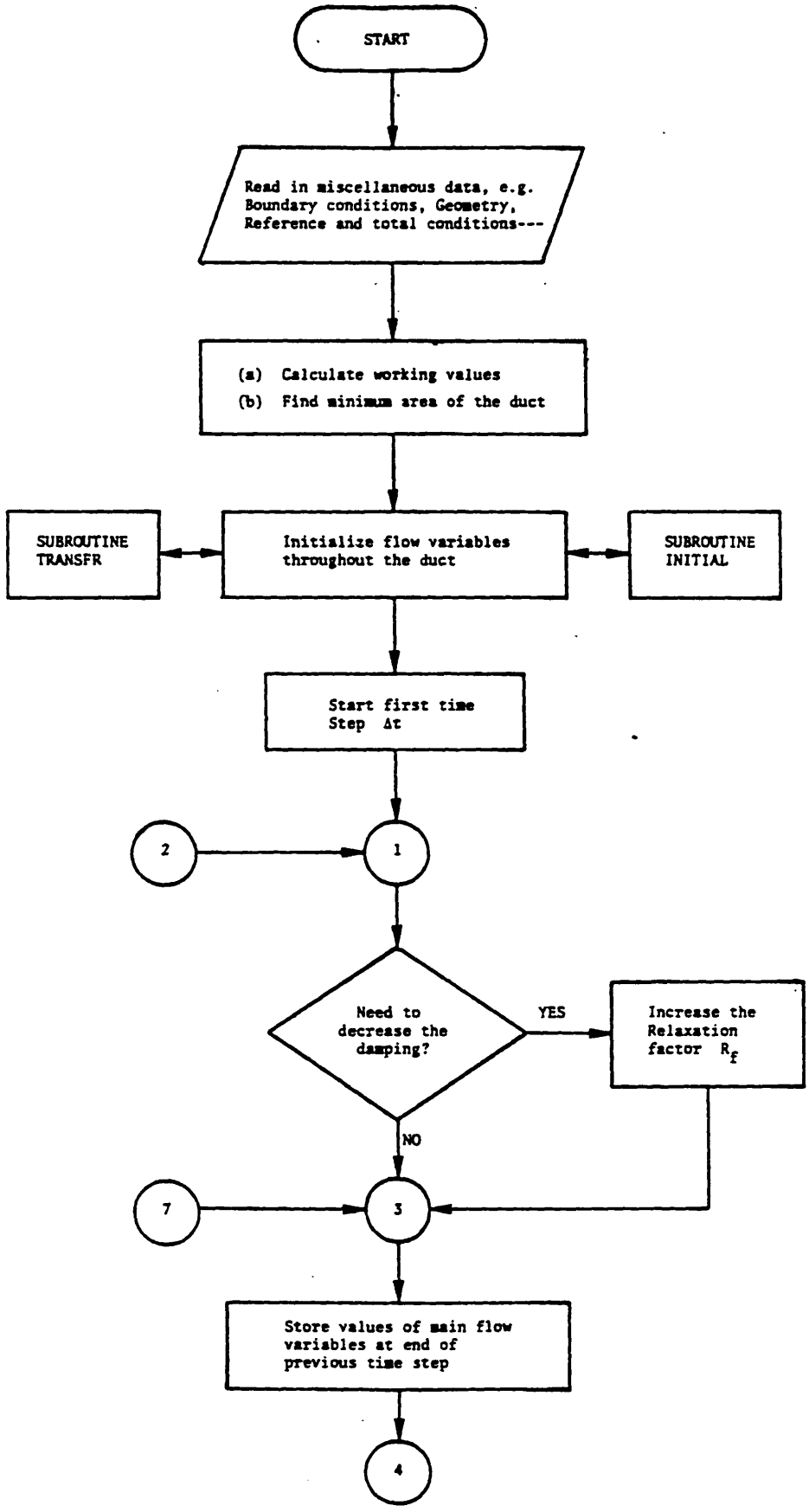


Fig. 4.2: Flowchart for the one-dimensional, two-phase flow, time-marching model

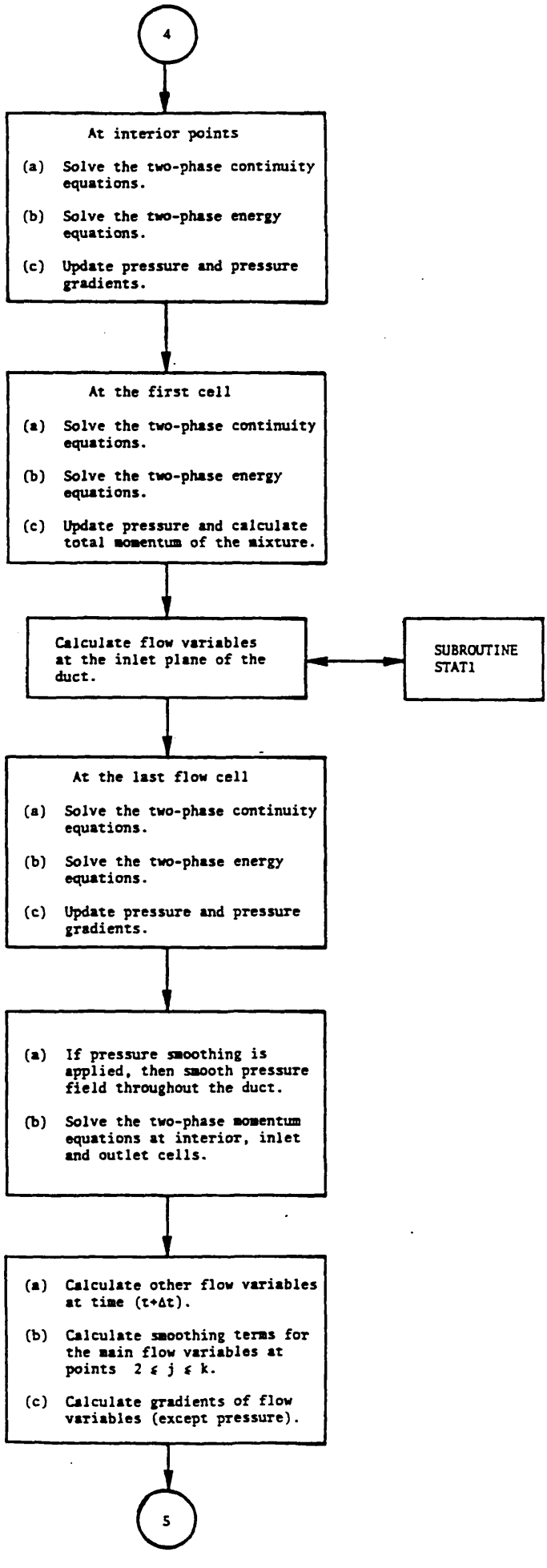


Fig. 4.2: Continued

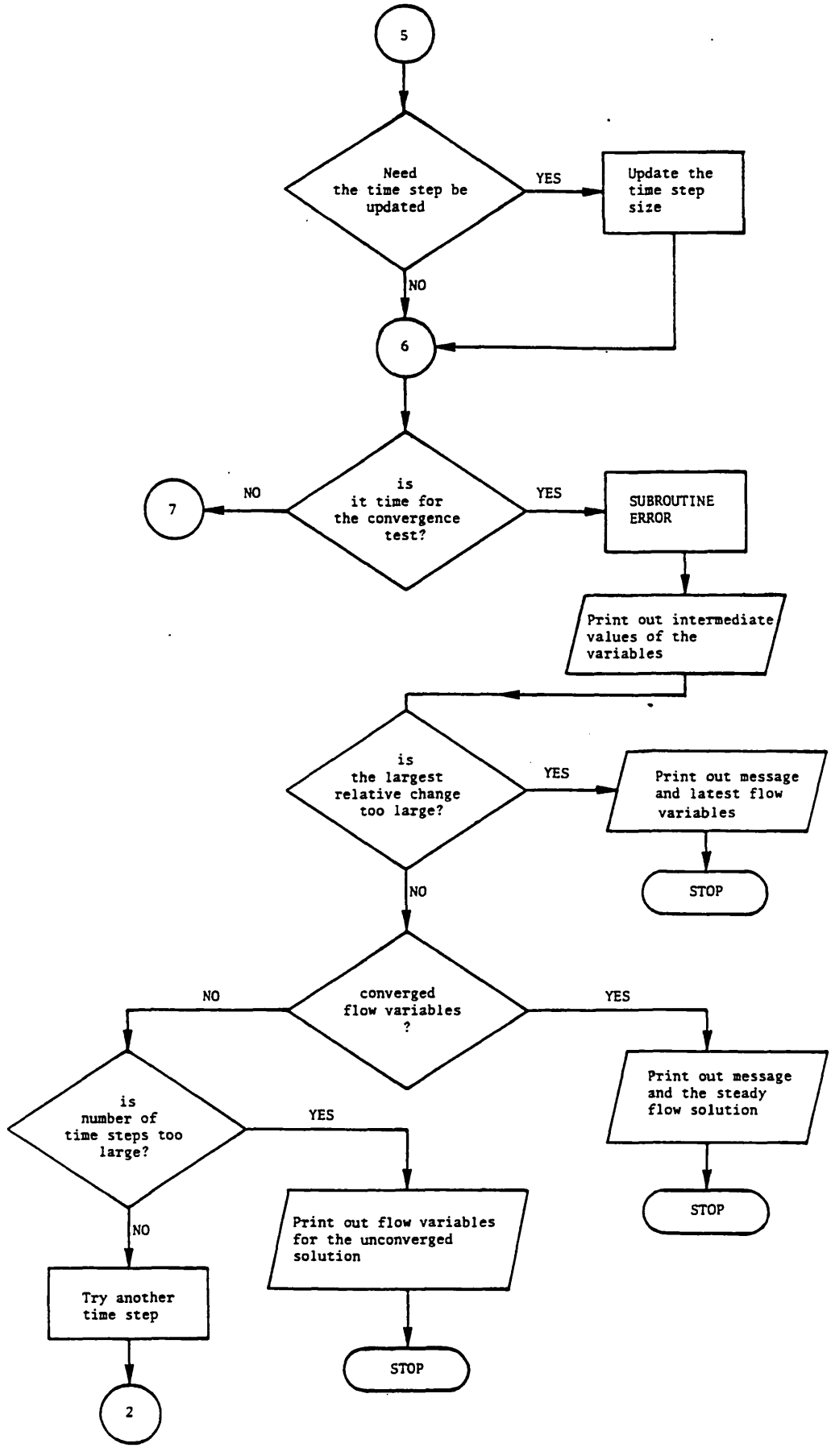


Fig. 4.2: Continued

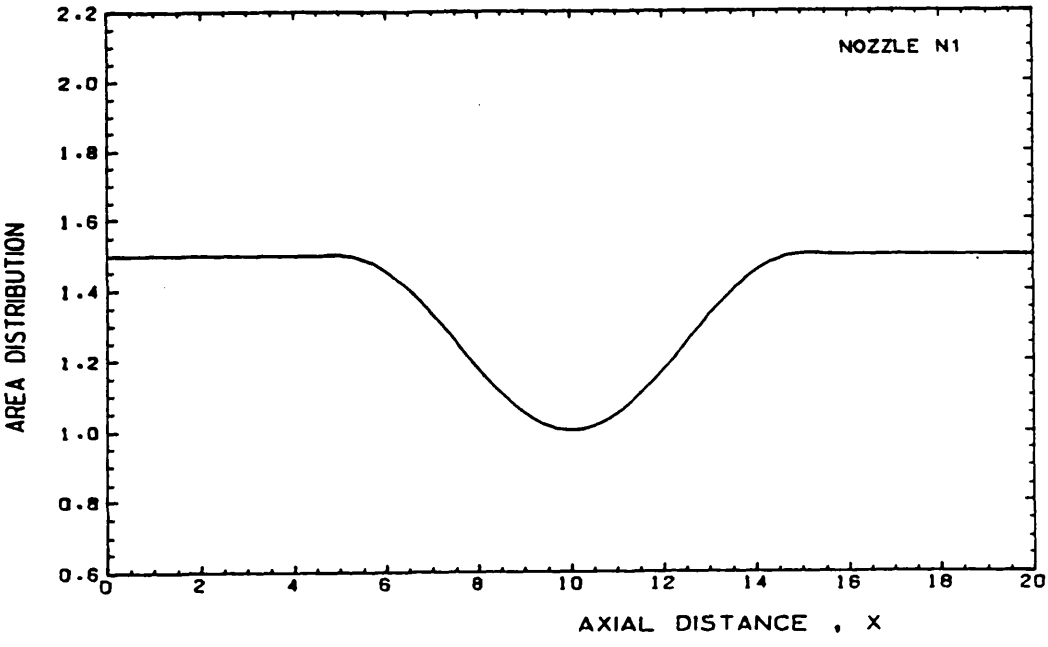


Fig. 5.1: Area distribution for nozzle N1

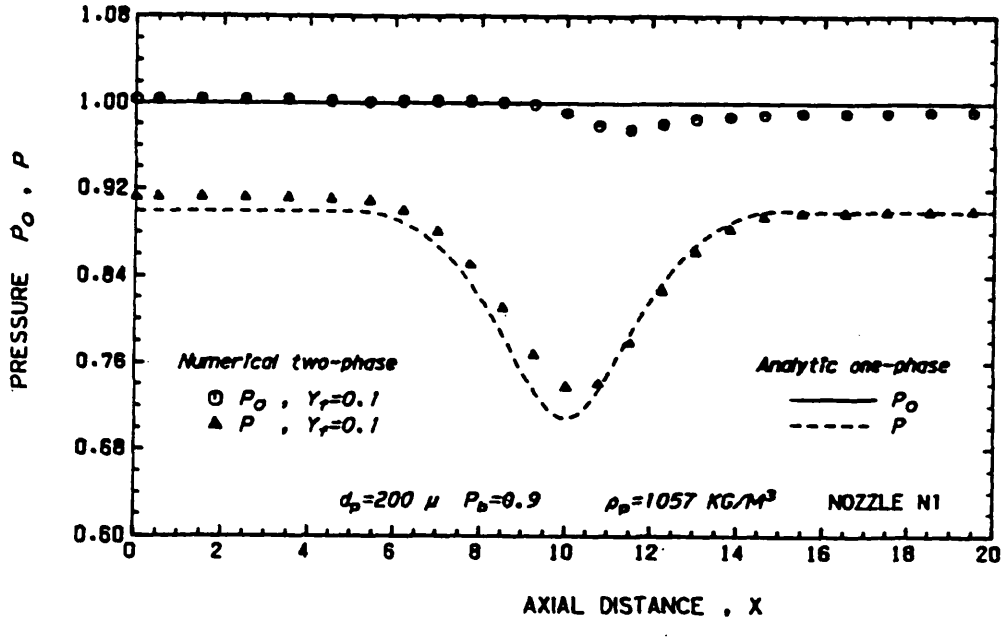


Fig. 5.2: Pressure distribution for fully subsonic mixture flow with Y_{fi} = 10%

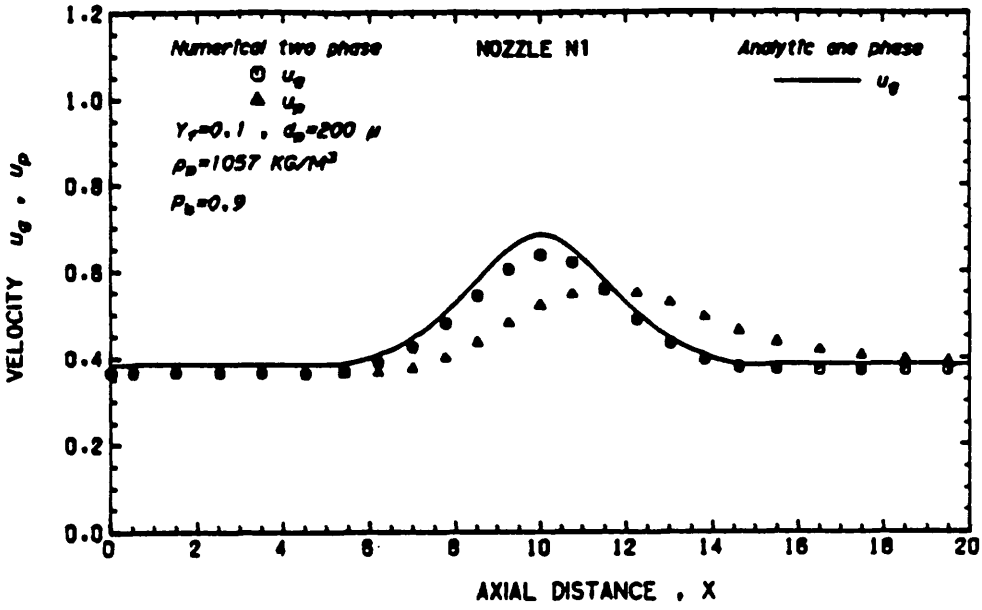


Fig. 5.3: Gas-phase and particle velocities for subsonic mixture flow with Y_{fi} = 10%

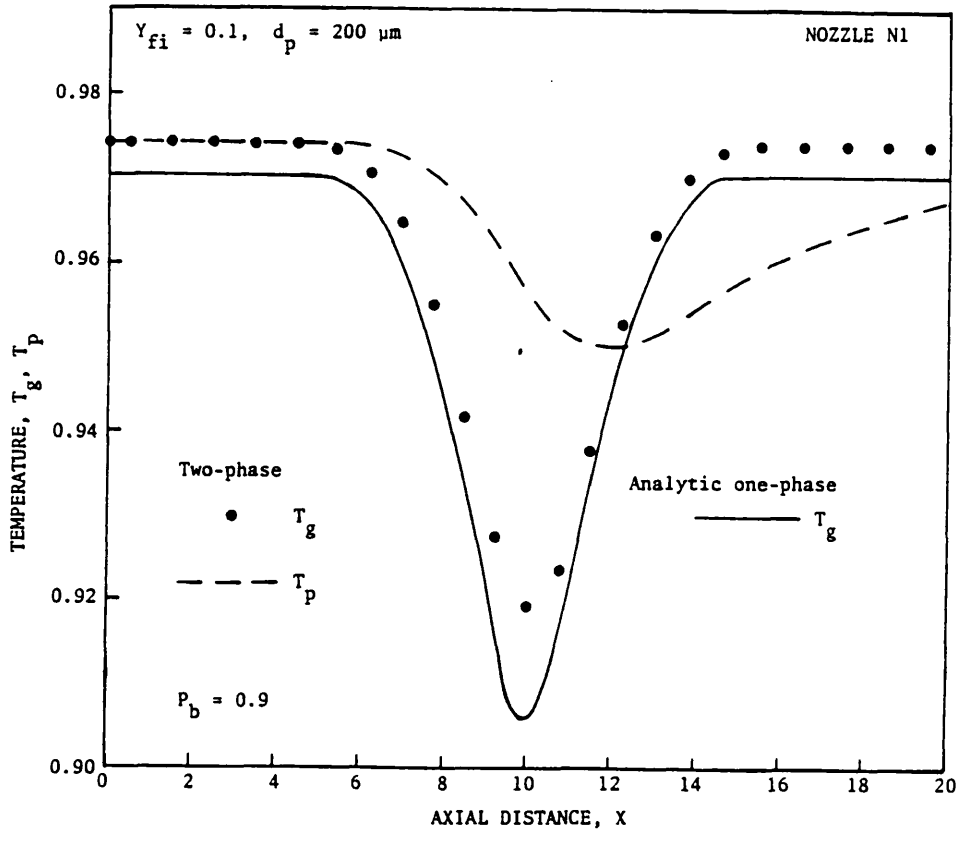


Fig. 5.4: Gas-phase and particle temperatures for fully subsonic flow with Y_{fi} = 10%

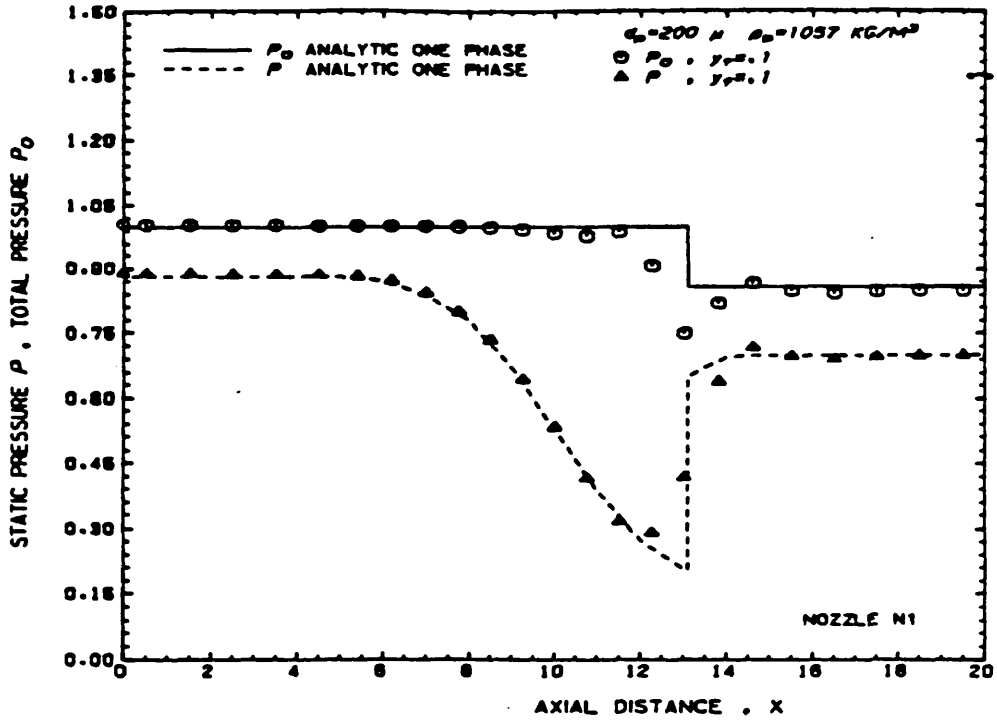


Fig. 5.5: Pressure distribution for shocked mixture flow with Y_{fi} = 10%

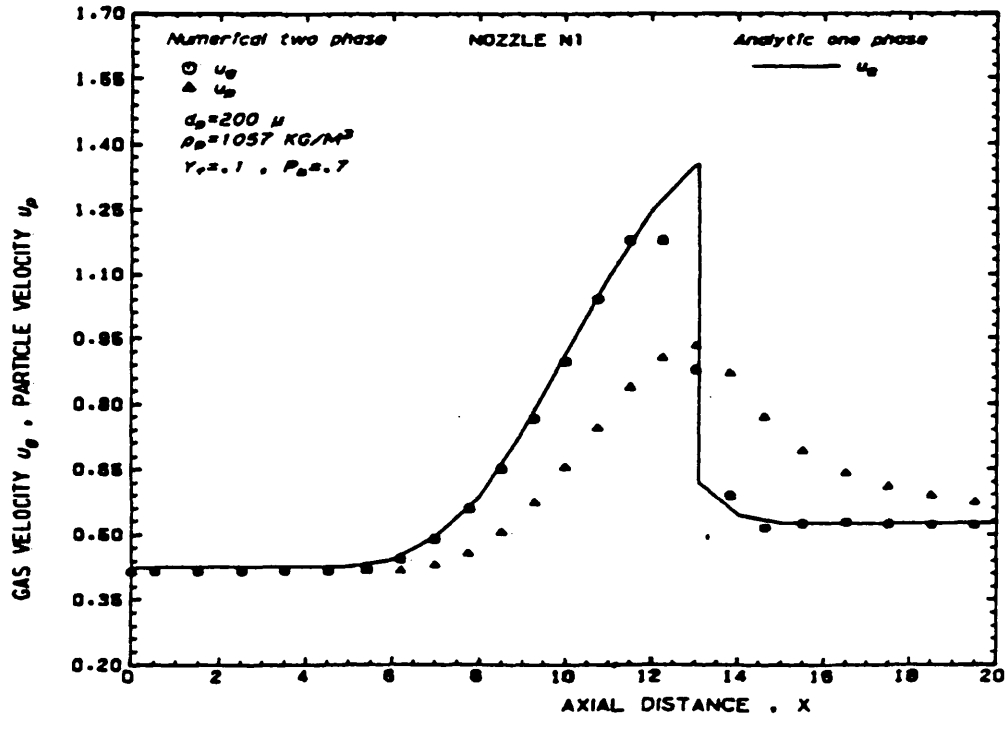


Fig. 5.6: Gas and particle velocities for shocked mixture flow with Y_{fi} = 10%

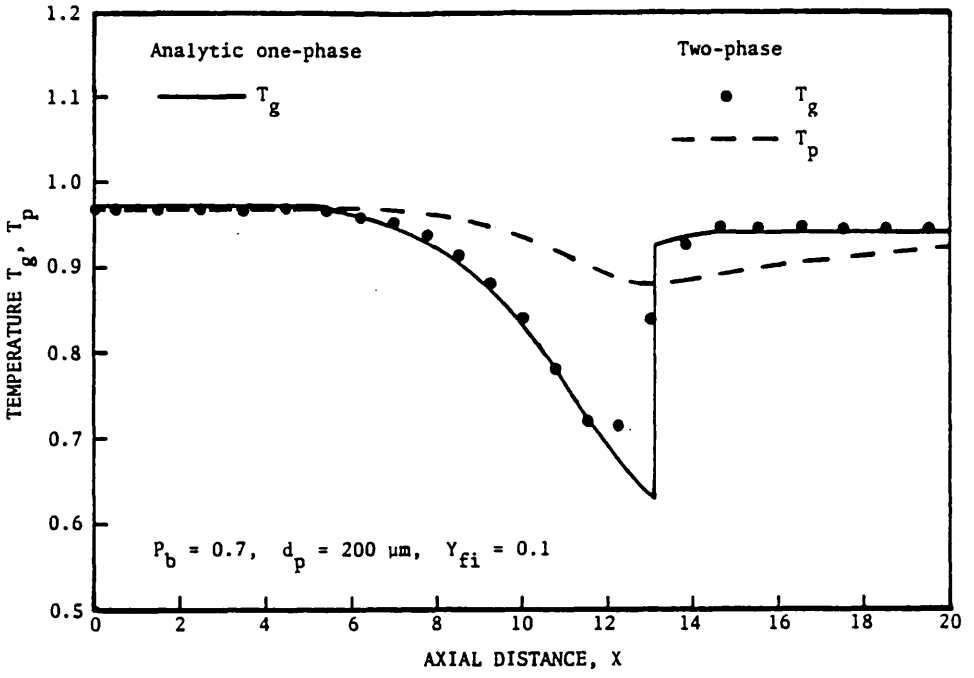


Fig. 5.7: Gas and particle temperatures for shocked mixture flow with Y_{fi} = 10%

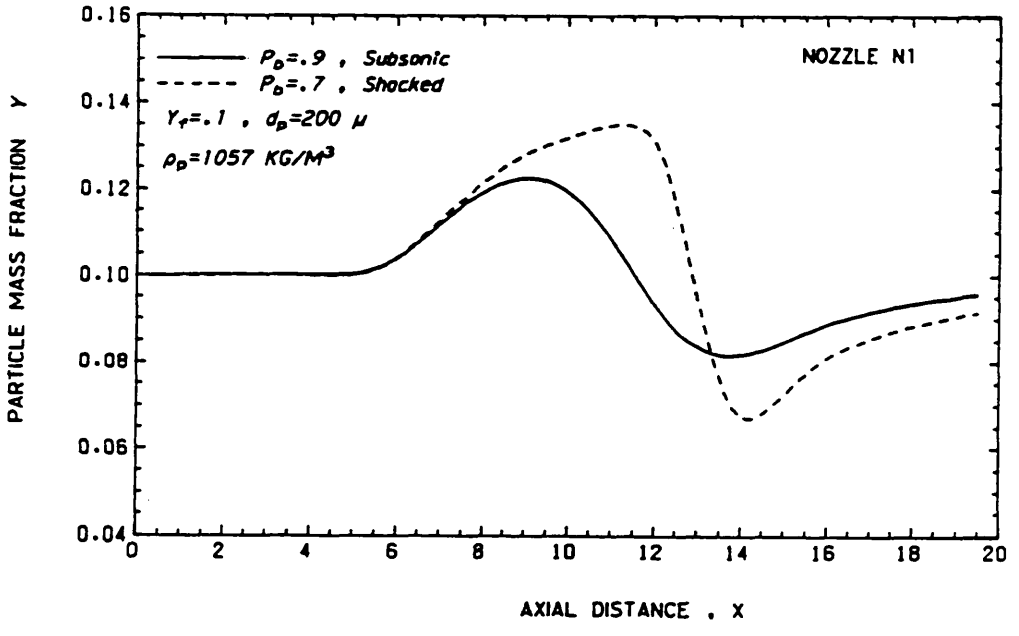


Fig. 5.8: Particle mass fraction distribution for subsonic and shocked mixture flow with Y_{fi} = 10%

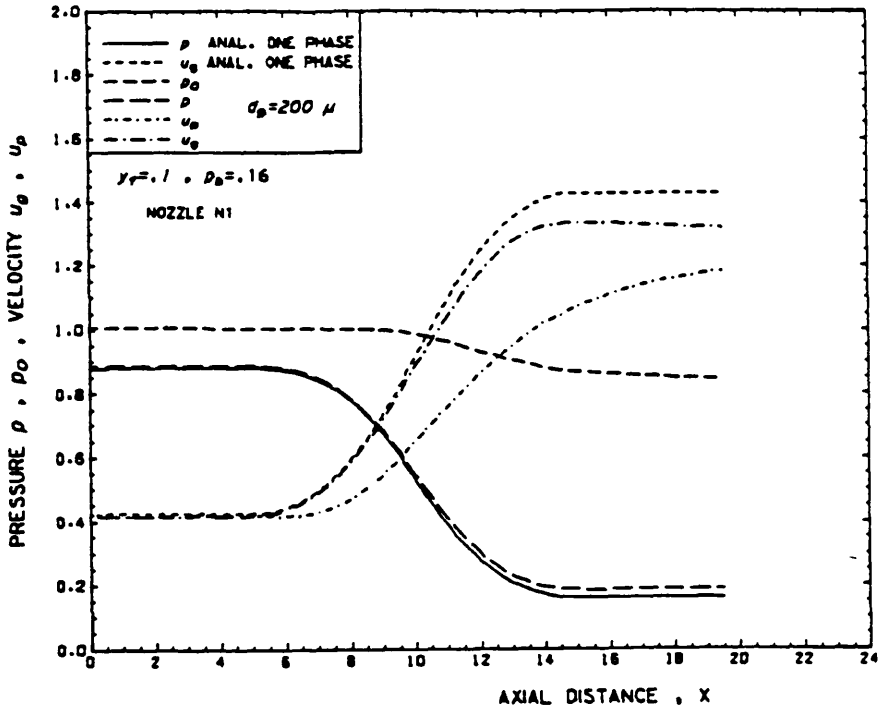


Fig. 5.9: Supersonic gas-particle flow in nozzle N1 (Y_{fi} = 10%)

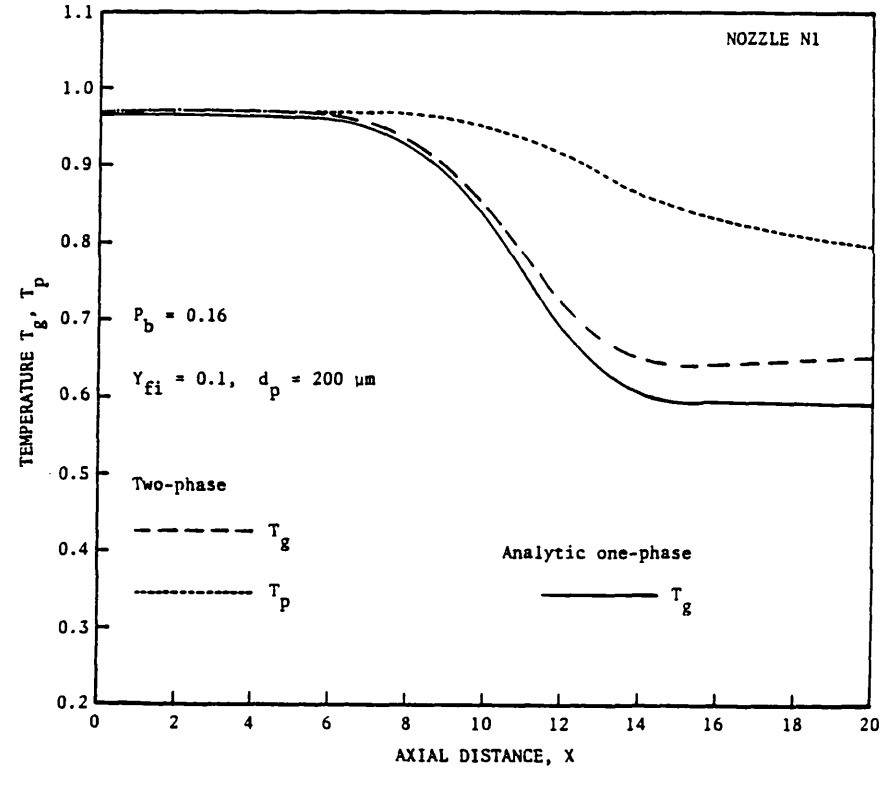


Fig. 5.10: Gas and particle temperatures for supersonic mixture flow with Y_{fi} = 10%

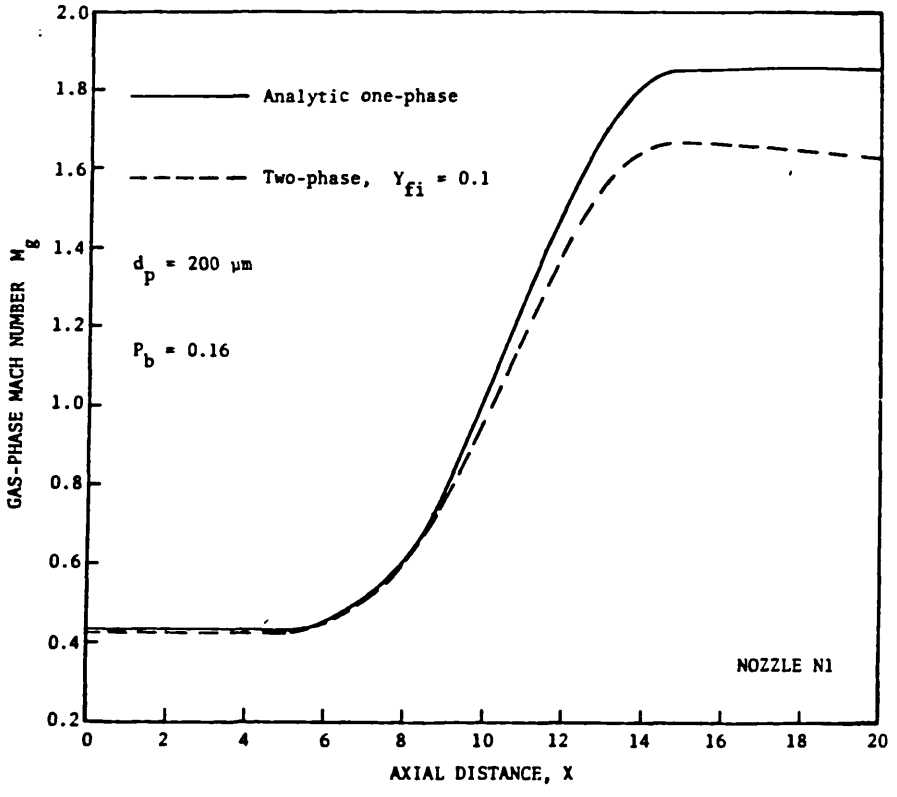


Fig. 5.11: Gas-phase Mach number distribution for supersonic mixture flow with Y_{fi} = 10%

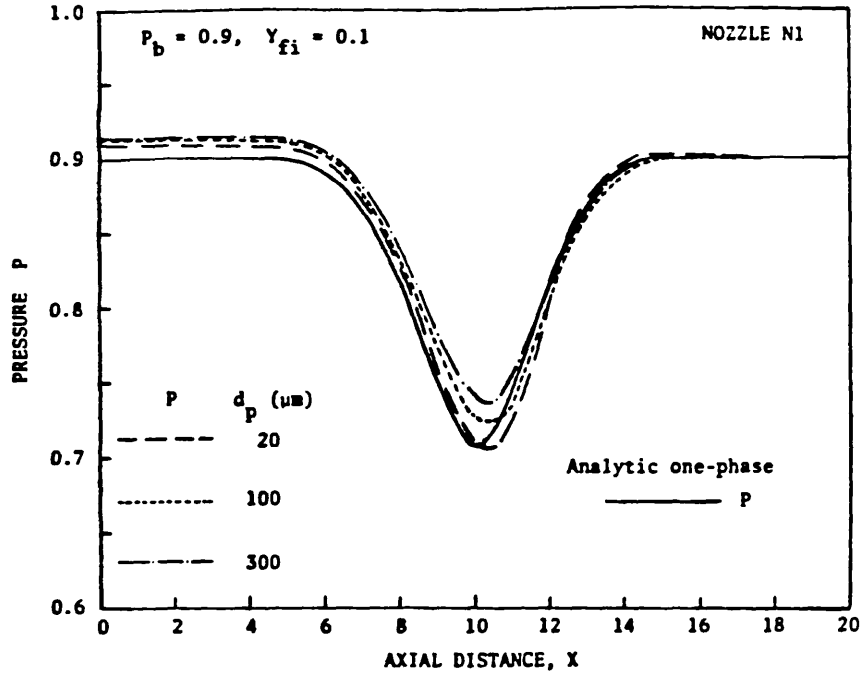


Fig. 5.12: Pressure distribution for various particle sizes for subsonic mixture flow in nozzle N1

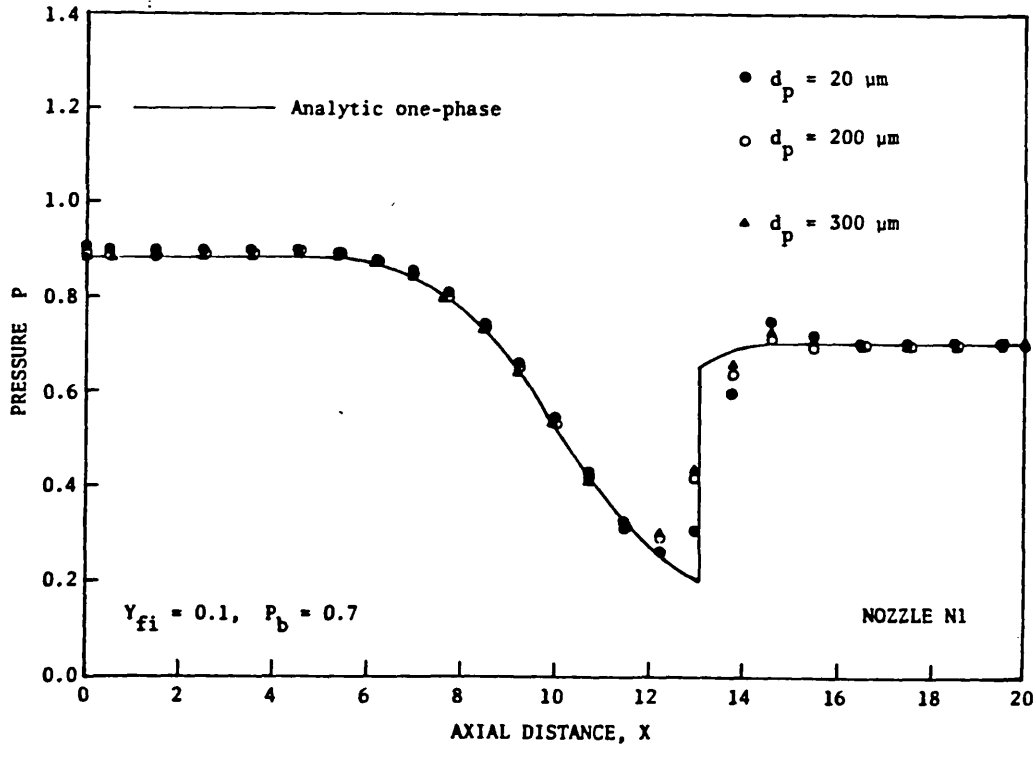


Fig. 5.13: Pressure distribution for various particle sizes for shocked mixture flow in nozzle N1

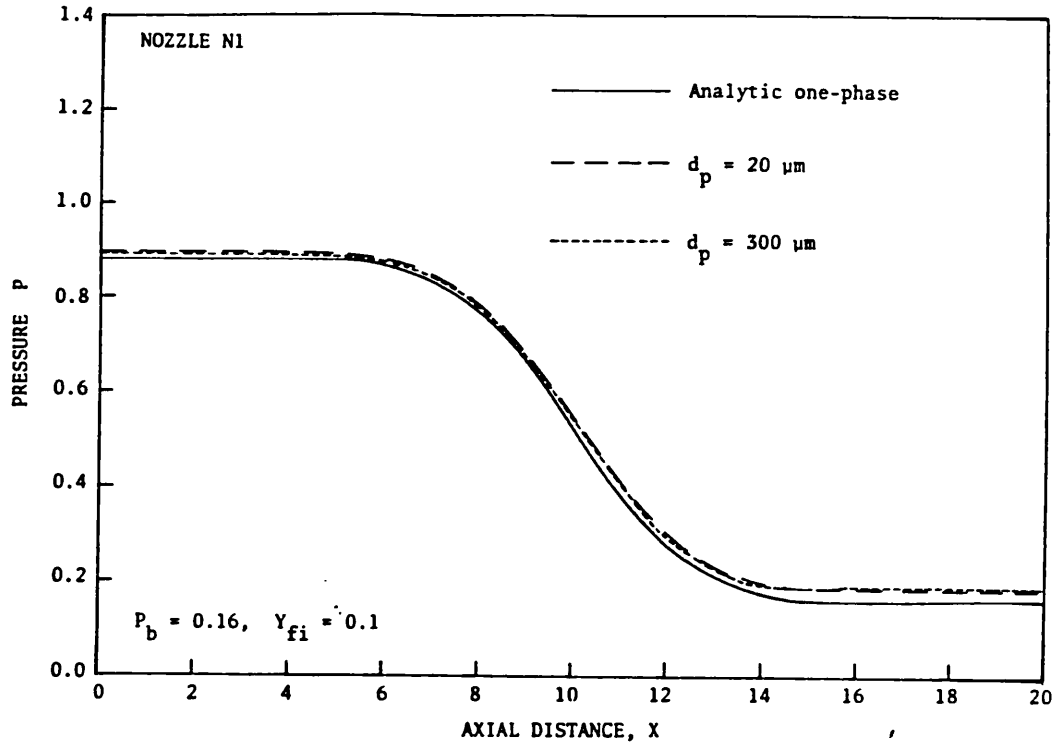


Fig. 5.14: Pressure distribution for various particle sizes for supersonic mixture flow in nozzle N1

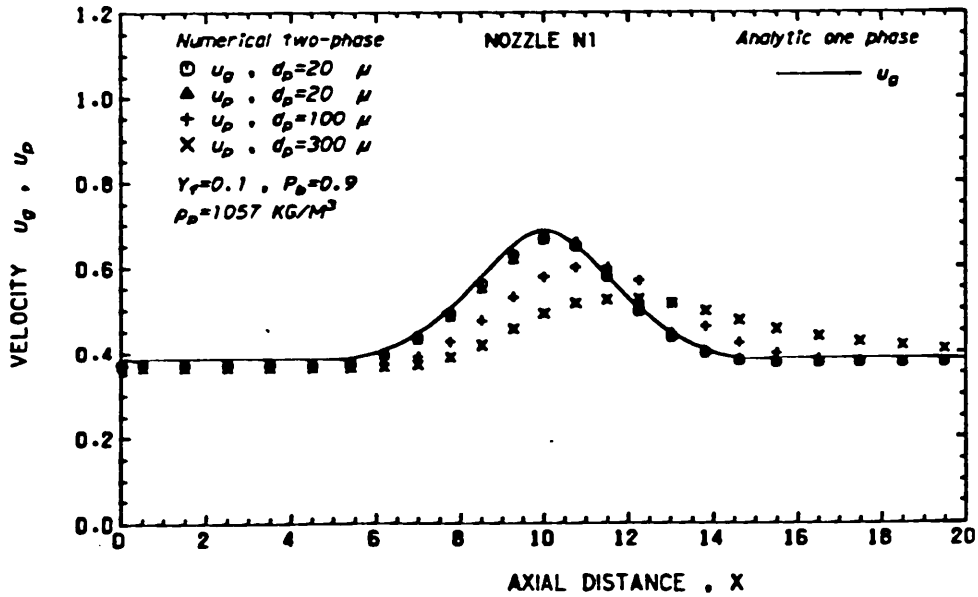


Fig. 5.15: Effects of particle size on its velocity in a fully subsonic flow in nozzle N1

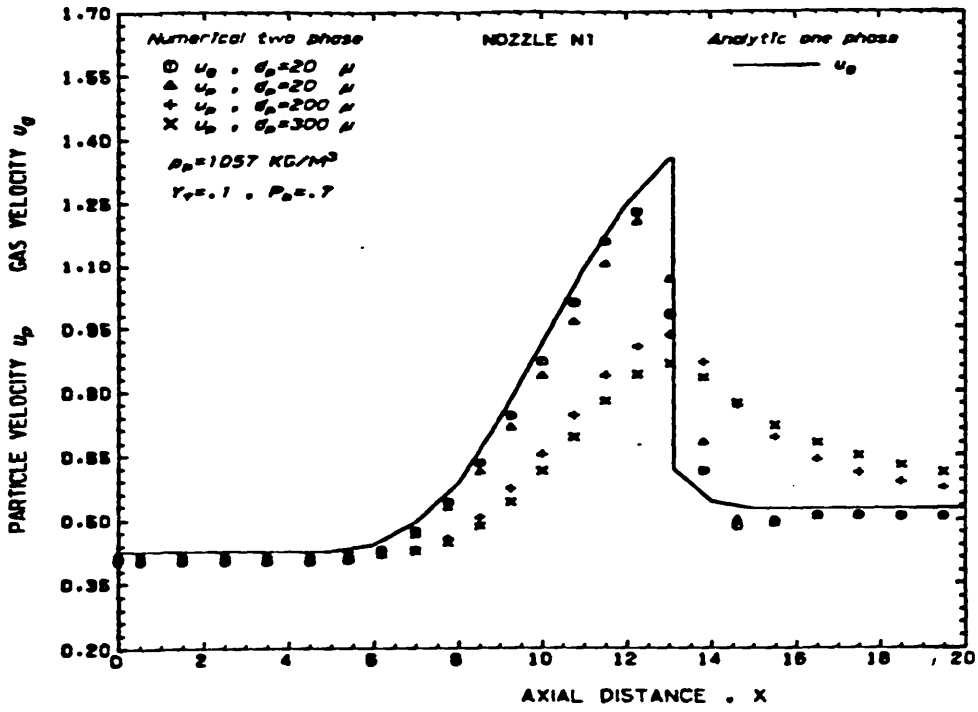


Fig. 5.16: Effects of particle size on its velocity in shocked mixture flow in nozzle N1

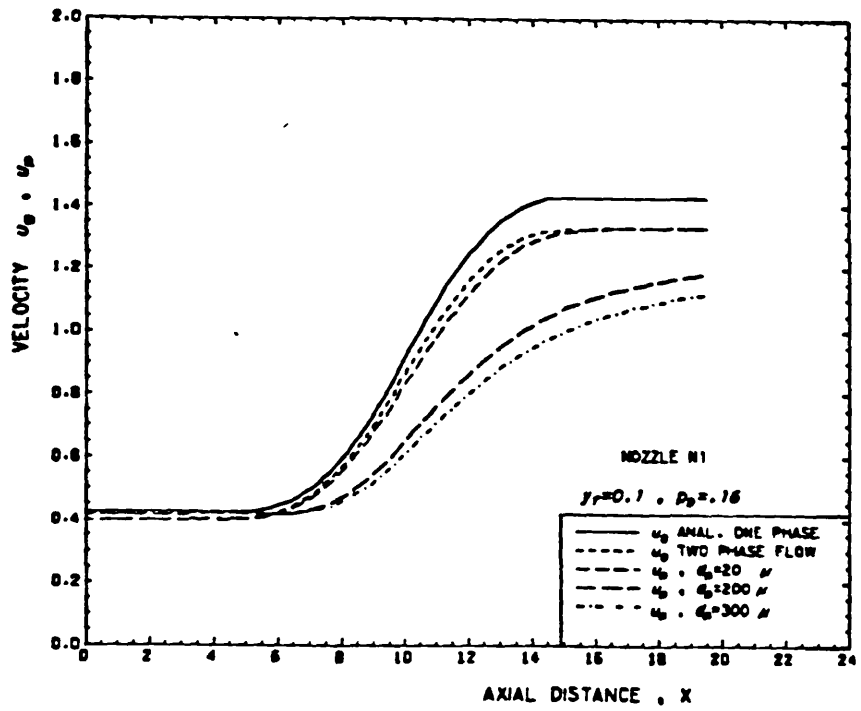


Fig. 5.17: Dispersed phase velocity for various particle sizes for supersonic mixture flow in nozzle N1

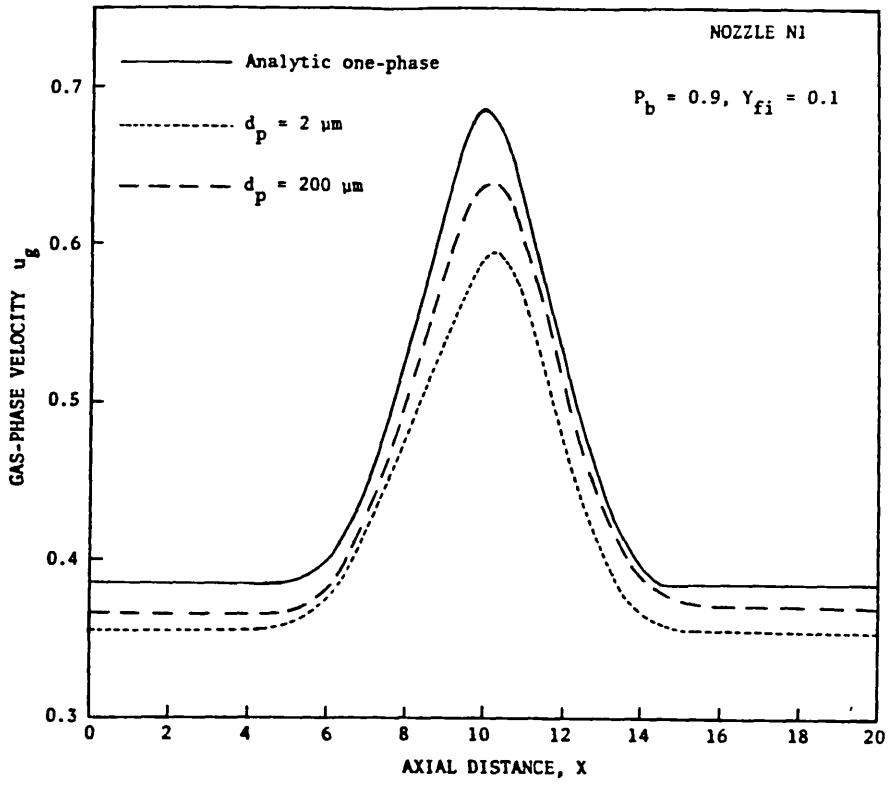


Fig. 5.18: Particle size effects on the gas velocity in a fully subsonic mixture flow in nozzle N1

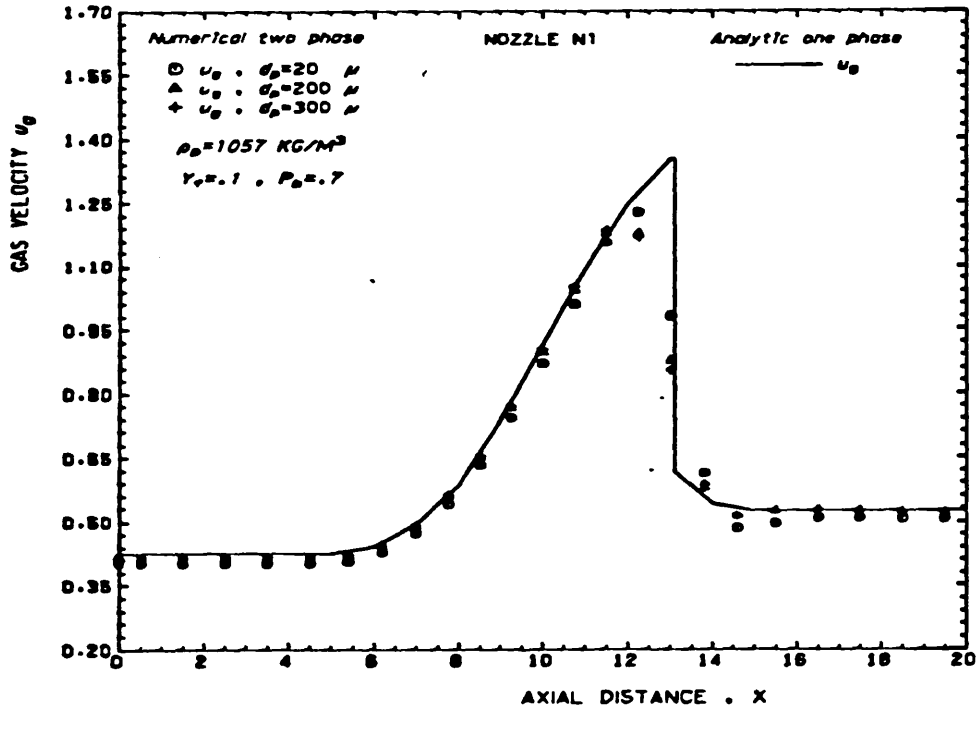


Fig. 5.19: Particle size effects on the gas velocity in shocked mixture flow in nozzle N1

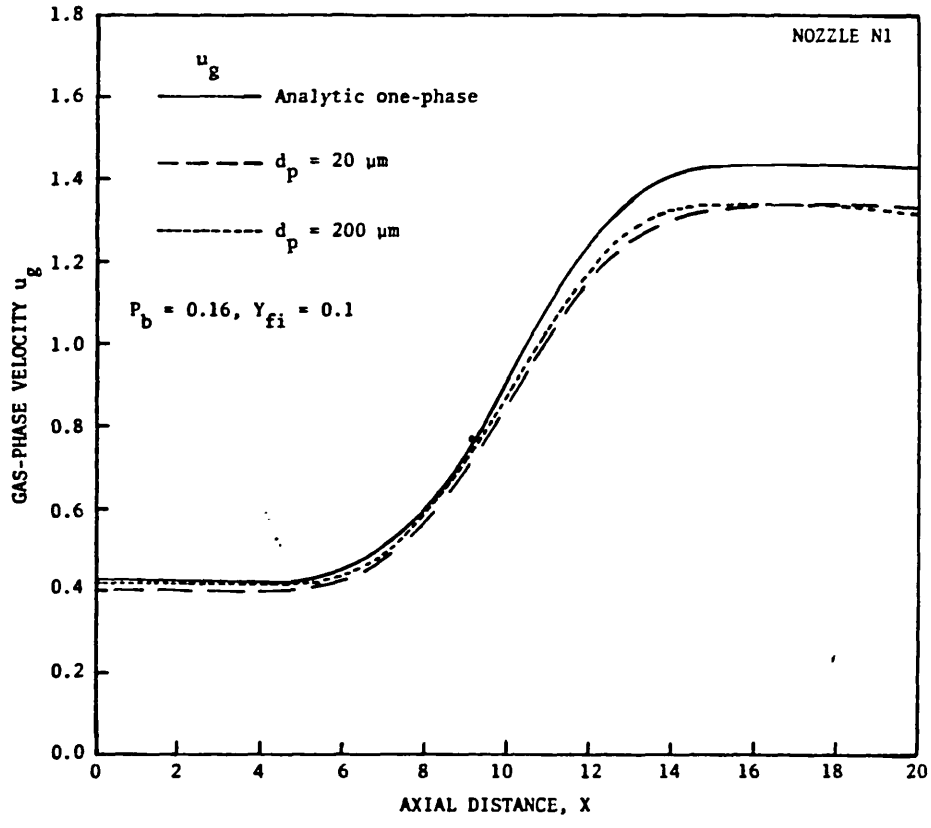


Fig. 5.20: Gas-phase velocity for various particle sizes for supersonic mixture flow in nozzle N1

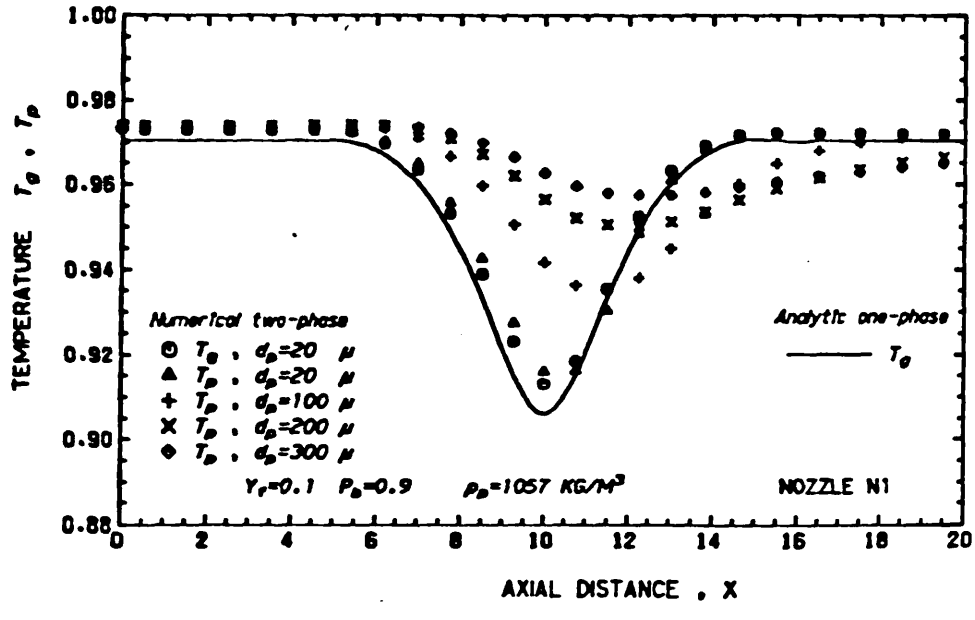


Fig. 5.21: Particle temperature for different particle sizes for a fully subsonic mixture flow in nozzle N1

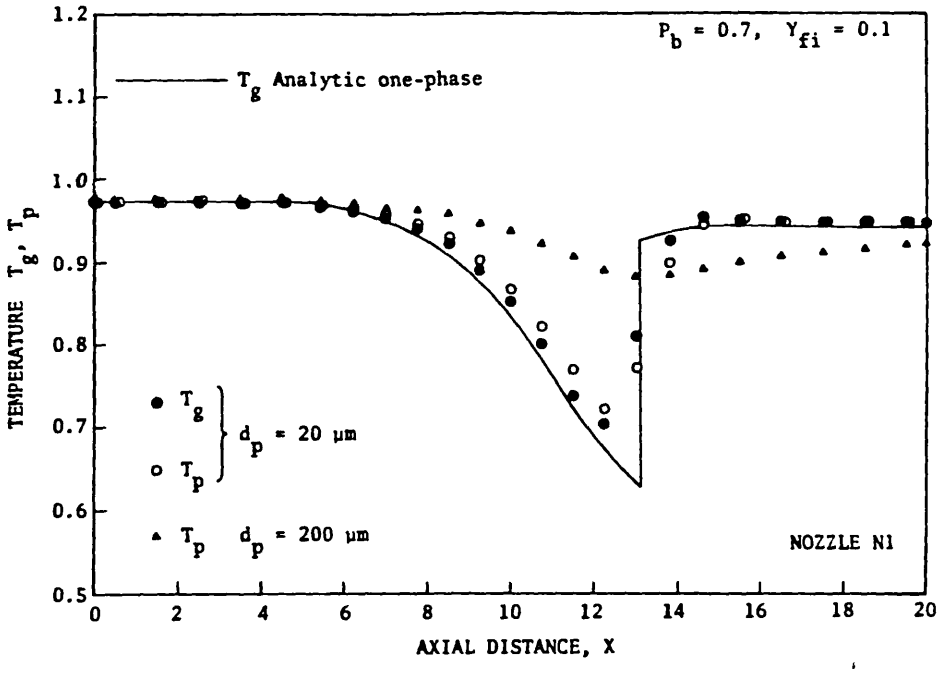


Fig. 5.22 Particle size effects on the particle temperature in shocked mixture flow in nozzle N1

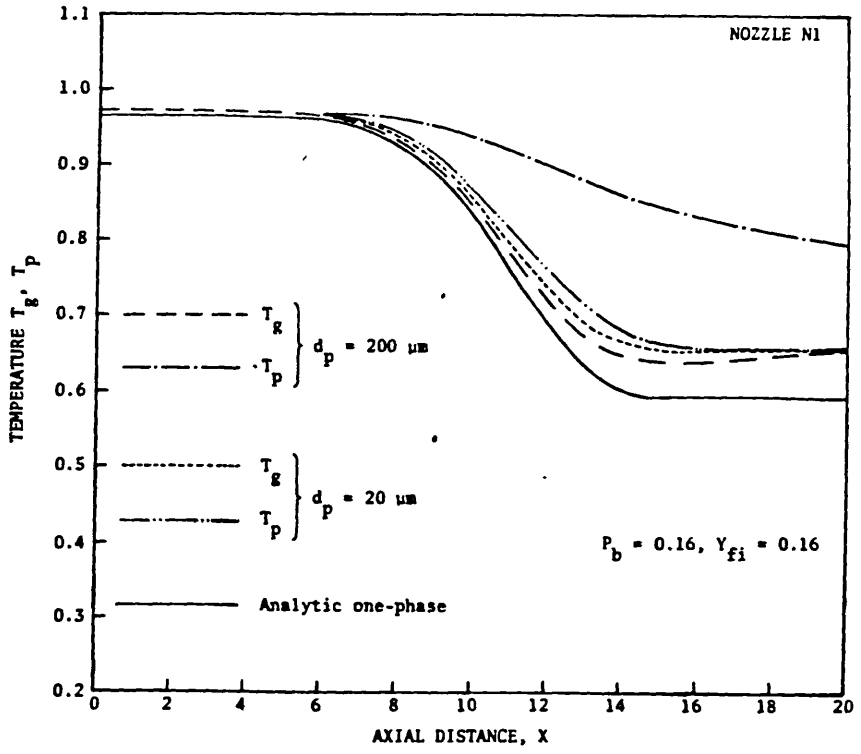


Fig. 5.23 Gas-phase and particle temperatures for a supersonic mixture flow in nozzle N1

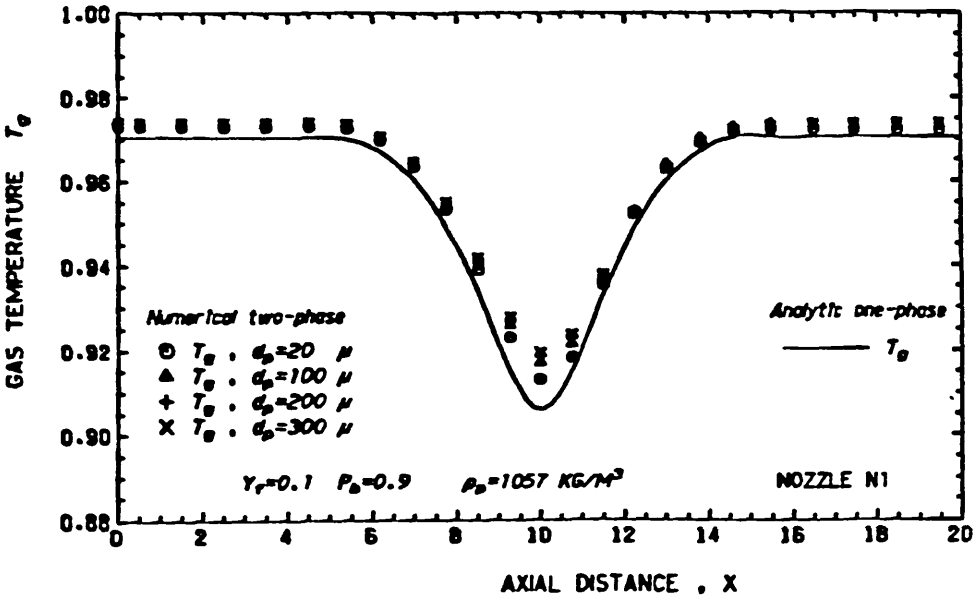


Fig. 5.24 Effects of various particle sizes on the gas-phase temperature for a fully subsonic flow in nozzle N1

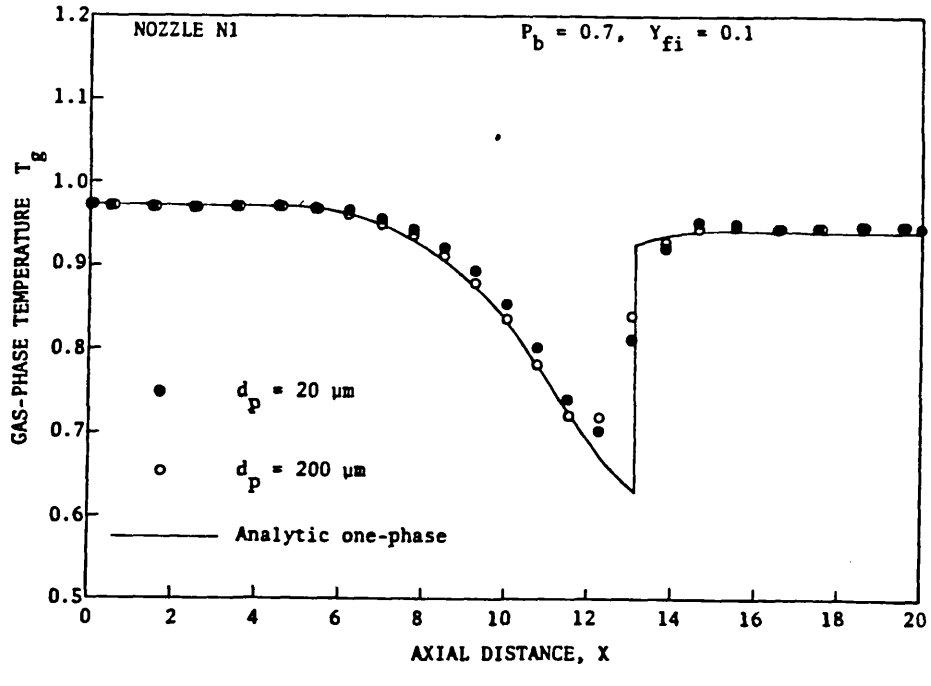


Fig. 5.25 Particle size effects on the gas-phase temperature in shocked mixture flow in nozzle N1

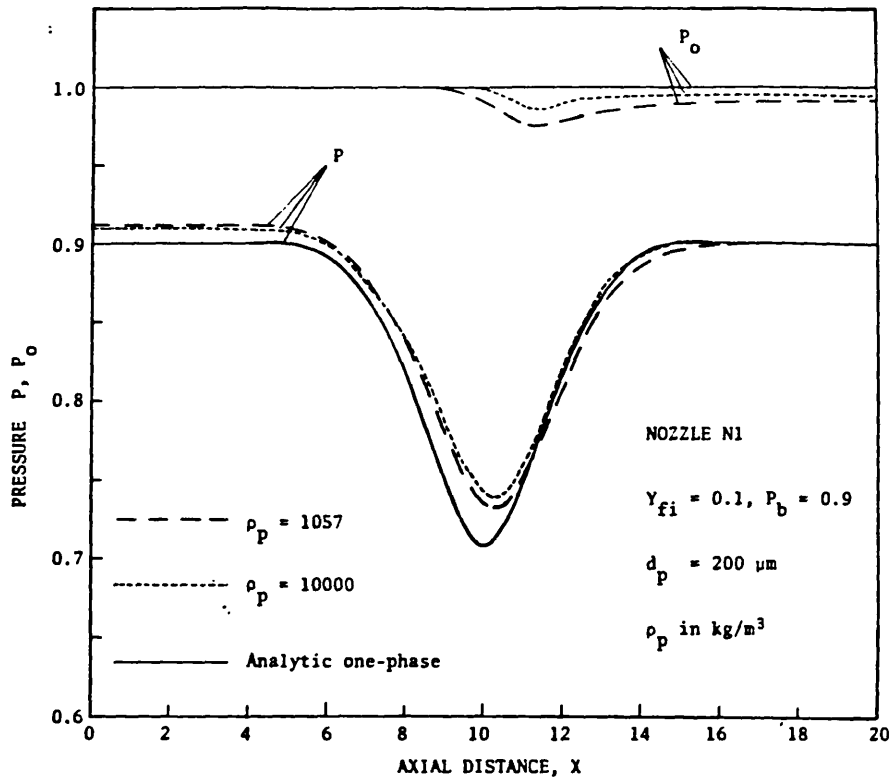


Fig. 5.26 Particle material density effects on the mixture pressure distribution for a fully subsonic flow in nozzle N1

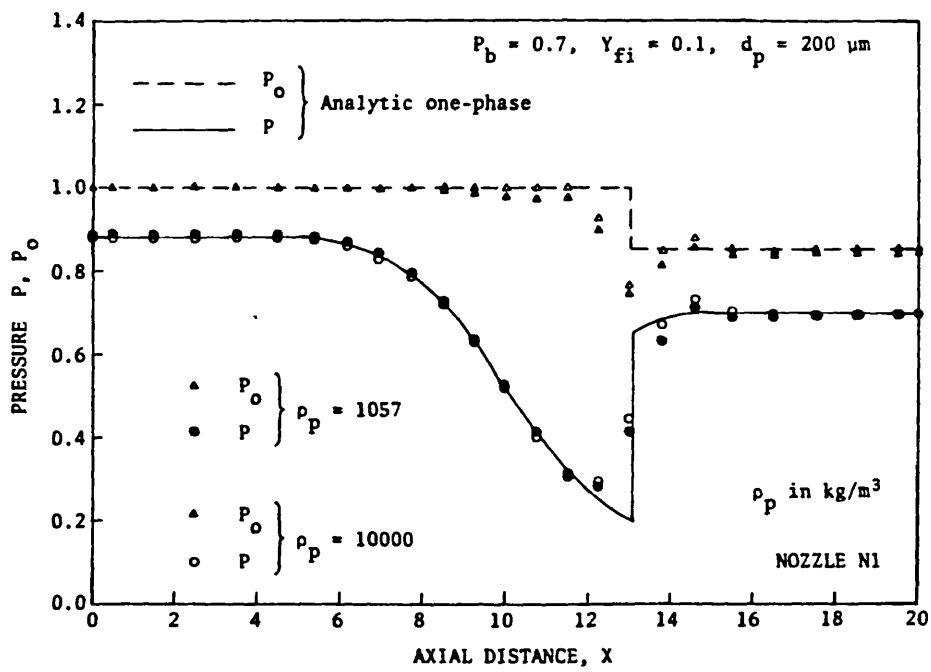


Fig. 5.27 Particle material density effects on the mixture pressure distribution for shocked flow in nozzle N1

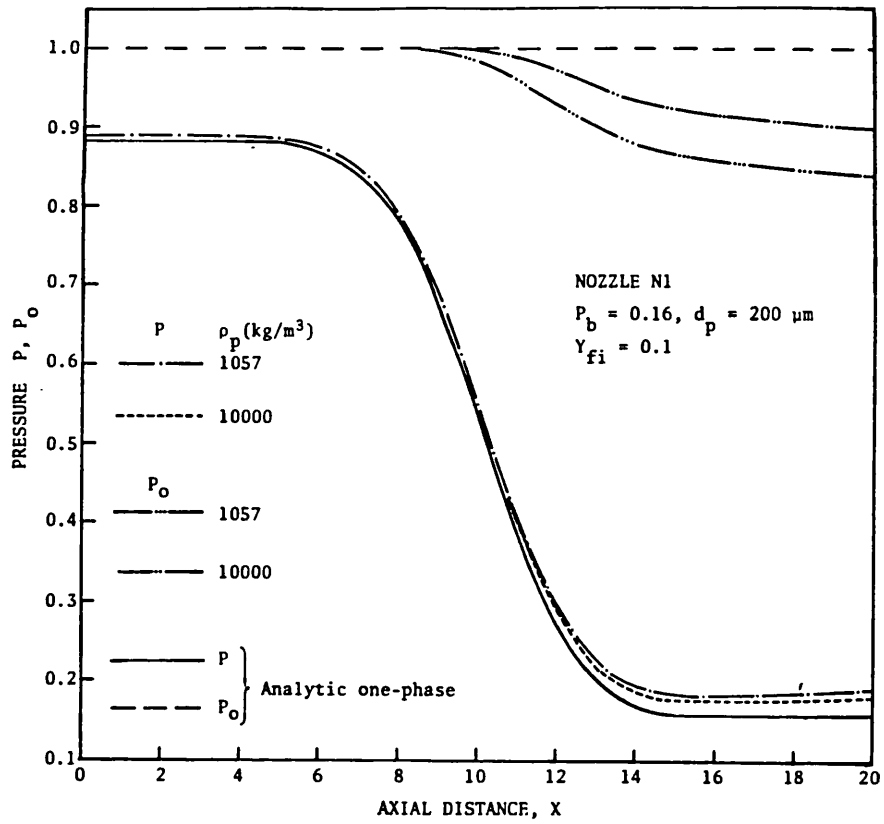


Fig. 5.28 Particle material density effects on the mixture pressure distribution for supersonic flow in nozzle N1

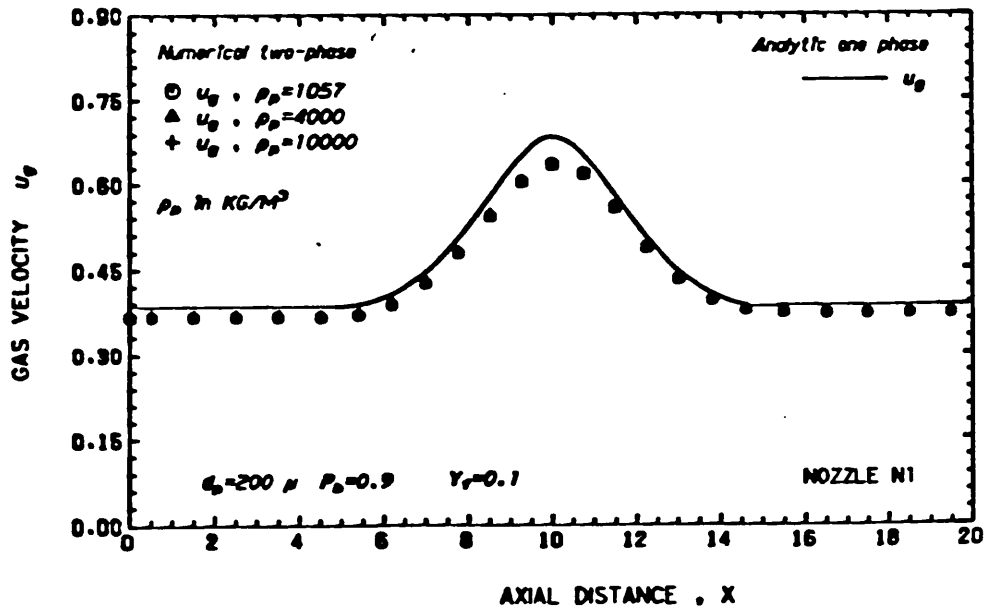


Fig. 5.29 Particle density effect on the gas-phase velocity for subsonic mixture flow in nozzle N1

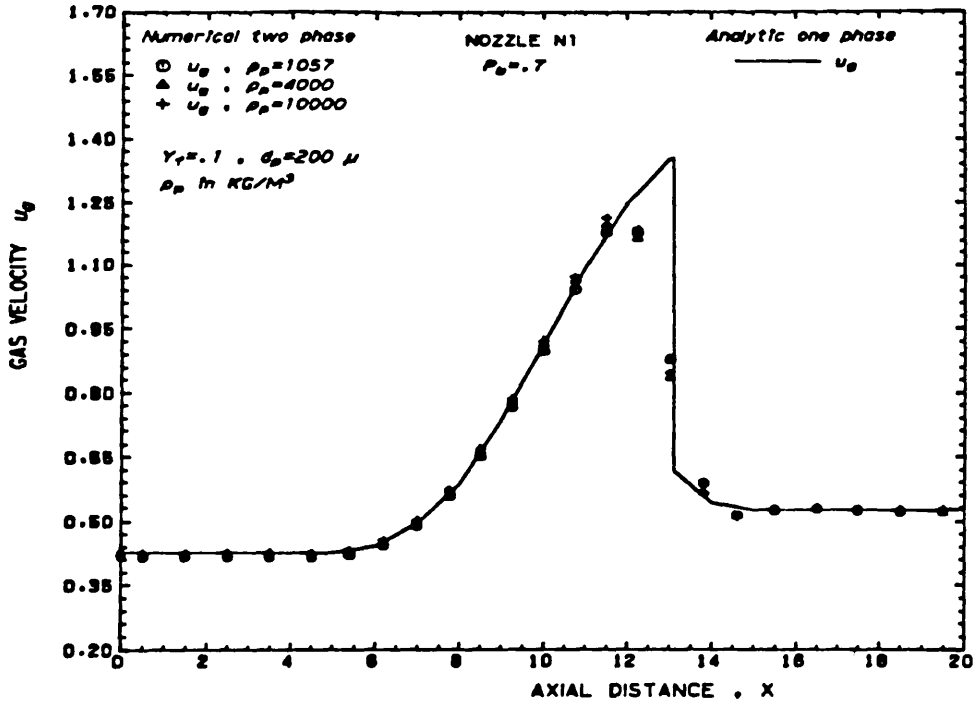


Fig. 5.30 Particle size effect on the gas-phase velocity for shocked mixture flow in nozzle N1

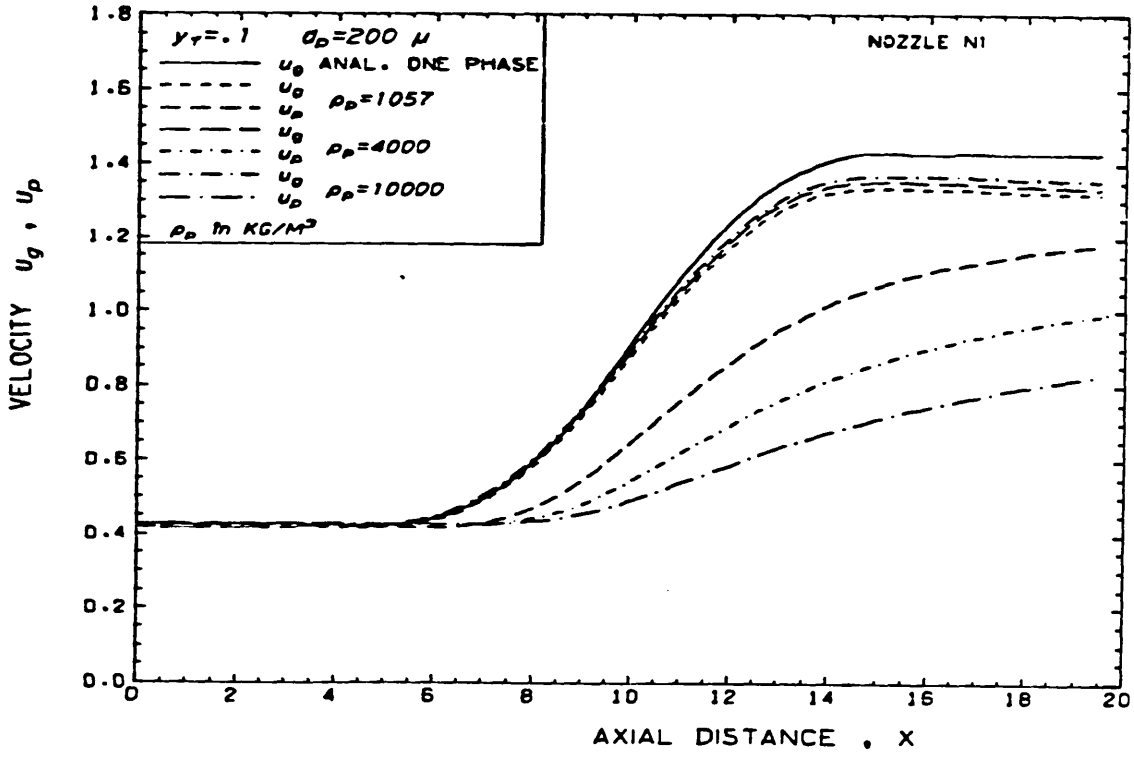


Fig. 5.31: Particle material density effects on the gas and particle velocities for supersonic mixture flow in nozzle N1

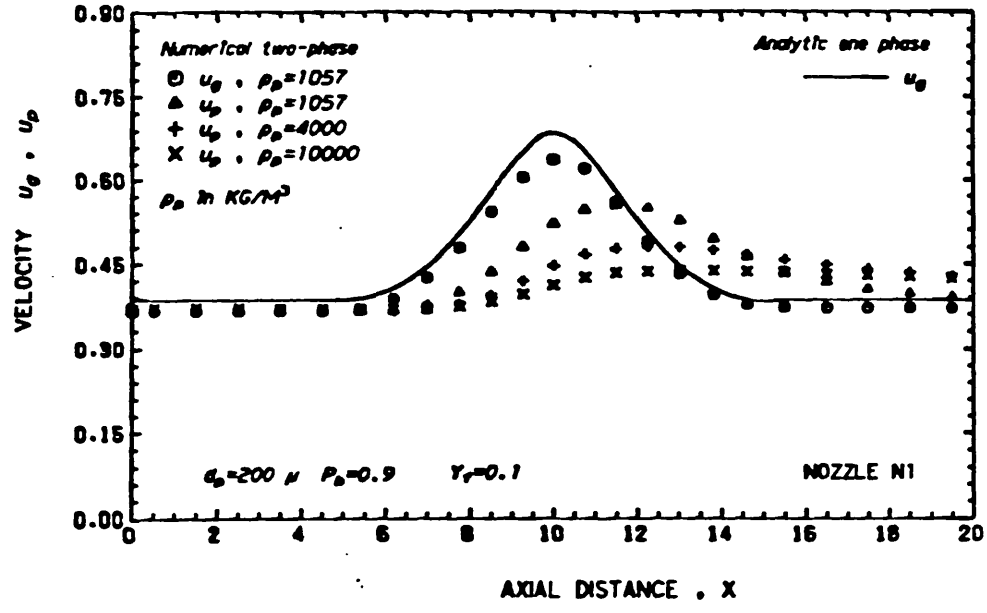


Fig. 5.32: Particle density effect on the dispersed phase velocity for fully subsonic flow in nozzle N1

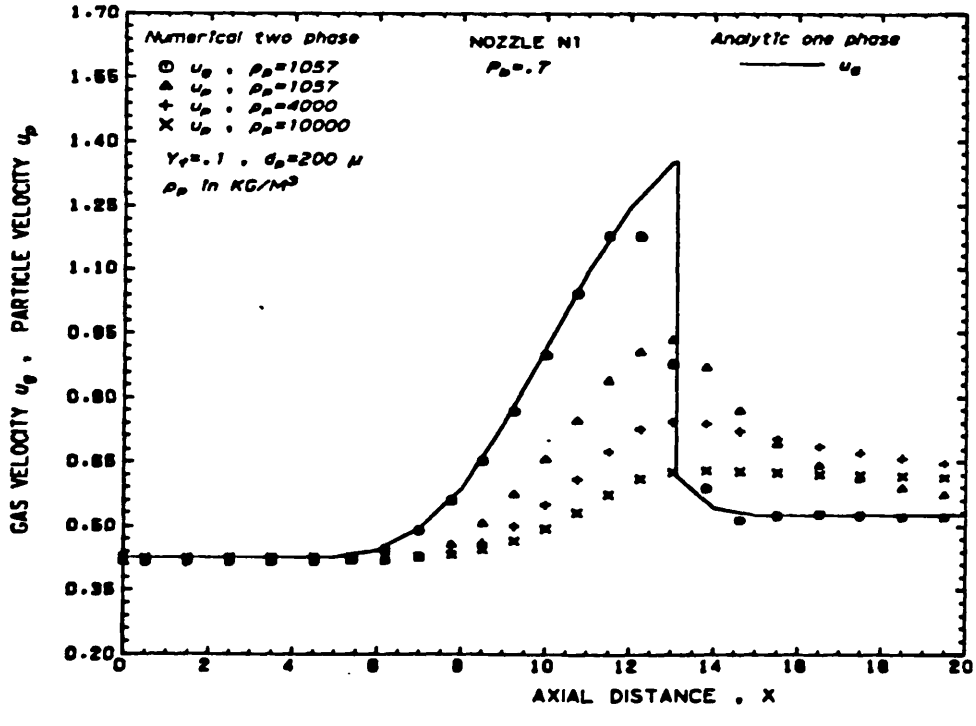


Fig. 5.33 Particle density effect on the dispersed phase velocity for shocked mixture flow in nozzle N1

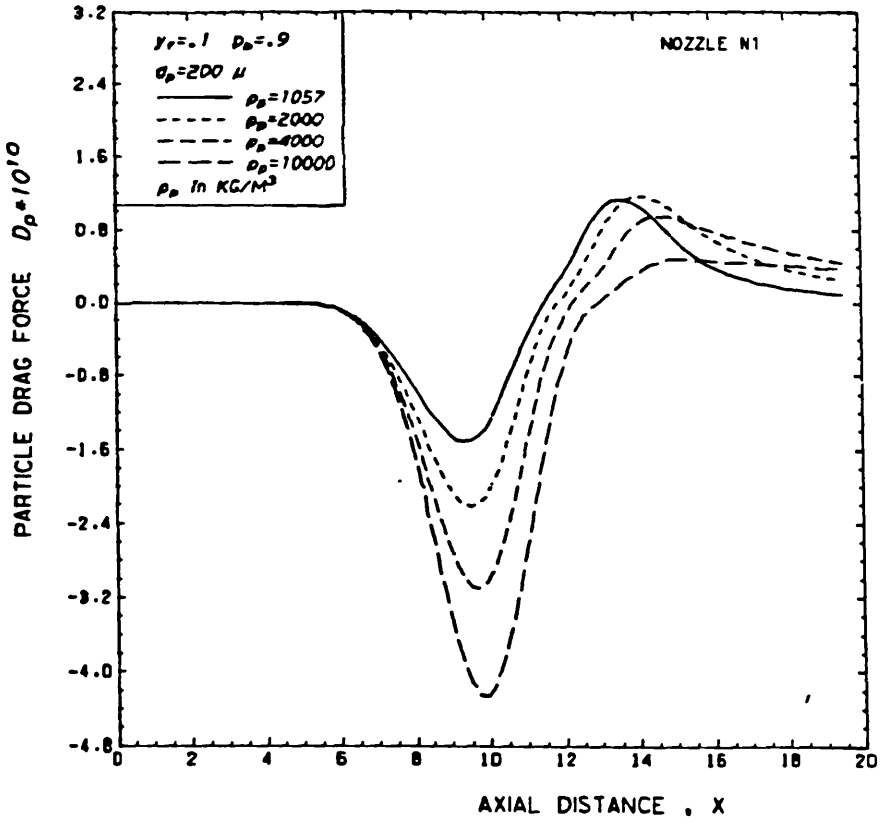


Fig. 5.34 Particle drag force for various particle densities for fully subsonic flow in nozzle N1

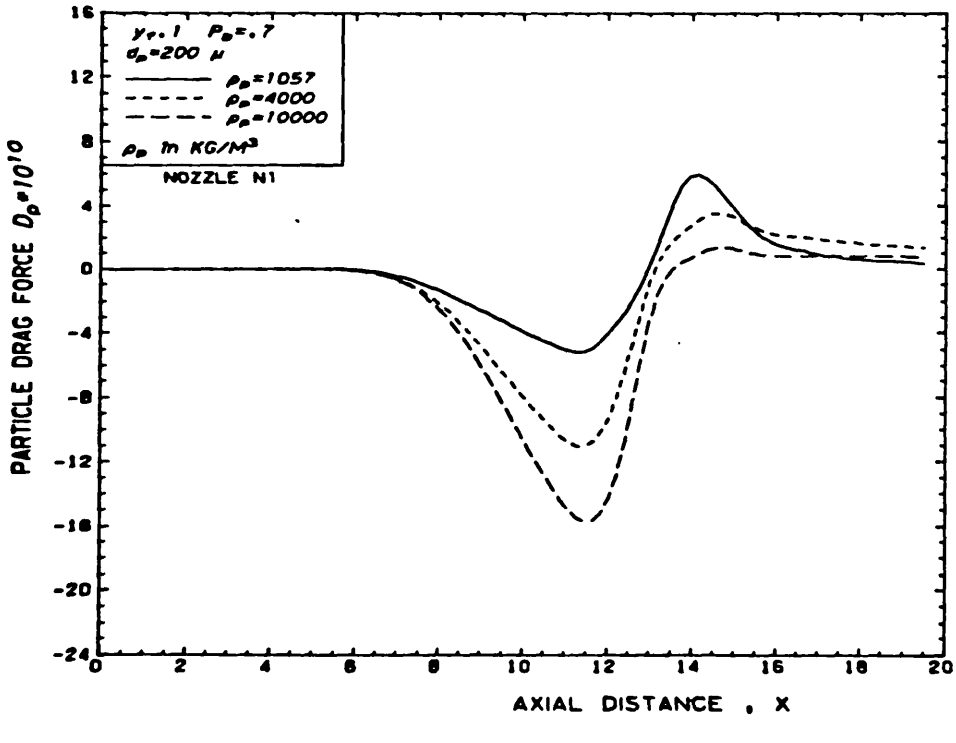


Fig. 5.35 Particle drag force for various particle densities for shocked mixture flow in nozzle N1

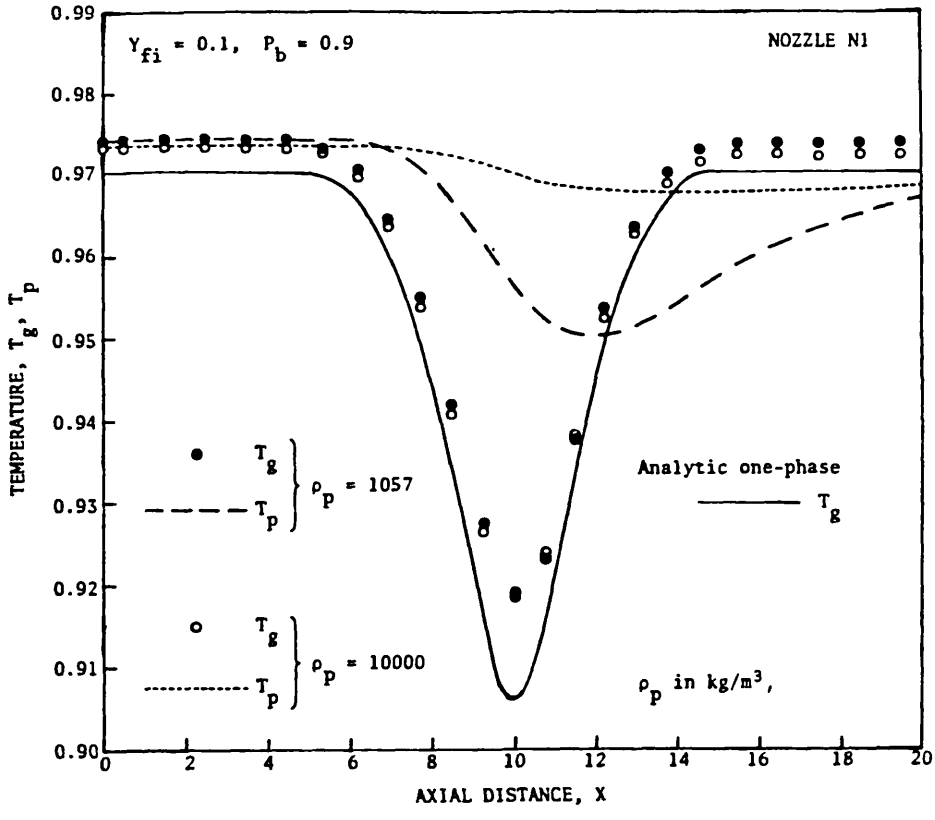


Fig. 5.36 Particle material density effects on the gas and particle temperatures for fully subsonic flow in nozzle N1

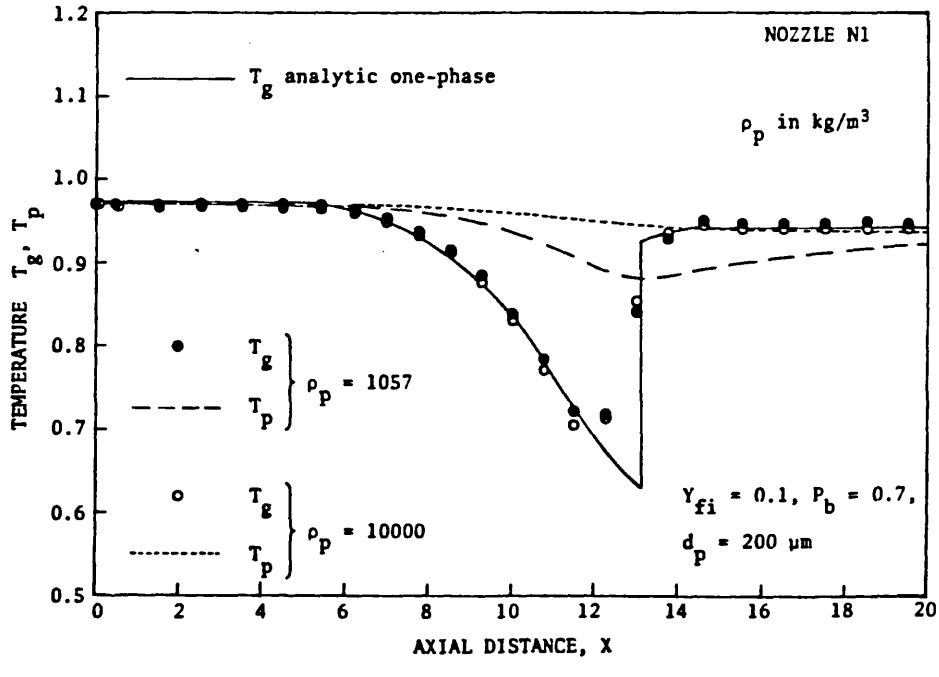


Fig. 5.37 Particle material density effects on the gas and particle temperatures for shocked flow in nozzle N1

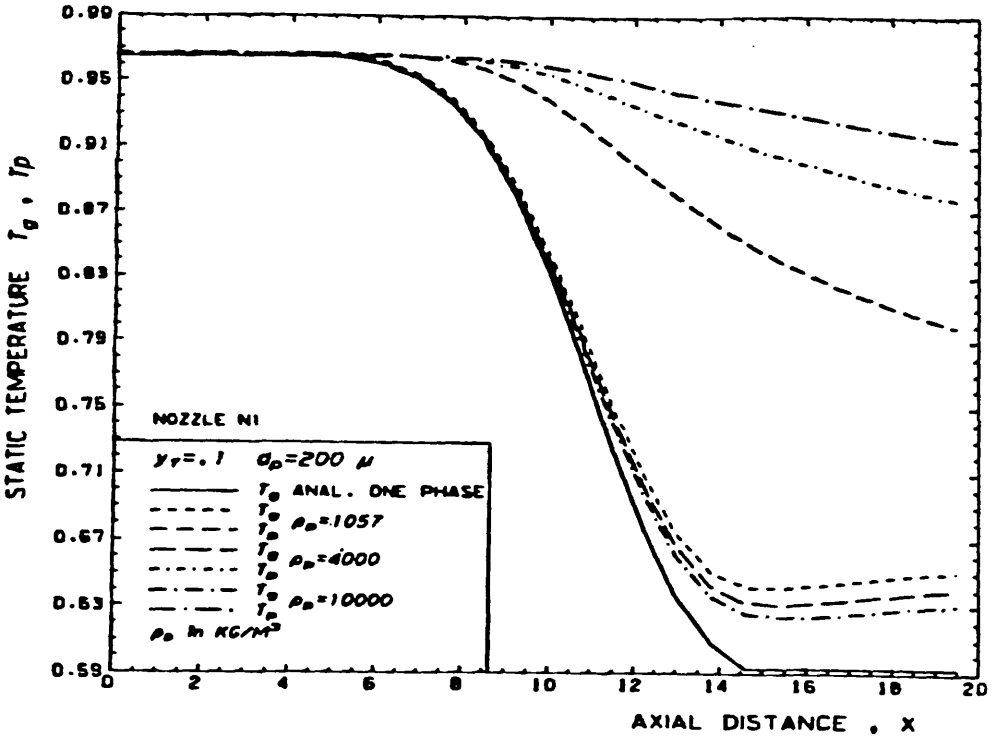


Fig. 5.38 Particle material density effects on the gas and particle temperatures for supersonic mixture flow in nozzle N1 (Y_{fi} = 10%)

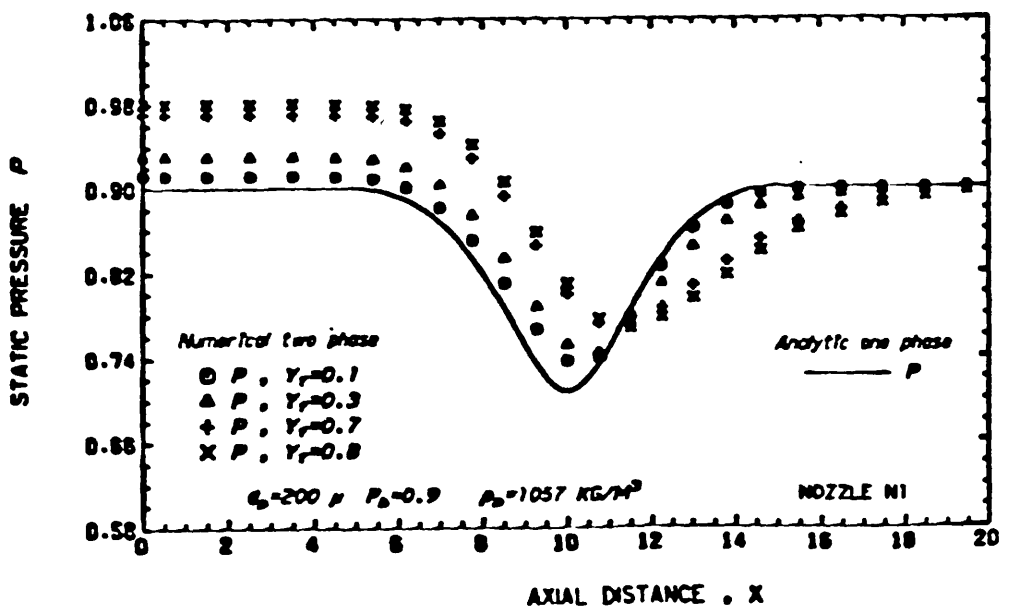


Fig. 5.39 Pressure distribution for different particle mass flow fractions for fully subsonic mixture flow in nozzle N1

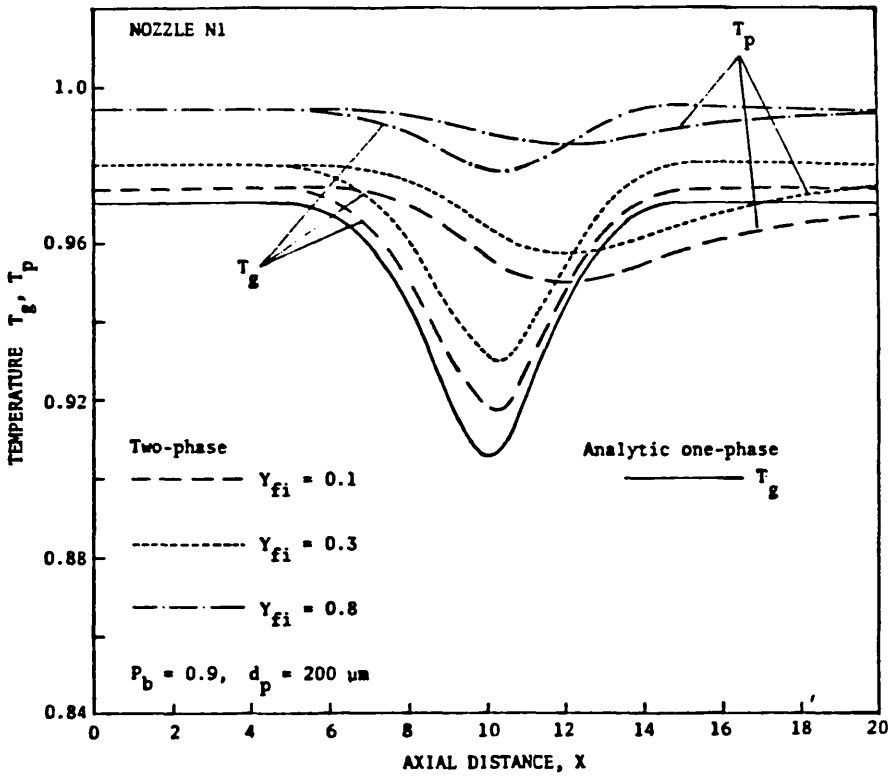


Fig. 5.40 Gas-phase and particle temperatures for different Y_{fi} values for fully subsonic mixture flow in nozzle N1

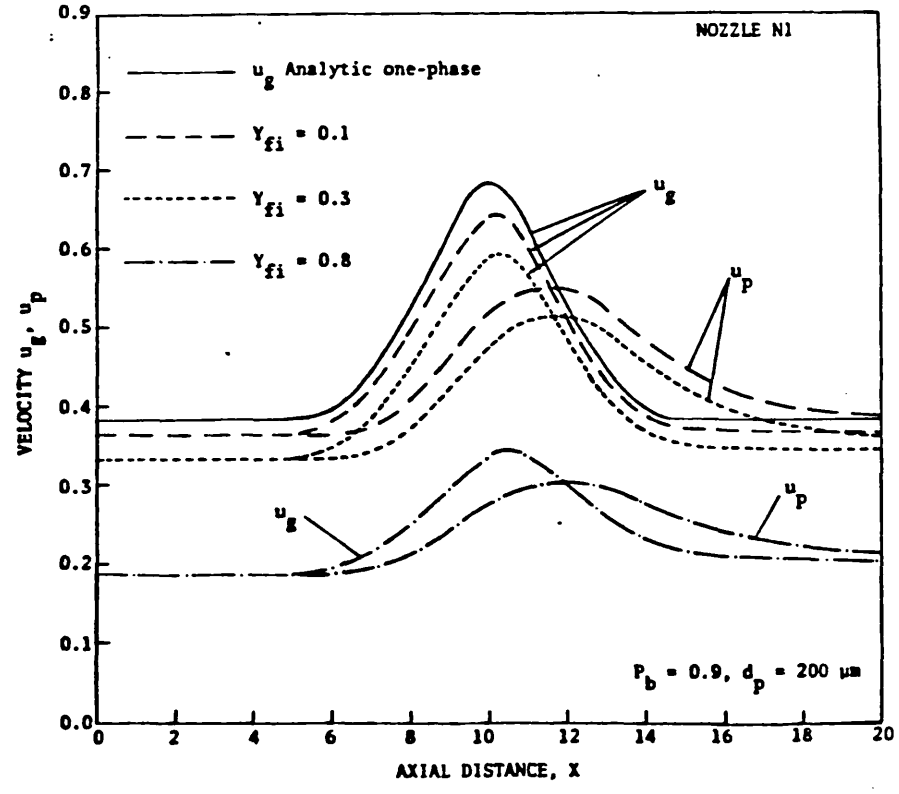


Fig. 5.41 Gas-phase and particle velocities for various Y_{fi} values for fully subsonic mixture flow in nozzle N1

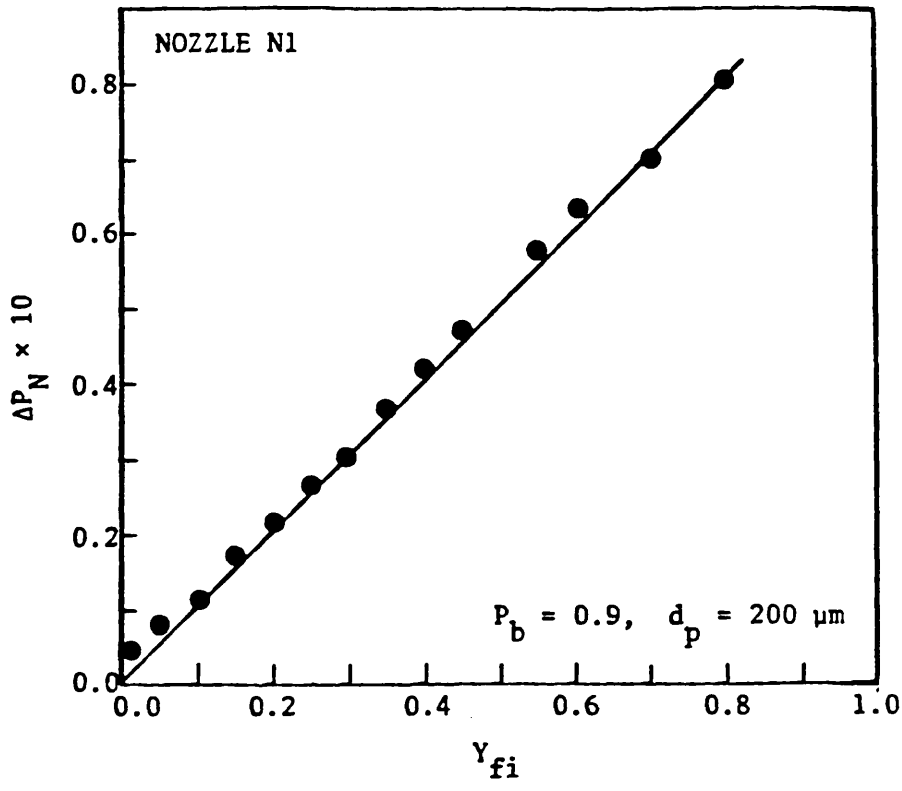


Fig. 5.42 Y_{fi} effects on the pressure drop across nozzle N1 for fully subsonic mixture flow

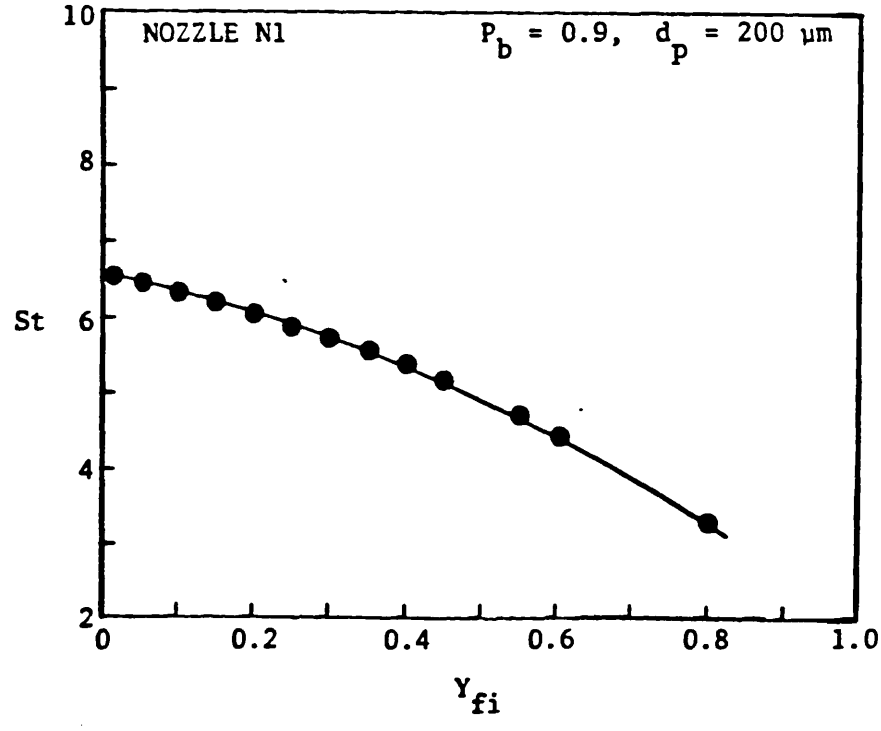


Fig. 5.43 Stokes number versus Y_{fi} for fully subsonic mixture flow in nozzle N1

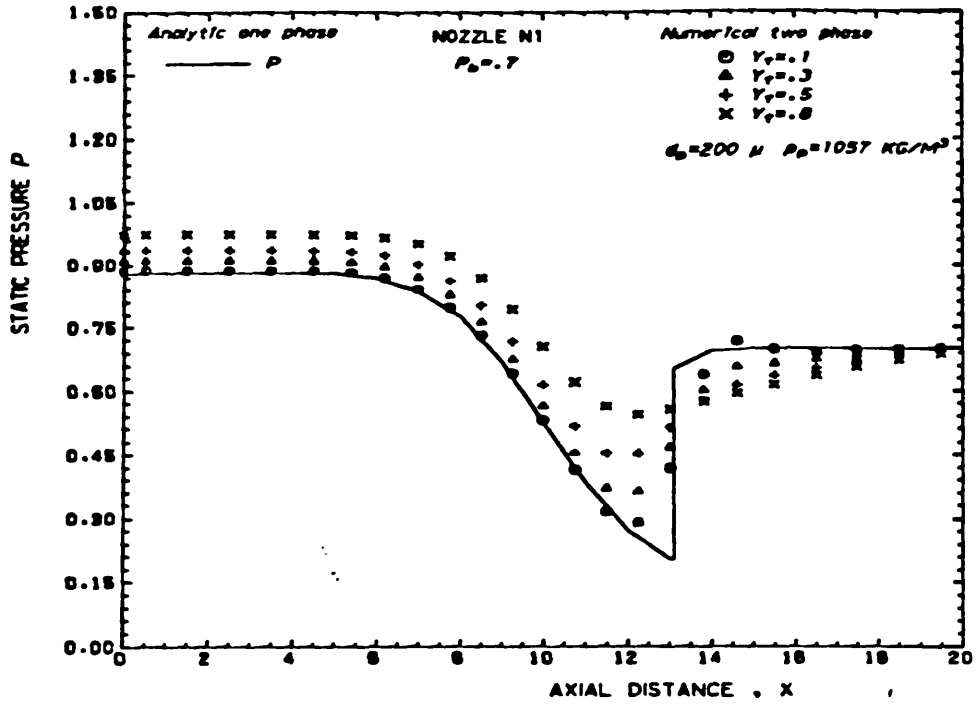


Fig. 5.44 Pressure distribution for different particle mass flow fractions for shocked mixture flow in nozzle N1

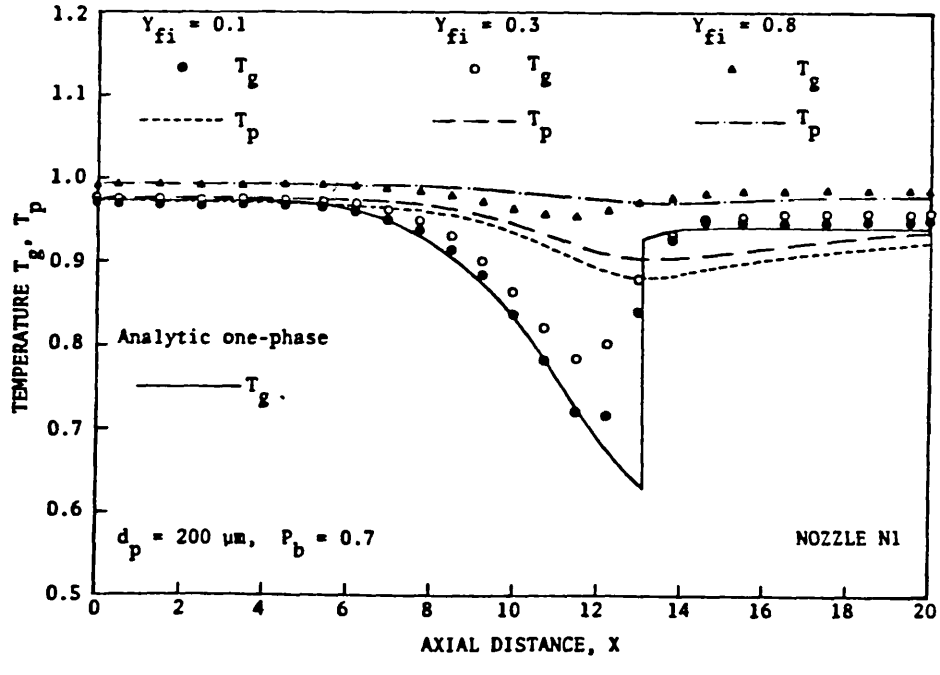


Fig. 5.45 Gas and particle temperatures for various Y_{fi} values for shocked mixture flow in nozzle N1

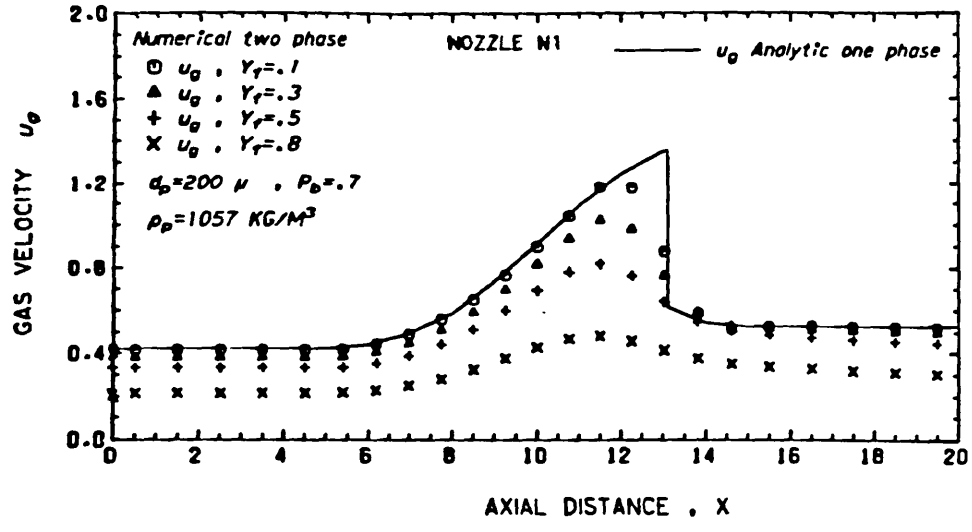


Fig. 5.46 Gas-phase velocity for various particle mass flow fractions for shocked mixture flow in nozzle N1

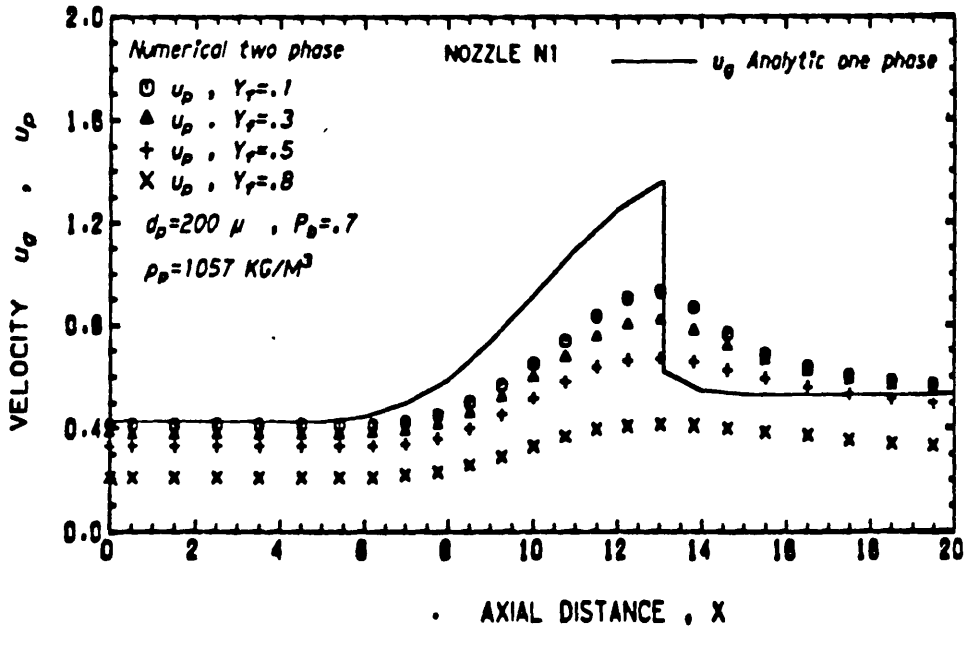


Fig. 5.47 Particle velocity for various particle mass flow fractions for shocked mixture flow in nozzle N1

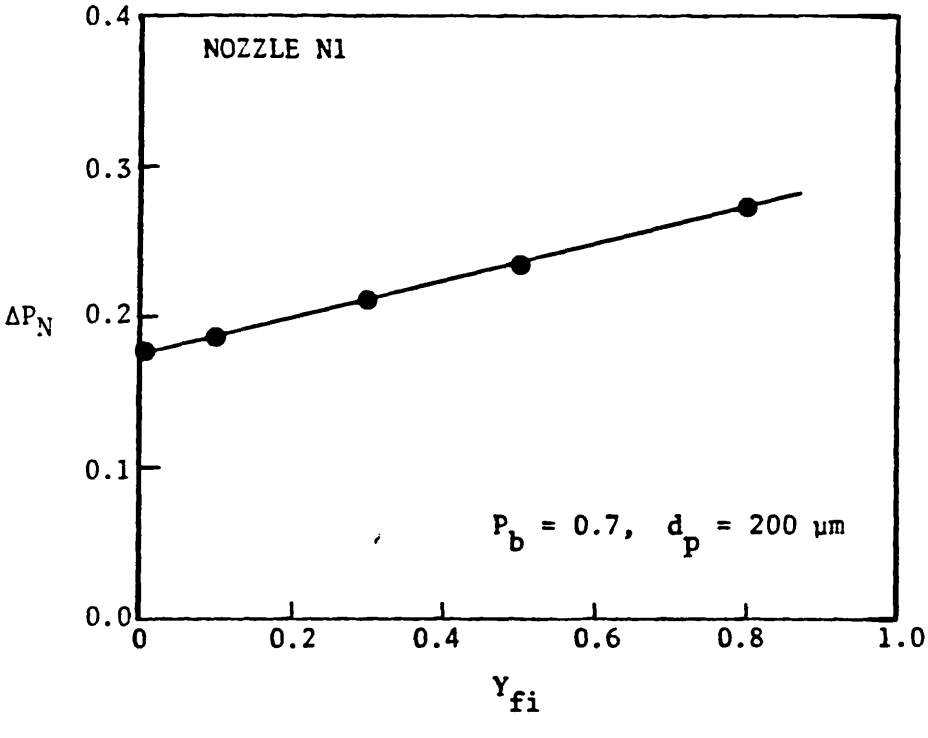


Fig. 5.48 Pressure drop across nozzle N1 versus Y_{fi} for shocked mixture flow

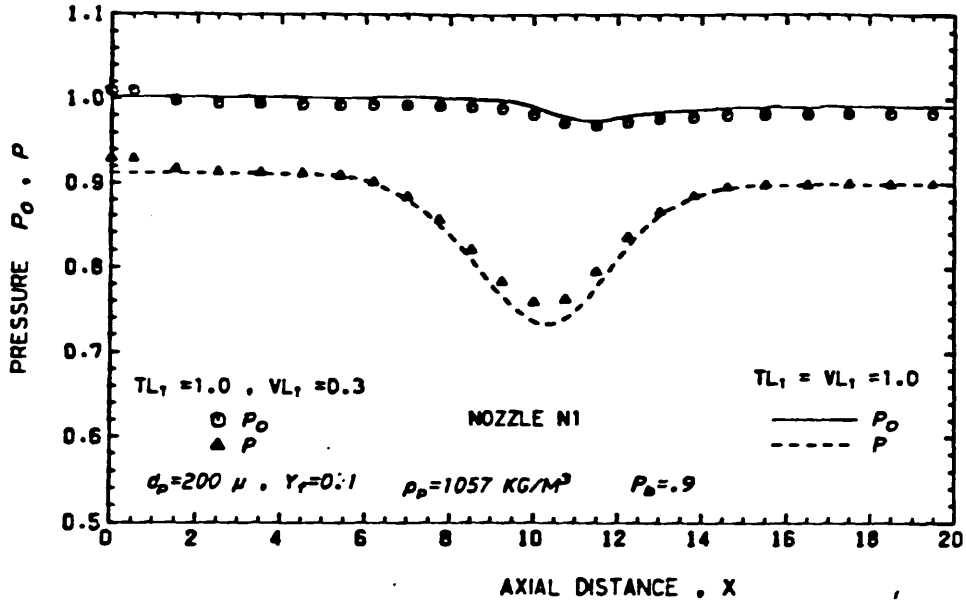


Fig. 5.49 Inlet velocity lag effects on the pressure distribution for the fully subsonic mixture flow in nozzle N1

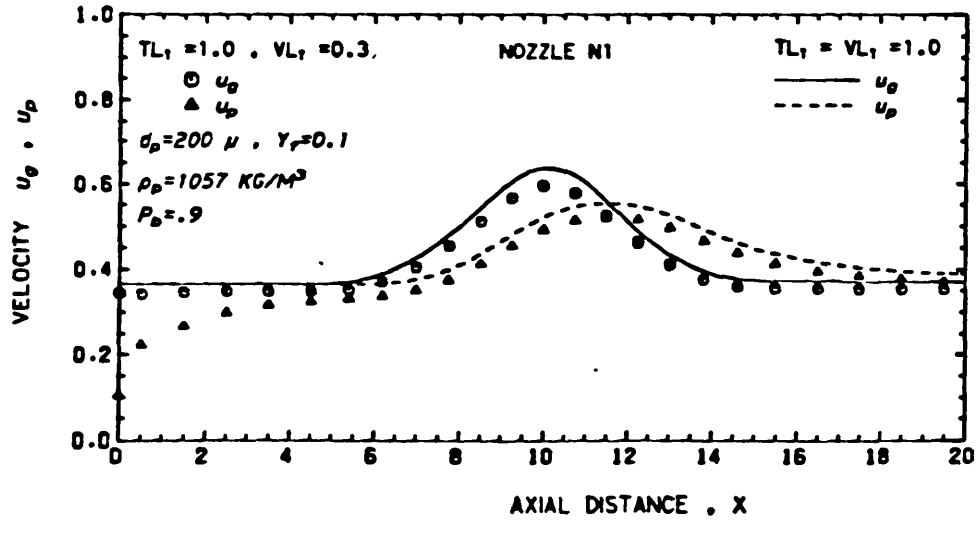


Fig. 5.50 Inlet velocity lag effects on the gas and particle velocities for subsonic mixture flow in nozzle N1

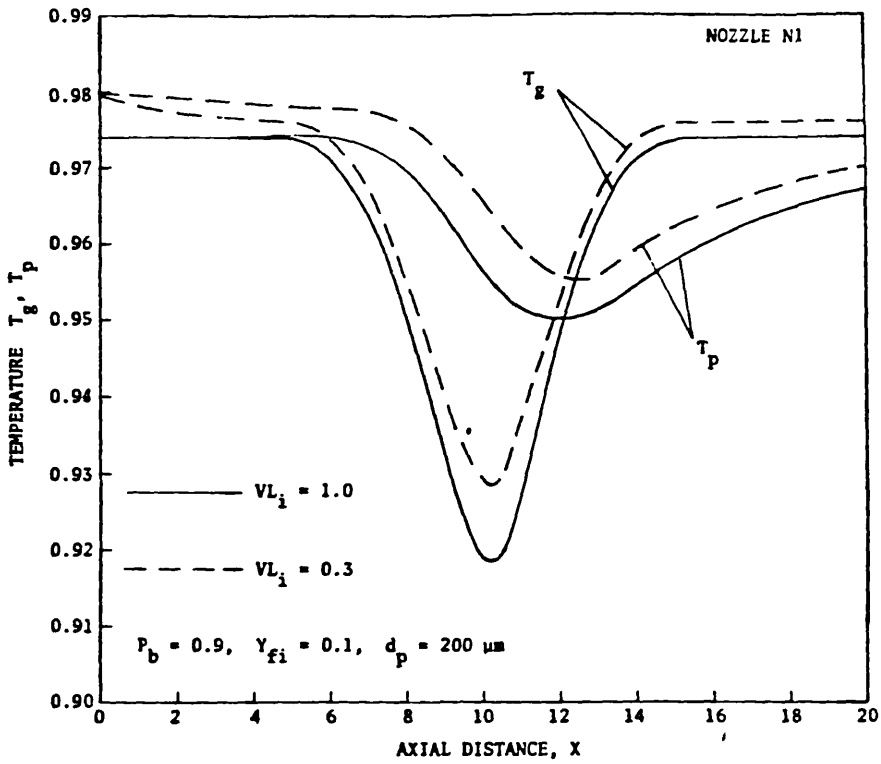


Fig. 5.51 Inlet velocity lag effects on the gas and particle temperatures for fully subsonic flow in nozzle N1

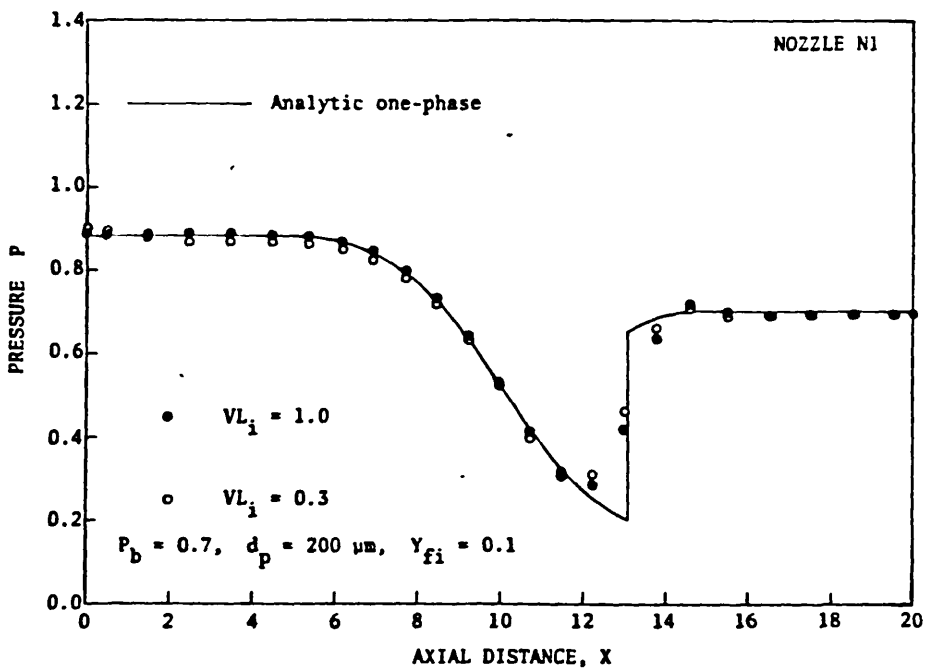


Fig. 5.52 Inlet velocity lag effects on the pressure for shocked mixture flow in nozzle N1

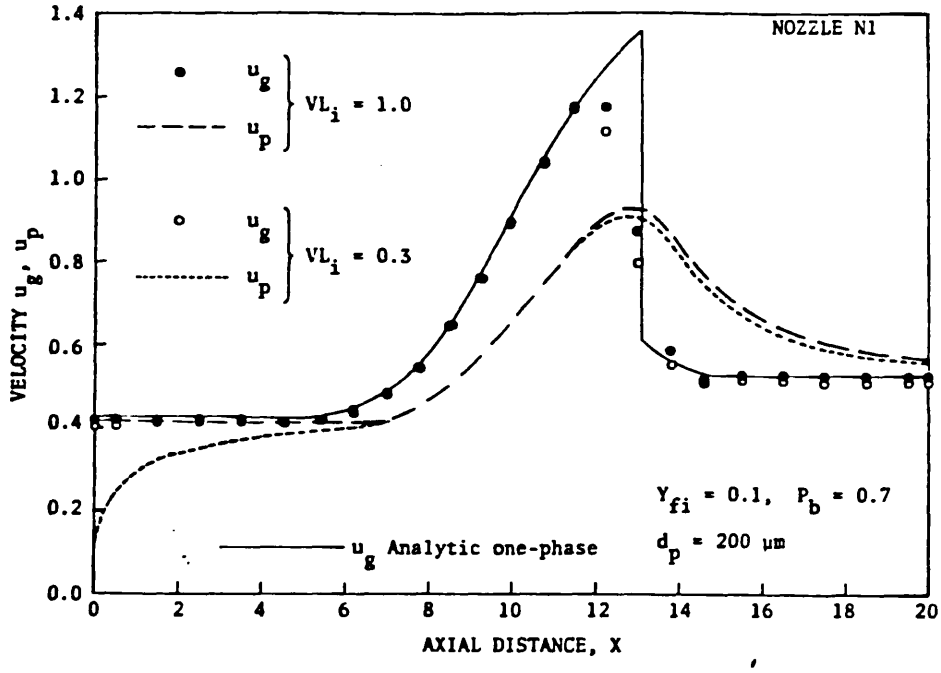


Fig. 5.53 Inlet velocity lag effects on the gas and particle velocities for shocked mixture flow in nozzle N1

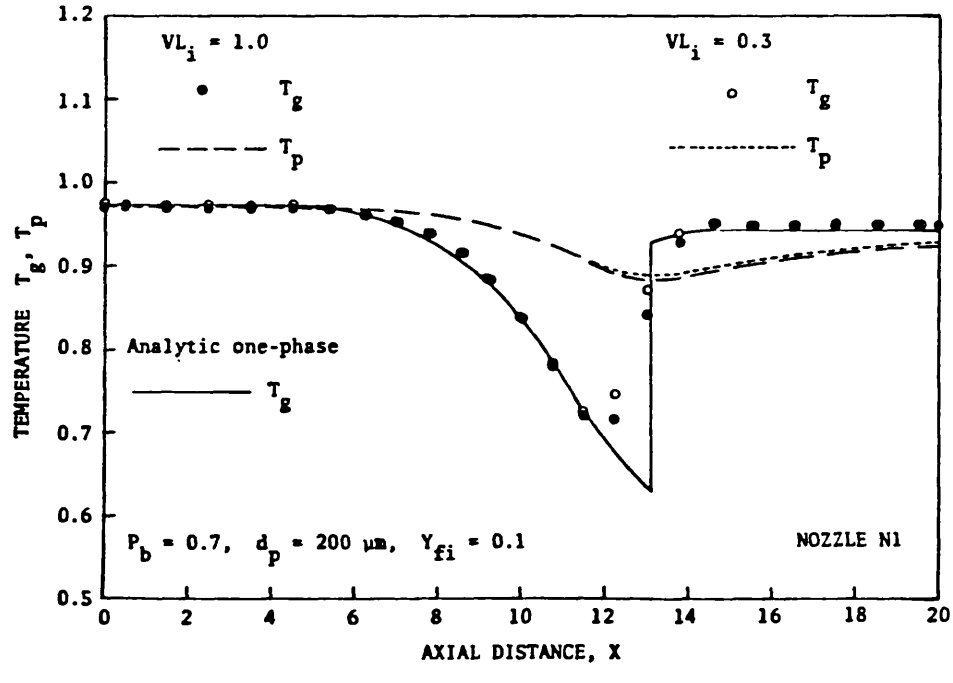


Fig. 5.54 Inlet velocity lag effects on the gas and particle temperatures for shocked mixture flow in nozzle N1

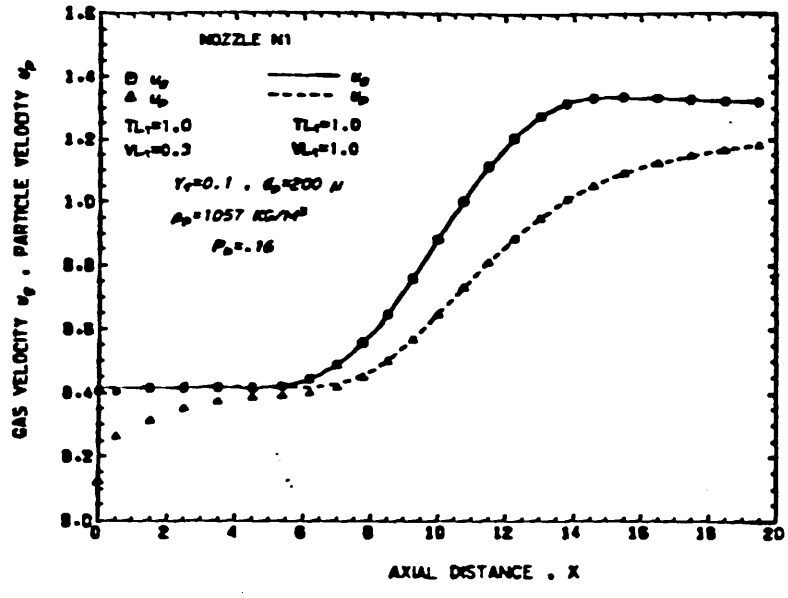


Fig. 5.55 Inlet velocity lag effects on the gas and particle velocities for supersonic mixture flow in nozzle N1 (Y_{fi} = 10%)

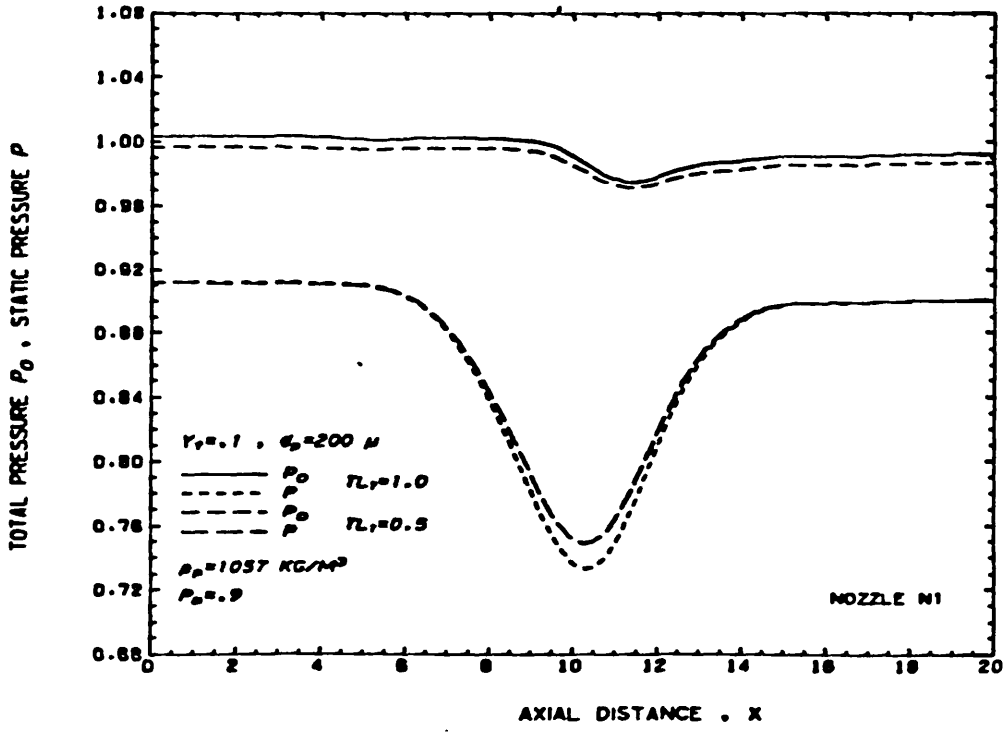


Fig. 5.56 Inlet temperature lag effects on the pressure for subsonic mixture flow in nozzle N1 .

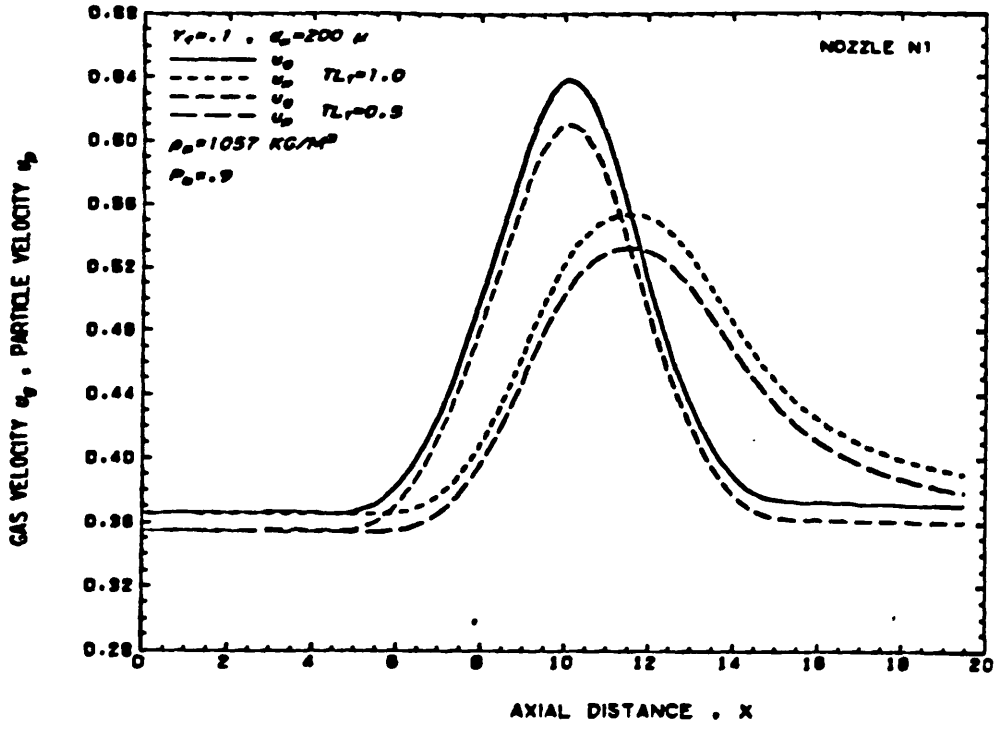


Fig. 5.57 Inlet temperature lag effects on the gas and particle velocities for subsonic mixture flow in nozzle N1

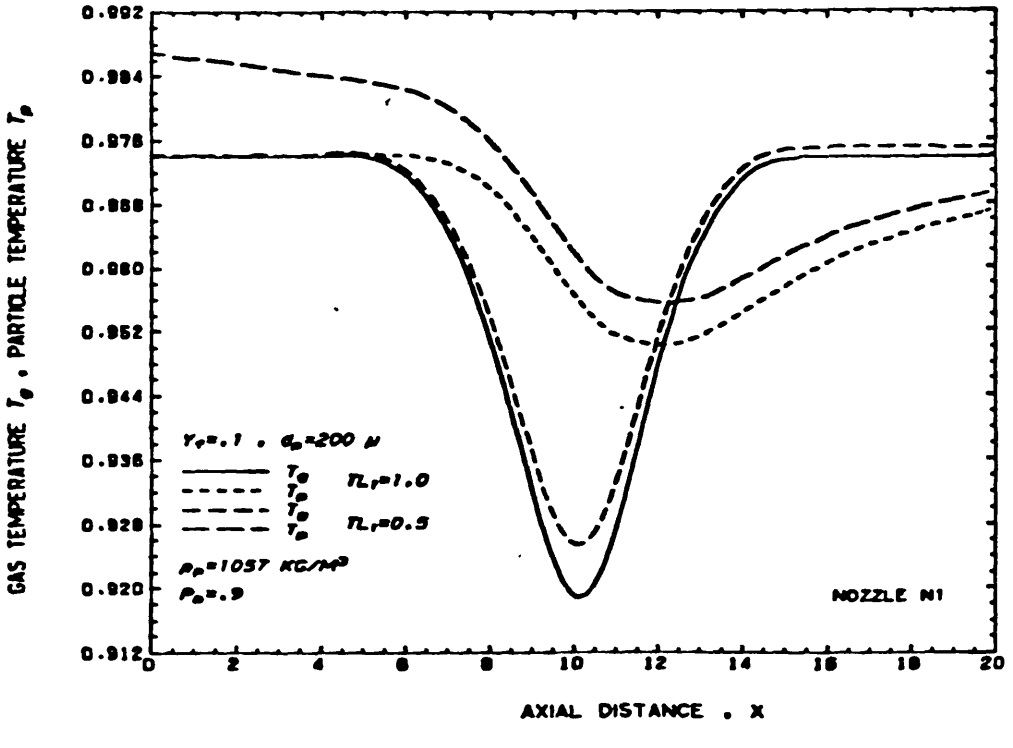


Fig. 5.58 Inlet temperature lag effects on the gas and particle temperatures for subsonic mixture flow in nozzle N1

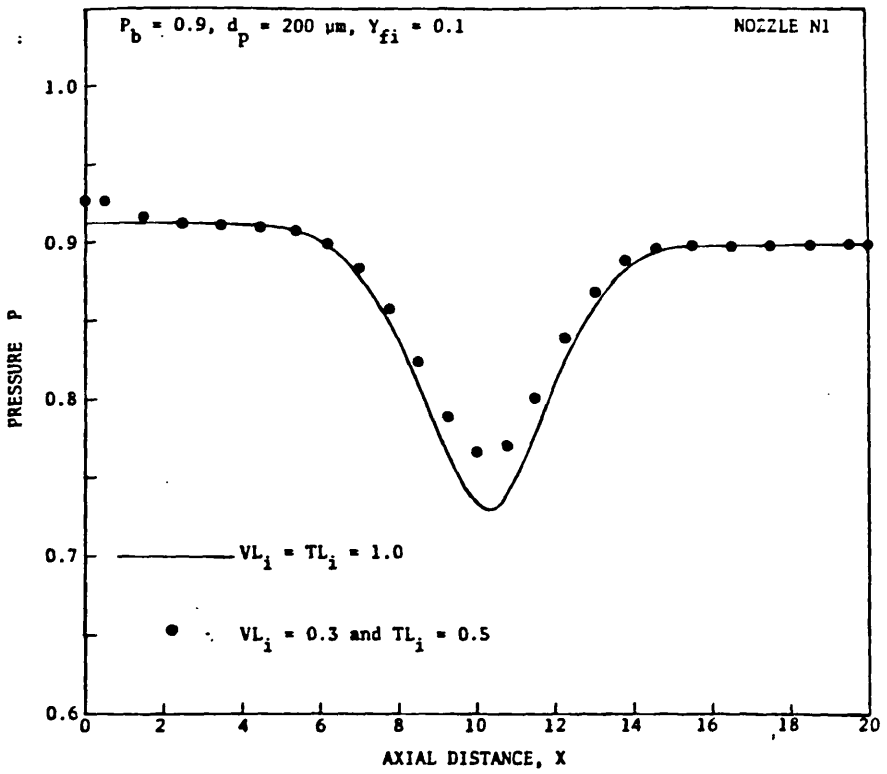


Fig. 5.59 Inlet velocity and temperature lags effect on the pressure for fully subsonic mixture flow in nozzle N1

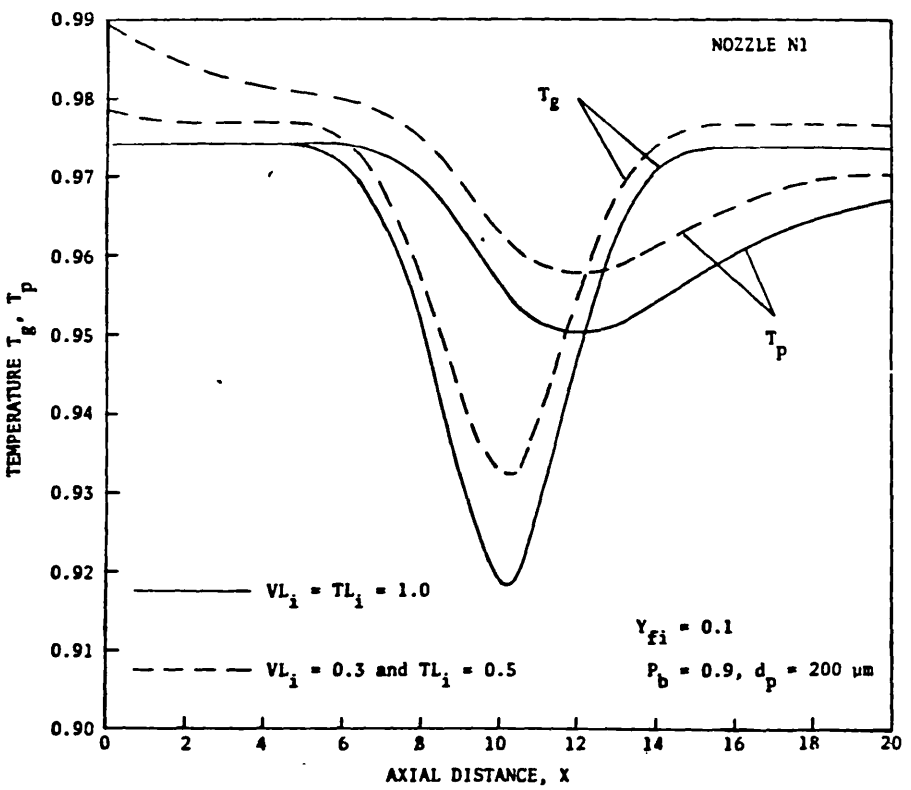


Fig. 5.60 Inlet velocity and temperature lags effect on the gas and particle temperatures for subsonic mixture flow in nozzle N1

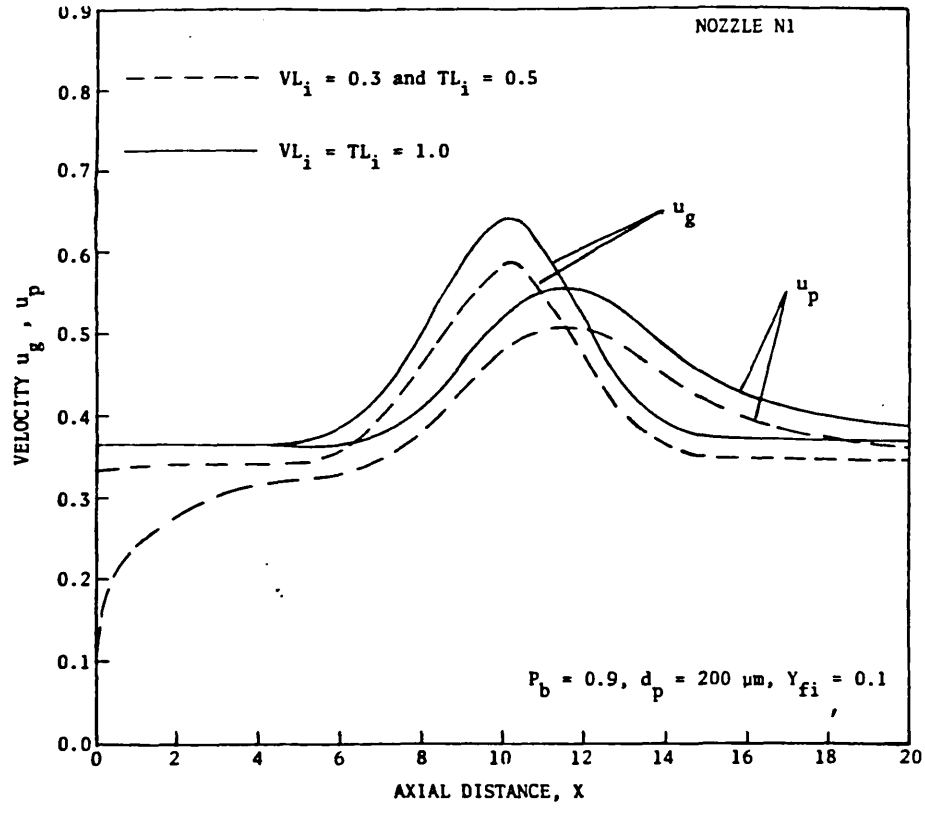


Fig. 5.61 Inlet velocity and temperature lags effect on the gas and particle velocities for subsonic mixture flow in nozzle N1

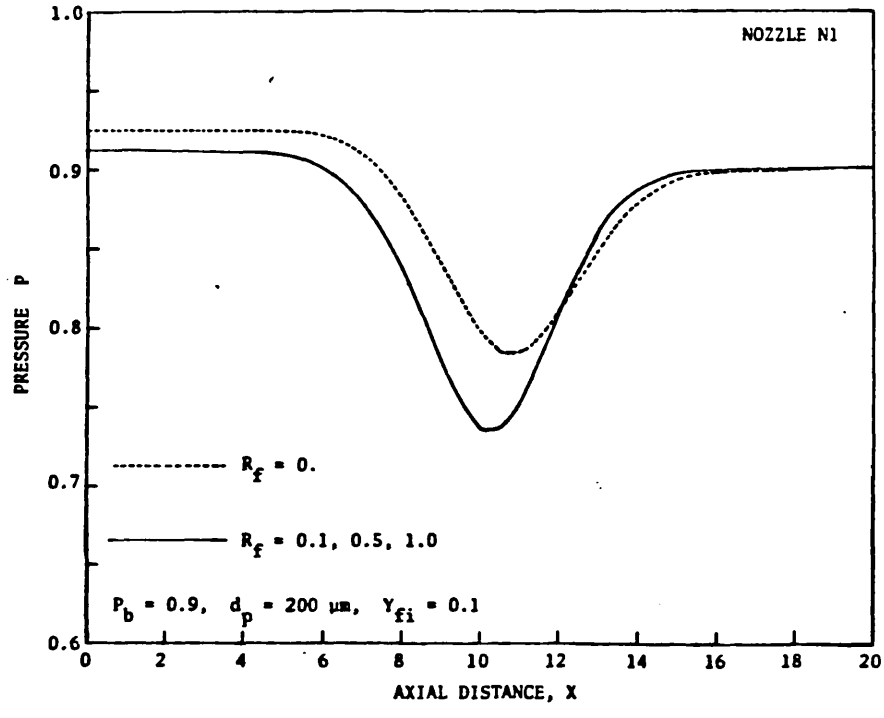


Fig. 5.62 Relaxation factor effects on the pressure distribution for subsonic mixture flow in nozzle N1

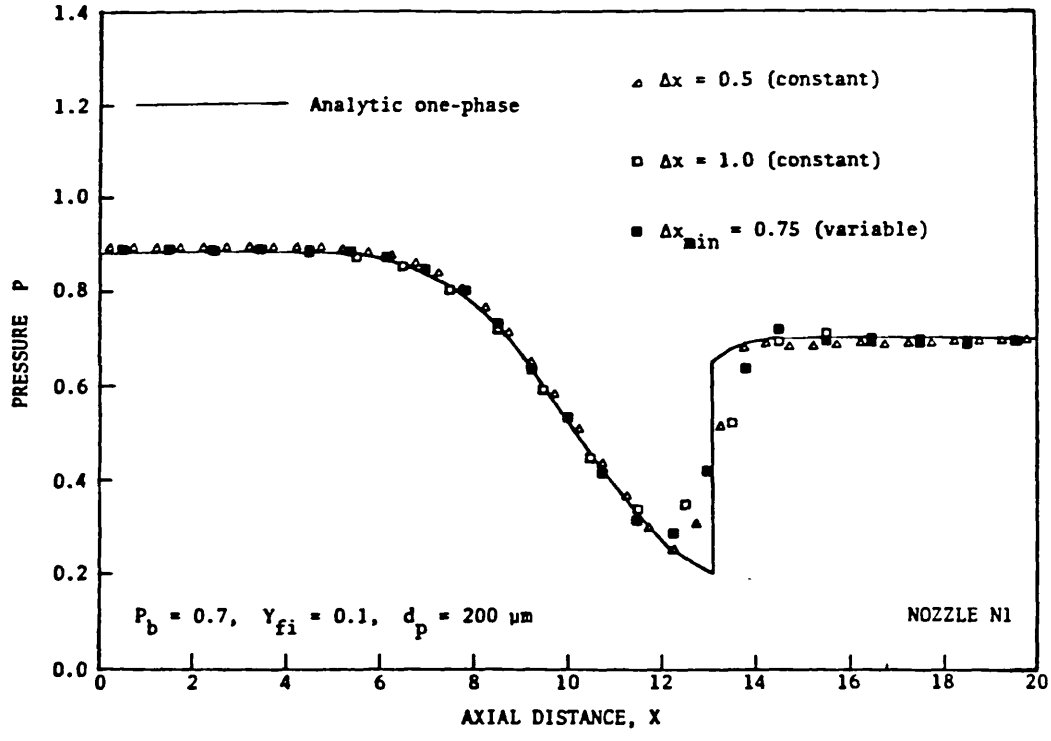


Fig. 5.63 Pressure distribution for different grids for the shocked mixture flow in nozzle N1

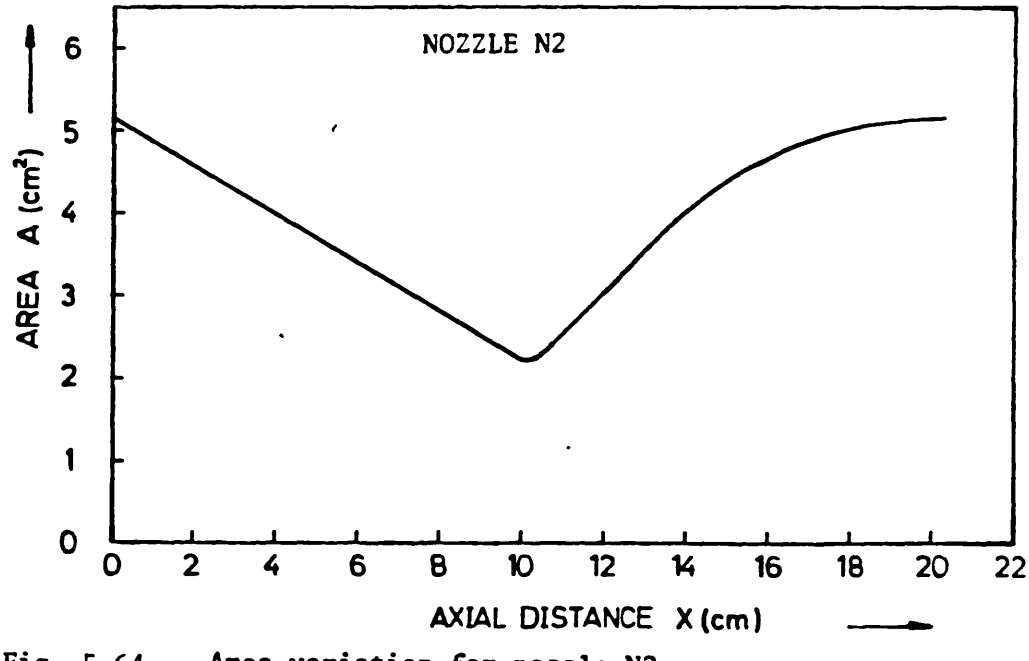


Fig. 5.64 Area variation for nozzle N2

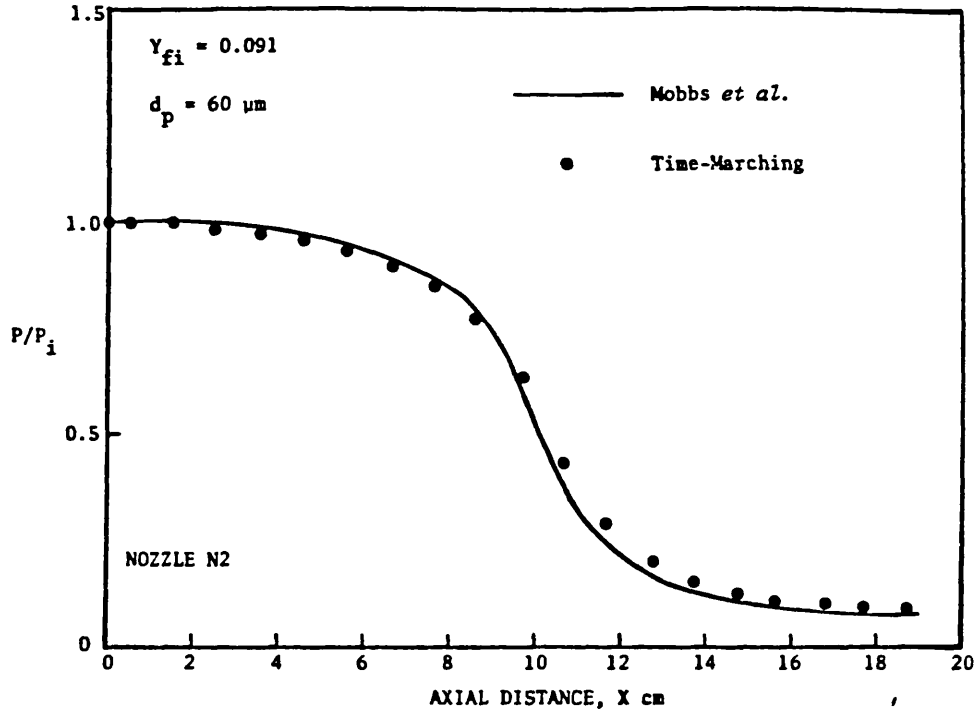


Fig. 5.65 Comparison of the pressure ratio predictions in nozzle N2 with those of Mobbs *et al.*[66] for Y_{fi} = 0.091

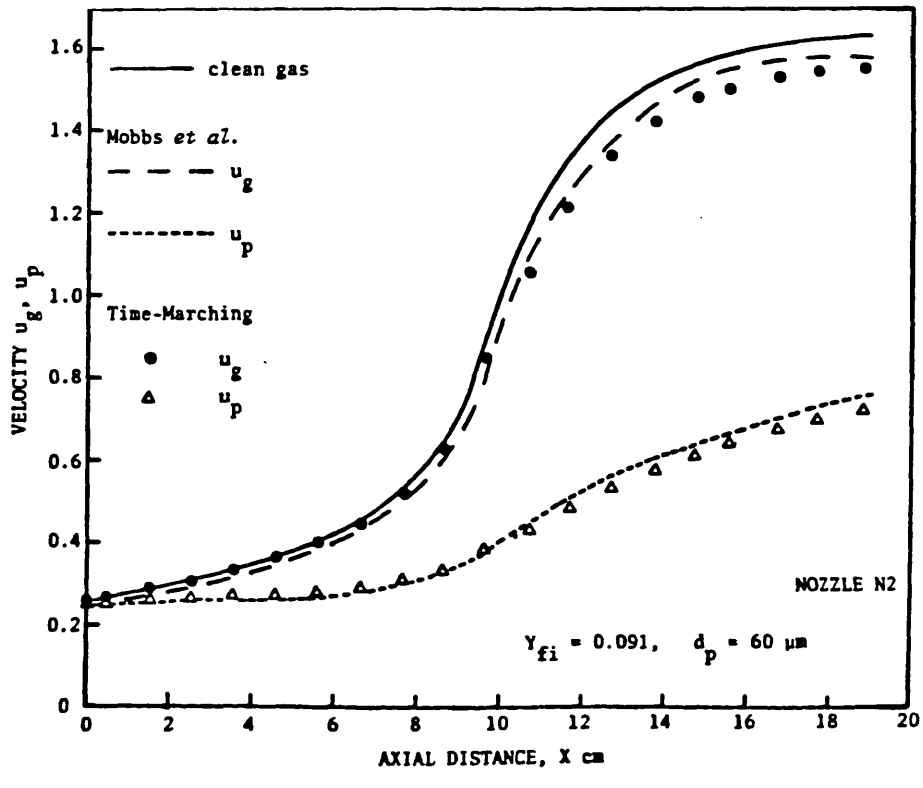


Fig. 5.66 Comparison of the gas and particle velocities predicted in nozzle N2 with those of Mobbs *et al.* for Y_{fi} = 0.091

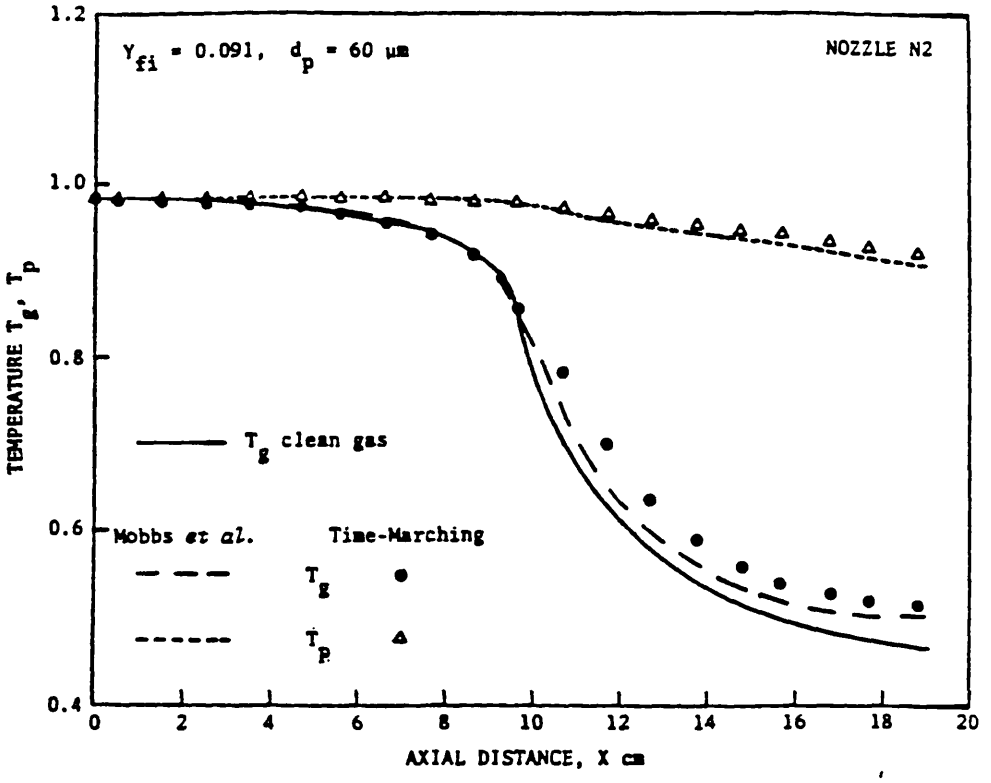


Fig. 5.67 Comparison of the gas and particle temperatures predictions with those of Mobbs *et al.* for Y_{fi} = 0.091

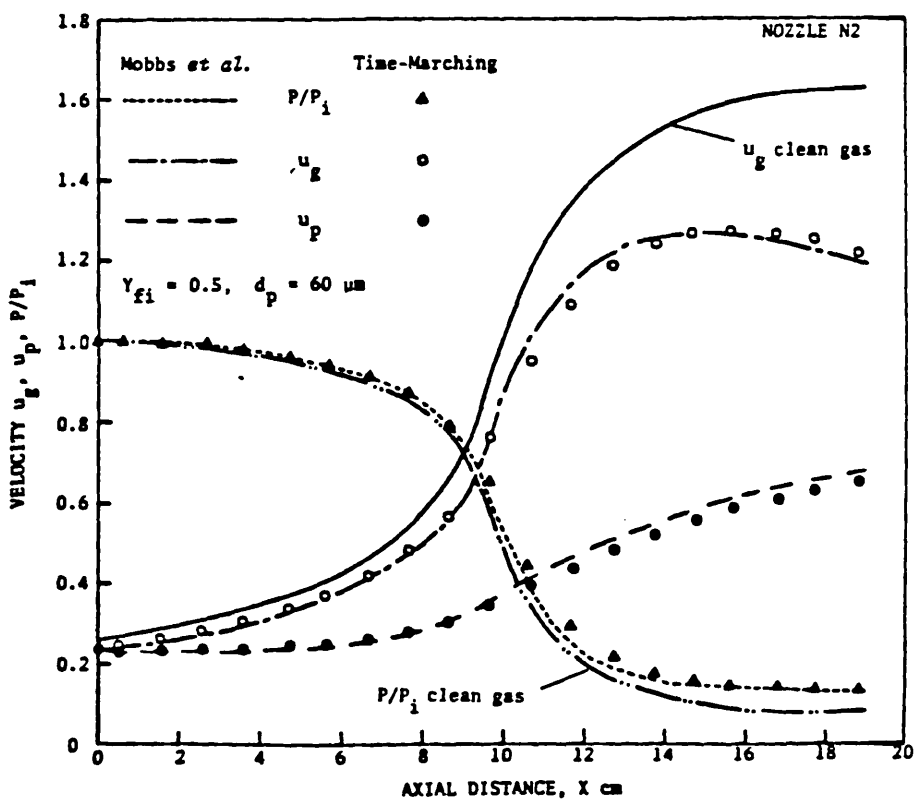


Fig. 5.68 Comparison of the time-marching model's predictions with those of Mobbs *et al.* for Y_{fi} = 0.5 in nozzle N2

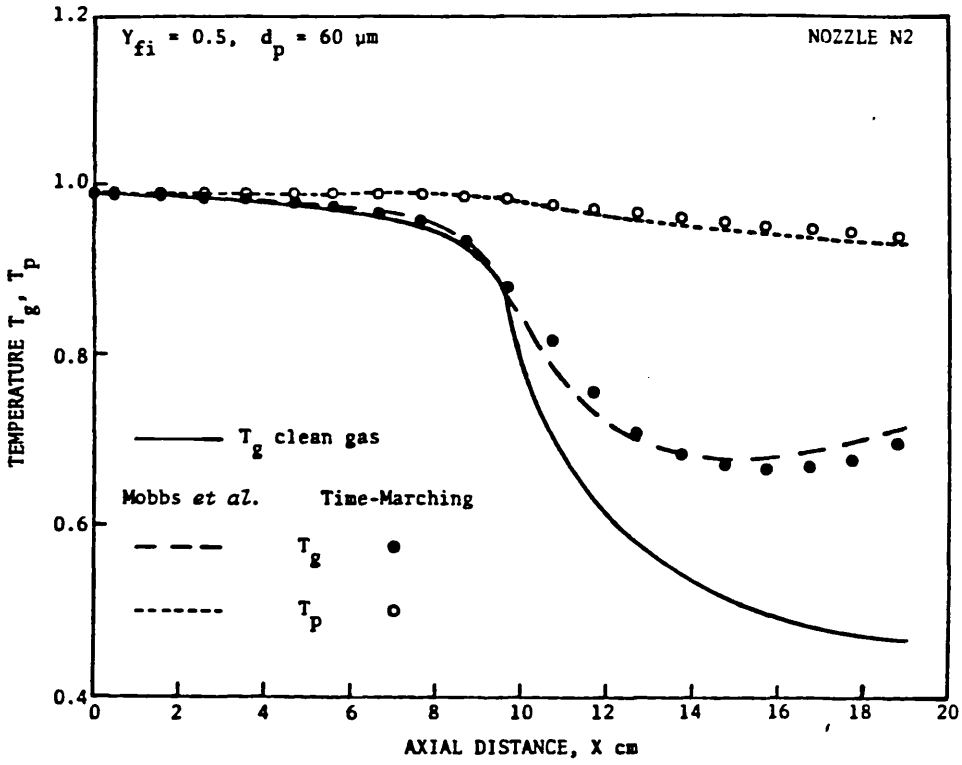


Fig. 5.69 Comparison of the gas and particle temperature predictions with those of Mobbs *et al.* for Y_{fi} = 0.5 in nozzle N2

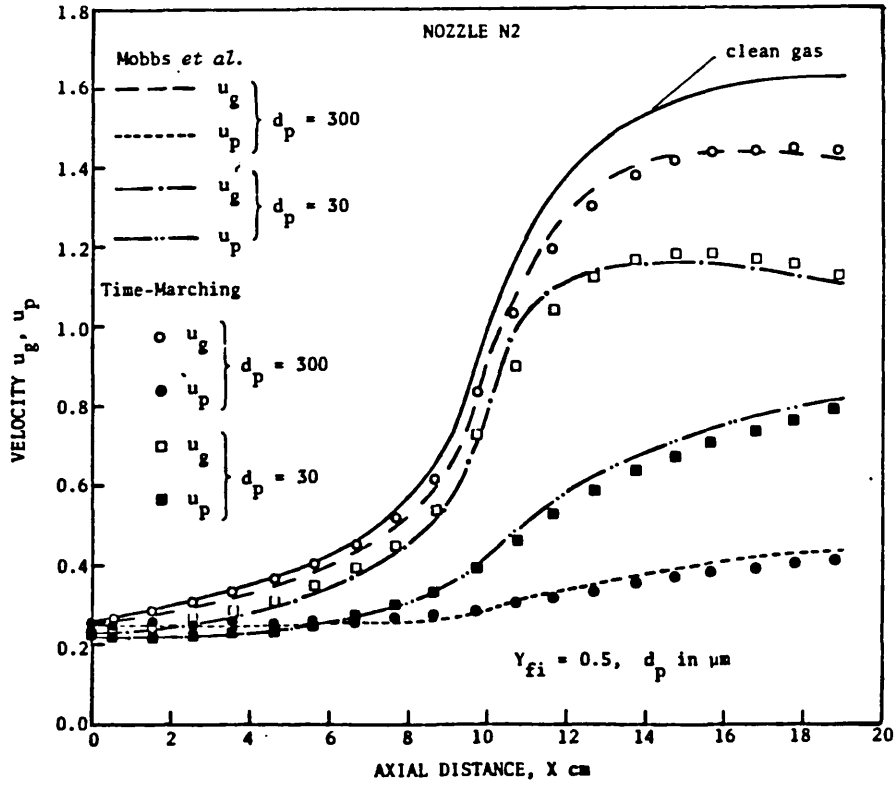


Fig. 5.70 Comparison of the predictions of gas and particle velocities for various particle sizes with those of Mobbs *et al.* for Y_{fi} = 0.5

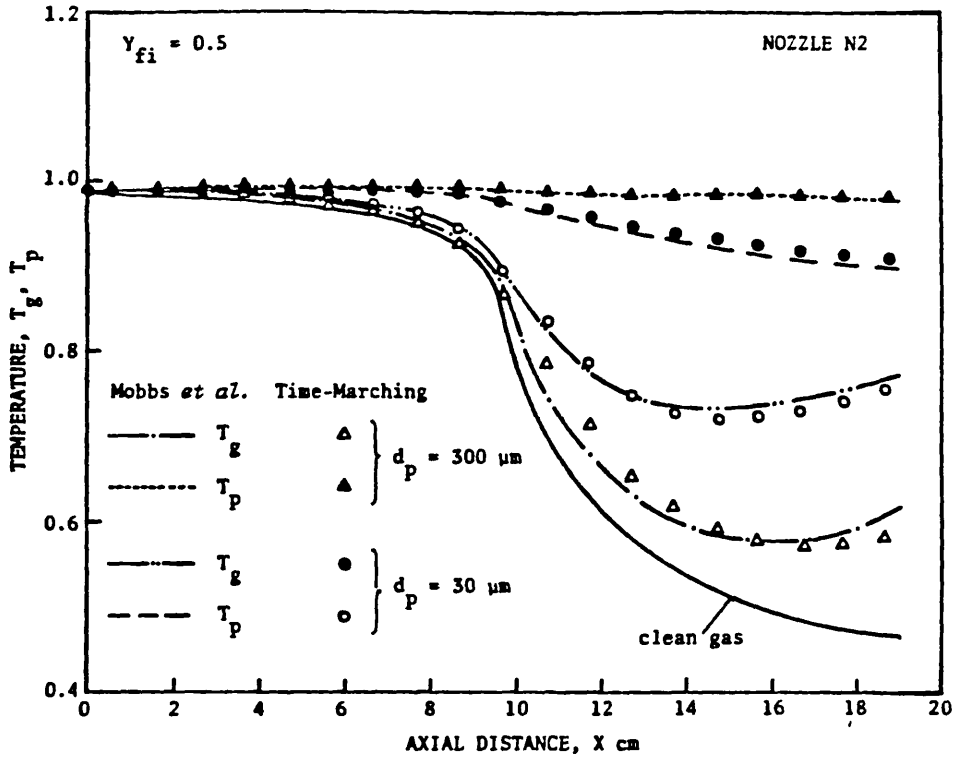


Fig. 5.71 Predictions of gas and particle temperatures for different particle sizes as compared with Mobbs *et al.* results

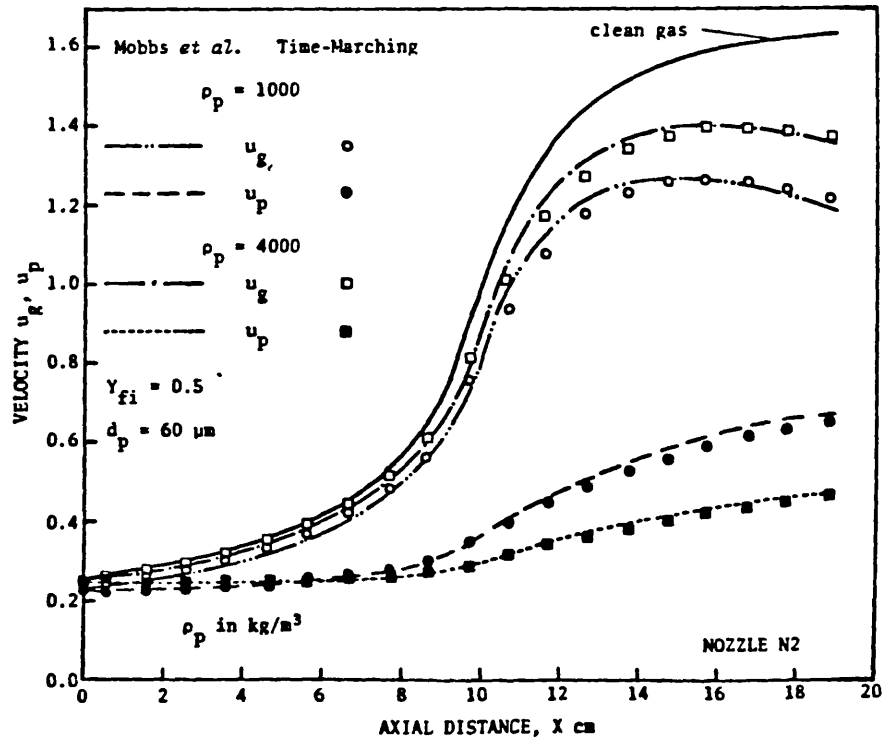


Fig. 5.72 Comparison of predicted gas and particle velocities for different particle material density with those obtained by Mobbs *et al.* in nozzle N2, Y_{fi} = 0.5

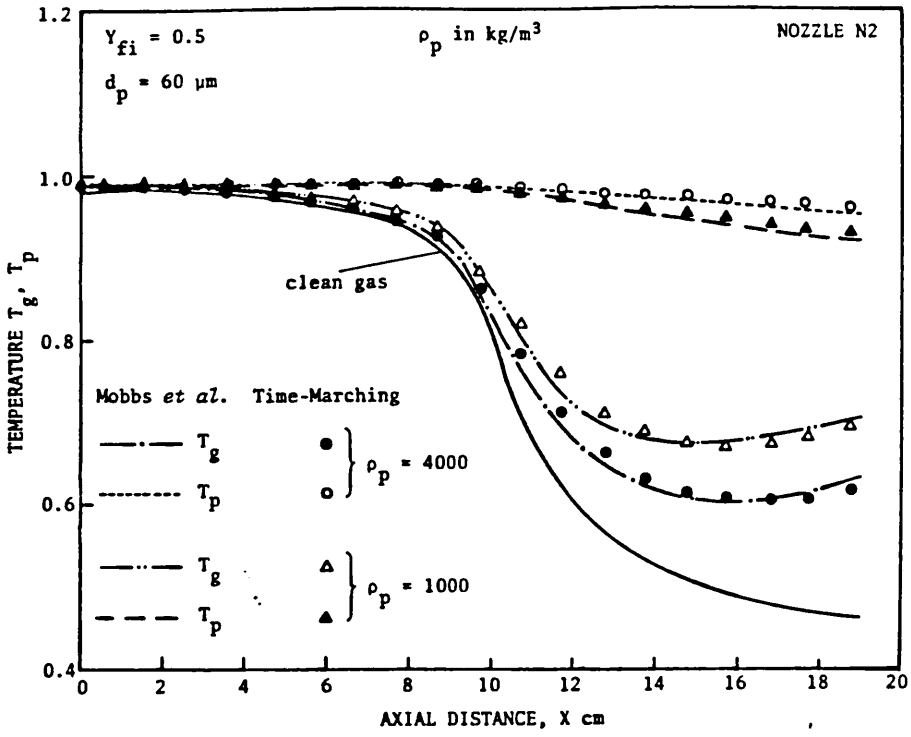


Fig. 5.73 Comparison of gas and particle temperatures for different particle densities with those of Mobbs *et al.* for Y_{fi} = 0.5

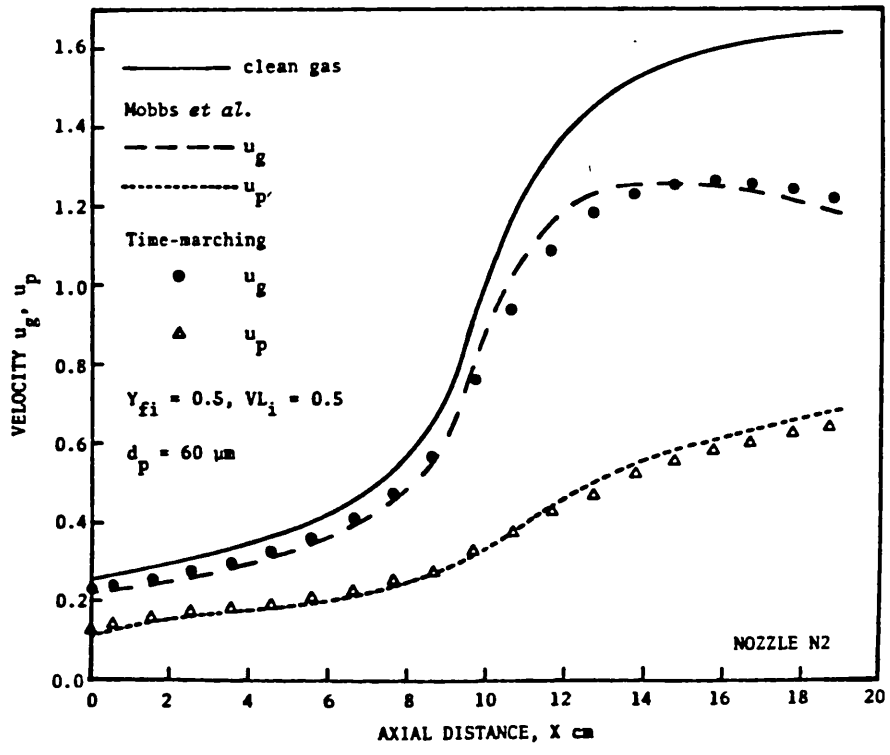


Fig. 5.74 Comparison of gas and particle velocities for VL_i = 0.5 with those obtained by Mobbs *et al.* for Y_{fi} = 0.5

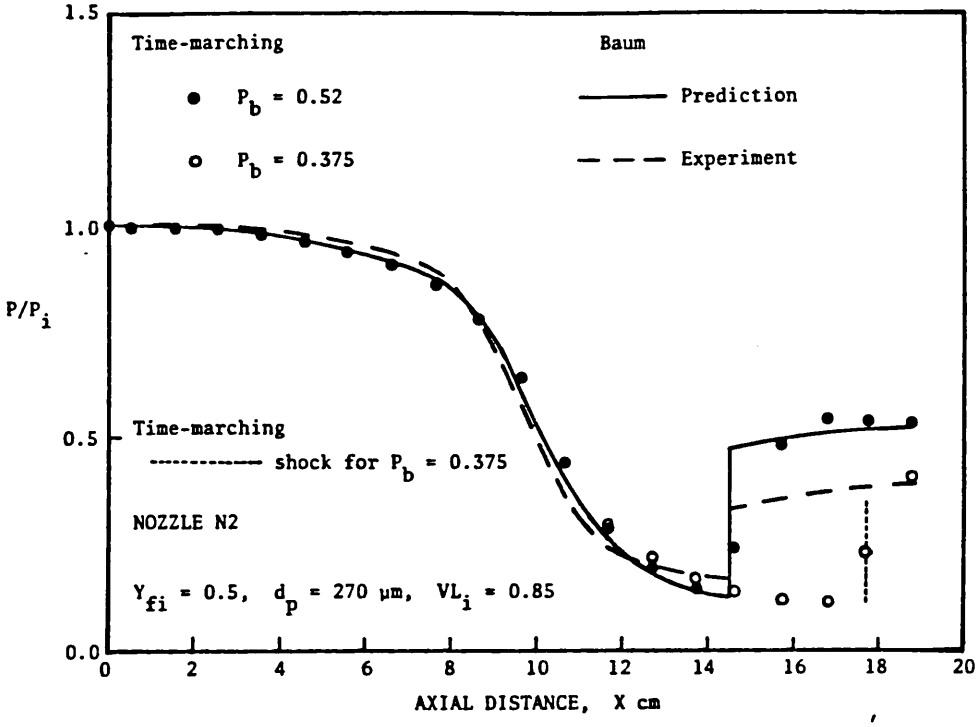


Fig. 5.75 Comparison of pressure ratio predictions along nozzle N2 with Baum's predictions and measurements (shock at x = 14.5 cm)

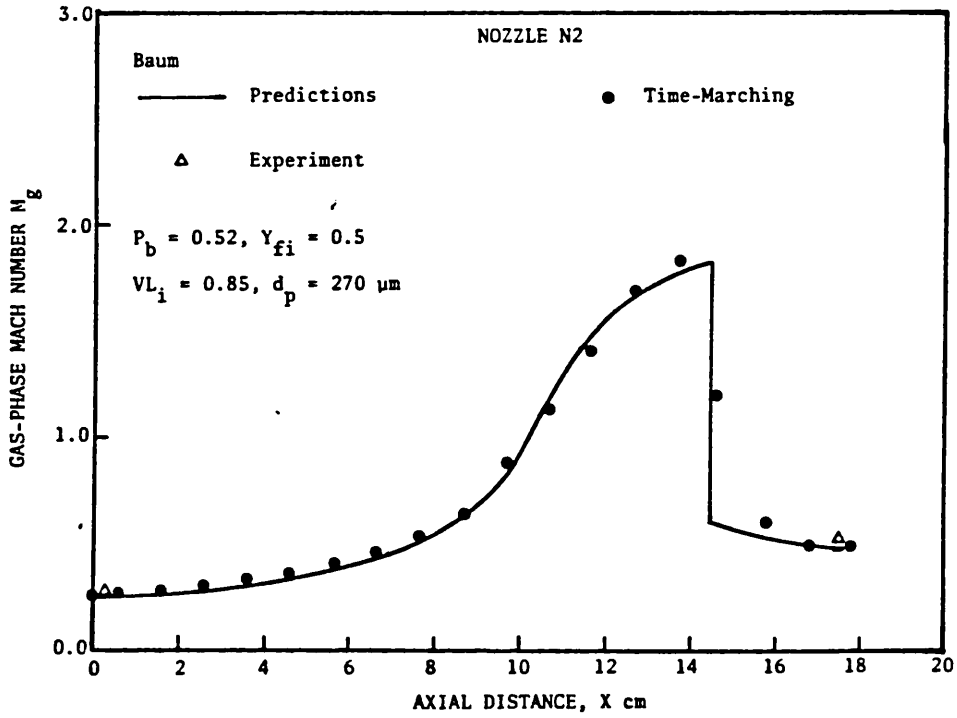


Fig. 5.76 Comparison of gas Mach number predictions along nozzle N2 with Baum's predictions and experiment (shock at x = 14.5 cm)

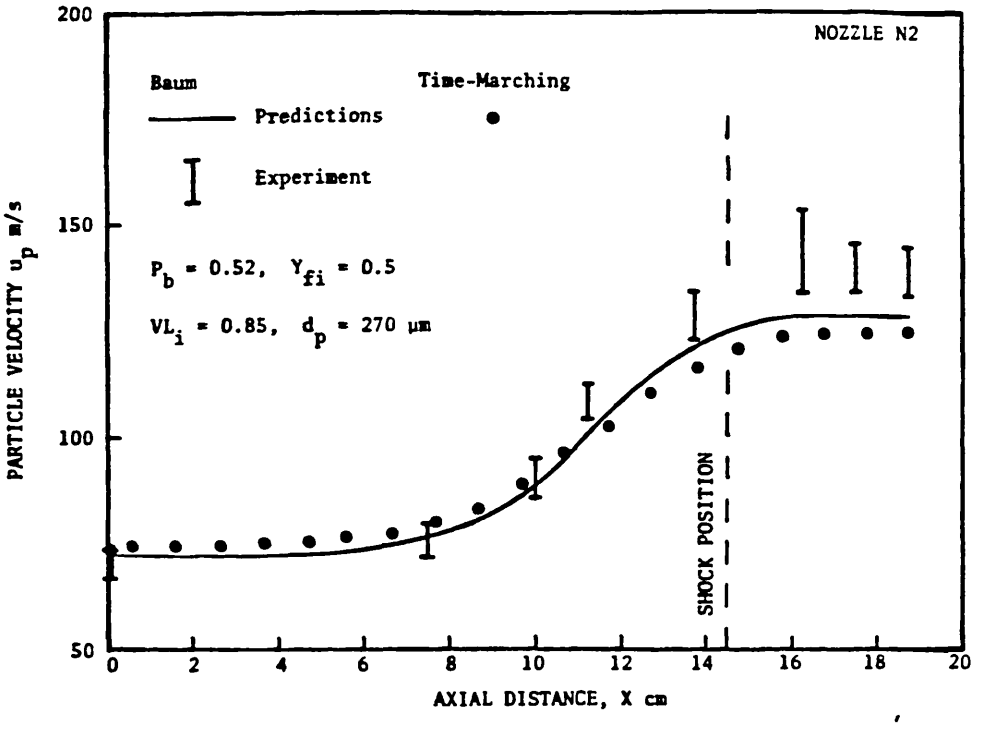


Fig. 5.77 Comparison of particle velocity predictions with Baum's predictions and experiment in nozzle N2 (shock at x = 14.5 cm)

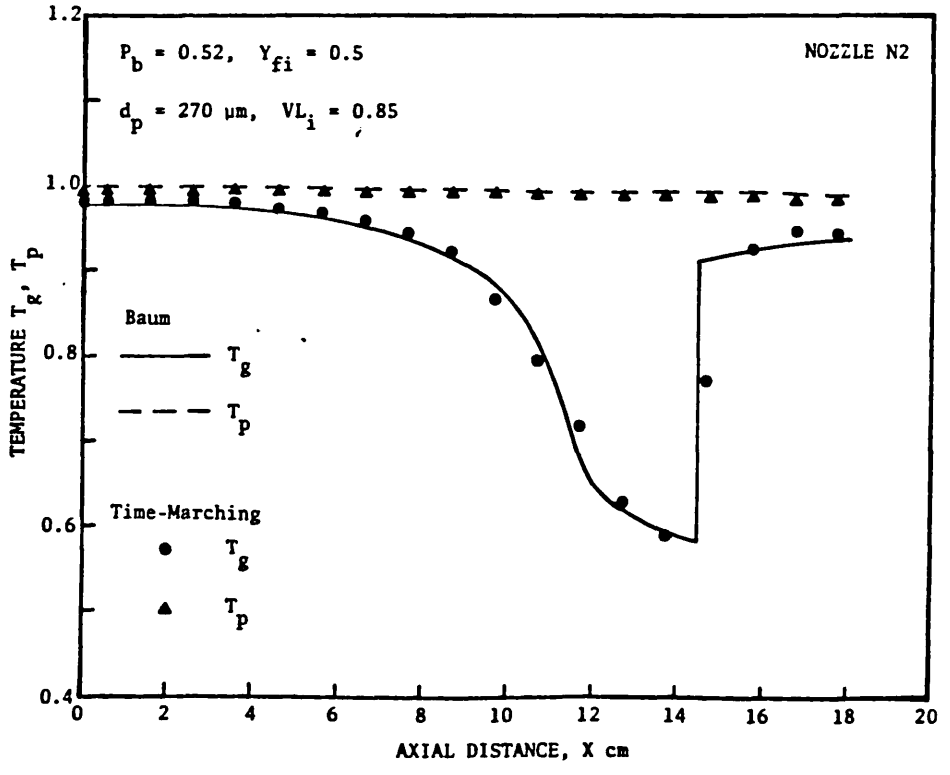


Fig. 5.78 Comparison of gas and particle temperatures predictions with Baum's predictions in nozzle N2 (shock at x = 14.5 cm)

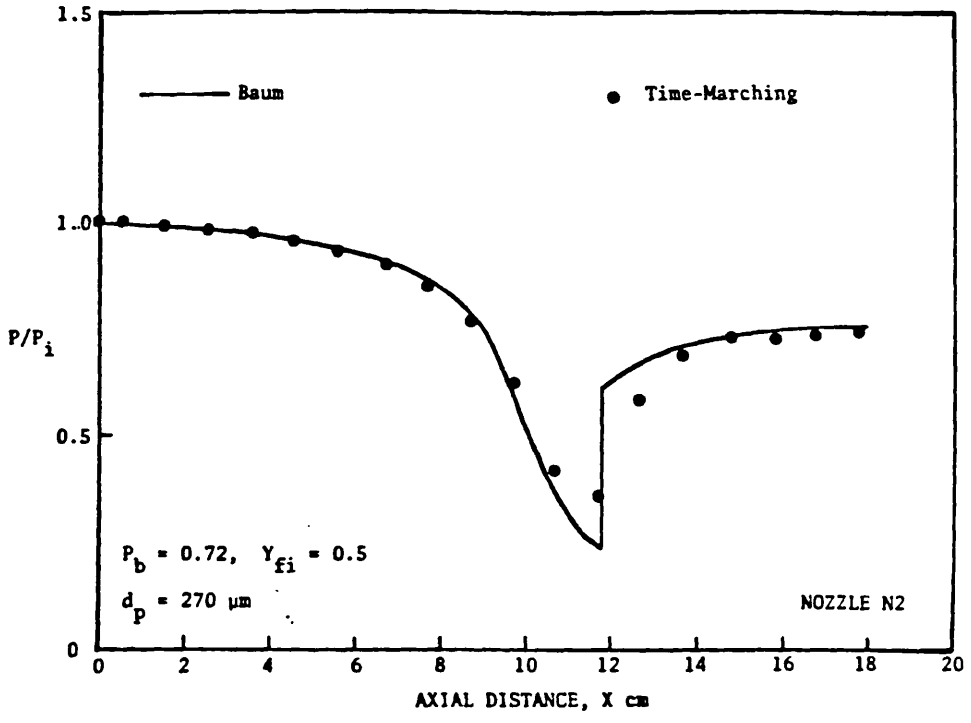


Fig. 5.79 Comparison of pressure ratio predictions in nozzle N2 with those of Baum (shock at x = 11.75 cm)

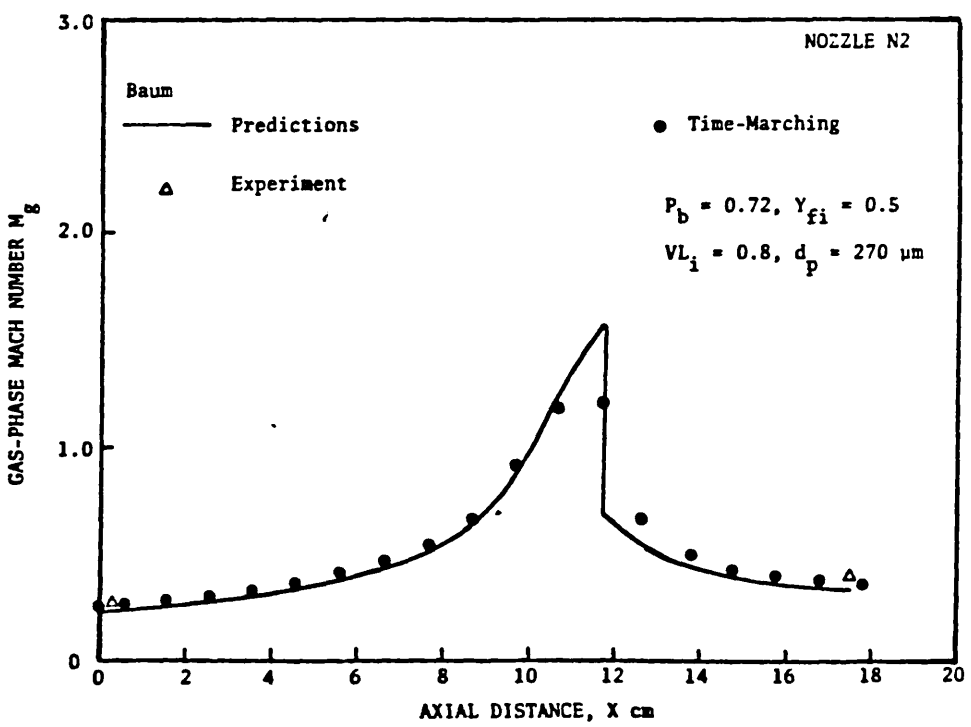


Fig. 5.80 Comparison of gas Mach number predictions with Baum's predictions and measurements (shock at x = 11.75 cm)

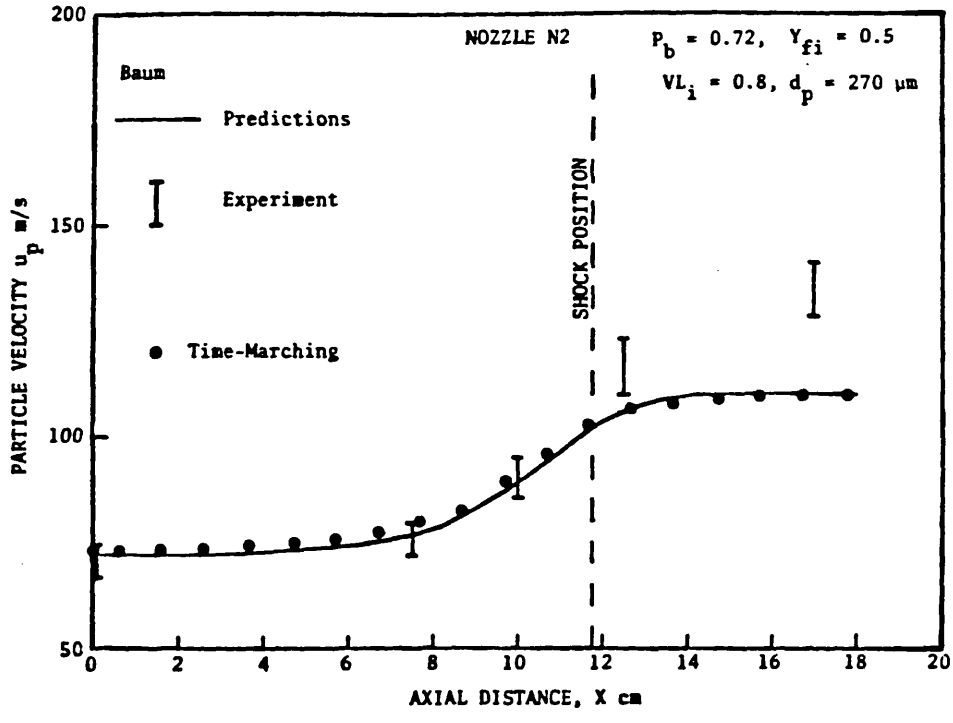


Fig. 5.81 Comparison of particle velocity predictions with Baum's predictions and measurements (shock at x = 11.75 cm)

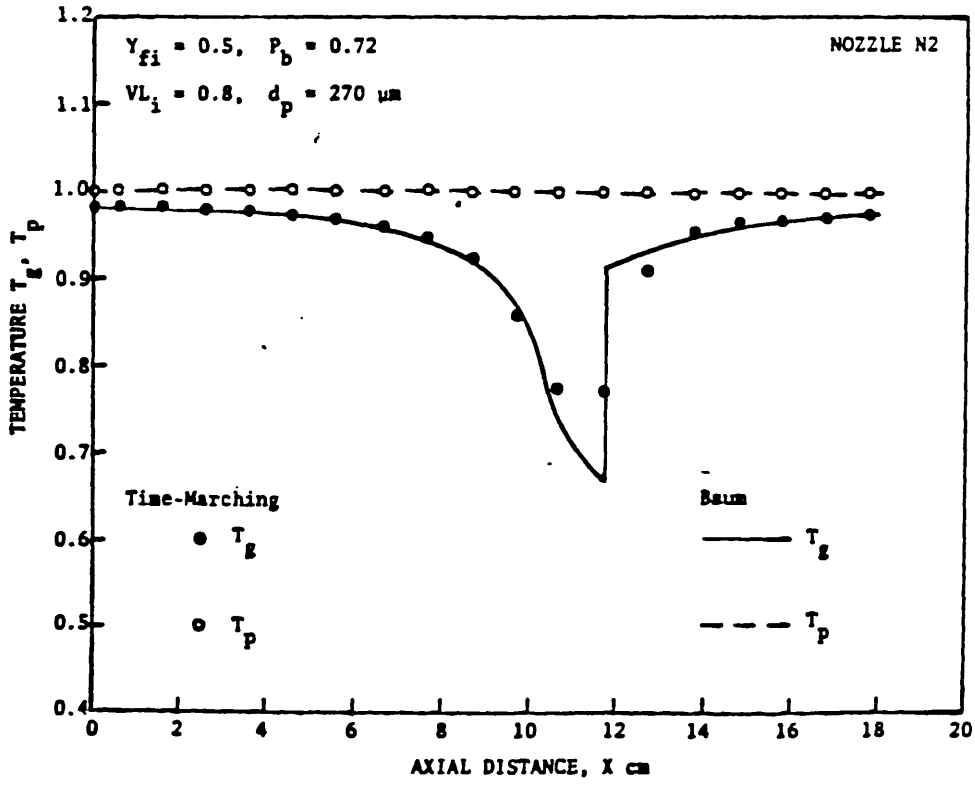


Fig. 5.82 Comparison of gas and particle temperatures predictions with Baum's predictions in nozzle N2 (shock at x = 11.75 cm)

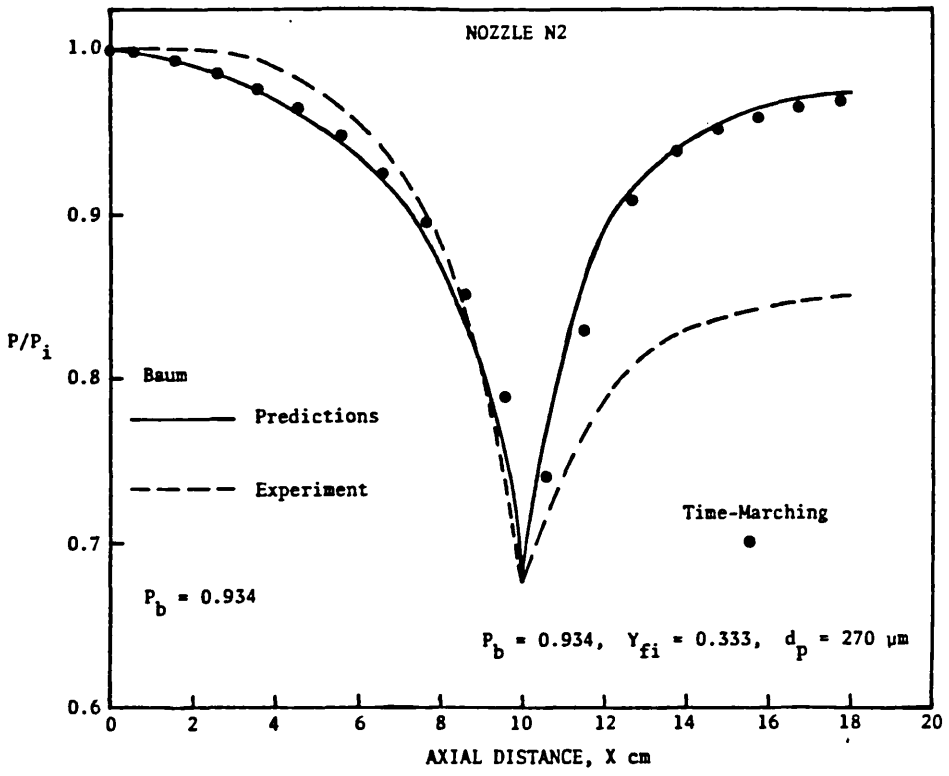


Fig. 5.83 Comparison of pressure ratio predictions with Baum's predictions and measurements in nozzle N2 (subsonic flow)

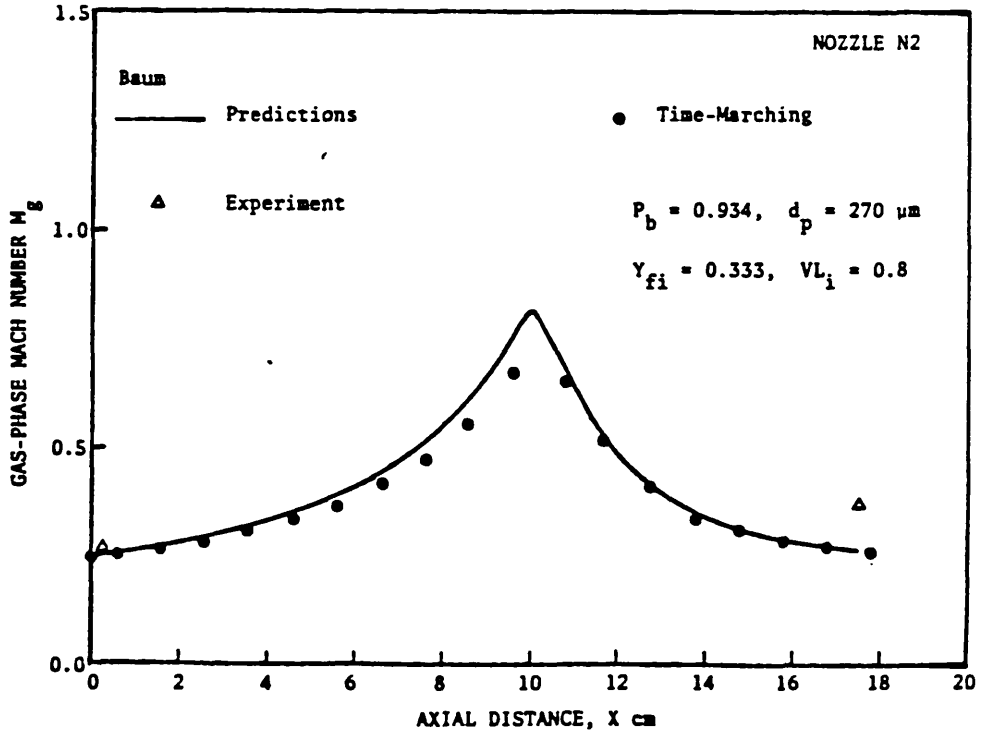


Fig. 5.84 Comparison of gas-phase Mach number predictions with Baum's predictions and measurements along nozzle N2 (subsonic flow)

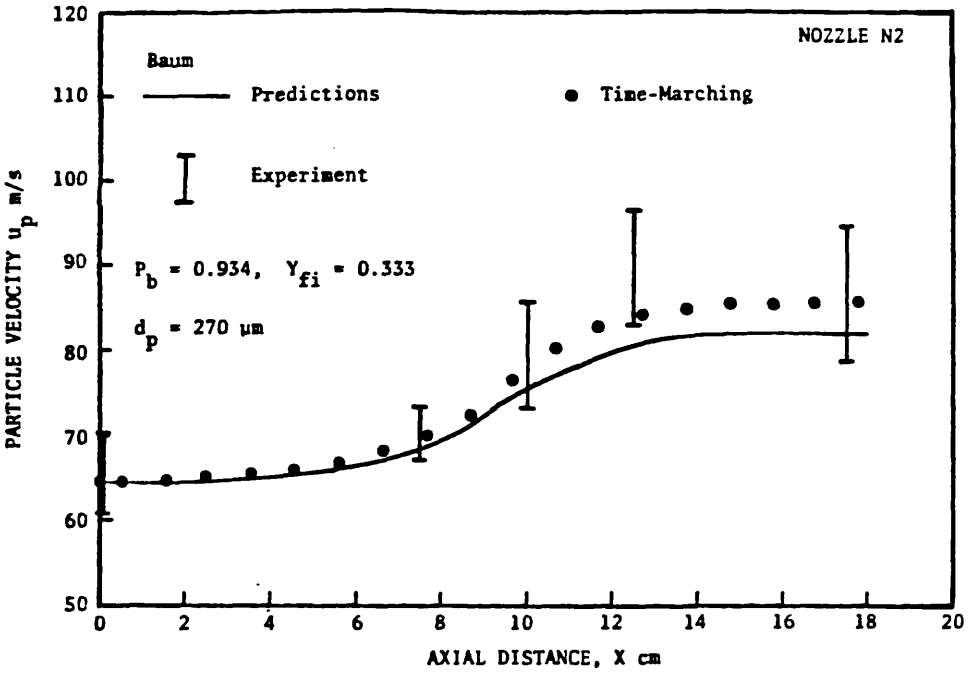


Fig. 5.85 Comparison of particle velocity predictions with Baum's predictions and measurements in nozzle N2 (subsonic flow)

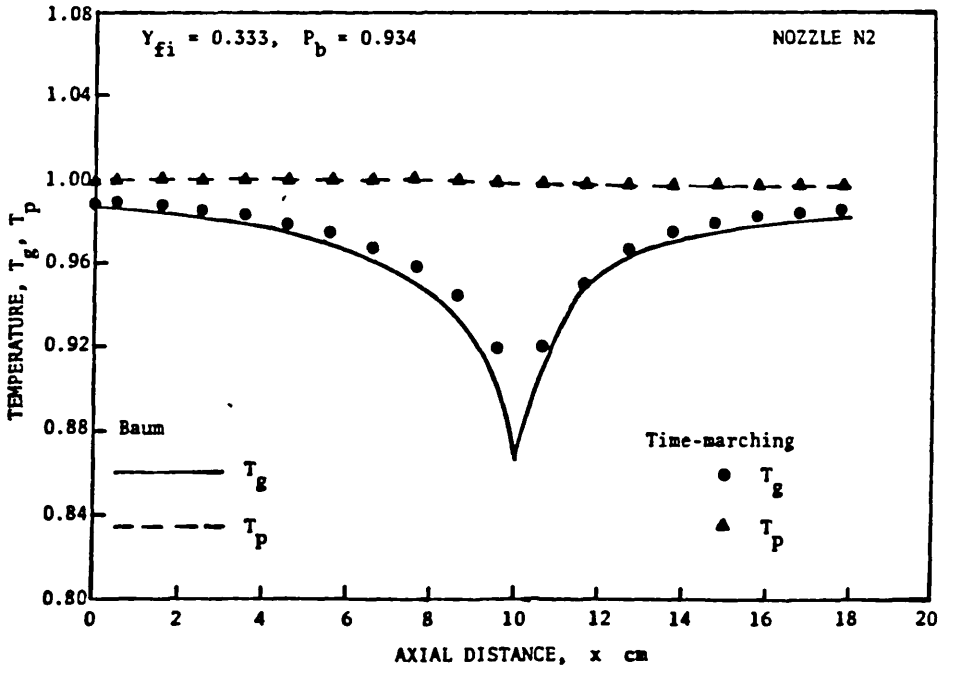


Fig. 5.86 Comparison of gas and particle temperature predictions with Baum's predictions for a subsonic mixture flow

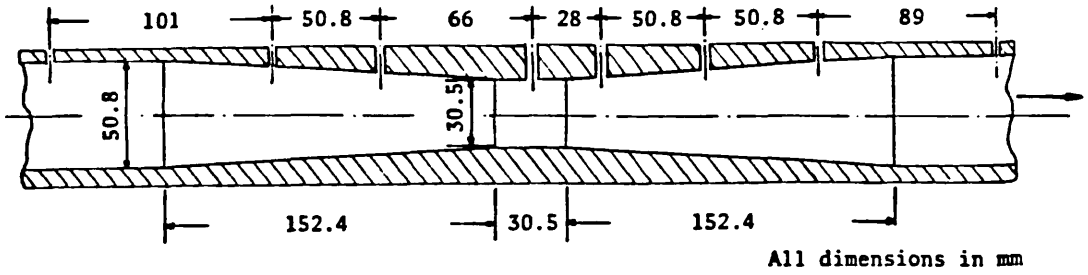


Fig. 5.87 Geometry of the venturi VE2 (ref. 29)

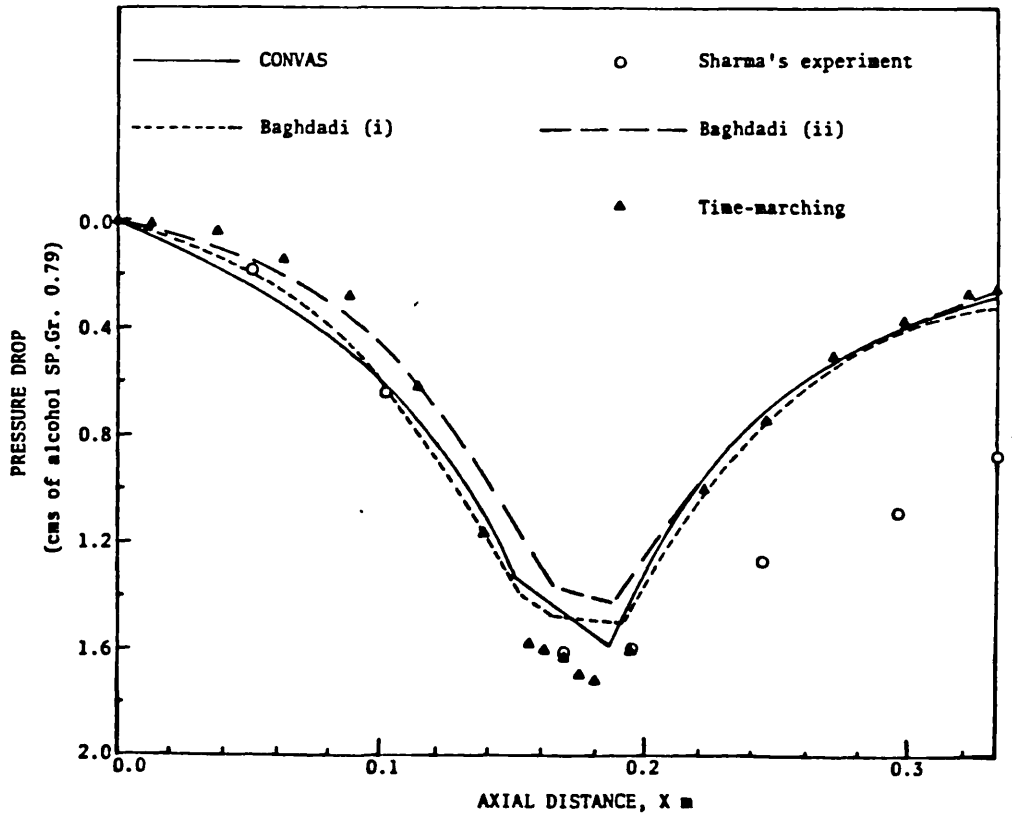


Fig. 5.88 Pressure drop along the venturi VE2 for loading ratio of 0.29

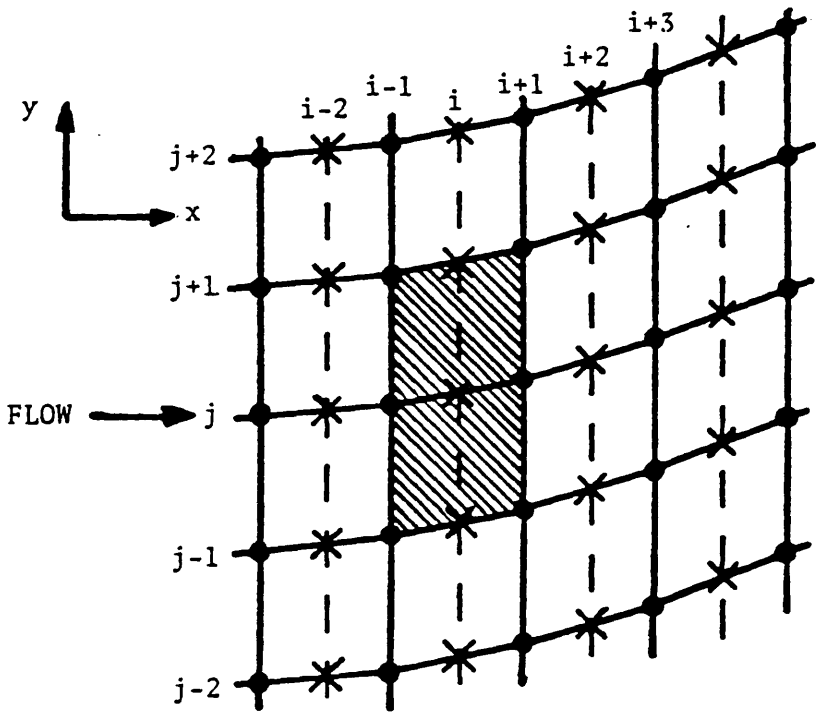


Fig. 6.1: Computational grid for the time-marching two-dimensional model showing an interior cell and surroundings

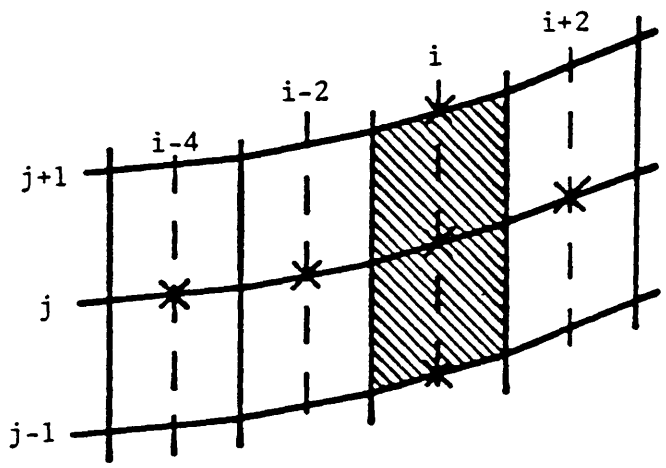


Fig. 6.2: Star of mesh points for calculating variables other than pressure

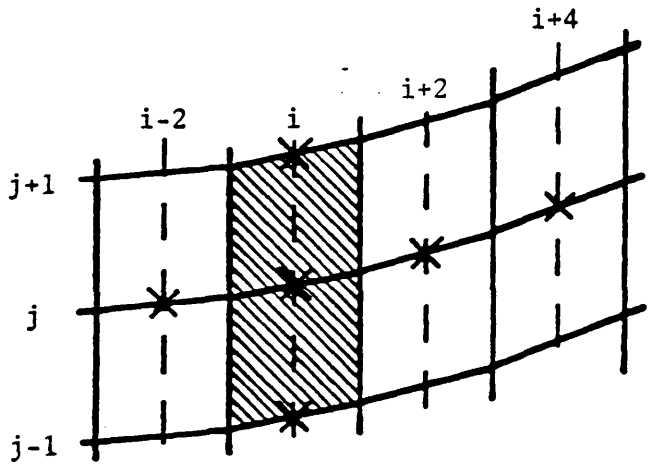


Fig. 6.3: Star of mesh points for pressure approximation

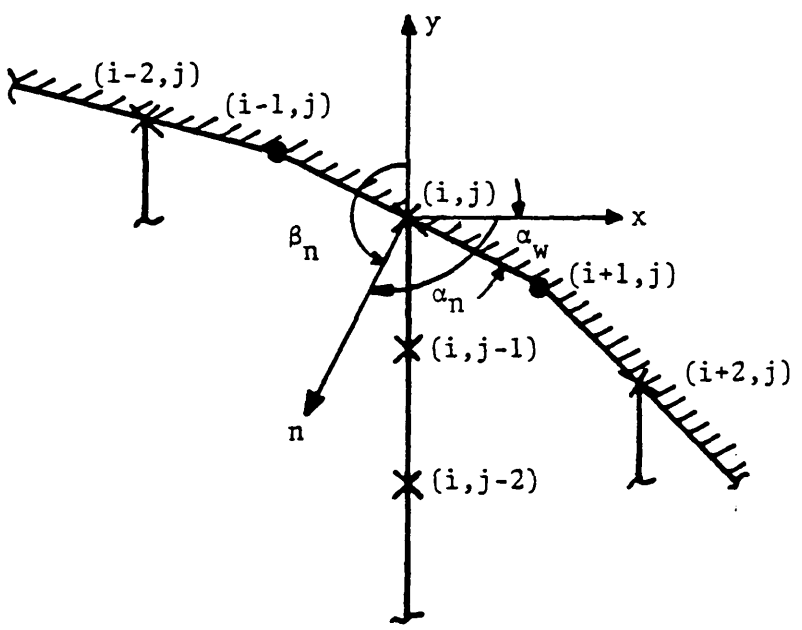


Fig. 6.4: Angles at wall calculation points

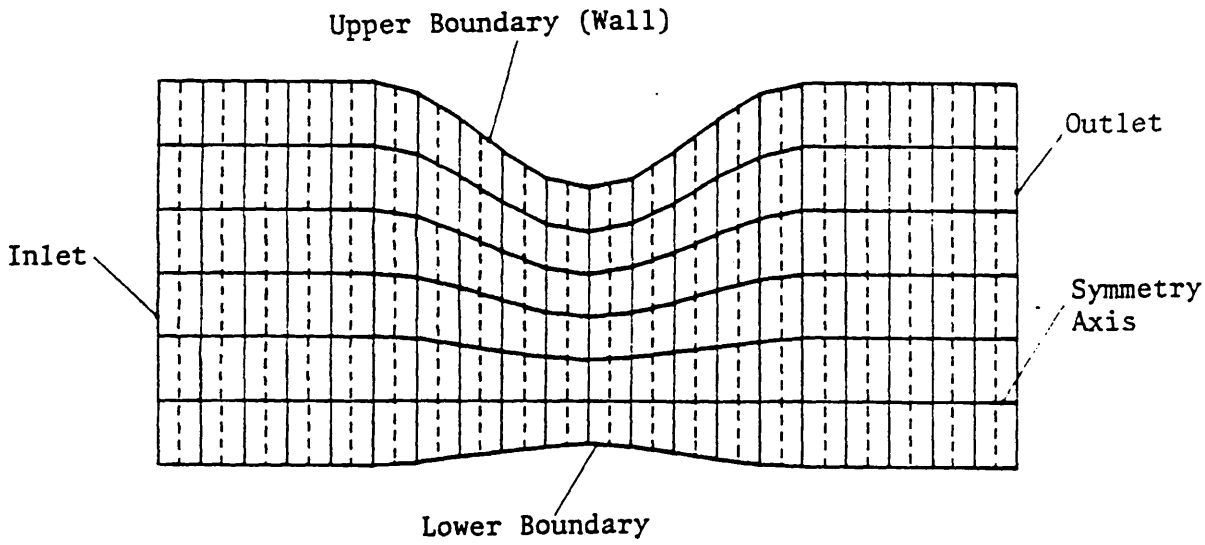


Fig. 6.5: Two-dimensional grid for nozzle N1 (not to scale)

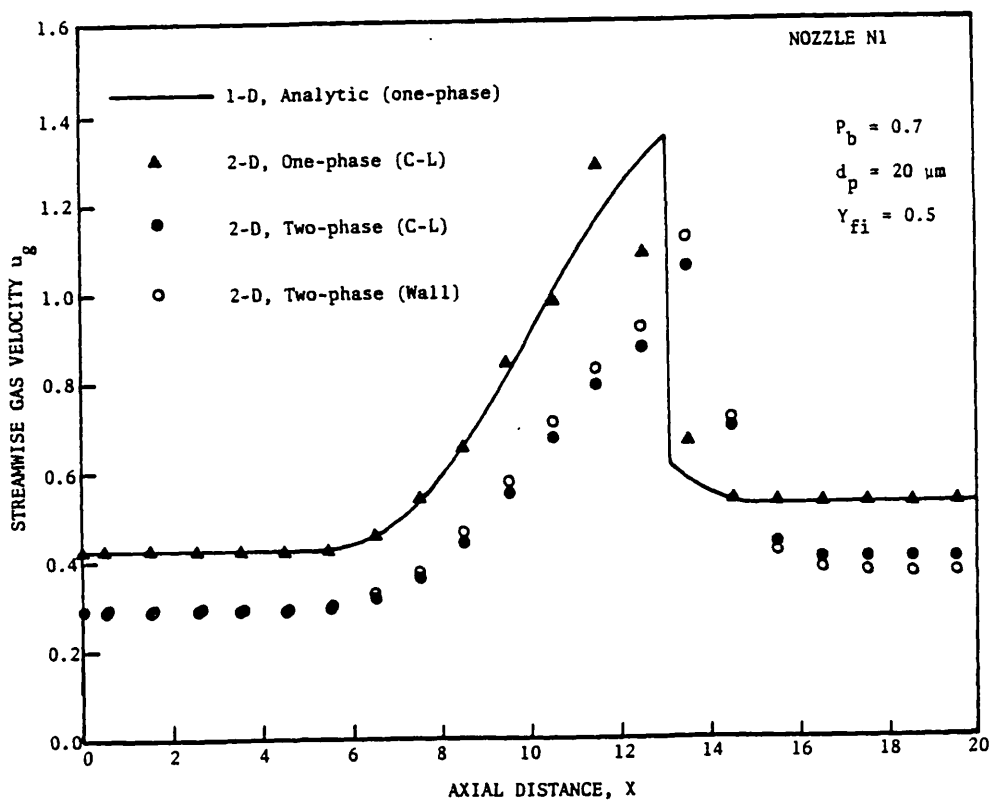


Fig. 6.6: Axis and wall gas-phase velocity profiles in nozzle N1 (shocked mixture flow)

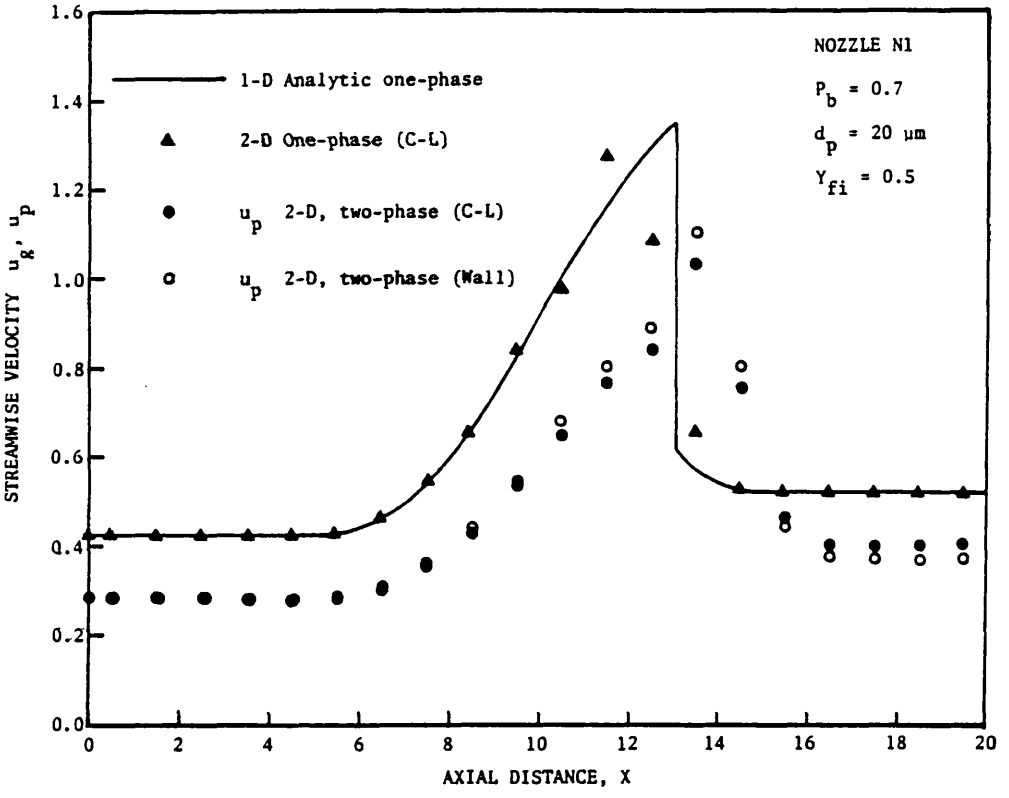


Fig. 6.7: Axis and wall particle velocity profiles in nozzle N1 (shocked mixture flow)

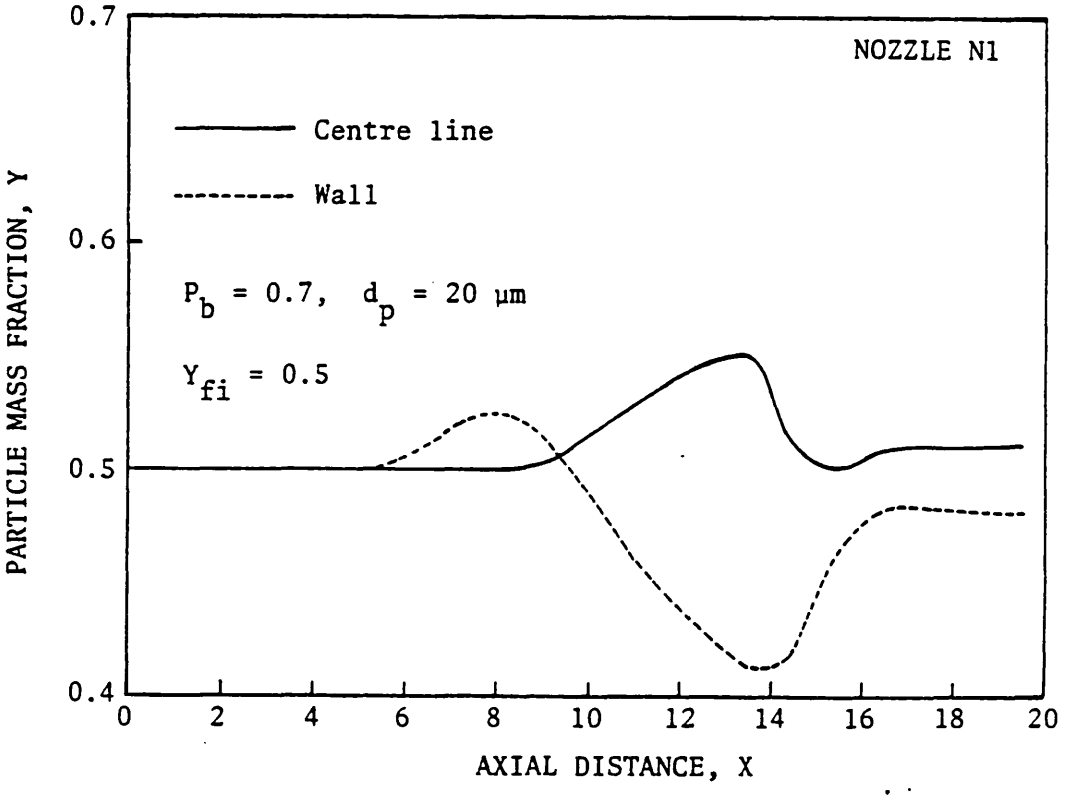
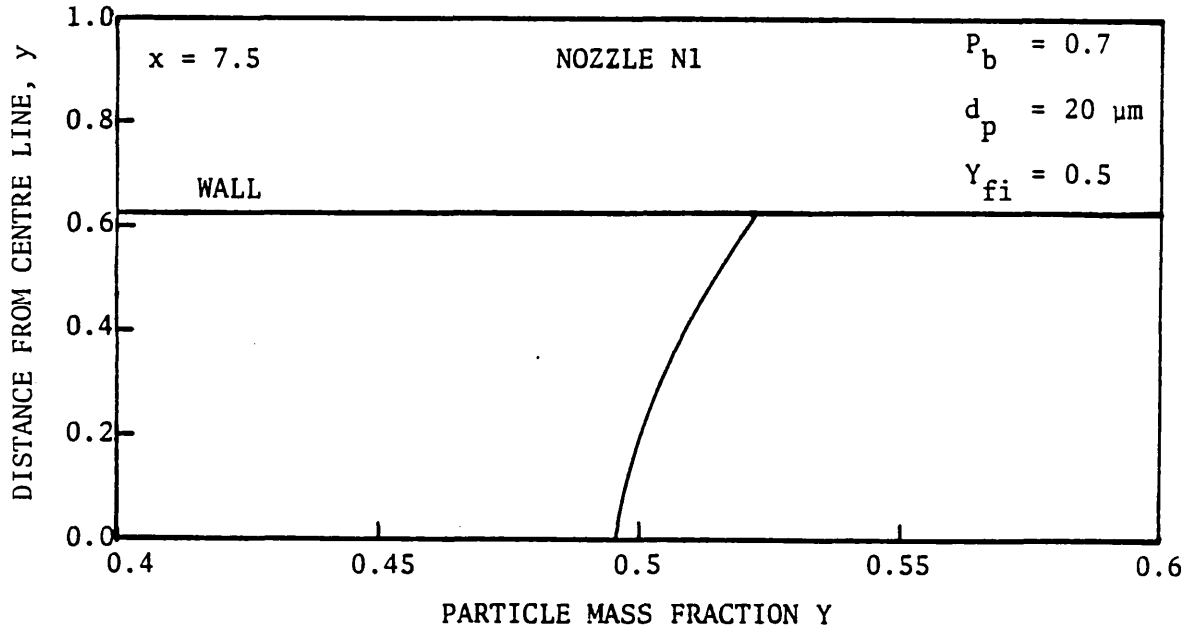
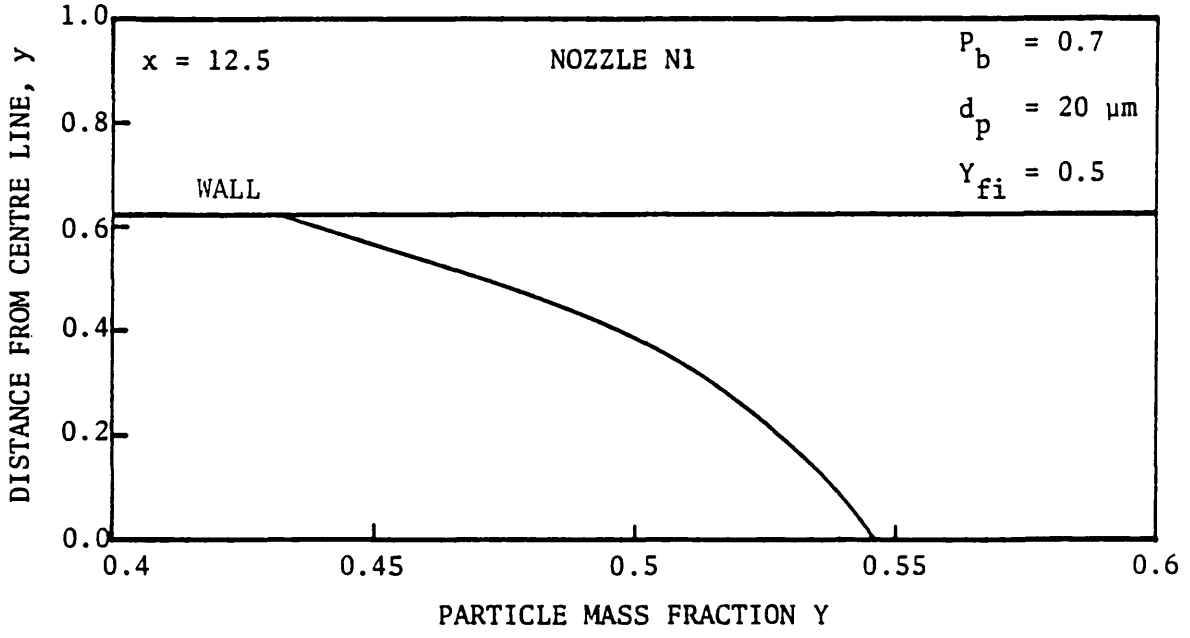


Fig. 6.8: Axis and wall particle mass fraction distribution in nozzle N1 (shocked mixture flow)



(a) before the throat



(b) After the throat

Fig. 6.9: Crosswise variations of particle mass fraction in nozzle N1

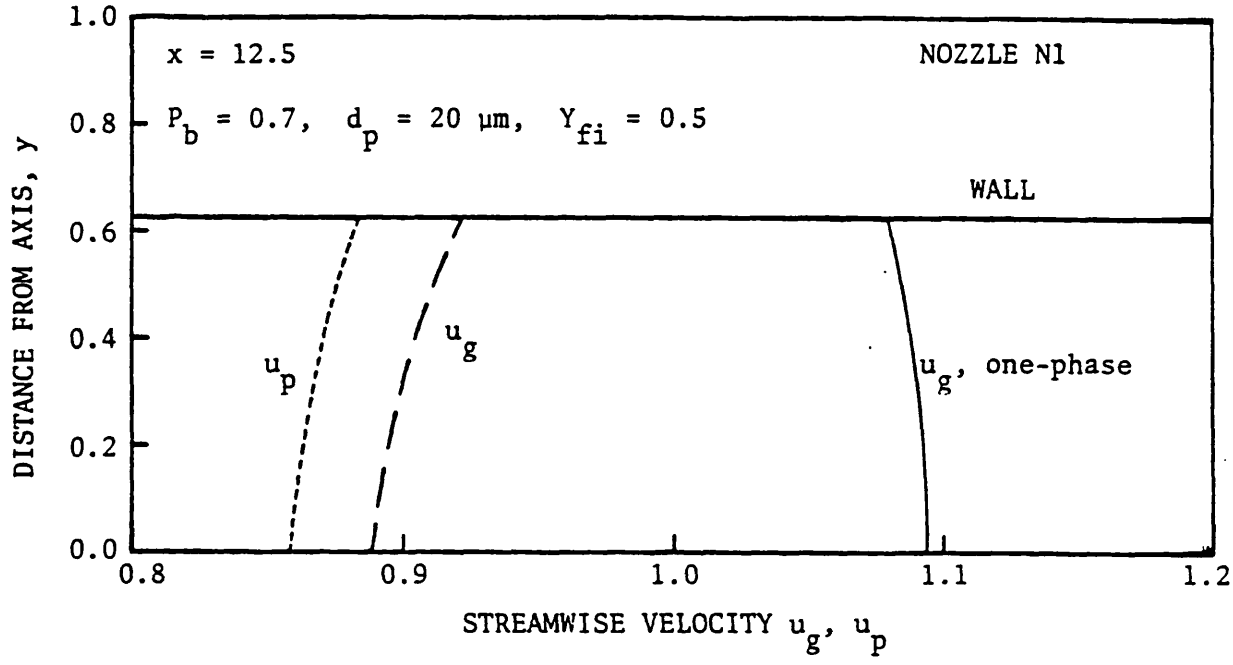


Fig. 6.10: Crosswise variations of the gas and particle velocities after the throat in nozzle N1

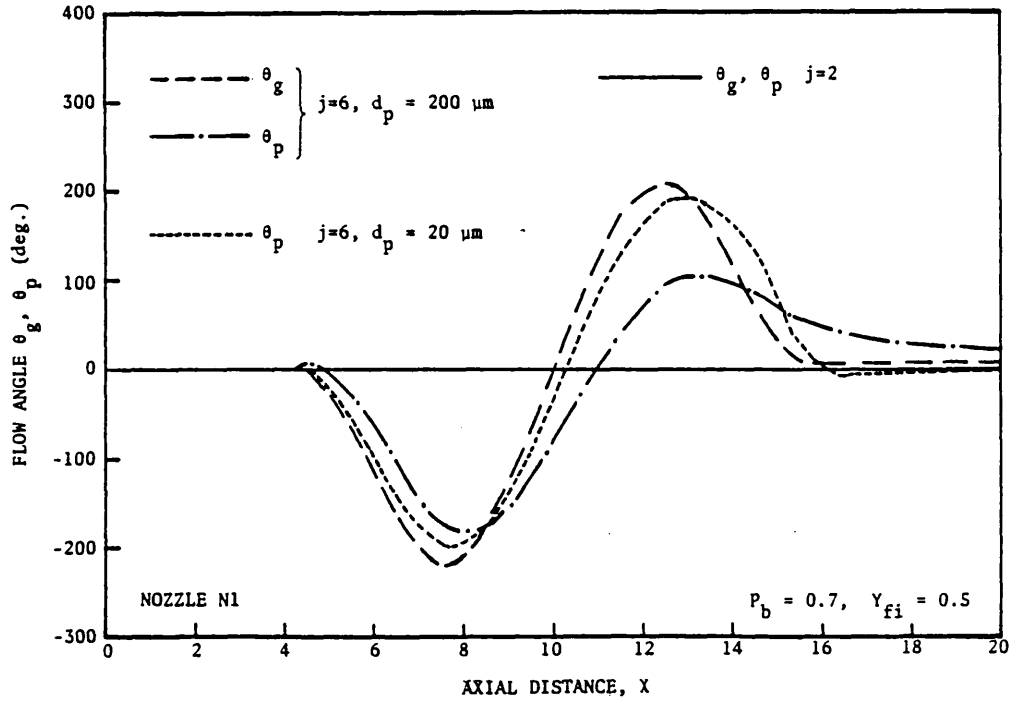


Fig. 6.11: Calculated flow angles for different particle sizes along quasi-streamlines j = 2 and 6

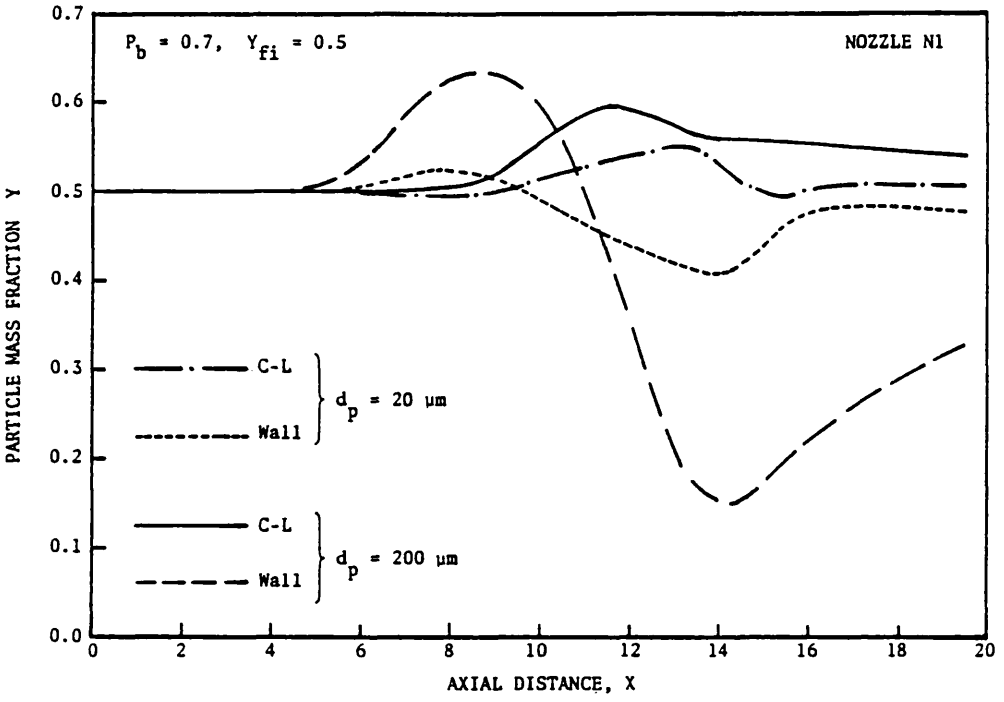
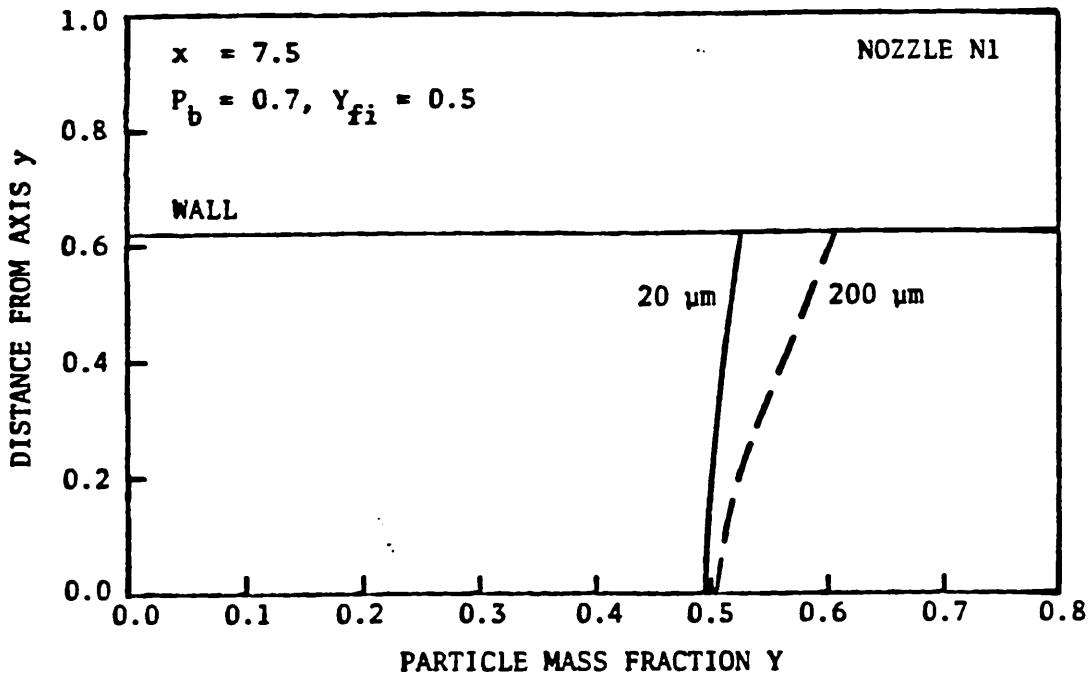
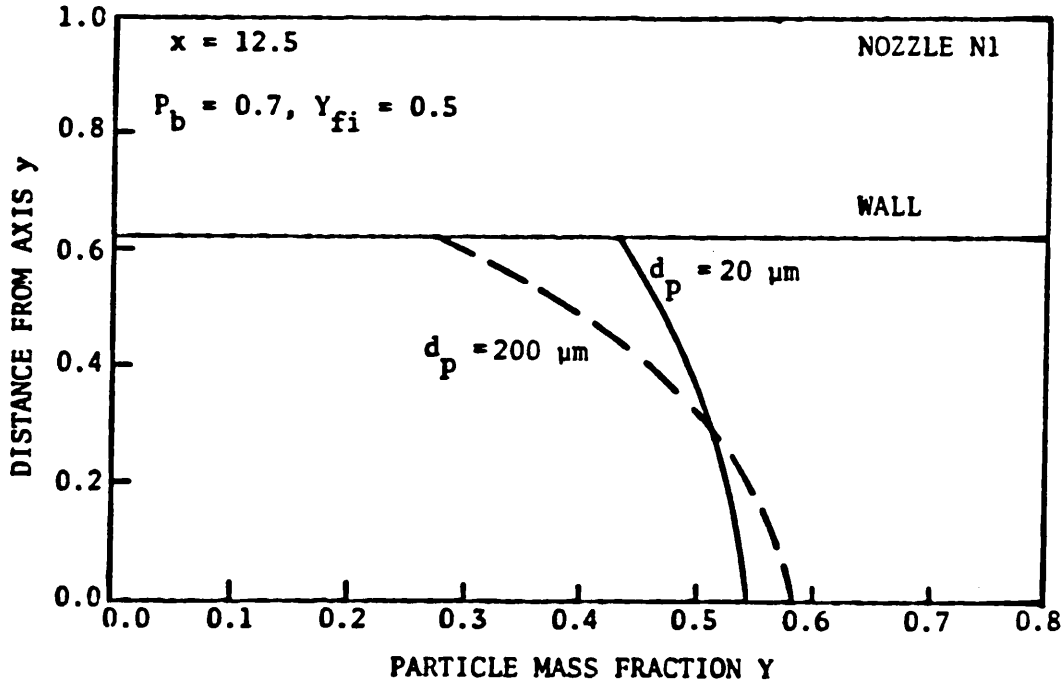


Fig. 6.12: Comparison of the particle mass fraction distribution for different particle sizes in nozzle N1

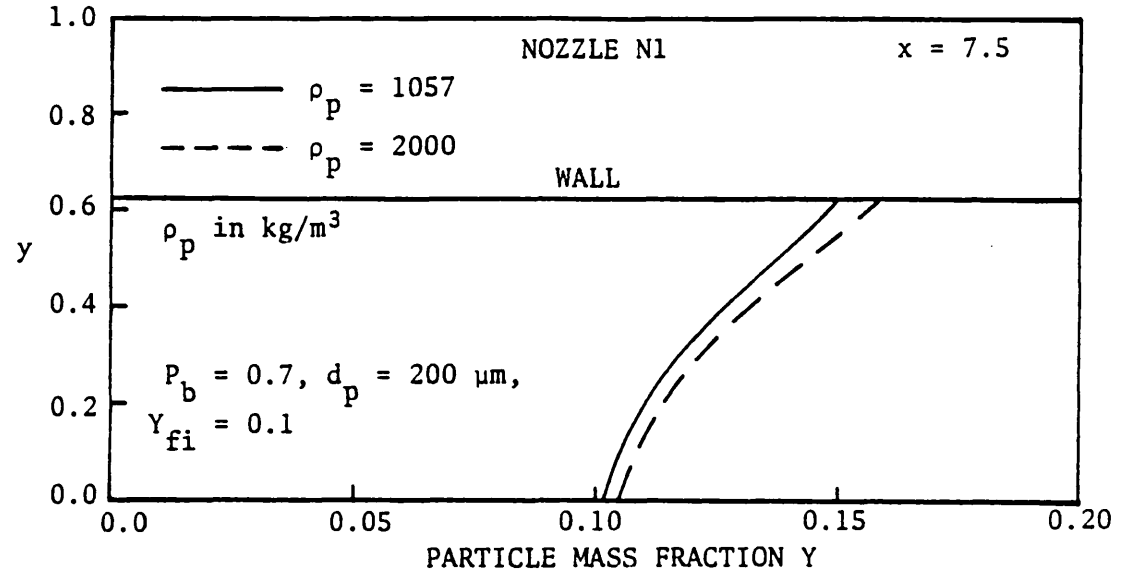


(a) Before the throat

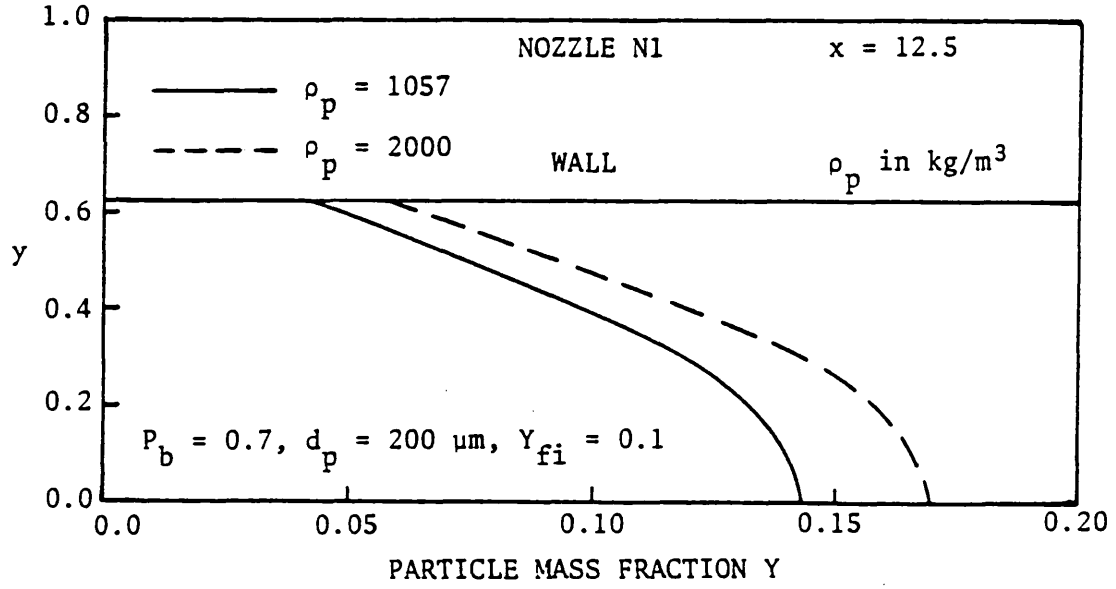


(b) After the throat

Fig. 6.13: Crosswise variations of the particle mass fraction for different particle sizes before and after the throat for shocked mixture flow in nozzle N1



(a) Before the throat



(b) After the throat

Fig. 6.14: Crosswise variations of the particle mass fraction for different particle material densities before and after the throat

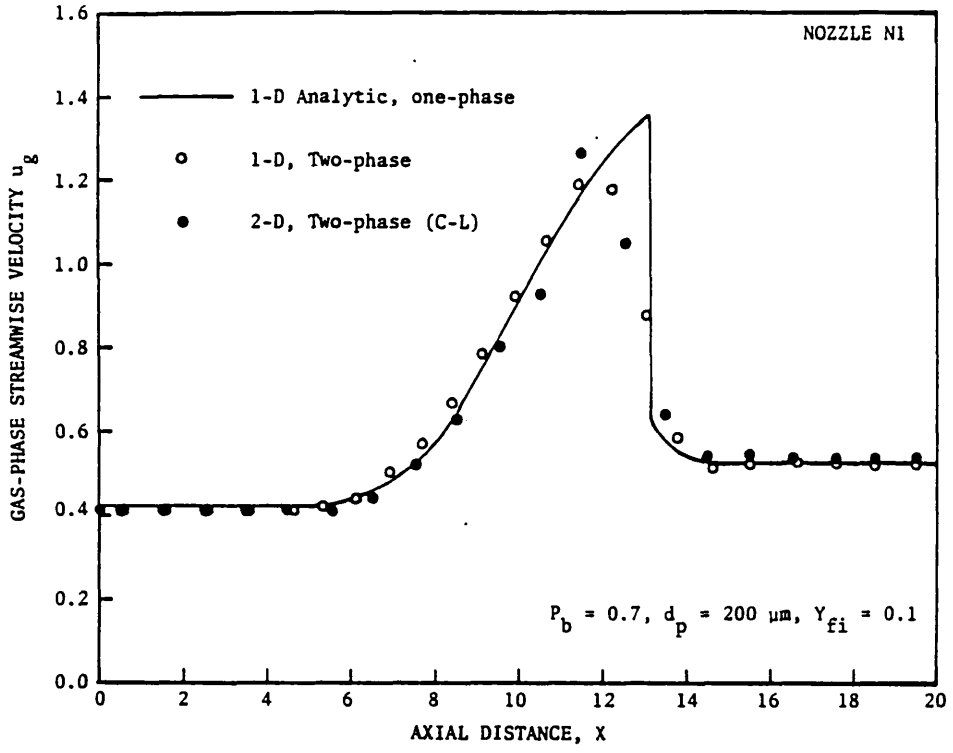


Fig. 6.15: Comparison between the gas-phase streamwise velocity along the nozzle (N1) axis as predicted by the one- and two-dimensional models

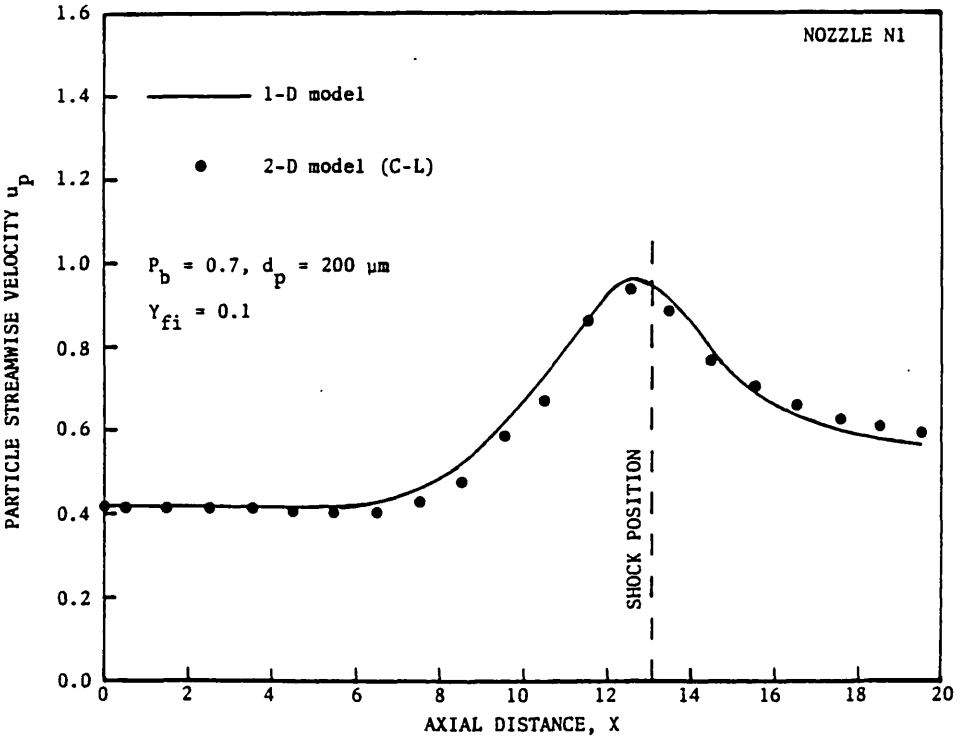


Fig. 6.16: Comparison between the particulate phase streamwise velocity along the nozzle (N1) axis as predicted by the one- and two-dimensional models

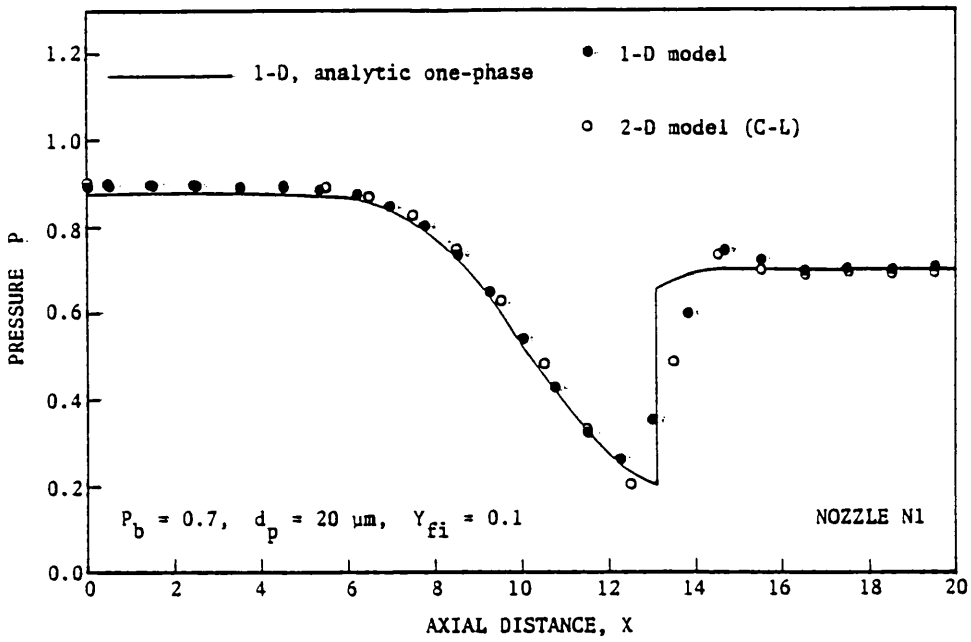


Fig. 6.17: Axial pressure along nozzle N1 as predicted by the one- and two-dimensional models

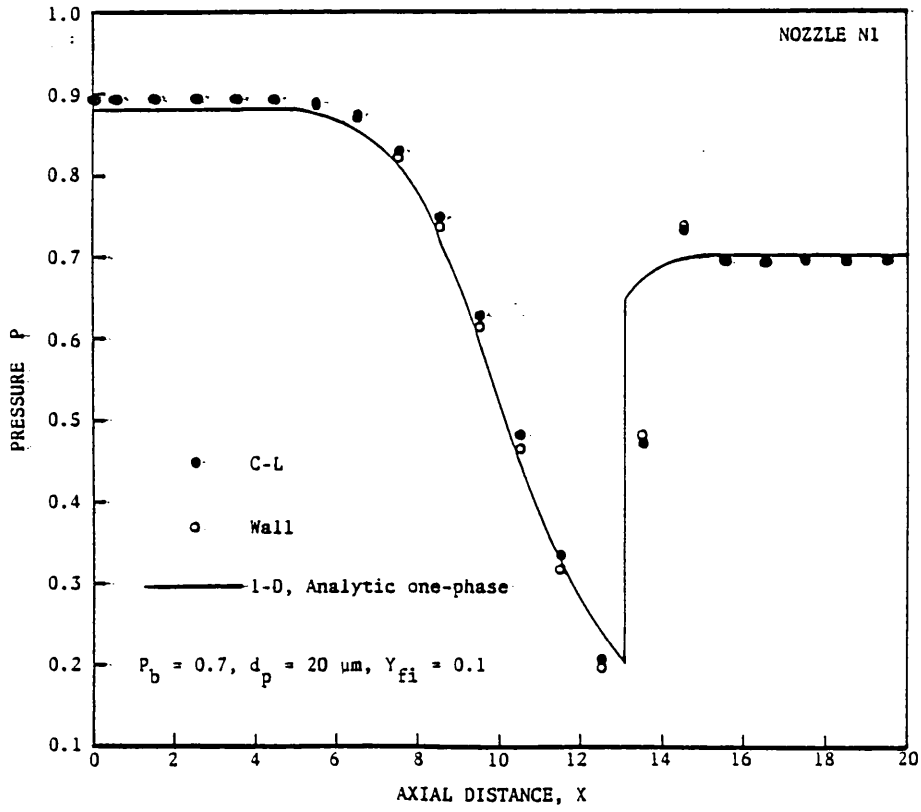


Fig. 6.18: Axis and wall pressures along nozzle N1 as predicted by the two-dimensional model

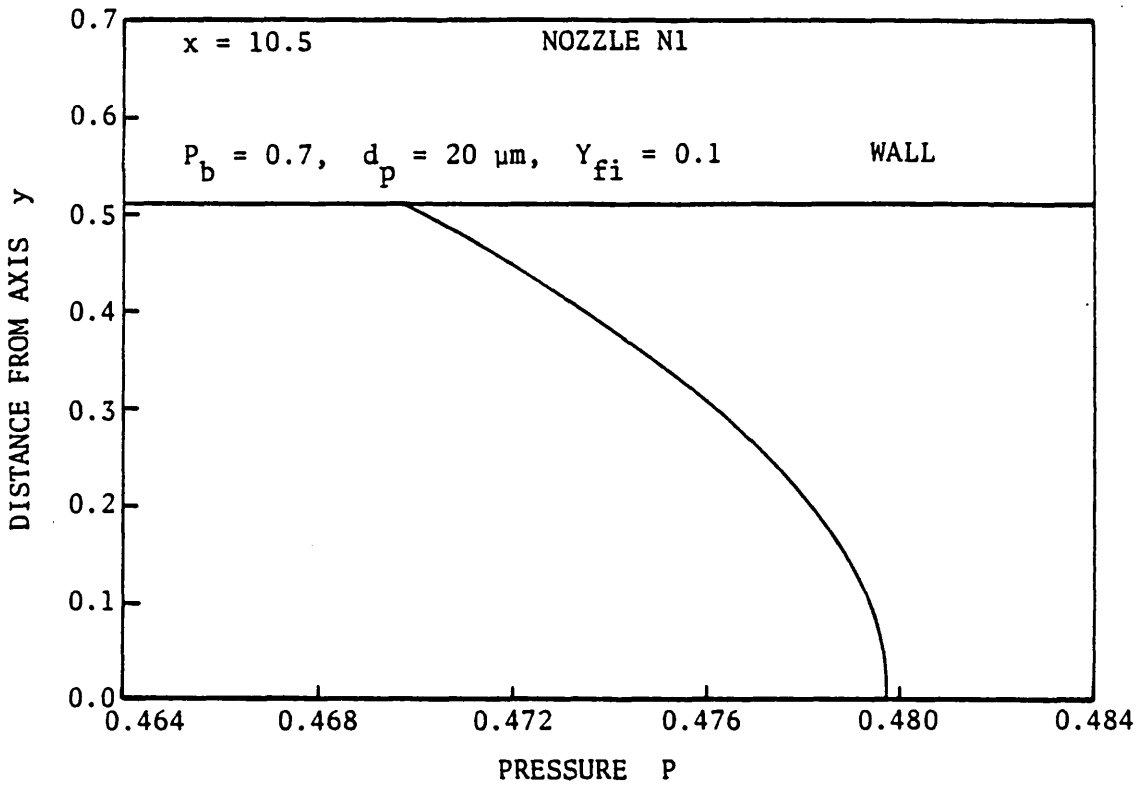


Fig. 6.19: Crosswise variation of the pressure in a shocked mixture flow at x = 10.5

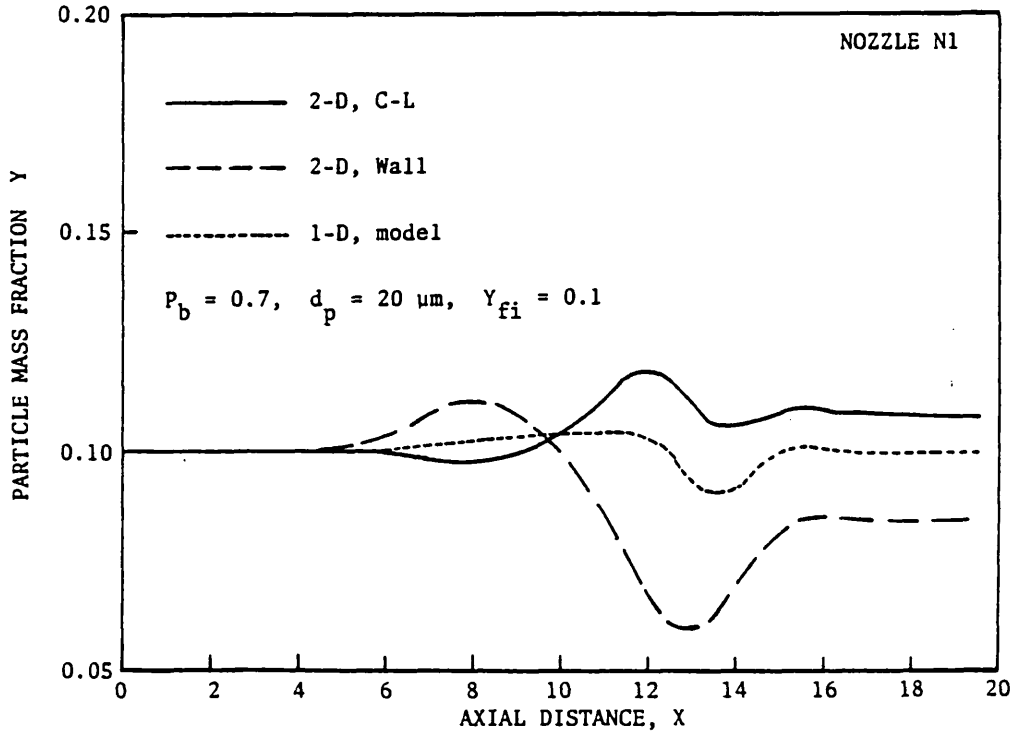


Fig. 6.20: Predicted one- and two-dimensional particle mass fractions along nozzle N1

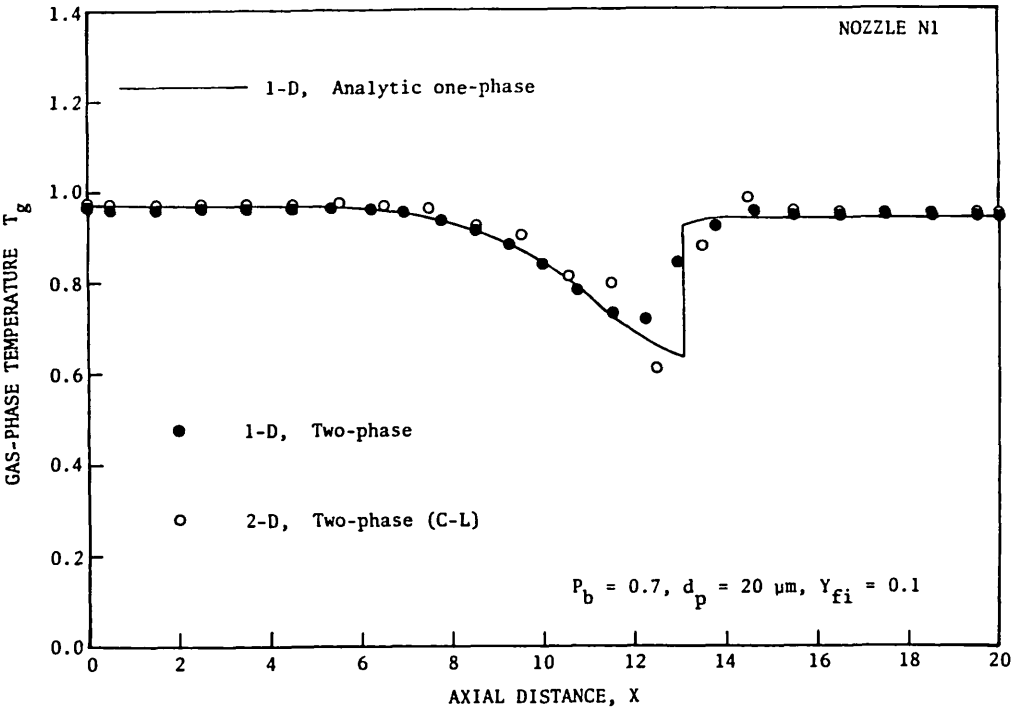


Fig. 6.21: Predicted one- and two-dimensional (axis) gas-phase temperature along nozzle N1

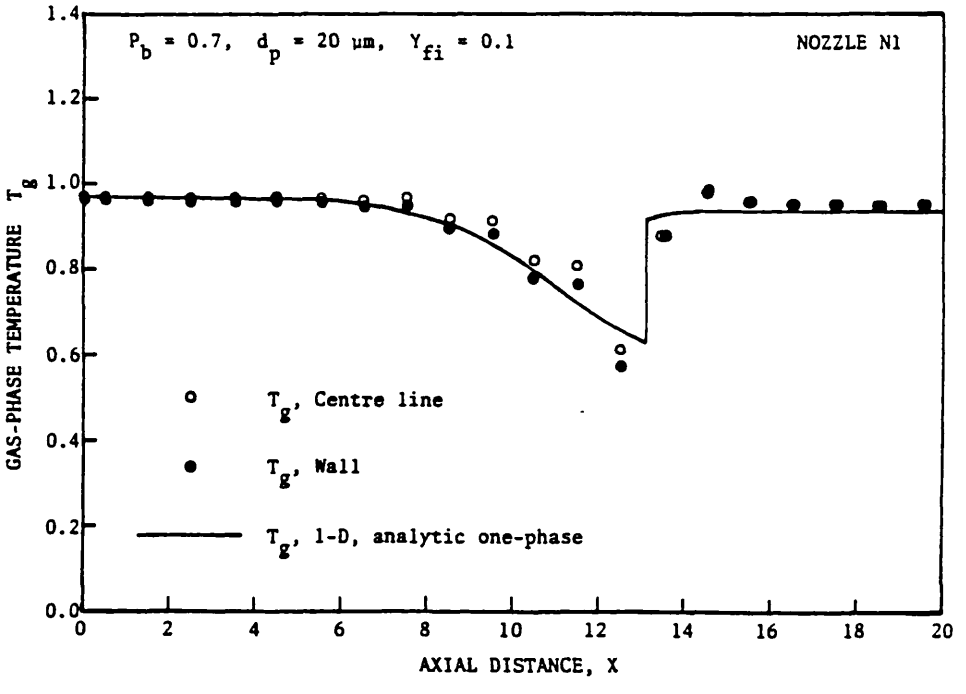


Fig. 6.22: Predicted axis and wall gas-phase temperatures along nozzle N1

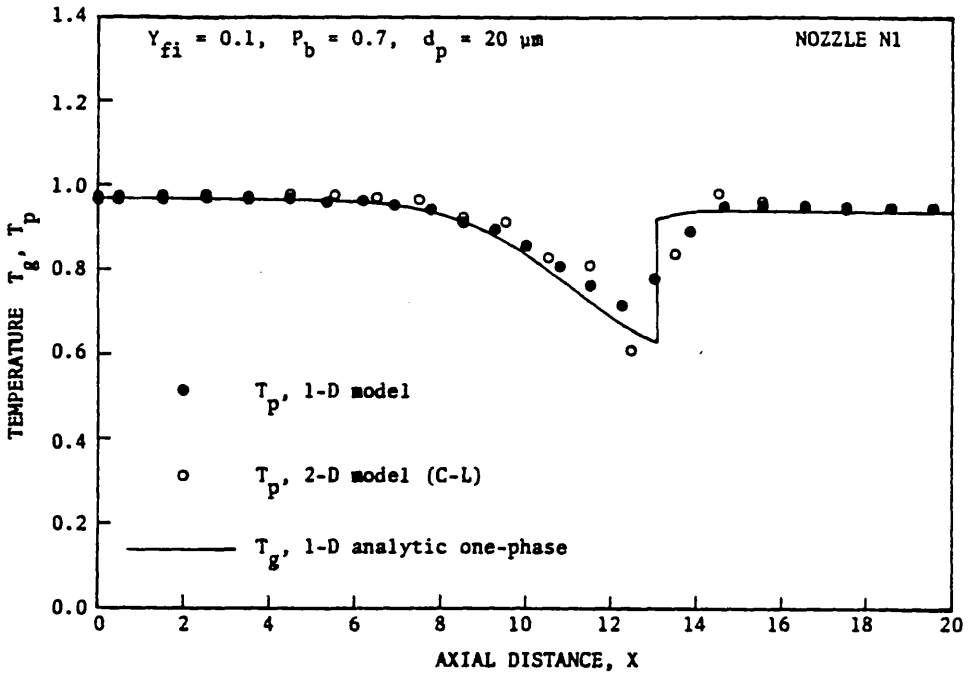


Fig. 6.23: Predicted one- and two-dimensional (axis) particle temperature along nozzle N1

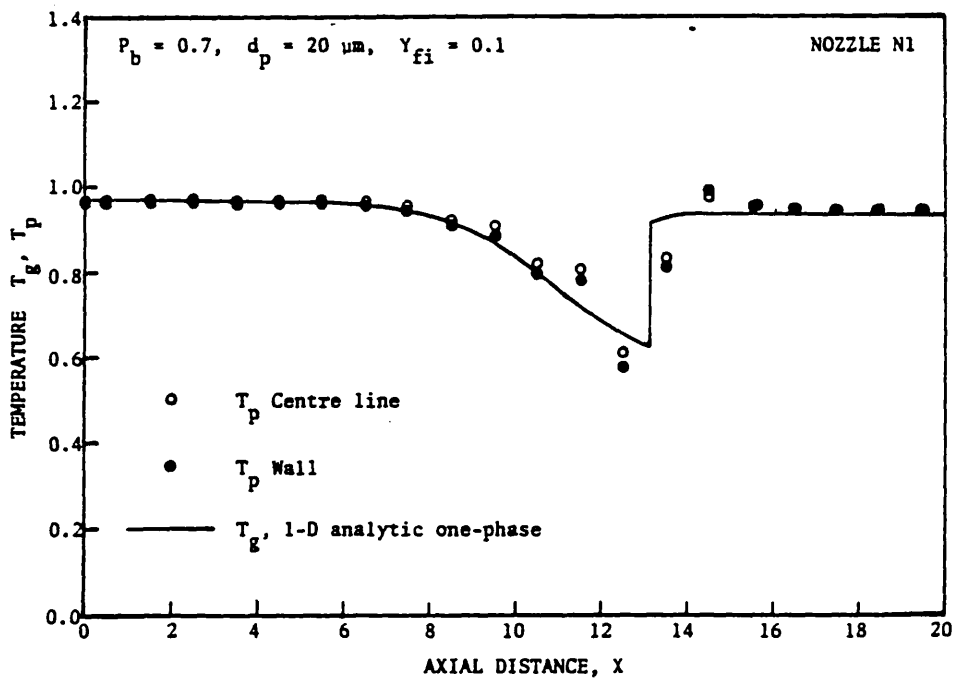


Fig. 6.24: Predicted axis and wall particle temperatures along nozzle N1

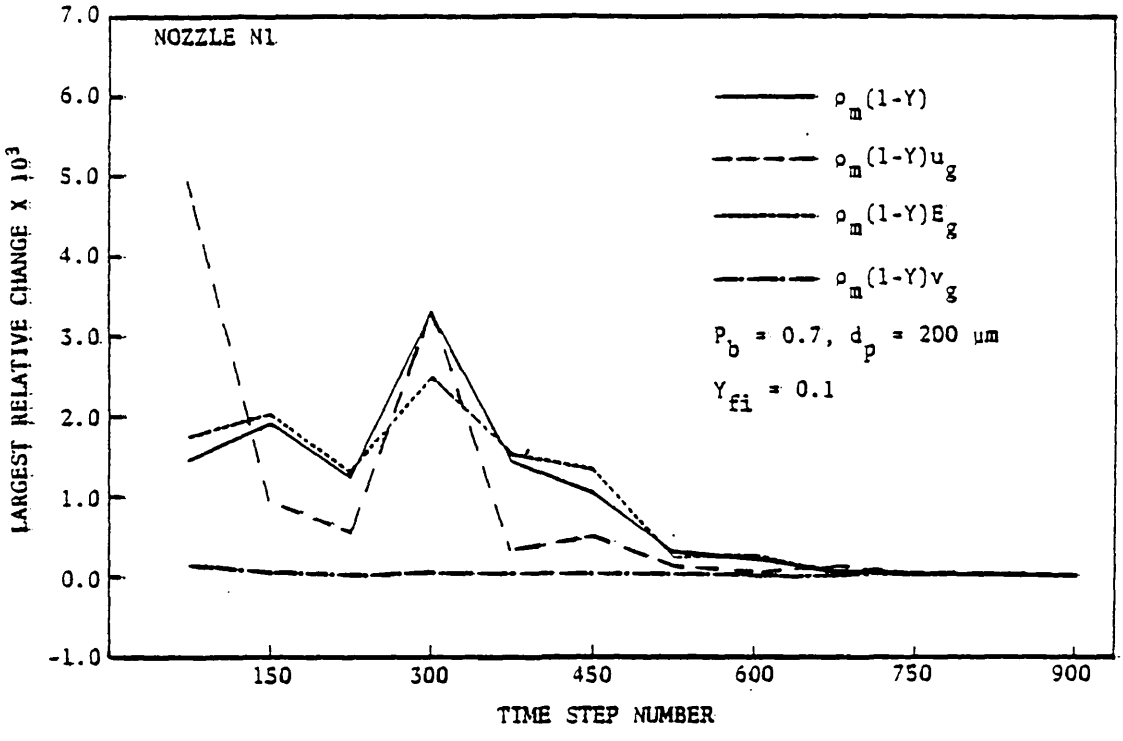


Fig. 6.25: Largest relative change of the gas-phase conserved flow variables versus number of time steps for shocked mixture flow

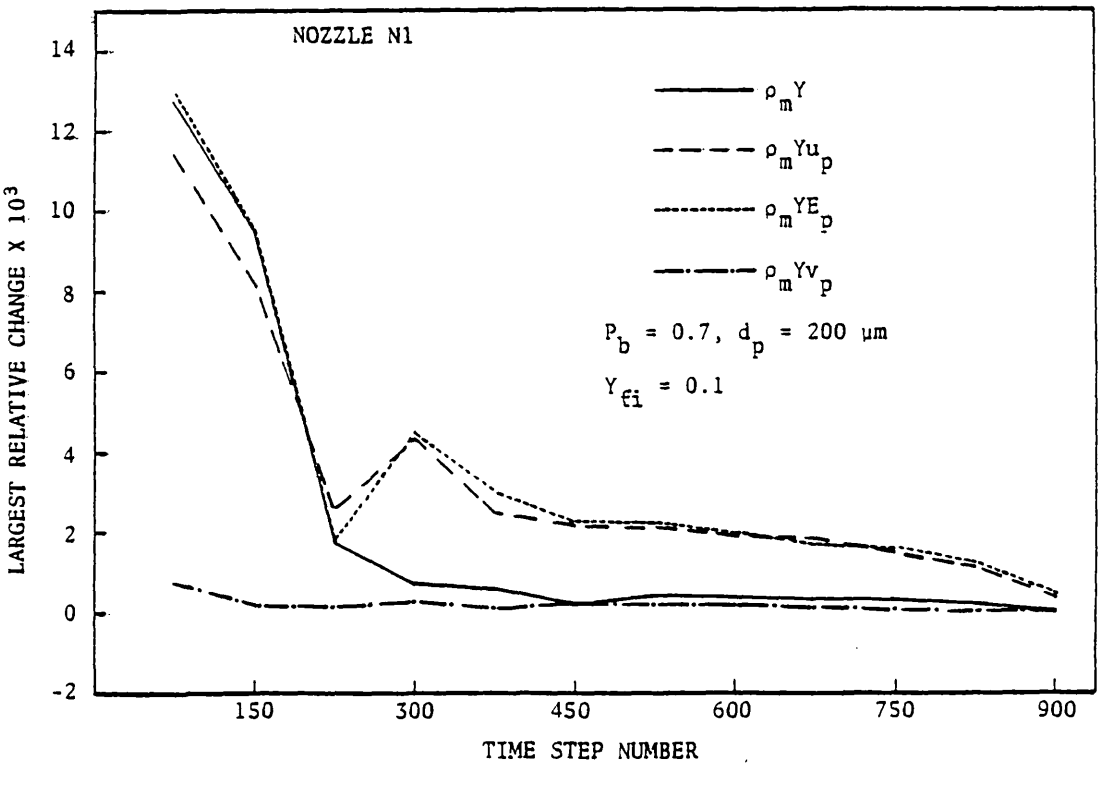
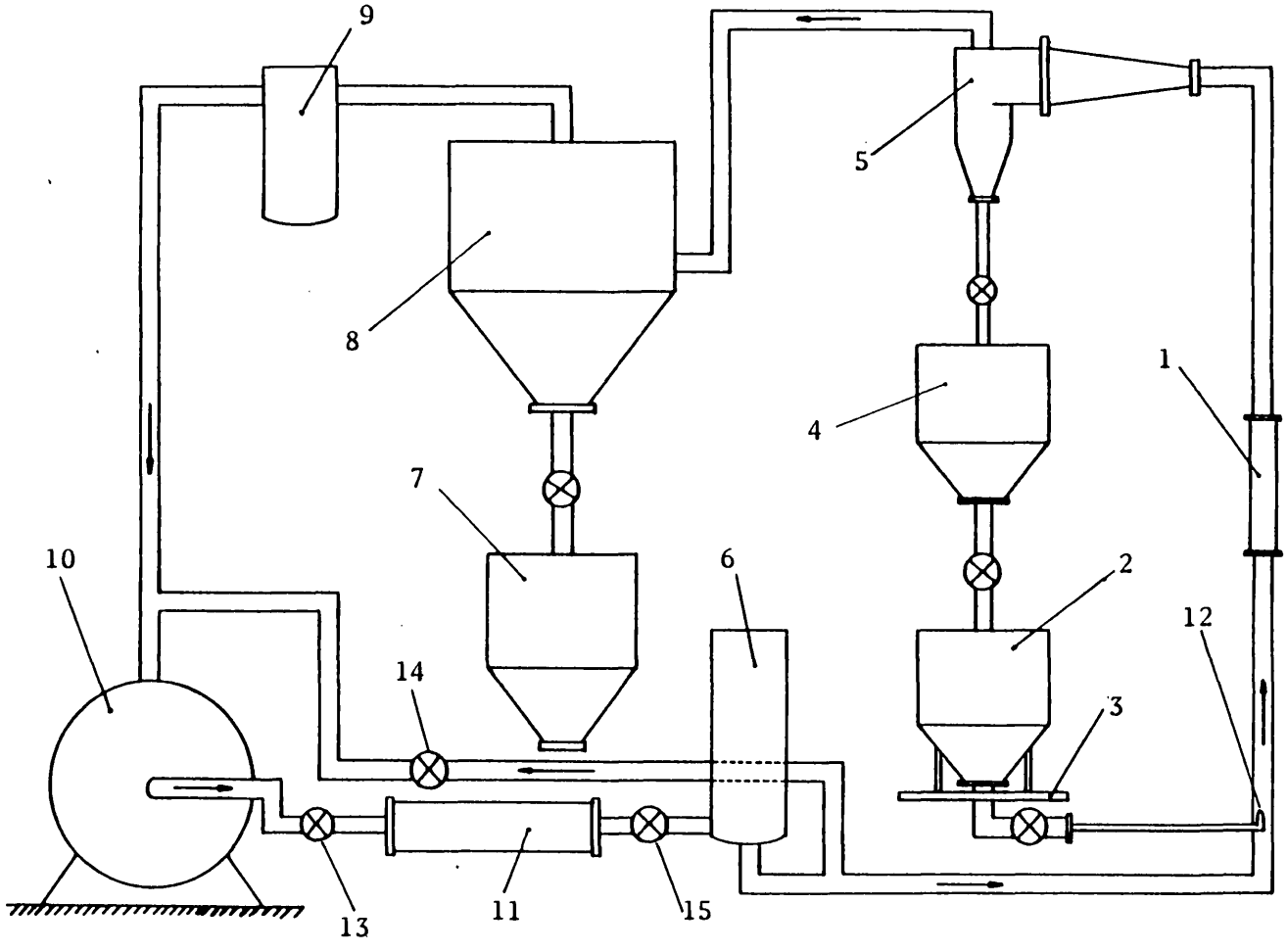


Fig. 6.26: Largest relative change of the particulate phase conserved flow variables versus number of time steps for shocked mixture flow



(1) Test section
(2) Feed hopper
(3) Scales
(4) Collection hopper
(5) Cyclone separator
(6) After cooler
(7) Collection hopper
(8) Pressure vessel (contains pocket filter unit)
(9) Compressor pipeline filter
(10) Blower
(11) Silencer
(12) Solid feed
(13) Check valve
(14) Throttling valve
(15) Pressure relief valve

Fig. 7.1: Arrangement of gas-solids flow rig

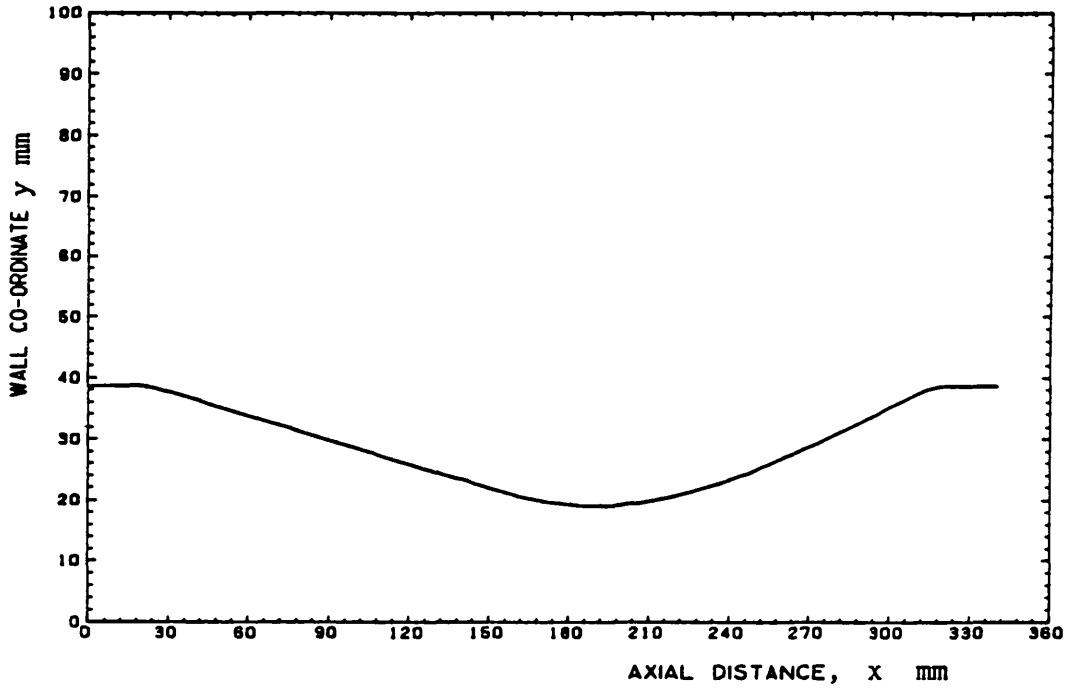


Fig. 7.2: Experimental nozzle profile

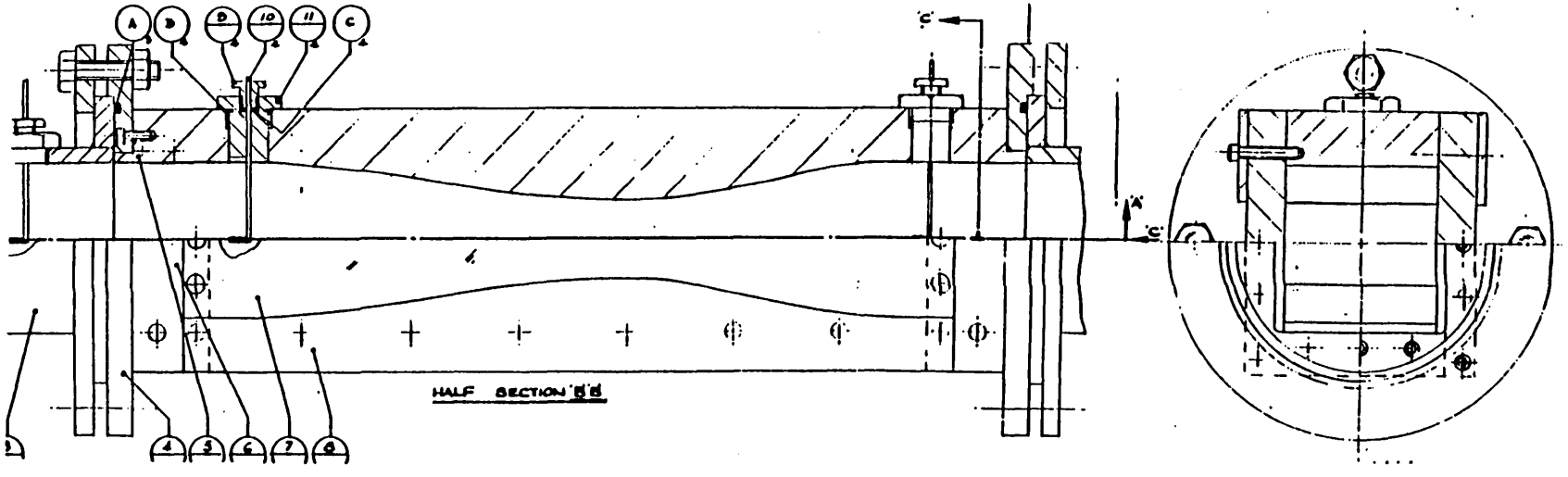


Fig. 7.3: The experimental test section

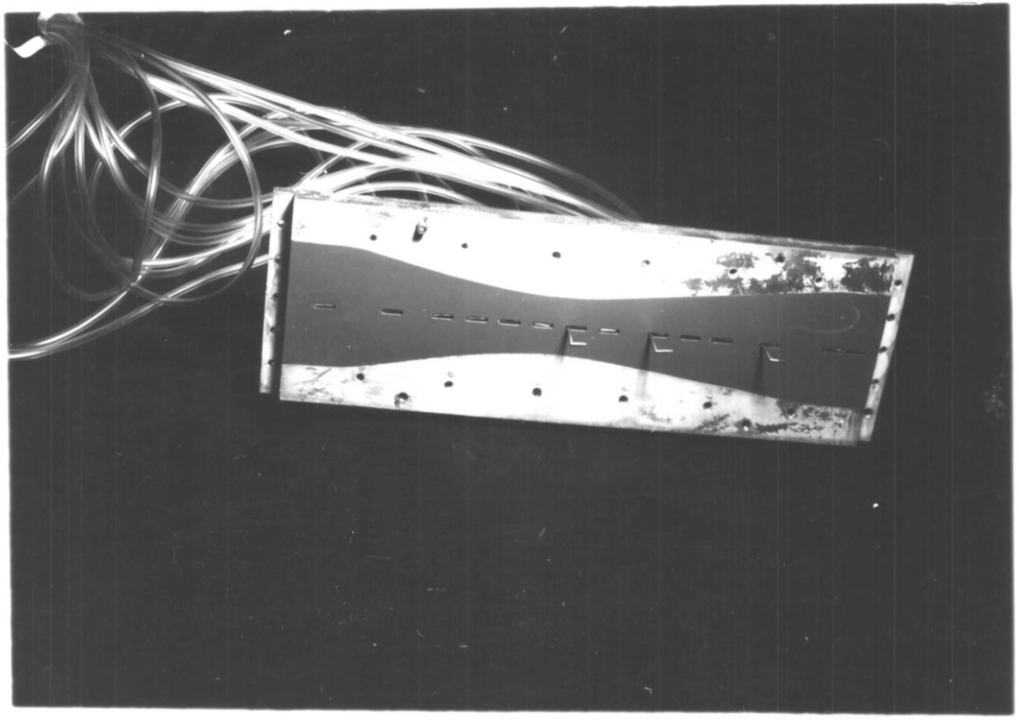


Fig. 7.4 Pitot tubes arrangement for gas-phase velocity measurements.

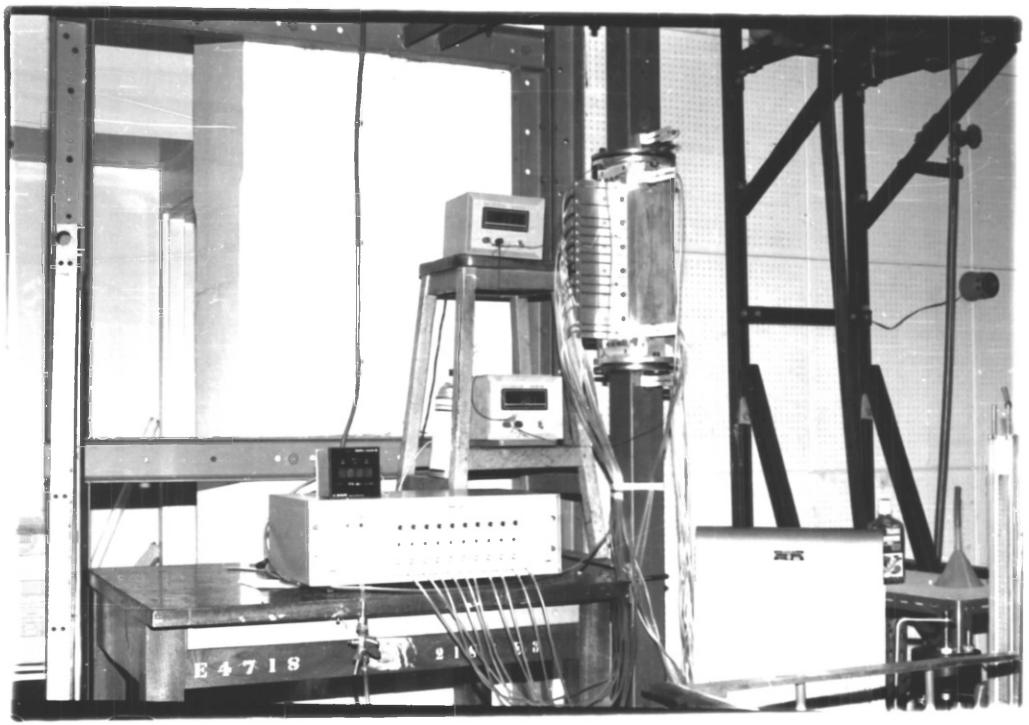


Fig. 7.5 Experimental arrangement for pressure measurements.

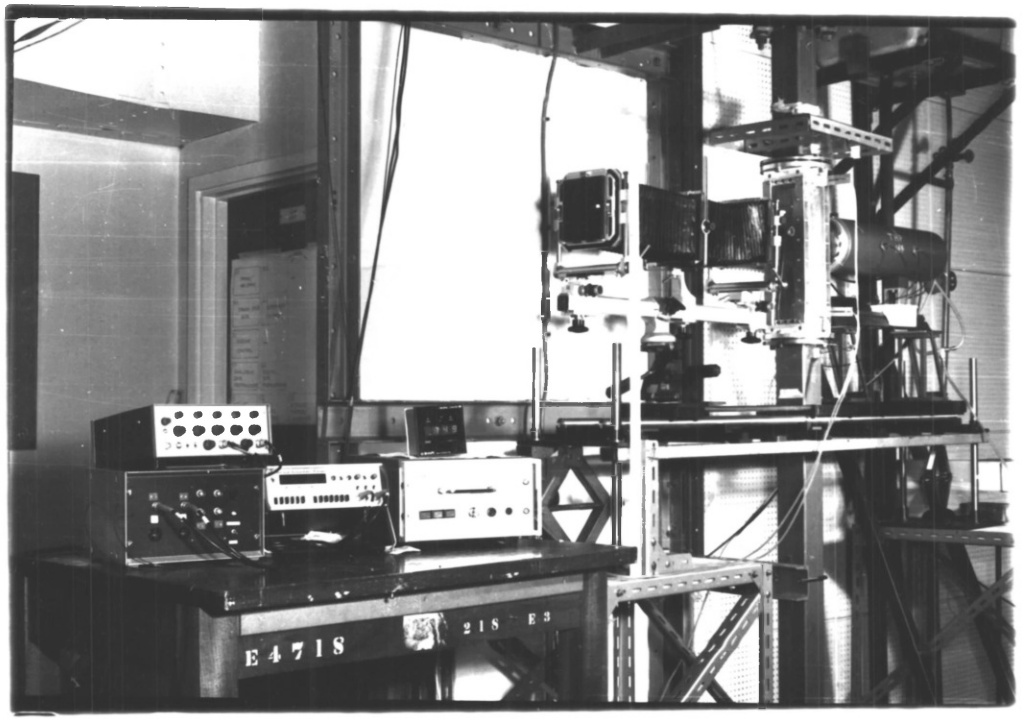


Fig. 7.6 Experimental arrangement for the double flash photography.

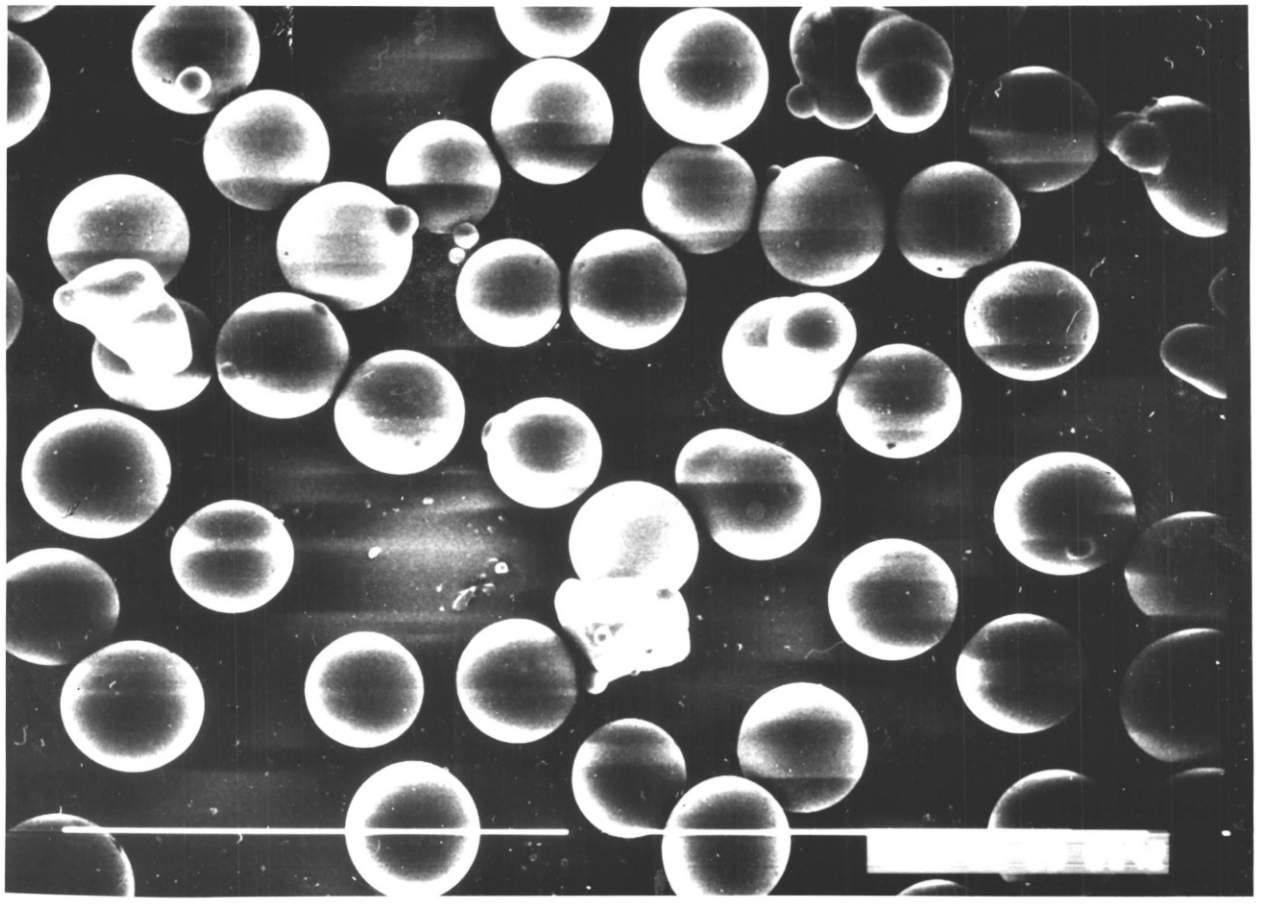


Fig. 7.7 Electron microscope photograph of the glass beads used in the experiment (each white line represents 1 mm).

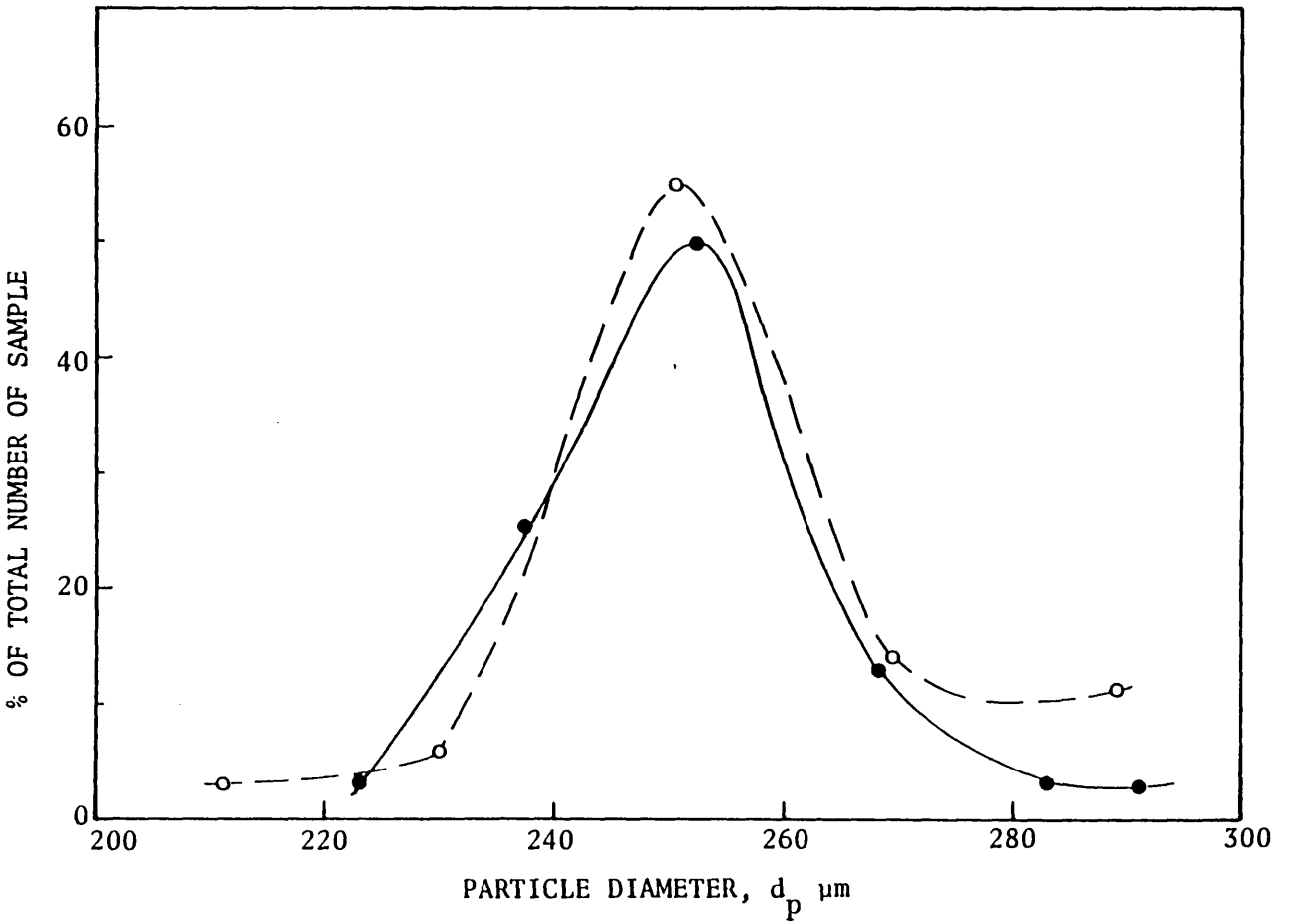


Fig. 7.8: Particle size distribution of the glass beads used in the experiment

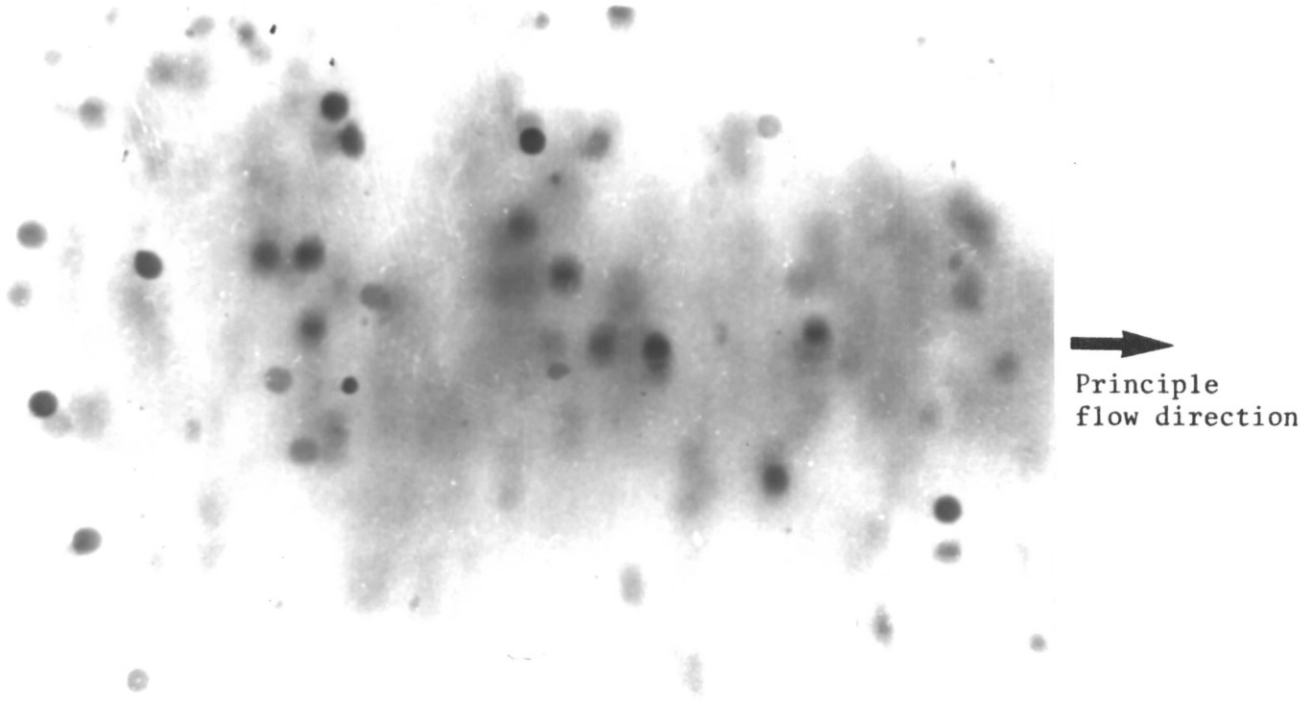


Fig. 7.9: Double flash photograph (half total area)

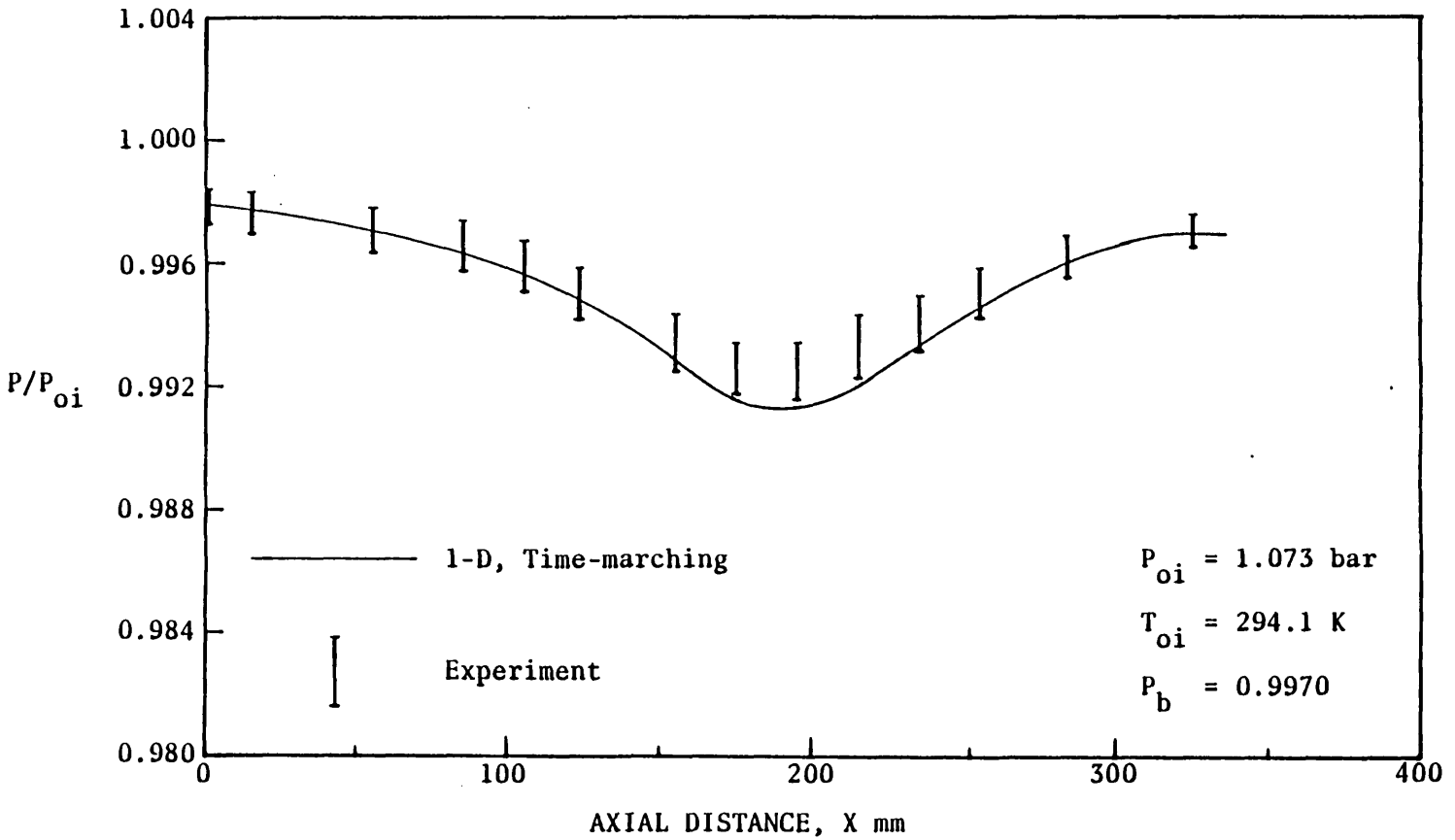


Fig. 7.10: Predicted and experimental pressure along the experimental nozzle axis (Y_{fi} = 0.092).

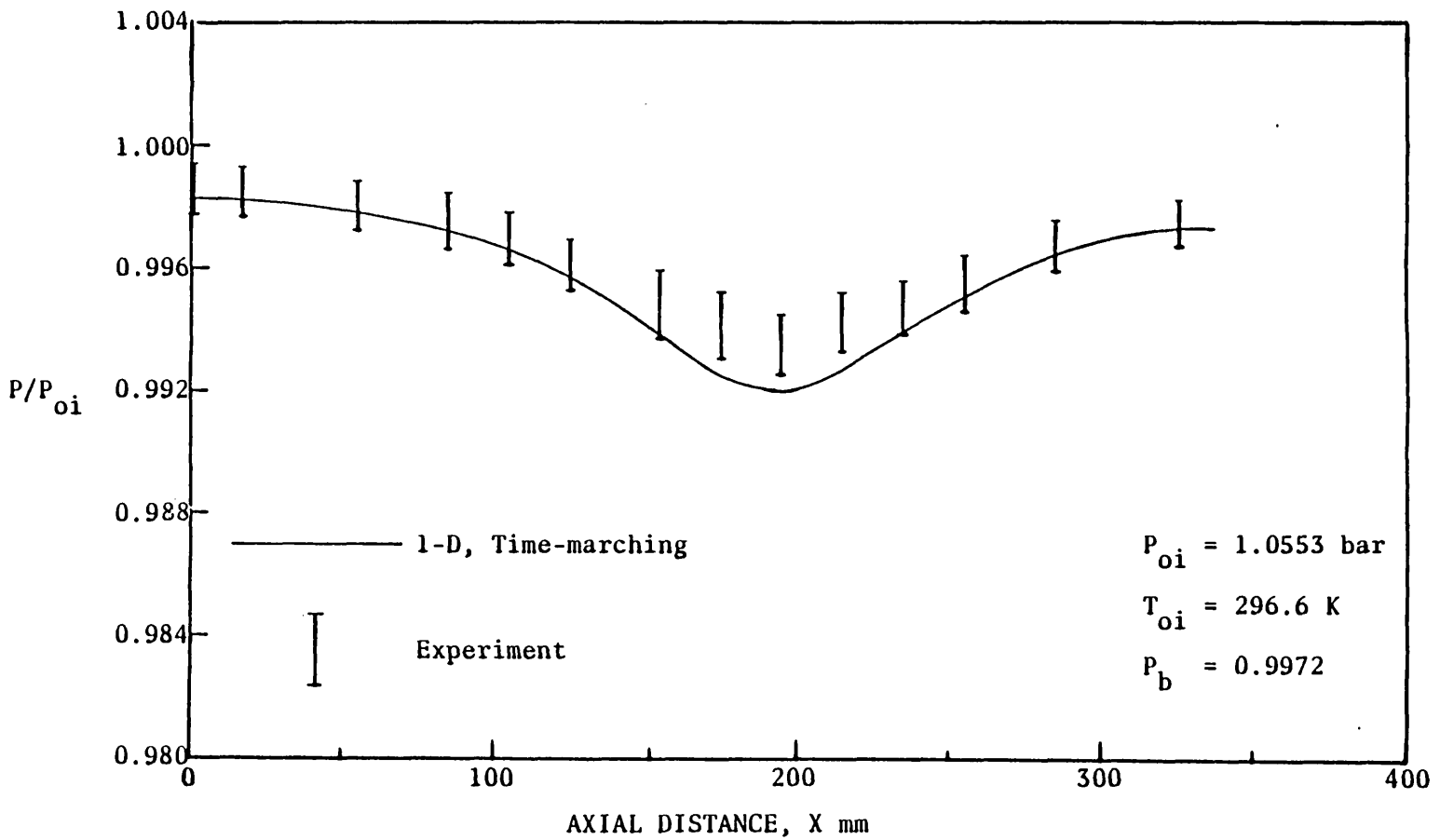


Fig. 7.11: Predicted and experimental pressure along the experimental nozzle axis for $Y_{fi} = 0.419$

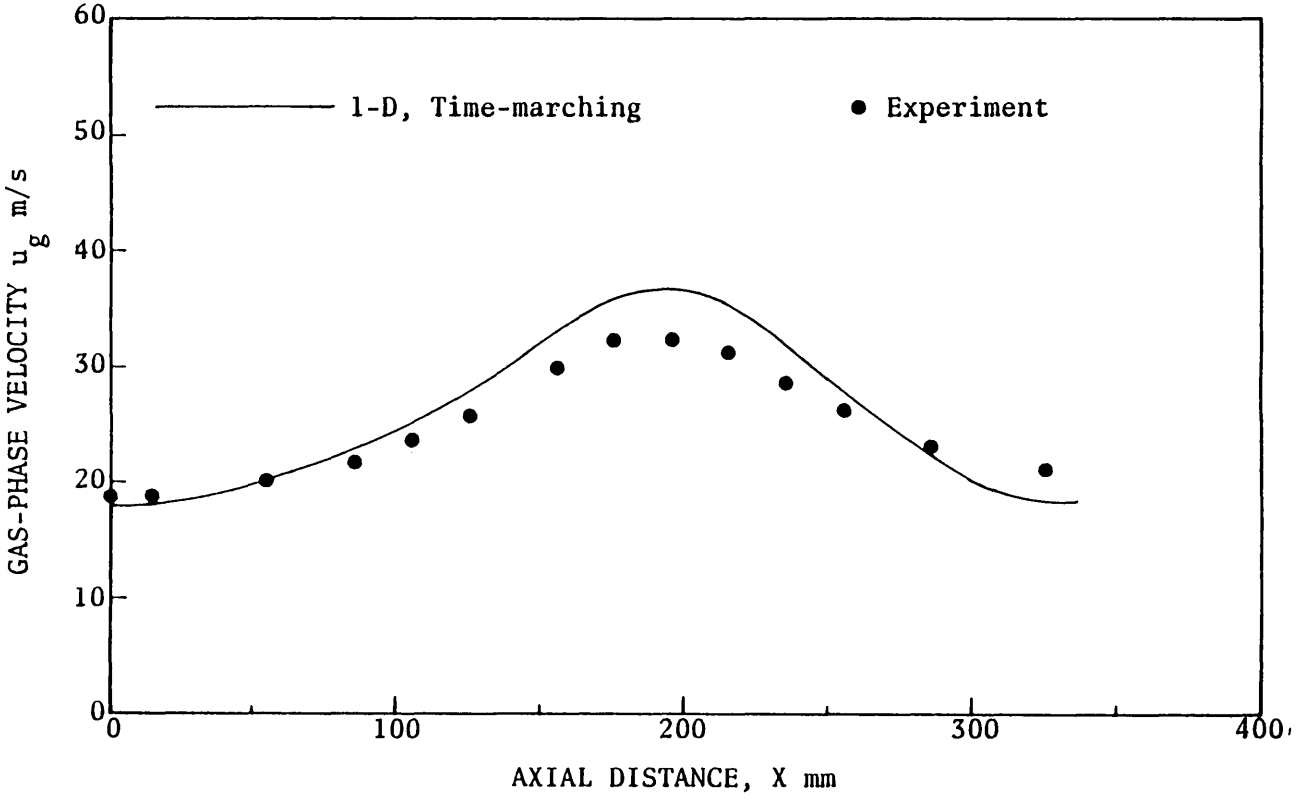


Fig. 7.12: Predicted and experimental gas-phase velocity along the experimental nozzle axis for a mixture with $Y_{fi} = 0.092$.

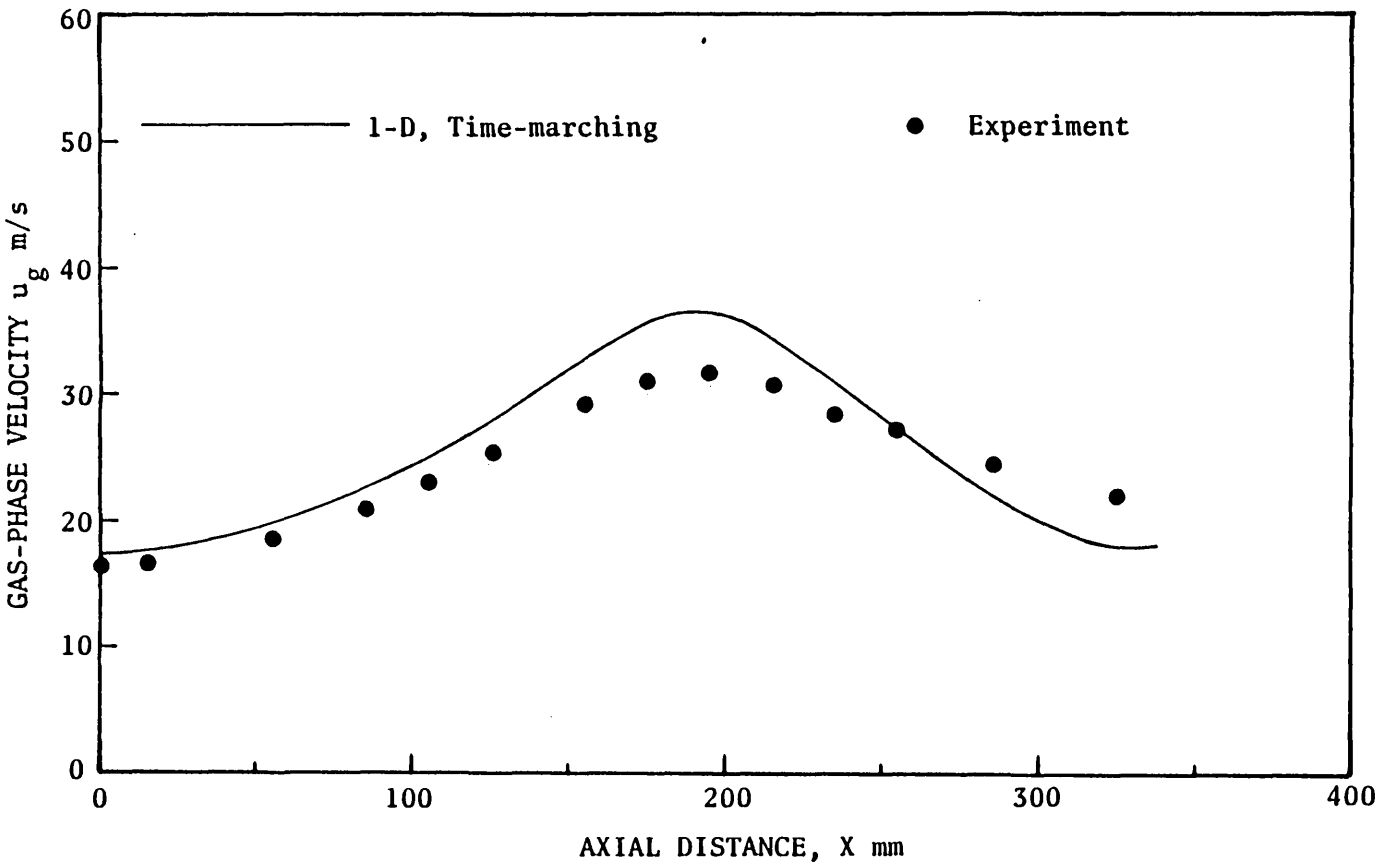


Fig. 7.13: Predicted and experimental gas-phase velocity along the experimental nozzle axis for a mixture with $Y_{fi} = 0.419$

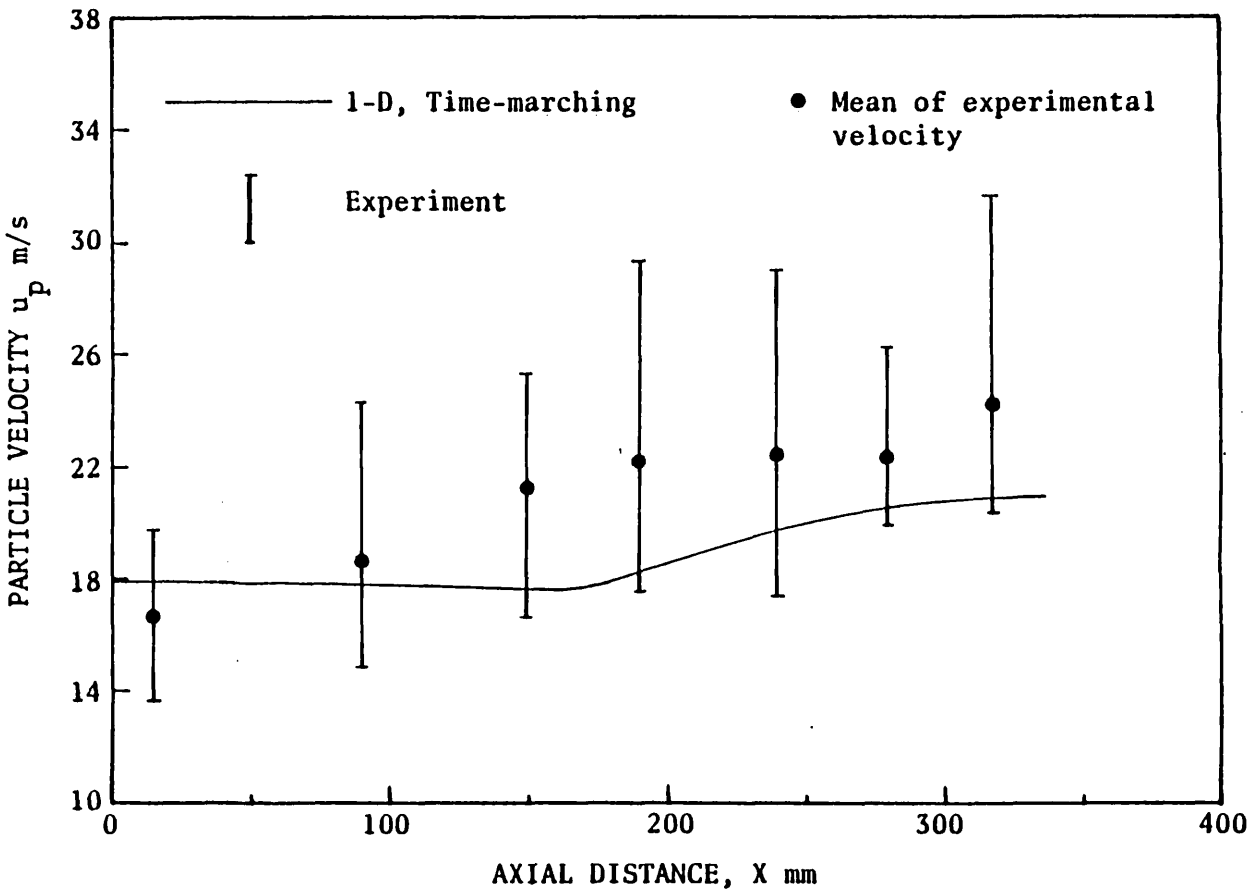


Fig. 7.14: Predicted and experimental particle velocity along the experimental nozzle axis (Y_{fi} = 0.092)

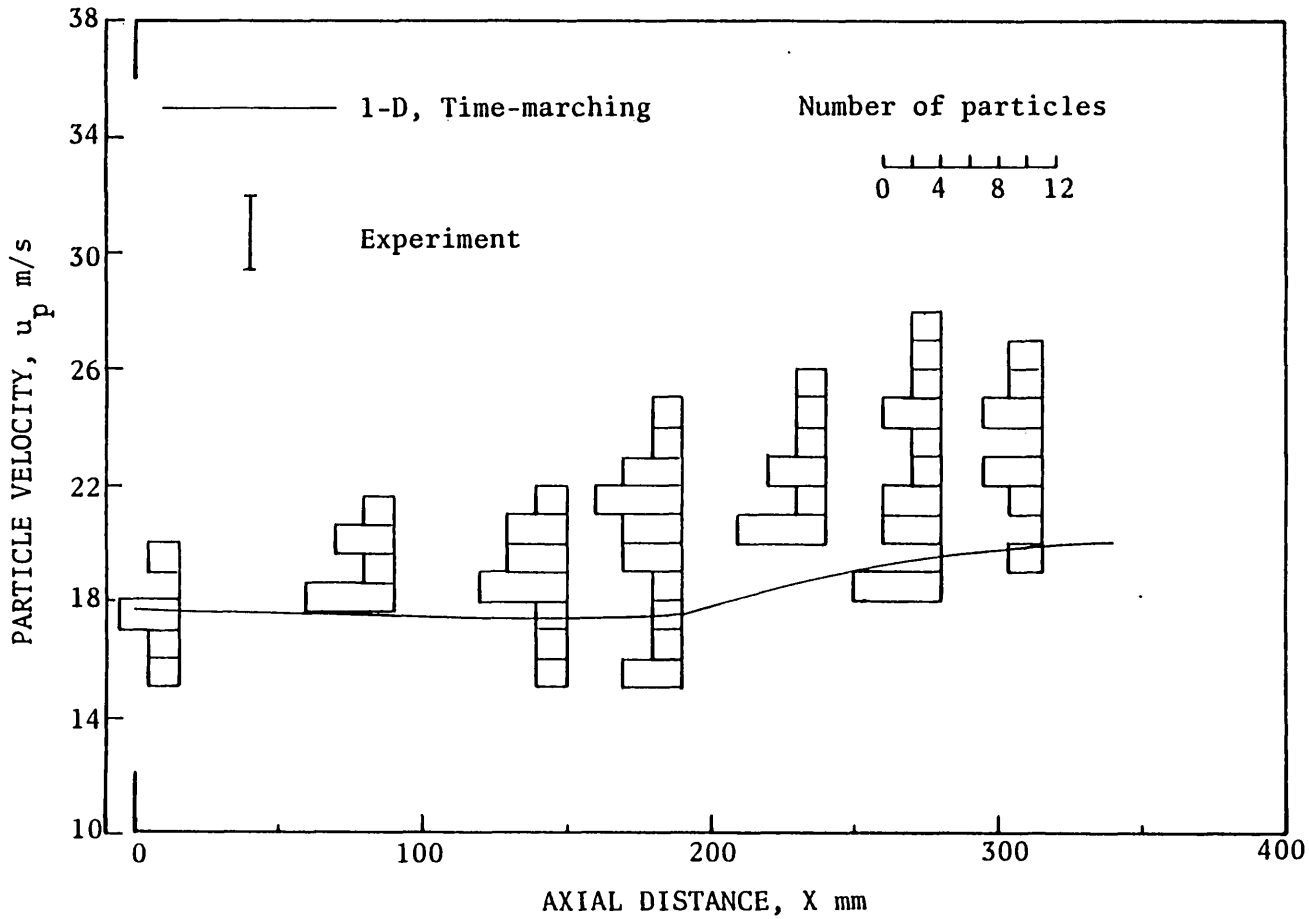


Fig. 7.15: Predicted and experimental particle velocity along the experimental nozzle axis (Y_{fi} = 0.419)